Experimental and Numerical Analysis of Three-Dimensional Free-Surface Turbulent Vortex Flows with Strong Circulation

a dissertation presented by

Sean Mulligan

in full fulfilment of the requirements

for the degree of

Doctor of Philosophy

Supervisors: John Casserly and Dr. Richard Sherlock

Submitted to the Institute of Technology, Sligo

September, 2015

Declaration of Authenticity

I declare that all material presented in this dissertation, to the Institute of Technology, Sligo, is my own work, or fully and specifically acknowledged wherever adapted from other sources. The work has been gathered and utilised to fulfil the purposes of this study and has not been previously submitted to any other university for a higher degree.

PhD Candidate: _____ **Date:** _____

Abstract

Strong free-surface vortex flows are widely employed in various civil engineering and industrial applications. However, a review of the state-of-the-art suggests that a number of areas surrounding the underlying flow mechanics in these systems requires additional attention and are therefore explored in this study. The research focuses on experimental and numerical analysis as well as analytical investigations of the flow problem.

Experimental modelling was performed in two phases: investigation into the effects of the approach flow geometry and an exploration of the mean three-dimensional velocity fields and secondary flow processes. Twelve geometries of a typical scroll type vortex chamber were constructed and independently tested in a customised hydraulic test rig. Model discharges were monitored using a magnetic flow meter and the approach flow depths and water surface profiles were monitored using a depth gauge apparatus. The horizontal velocity field in the far- to mid-field was measured using a 2D particle tracking velocimetry system. Particle streak velocimetry was employed to determine the near-field tangential and axial velocity fields. The results highlighted an explicit dependence of the circulation number N_Γ and the discharge number N_Q on the approach flow conditions. Two empirical auxiliary parameters k_α and n_α were proposed and further modelled to yield an alternative depth-discharge equation. The model was validated using a scaled model and a prototype. Scale effects in the physical models were found to be negligible.

The investigation of the primary flow field indicated that the tangential velocity field was independent of the sub-surface depth away from the tank boundaries. Using the available velocity data and laser-induced fluorescence images, the radial velocity was observed to be confined at the vessel floor and free-surface. The axial velocity appeared to be concentrated in a downward direction in the core region as well as in a newly observed upward direction at the tank periphery. Further analysis showed that the ideal irrotational tangential velocity model agrees with the experimental data in the far-field. However, large discrepancies were observed in the near-field close to the vortex core. Based on analytical and numerical analysis, it was proposed that the discrepancy was as a result of the axial velocity gradient in the core region which was not accounted for in the original assumptions of the model. As a result, an alternative tangential velocity profile was devised based on a correction multiplier containing the inverse of the circulation number and the empirical exponent m. The model relieves the discrepancy of the ideal model by reducing it in areas of strong axial flow to within reasonable levels.

Three-dimensional numerical modelling of the strong free-surface vortex was performed using an Eulerian-Eulerian homogeneous multiphase flow model in the ANSYS CFX computational fluid dynamics code. The experimental data was used as a benchmark to compare the solutions of the numerical model for various test cases in a single model. The comparison showed that the maximum solution accuracy was obtained using a radially structured mesh and a solution independent mesh density was presented. The model was strongly dependent on the type of turbulence model used. Standard Reynolds averaged Navier-Stokes equations appeared to be highly dissipative and overestimated the generation of turbulence in the core region which generated significant errors in the solution. The modified shear stress transport with curvature correction as well as the Reynolds stress models delivered the greatest model accuracy. It was also found that transient modelling was necessary to resolve the unsteady features of the flow field, namely that of free-surface oscillations and the radial flow field. However, the final comparison using the Reynold Stress models nonetheless rendered a significant error in under predicting the free-surface and over predicting the tangential velocity distribution by approximately 12 and 22 % respectively. It was concluded that further refinement of the mesh at the free-surface and in the drop shaft region was required to further improve the numerical solution.

In a final contribution, based on the experimental and numerical observations of the primary and secondary flow fields, an alternative description of the flow mechanics in a strong free-surface vortex was made based on the concept of a newly defined ‘virtual Taylor-Couette’ flow system. Based on this flow representation, a hypothetical description highlighting the likely stages of stability based on various states of the ‘Taylor-like’ vortices which occur in the secondary flow field was proposed. The overall description serves to provide a universal scientific understanding of both ‘weak’ and ‘strong’ free-surface vortices as well as the transitional dissipative state at a depth coinciding with the critical submergence.

Acknowledgments

A PhD study is a truly challenging journey. For me, this would not have been possible without the aid and support provided by countless numbers of people which I have encountered over the past five years. I would like to take this opportunity to express my gratitude to a number of these people.

- I would firstly like to thank my supervisors John Casserly and Dr. Richard Sherlock for their continuous support, enthusiasm and professional guidance throughout the project.
- I would also like to thank Dr. Philip Hull for his involvement as an academic supervisor in the project in its initial stages.
- Thanks to Head of Research, John Bartlett and research administrators Mary Mc Loughlin and Ursula Cox for their continuous support.
- I am especially grateful to my mother and father. Mum and Dad, I can't describe enough the value of your presence, love and kind support during each and every stage of my academic work. You have always realised the importance of my studies and for that reason you have persistently went out of your way to ensure that I had very little to do but concentrate on my work. Thank you!
- Special thanks to Dr. Leo Creedon for contributing his time to have fruitful mathematical discussions on the topic of vortex flow throughout the later stages of the study.
- I am very thankful to Kathleen and Gerry Foley who have always welcomed me in their home for respite and great discussion. Also to my auntie Maria Keeney for her perpetual kindness and support throughout my academic studies.
- I would like to express thanks to my postgraduate colleagues and friends Glenn Gordon, William Wilson, James Feighan, James Murray, Fionn Downes and Micheal O Cearbhallain (to name a few) who would never shy away from lending a helping hand when it was needed.
- I appreciate the support provided by technical staff at IT Sligo, namely Joe Kelly and John Comiskey.
- I am grateful to the efforts made by the IT Sligo Development/Business Operations, Estates Management and associated staff in securing laboratory space and allocating resources to develop the hydraulics facility.
- I would like to thank a number of very close friends of mine: Adrian, Scott, Shane, Cian, Alan Liam W, Liam R and Paul who have continuously showed interest in my work and have always been there when the going got tough.
- I am grateful to my colleague and friend, Sean Mullery (www.seanmullery.com) for contributing his time on a number of occasions to take exceptional photographs of the hydraulic test rig and vortex flows.
- Finally, I would like to thank the Institute of Technology, Sligo and the Irish Research Council (IRC) for their financial support of this project.

Contents

Abbreviations

Notation	Description
HPP	hydroelectric power plant
SFR	sodium fast reactor
PTV	particle tracking velocimetry
PIV	particle image velocimetry
PSV	particle streak velocimetry
RSM	Reynolds stress model
SST	shear stress transport
CC	curvature correction
BSL	baseline
SSG	Speziale, Sarkar, Gatski
EARSM	explicit algebraic Reynolds stress model
LES	large eddy simulation
RANS	Reynolds averaged Navier-Stokes equations
SAS	scale adaptive simulation
RNG	renormalisation group
DNS	direct numerical simulation
CFD	computational fluid dynamics
LIF	laser induced fluorescence
P-LIF	planar laser induced fluorescence
ICHEC	Ireland centre for high-end computing
AOI	area-of-interest
FOV	field-of-view
FEA	finite element analysis
FVM	finite volume method
NPSS	non-purely stretching sustained
PSS	purely stretching sustained
ARL	Alden research laboratory
DOF	degrees-of-freedom
LDA	laser doppler anemometry
LDV	laser doppler velocimetry
ADV	acoustic doppler velocimetry
VOF	volume-of-fluid
URANS	unsteady Reynolds averaged Navier-Stokes equations

Notation	Description
CFL	Courant, Friedrichs, Lewy
VTC	Virtual Taylor-Couette
CCD	charged coupled device
SMC	second moment closure
RMS	root mean square

Notation

Basic dimensions	
L	length
M	mass
T	time

Notation	**Description**	**Unit**	**Equation**
Essential dimensional parameters and variables			
A	cross sectional area	m^2	
a	air core diameter	m	
a_c	critical air core diameter	m	
a_{cc}	centrifugal acceleration	$m.\ s^{-2}$	
α_a	approach flow angle	°	
b	inlet width	m	
c	constant vortex strength	$m^2.s^{-1}$	$c = v_\theta r$
c_a	vortex strength as a consequence of the approach flow geometry	$m^2.\ s^{-1}$	$c = \widetilde{v_{in}} r$
d	orifice diameter	m	
D_{eff}	outlet diameter	m	
d_p	mean particle diameter	m	
d_τ	diffracted particle image diameter	m	
d_{diff}	diffraction limited image diameter	m	
d_s	drop shaft diameter	m	
E	energy head	m	
$f_\#$	f-stop or f-number	-	
g	gravitational acceleration	$m.\ s^{-2}$	
h_{cr}	critical submergence	m	
h	approach flow depth	m	
h_d	Free-surface depth at the orifice perimeter	m	

Notation	Description	Unit	Equation
h_r	Free-surface depth at radial distance r	m	
h_∞	Water depth in the far-field	m	
h_{PTV}	height of the laser light sheet above the vessel floor	m	
k	turbulent kinetic energy	m	
l	characteristic length	m	
l_m	model characteristic length	m	
lp	Prototype characteristic length	m	
Mo	magnification	-	
n	exponent or time step	-	
N_P	number of fluid phases	-	
p	pressure	kg. m. s^{-2}	
p_∞	Far-field pressure	kg. m. s^{-2}	
P_k	turbulence energy	m	
Q	bulk discharge	$m^3. s^{-1}$	
Q_o	radial flow at core radius	$m^3. s^{-1}$	$Q_o = -2\pi r_c h v_{r_c}$
Q_w	water discharge	$m^3. s^{-1}$	
Q_a	air discharge or air entrainment rate	$m^3. s^{-1}$	
r_o	radius of orifice	m	$r_o = d/2$
r_{in}	inlet radius	m	$r_{in} = D_{\text{eff}}/2 + b/2$
r_∞	arbitrary far-field radial position	m	
r	radial position from the vortex origin	$m^2. s^{-1}$	
r_c	Vortex viscous core radius	m	
r_t	Vortex turbulent core radius	m	
r_D	radius of inlet	m	$r_D = D_{\text{eff}}/2$
r_p	radius of the perimeter at θ_p	m	
r_p	radius of inlet perimeter	m	$r_p = \frac{D_{\text{eff}}}{2} + b + t_w$
So	bottom slope	m/m	
S_{oe}	Stream wise bottom slope	m/m	
S_{MS}	body force	kg. m . s^{-2}	
t_w	thickness of the chamber wall	m	

Notation	Description	Unit	Equation
t	time	s	
t_{PTV}	time separation between laser pulses	s	
$\Delta t_{radialjet}$	thickness of the bottom radial jet	m	
$T\sigma$	surface tension	kg. s^{-2}	
$\vec{u}_r$	Rotational velocity component	m. s^{-1}	
$\vec{u}_t$	translational velocity component	m. s^{-1}	
$\vec{u}_d$	deformation velocity component	m. s^{-1}	
u_τ	friction velocity at the nearest wall	m/s	
U	total velocity vector	m. s^{-1}	
v_θ, v_r, v_z	tangential, radial and axial velocity components	m. s^{-1}	
$v_{\theta max}$,	maximum tangential velocity	m. s^{-1}	
v, u, w	Cartesian velocity components	m. s^{-1}	
v_L	velocity component tangent to the line L	m. s^{-1}	
v_{zo}	constant axial velocity profile at the orifice	m. s^{-1}	
$\tilde{v_z}$	bulk velocity through the orifice	m. s^{-1}	$\tilde{v}_z = 4Q/\pi d^2$
$\tilde{v}_{in}$	average inlet velocity	m. s^{-1}	$\tilde{v}_{in} = Q/bh$
V	volume	m^3	
x, y, z	cartesian coordinates	-	
θ, r, z	cylindrical coordinates	-	
γ	Specific weight	kg. m^{-2}. s^{-2}	
Γ	general circulation	m^2. s^{-1}	
Γ_∞	field circulation	m^2. s^{-1}	$\Gamma_\infty = 2\pi r_\infty v_{\theta\infty}$
Γ_r	circulation at radius r	m^2. s^{-1}	$\Gamma_r = 2\pi r v_\theta$
$\tilde{\Gamma}$	bulk circulation	m^2. s^{-1}	$\tilde{\Gamma} = 2\pi r_{in} Q/bh$
δt	image exposure time	s	
ε	eddy viscosity	m^2. s^{-1}	
θ_p	angle to the point of interest from the inlet	∘	
λ_{wl}	wavelength	nm	
μ	dynamic viscosity	kg. m^{-1}. s^{-1}	
μ_t	eddy viscosity (dynamic based)		

Notation	Description	Unit	Equation
ν	kinematic viscosity or momentum diffusivity	$m^2.s^{-1}$	
ξ	positive factor of proportionality	-	
π	pi - mathematical constant ~ 3.142	-	
ρ	density	$kg.m^{-3}$	
ρ_p	Particle density	$kg.m^{-3}$	
σ	shear stress	$kg.m.s^{-2}$	
τ	shear stress	$kg.m.s^{-2}$	
τ_l	local laminar shear stress	$kg.m.s^{-2}$	
ν	kinematic viscosity or momentum diffusivity	$m^2.s^{-1}$	
ν_e	effective viscosity	$m^2.s^{-1}$	$\nu_e = \nu + \varepsilon$
ϕ	volume fraction	-	
ω	rate of rotation	s^{-1}	
$\Omega_\theta, \Omega_r, \Omega_z$	vorticity components	s^{-1}	

Notation	Description	Equation
Dimensionless parameters, coefficients and factors		
a_c/d	dimensionless air core diameter	-
A_o	Einstein and Li's (1955) dimensionless Reynolds number	$A_{oe} = Q_o/2\pi h(\nu)$
A_{oe}	Einstein and Li's (1955) dimensionless turbulent Reynolds number	$A_{oe} = Q_o/2\pi h(\varepsilon + \nu)$
C_d	coefficient of discharge	$C_d = 4Q/(\pi d^2\sqrt{2gh})$
C_{λ,N_Γ}	Viparelli's coefficient of discharge	
C	Courant number	$C = u\Delta t/\Delta x$
Fr	standard Froude number	$Fr_d = u/\sqrt{gl}$
Fr_d	intake Froude number	$Fr_d = \widetilde{v_z}/\sqrt{gd}$
Fr_{in}	inlet Froude number	$Fr_{in} = \widetilde{v_{in}}/\sqrt{gh}$
h/d	dimensionless approach flow depth	-
$(h/d)_{cr}$	dimensionless critical approach flow depth	-
K	Kolf number	$K = \frac{\pi}{4} N_\Gamma = \pi\Gamma_\infty d/4Q$

Notation	Description	Equation
k	factor of proportionality	-
k_α	empirical coefficient	-
m	empirical parameter designating the extent of the axial flow field	-
n	exponent or time step representation	-
n_α	empirical exponent	-
N_Γ	swirl parameter	$\mathrm{N}_\Gamma = \Gamma d/Q$
$\mathrm{N}_{\Gamma E}$	Viperellis circulation number	$\mathrm{N}_{\Gamma E} = \Gamma^2/2gEd^2$
N_c	swirl parameter	$\mathrm{N}_c = \mathrm{N}_\Gamma \mathrm{Fr}_d = c/\sqrt{g}d^{\frac{3}{2}}$
N_v	vortex number (Stevens and Kolf, 1957)	$\mathrm{N}_v = \Gamma/d\sqrt{2gh}$
N_Q	standard discharge number	$\mathrm{N}_Q = Q/d^{\frac{5}{2}}\sqrt{g}$
Re	standard Reynolds number	$Re_d = ul/\nu$
Re_v	vortex Reynolds number	$\mathrm{Re}_v = \Gamma_\infty/\nu$
Re_d	intake Reynolds number	$\mathrm{Re}_d = 4Q/\pi d\nu$
Re_r	radial Reynolds number	$\mathrm{Re}_r = Q/h\nu$
Re_p	particle slip Reynolds number	$\mathrm{Re}p = \lvert u - v_p \rvert d_p/\nu$
Ro_r	radial Rossby number	$\mathrm{Ro}_r = v_r/(\Gamma\Omega_z)^{\frac{1}{2}}$
Ro_z	axial Rossby number	$\mathrm{Ro}_z = \mathrm{Ro}_u\frac{z}{r} = v_z/(\Gamma\Omega_z)^{\frac{1}{2}}$
Sc_t	turbulence Schmidt number	$\mathrm{Sc}_t = \varepsilon/\Gamma_t$
Ta	Taylor number	$\mathrm{Ta} = \frac{\omega^2 {a_c}^4}{\nu^2} = \frac{\Gamma_{a_c}}{2\pi\nu}$
Ta_t	turbulent Taylor number	$\mathrm{Ta}_t = \frac{\omega^2 {a_c}^4}{(\nu+\varepsilon)^2} = \frac{\Gamma_{a_c}}{2\pi(\nu+\varepsilon)}$
We	standard Weber number	$\mathrm{We} = \rho v^2 l/\sigma$
We_d	intake Weber number	$\mathrm{We}_d = \rho {\tilde{v}_z}^2 d/\sigma$
y_α	dimensionless approach flow factor	$y_\alpha = bh/r_{in}d$
y^+	dimensionless wall distance	$y^+ = \frac{u_\tau \Delta y}{\nu}$
α	approach flow geometry parameter	$\alpha = r/d$
β	blend factor	-
λ	dimensionless critical cross sectional area	$\lambda = (a_c/d)^2$
ξ	positive factor of proportionality	-

Notation	Description
Mathematics	
Δ	difference
f	function
∞	infinity
∇	grad – del operator represented by the 'nabla' symbol
∂	partial operator
$\tilde{o}$	bulk quantity
$\bar{o}$	average quantity
$\vec{o}$	vector quantity
o'	fluctuating quantity
φ	scalar variable
$\Delta\vec{n}$	surface vector at ip
δ	standard deviation
Subscripts	
i, j, k	unit vector notation
ip	integration points
up	upwind node
max	maximum limiting state or condition
min	minimum limiting state or condition
p	Displacement or velocity component of particle
act	actual value

Note: due to the large number of variables used as a consequence of the combined analytical, experimental and numerical phases of this study, some of the above notation may differ briefly in the main text. However, the coincidence of notation in some parts of the text is only temporary in order to be consistent with previous literature, theoretical manuals (i.e. ANSYS, 2009) or other. The notation in the above table is consistent for the essential variable and parameters throughout the main body of the study.

Chapter 1.

Introduction

SUMMARY

Vortices have long been at the forefront of investigation in natural and industrial fluid mechanics. Their existence have been studied on a far-reaching spectrum spanning from the smallest observable quantised vortices in superfluid liquid helium (order of 10-10 meters) (White et al., 2014) to the rotation of immense galactic systems (on the order of light years) (Shetty et al., 2007) across a broad range of scientific and engineering disciplines. Despite the fact that vortex fluid mechanics is a long studied field, there are still many questions on the nature of these phenomenal flow processes that still remain unanswered. In this study a focus is made on the topic of free-surface vortex flows in the context of civil engineering hydraulic flows; paying particular attention to that of the 'strong' free-surface vortex.

1.1.Overview and Project Motivation

Free-surface vortex flows occur as a result of the interaction of concentrated vortices with the fluid surface in an open channel. This remarkable interaction results in a local depression of the free-surface together with increased rotation in a formation which is commonly referred to as a whirlpool or maelstrom[1]. It's not surprising therefore that free-surface vortex flows have significant implication in civil engineering hydraulics. Apart from their formation as a result of conflicting flow direction (e.g. tidal whirlpools) free-surface vortices are a common occurrence at hydraulic intakes (hydroelectric power plants or pump intakes) where flows are induced by gravitation or local pressure gradients. Under such conditions, there exists an intrinsic competition between the

[1] Originating from the Nordic word (malstrøm) which was first used in English by Edgar Allan Poe in his mythical tale "*A Descent into the Maelström*" in 1841. This story was based on the Moskstraumen: a powerful tidal whirlpool off the Norwegian coast.

rotational motion (which will be described later by the circulation parameter Γ) and the axial flow through the intake. This rotational movement or circulation may be naturally or artificially induced. There are typically two main categories of free-surface vortex flow: 'weak' vortex flow (axial flow dominates) and 'strong' vortex flow (circulation dominates). Both types of free-surface vortex flow are highlighted in Figure 1.1. A weak vortex Figure 1.1(a) tends to exist as a flow instability and exhibits unsteady characteristics. These systems present undesirable and in many cases, severe conditions at hydroelectric power-plant (HPP) intakes (Möller, 2013), pump intakes (Amphlett, 1978) and in sodium-cooled fast reactors (SFR) in nuclear power plants (Kimura et al., 2008). The formation of a weak vortex typically occurs when the flow depth approaches the critical submergence[2] h_{cr} and air is drawn into the intake. Such an event is detrimental to operational efficiencies and machinery life span. The occurrence can also trigger overflowing conditions which are a crucial aspect in the safe design of HPP's. As a result of such industrial hazards, it is not surprising therefore that the topic of weak vortex flows is very well progressed in the current literature (Knauss, 1987; Möller, 2013).

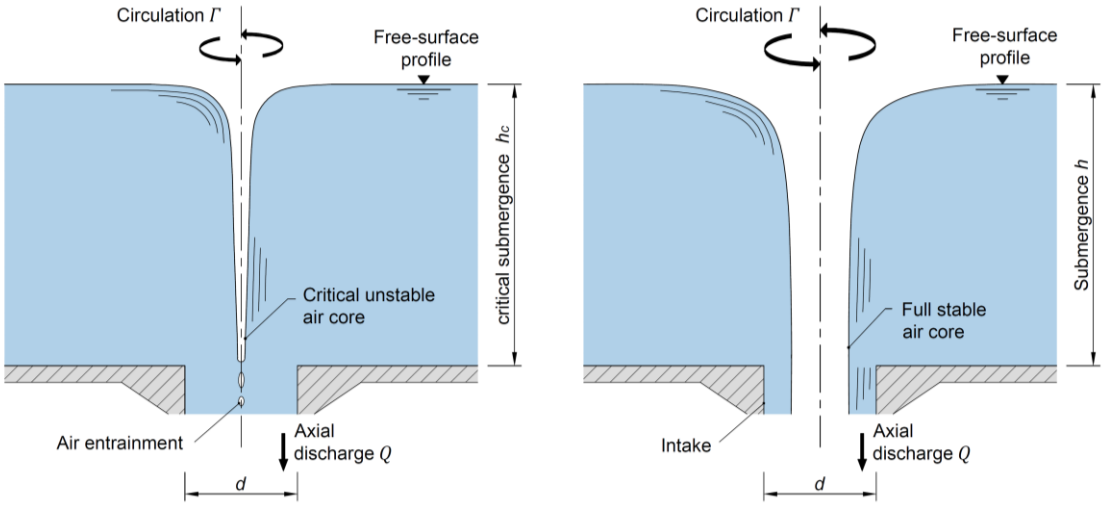

(a) Weak vortex (b) Strong vortex

Figure 1.1: Schematics of a typical horizontal intake structure with (a) a weak vortex structure during the onset of air entrainment at the critical submergence $\boldsymbol{h_c}$ and (b) a stable full air core vortex under strong circulation conditions.

[2] The critical submergence is the fluid depth according to a reference datum below which the onset of air entrainment at an intake, due to a fully protruding vortex air core, is imminent.

Contrary to the ‘weak’ vortex, a ‘strong’ vortex Figure 1.1(b) generally forms as a result of an induced circulation or a steady supply of vorticity in the flow field. The resulting formation is a free-surface vortex with a stable full air core extending deep into the intake (see Figure 1.3 and 1.4). As a consequence of rotation, increased flow retention and stability; strong vortices have proven to be beneficial in many industrial systems (Drioli, 1947; Vatistas et al., 1986; Brombach, 1982; Zotloeterer, 2009).

One of the earliest records of the use of strong vortex flows in hydraulic engineering is that of the vortex drop shaft (Drioli, 1947). It is argued that Drioli (1947) originally conceived this device; however, there are other reports that the device may have originated in Vancouver in the mid-1930s (Motzet and Valentin, 2002). Nonetheless, Drioli’s (1947; 1969) designs are still the most favourable. The vortex drop shaft structure, highlighted in Figure 1.2(a) & 1.2(b), is used to safely convey flows vertically in sewer systems or for safe energy dissipation in HPP’s. Just downstream of the horizontal intake, the vortex flow converts to annular flow where the fluid clings to the walls of the drop shaft. This encourages dissipation of fluid energy through friction and shear stresses. Because the vortex dropshaft is of popular interest in hydraulic structures, it will be heavily featured throughout the content of this study.

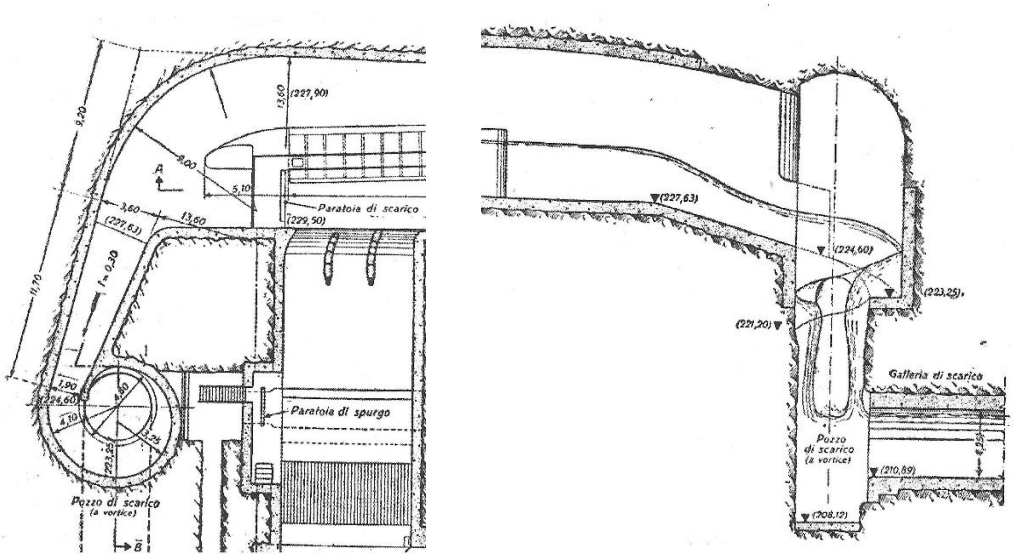

(a) Plan (b) End view

Figure 1.2: Original engineering schematics of Drioli’s (1947) design for a supercritical vortex drop shaft highlighting (a) the plan view and (b) end view of the structure (Drioli, 1947).

Strong free-surface vortex flows have, in recent years, found a novel use in the application of hydroelectric power generation. The design (Zotloeterer, 2009) is comparable in structural arrangement to that of the subcritical vortex drop shaft structure but differs by harnessing energy at the vortex core through a coaxial turbine runner (Dhakal et al., 2015). The full potential of vortex flows in hydropower generation have not yet been fully recognised due to the lack of a technical understanding of the flow mechanics as well as the absence of a generic engineering design procedure (Urbani and Steinmann, 2010).

Figure 1.3: Full air core vortex in a laboratory model at the IT Sligo Hydraulics Research Laboratory (photograph by Sean Mullery).

Figure 1.4: Strong free-surface vortex in a hydropower unit under construction in Co. Sligo, Ireland (photograph by author).

Other devices that have incorporated free-surface vortex flows are confined hydrodynamic vortex chambers for particle separation (Vatistas et al., 1986), fluidic

throttling devices for discharge control (Conway, 1971; Brombach, 1982) and in various devices in the water treatment industry (Levi, 1983; Wójtowicz and Szlachta, 2013).

In conclusion, despite the extensive industrial application of strong free-surface vortex flows as well as signs of growing interest (Dhakal et al., 2015, Shabara, H. M., et al. 2015) the lack of a generic design procedure for vortex flow structures is restricting further development of these technologies (Urbani and Steinmann, 2010). As will be discussed in Chapter 2, there is an abundance of theoretical research material on free-surface vortex flows presented in the current literature (Rouse, 1943; Hager, 1985) however, the field lacks a comprehensive experimental review of the governing hydraulic parameters, particularly surrounding the effect of the approach flow geometry on circulation and discharge (Knauss, 1987). Furthermore, computational fluid dynamics (CFD) has become an affordable and an attractive form of analysis in engineering fluid mechanics in recent years (Shaari and Awang, M. 2015). Nonetheless, CFD modelling of strongly curving and turbulent multiphase flows is still poorly developed topic in this field (Spalart and Shur, 1997; Suerich-Gulick, 2013) and has not been widely applied to strong vortex flow technologies to date.

This study therefore sets out to deliver a comprehensive program of experimental and numerical investigations on strong free-surface vortices including both experimental and numerical modelling along with associated analytical investigations of the flow problem. It is expected that the outcomes of this work will subsequently aid in providing a deeper engineering/scientific understanding of the flow phenomena surrounding free-surface vortices.

1.2. Project Scope: Aims and Objectives

The aims of the following PhD study are to provide a deeper insight into strong free-surface vortex flows through experimental and numerical analysis together with supporting analytical investigations. The primary purpose is to therefore deliver an enhanced understanding of the hydraulic principles and inherent flow mechanics.

The following are a list of the original project aims:

1. Investigate the effect of the approach flow geometry, namely that of the inlet width b, approach flow radius r, approach flow depth h and outlet diameter d on the circulation and discharge in a strong free-surface vortex.
2. Monitor the effects of the inlet Froude number Fr_i on vortex formation.
3. Determine relationships between the dependent variables in a strong free-surface vortex such as the depth-discharge, depth-circulation and circulation-air core diameter relationship.
4. Provide a detailed commentary on the coefficient of discharge in strong vortex flows.
5. Derive an alternative depth-discharge equation based on empirical findings.
6. Consider the scale effects of the physical model study and their potential effects on the results.
7. Investigate the primary flow field tangential velocity distribution for a range of sub-surface depths.
8. Compare the experimental data to available analytical models and, if required, make an attempt to derive an alternative tangential velocity model based on the experimental data.
9. Investigate the secondary flow fields relating to the radial and axial flow regions.
10. Perform a laser-induced fluorescence study in the flow to further visually highlight the secondary flows and turbulence.
11. Perform a detailed multiphase numerical modelling program using the homogeneous Eulerian-Eulerian approach.
12. Investigate the effect of structured and unstructured mesh arrangements and in addition, solution sensitivity to mesh density and refinement.
13. Perform a steady state and transient analysis of the various laminar and turbulence models.
14. Compare the results from each approach to the data acquired in the experimental study.
15. Present a best practice guideline for multiphase numerical modelling and comment on the accuracy and uncertainty of results obtained as well as areas to improve the model if necessary.

It was deemed necessary that the following list of topics were to be omitted from the scope of the research:

1. Experimental investigation of the annular jet.
2. Transient monitoring of unsteady features in the flow field i.e. velocity profiles, water surface and air core oscillations.
3. Supercritical approach flows.
4. Manipulation of numerical schemes, models and approaches in the numerical code.

Based on the extensive list of project aims that were proposed, the research project was subdivided into three strands:

a) Effect of the Approach Flow Geometry

This section deals with a thorough investigation of the effects of the approach flow geometry on the vortex flow by analysing and monitoring the governing dependent parameters.

b) Investigation of the Three-dimensional Velocity Fields and Secondary Flows

In this strand of the experimental work, a study of the mean three dimensional velocity profiles throughout the vortex is performed using velocimetry techniques. The primary tangential velocity field at various subsurface depths as well as the radial and axial velocity distributions are investigated. Flow visualisation is performed on the turbulence and secondary flow fields using laser-induced fluorescence.

c) Numerical Modelling and Comparative Analysis

Multiphase numerical modelling of strong vortex flow is performed to investigate solution sensitivity to mesh, steady and transient turbulence modelling and time-step. A best practice guide will be introduced by comparing the results of the numerical model to the results obtained in (a) and (b).

The results and discussions from the thesis are structured and presented according to each of the primary phases (a), (b) and (c) in the main body of the thesis.

1.3. Layout of the Dissertation

The overall thesis consists of 9 Chapters and relevant Appendices. Chapters 2 - 4 comprise the technical literature review for theoretical analysis, experimental modelling and numerical modelling respectively. A summary of each will be discussed at the end of each chapter highlighting the specific gaps in the current literature which are pursued in this research project. Subsequently, the main body of work in the experimental methodologies and results are contained in Chapters 5 and 6. Chapter 5 provides a complete overview of the design and planning of the experimental work including laboratory configuration, testing and procedures in addition to notes on uncertainty of the experimental results. Subsequently, the results of the experimental analysis are presented in Chapter 6 alongside analysis to complete the aims that have been defined in sections 1.2.1 and 1.2.2. Chapter 7 provides description of the methodology and strategy for the CFD program and a subsequent comparative analysis using the numerical data. This is followed by analysis of results obtained in the optimum models by a comprehensive interrelationship between numerical and physical data. This accentuates the advantages and disadvantages of multiphase modelling of strong vortex flows. Next, in Chapter 8, a brief qualitative description is made of the newly defined 'Virtual Taylor Couette' (VTC) flow system as a means of describing the flow mechanics in a strong full air core vortex. This topic is then closed with a hypothetical universal description of the stability of free-surface vortex flows which may have significant implication in the further scientific development of this field. Finally, the conclusions to the overall study are presented in Chapter 9 outlining the chief findings and advancements in this field as a result of the projects scientific contributions. An outlook and recommendations for other important areas of studies are also outlined.

1.4. Publications and Contributions

The following are a list of peer reviewed publications and pending publications which have been composed as a result of this PhD research project:

- **Mulligan, S**., Sherlock, R. and Casserly, J. (2012). Numerical and experimental modeling of the water surface in a vortex hydroelectric plant in the absence of a turbine impeller. *Proceedings of the 23rd Conference of Hydraulics and Hydraulic Engineering*. IDRA. Brescia, Italy, 10-15 September.
- **Mulligan, S**., Sherlock, R. and Casserly, J. (2014). Experimental and numerical modelling of free-surface turbulent flows in full air core water vortices. *Proceedings of the SimHydro 2014 International Conference: Modelling of rapid transitory flows.* Nice, France, 11-13 June.
- **Mulligan, S**., Casserly, J. and Sherlock, R. (2014). Hydrodynamic investigation of free-surface turbulent vortex flows with strong circulation in a vortex chamber. *Proceedings of the 5th IAHR International Junior Workshop on Hydraulic Structures.* Spa, Belgium, 28-30 August.
- **Mulligan, S**., Casserly, J. and Sherlock, R. (2014). Experimental and Numerical Modelling of Free-Surface Turbulent Flows in Full Air Core Water Vortices. *1st CADFEM Ireland Users' Meeting & ANSYS Regional Conference.* Engineers Ireland, Dublin, Ireland, 11th and 12th September.
- **Mulligan, S**., Casserly, J., and Sherlock, R. (2014). Experimental analysis of flow in an open channel vortex chamber. *Proceedings of the 36th IAHR World Congress 28 June – 3 July, 2015,* The Hague, the Netherlands 2014.
- **Mulligan, S**., Casserly, J., and Sherlock, R. Effects of geometry on strong free-surface vortices with a subcritical approach flow. *Journal of Hydraulic Engineering (ASCE) (Submitted May 2015)*
- **Mulligan, S.,** Casserly, J., and Sherlock, R. (2016). Experimental and Numerical Modelling of Free-Surface Turbulent Flows in Full Air-Core Water Vortices. In Advances in Hydroinformatics (pp. 549-569). Springer Singapore.

Chapter 2.

Theoretical Literature

2.1. General Description

2.1.1. Characteristics of Vortices

Vortices are commonly described as ordered, self-organised structures of fluid motion which nature prefers over chaos (Johansson et al., 2002) and thus have been an impetus for deep scientific inquiry for centuries[3]. Despite the fact that fluid mechanics is a long studied field, the definition of a 'vortex' still lacks a universal acceptance. As noted by Chong et al., (1990) ". . . *it is unlikely that any definition of a vortex will win universal acceptance*". In the current study, a strong concentrated free-surface vortex flow is described using Lugts (1983) following definition –*"A vortex is the rotating motion of a multitude of material particles around a common centre".* In other words, vortices are any fluid systems that undergo rotation. For this reason, the topic of vortices in fluid dynamics envelopes a wide range of disciplines ranging from quantum vortices (Feynman, 1955; Tsubota, 2009), fluid turbulence (Burgers, 1948), macro coherent vortices (bathtub vortices, tidal whirlpools) (Lundgren, 1985), geophysical (Morton, 1966) and astrophysical/extra-terrestrial (Sommeria et al., 1988; Shetty et al., 2007) . Although focus in this research is made on macro coherent vortices, seminal theoretical paradigms have been introduced in other areas which will be discussed in this work where necessary. Lugt's (1983) previous definition of a vortex) is a form of Lagrangian[4]

[3] The most noteworthy and earliest form of scientific contributions from the work of Leonardo da Vinci (1452-1519). Although he did not yet have the resources of rationale mechanics and mathematics, he pioneered the flow visualisation genre with his accurate insight of vortex flows.

[4] Lagrangian specification of the field is a perception of fluid motion where the observer follows an individual fluid parcel as it moves through space and time.

description; however, it can also be described through its behaviour in a point in space. This Eulerian description was first defined by Augustin-Louis Cauchy[5] and George Gabriel Stokes[6] in what is known as the Cauchy-Stokes decomposition (Mihalas and Weibel-Mihalas, 1999) where the angular velocity of an instantaneous state of a fluid particle in space is defined by the 'vorticity' of that element. The vorticity, will be discussed in greater detail in subsequent sections, can be imagined as the local rotation of a fluid particle in Eulerian space or the curl[7] of the velocity vector.

2.1.2. Types and Classification

Lugt (1983) categorised vortices by the path of their streamlines. The ideal description are either two-dimensional planar systems (concentric circular or asymmetrical) or three-dimensional planar (cylindrical or planar). In both of these descriptions, the streamlines are described in plane normal to the axis of rotation. However, in a real fluid application, streamlines tend to have a component which is parallel to the axis of rotation and are therefore termed 'spatial' or three-dimensional vortices. The prime example of a spatial vortex is the spiral vortex (Quick, 1961) which is the type under investigation in this work. A measure for the spatial structure of the vortex is the ratio of the diameter to the length of its axis. Extreme examples are disk-like (e.g. hurricanes 100/1 ratio) and columnar (dust devils 1/100). Typically, vortices in drop shaft structures have a spatial value of the order of 1.

Further classification of vortex type relative to the context of this study was made by Denny (1956) and later advanced by the Alden Research Laboratory (ARL) Holden, USA (Knauss, 1987). Here, a convention is established to rate the stages of free-surface vortex development through identification 'vortex types' (VT) at intakes and is presented in Figure 2.1 together with laboratory images of the observed VT's in the laboratory. The system ranks the vortex formation in stages from VT1, coherent surface swirl to VT6, a

[5] Baron Augustin-Louis Cauchy (1789 –1857) was a French pioneering mathematician.

[6] Sir George Gabriel Stokes 1st Baronet (1819 – 1903) was an Irish mathematician, physicist, politician and theologian.

[7] In vector calculus, the curl is a vector operator that describes the infinitesimal rotation of a three-dimensional vector field. At every point in the field, the curl of that point is represented by a vector.

full air core vortex (Knauss, 1987). If the local rotation is small or the submergence is large, only coherent surface swirl VT1 or a dimple VT2 will develop. For stronger rotation or less submergence, the dimple develops into an air core VT3-VT5. When the tip of the air core reaches the intake a critical state has been reached whereby air is entrained into the discharging flow VT6. Recently, this application has been expanded to vortex type VT0, i.e. stage with no activity (Möller et al., 2012; 2013). Further rotation or lesser submergence results in the production of a strong stable vortex (Lugt, 1983). This is shown in Figure 2.2 and is identified as a VT7 for completeness in the current body of work. The difference between a strong vortex (i.e. VT7) and the weak vortex (VT1-VT6) was briefly described in Chapter 1 through the inherent competition between the axial flow and moment of circulation.

This state of the competition between the axial and circulatory inertial is used to describe if a vortex is 'weak' or 'strong' as follows based on the analytical description made by Klimenko (1998). In his analysis, Klimenko (1998) aligns the the core of the vortex along the z −axis in a cylindrical coordinate system. He then defined the Rossby[8] number[9] Ro, whose different versions Ro_u and Ro_z given as follows:

$$\mathrm{Ro}_r = \frac{v_r}{(\Gamma\Omega_z)^{\frac{1}{2}}}; \qquad \mathrm{Ro}_z = \mathrm{Ro}_u\frac{z}{r} = \frac{v_z}{(\Gamma\Omega_z)^{\frac{1}{2}}} \tag{2.1}$$

are used in a stability analysis where v_r and v_z are the radial and axial velocity components, $\Gamma = 2\pi r v_\theta$ is the circulation, v_θ is the tangential or azimuthal (circumferential) velocity component at a spatial radial position r and Ω_z is the vorticity around the z −axis. If either Ro_r or Ro_z is large then the magnitude of the vorticity Ω_z is not great enough to significantly alter the flow in the $z - r$ plane and the vortex is said to be in a 'weak' state. However, if the vorticity Ω_z and Γ are both large ($\mathrm{Ro}_z \ll 1$) and have the same sign, that is $\Omega_z\Gamma > 0$, "*this has a stabilizing effect on the flow*" (Klimenko, 1998) and the vortex is said to be in its 'strong' state.

[8] Named after Carl-Gustaf Arvid Rossby who was a Swedish born American meteorologist. He was one of the first to explain the large-scale motions of the atmosphere in terms of fluid mechanics.

[9] The Rossby number, discussed further in a later section, is the ratio of inertial to Coriolis (rotational) force terms in a fluid system.

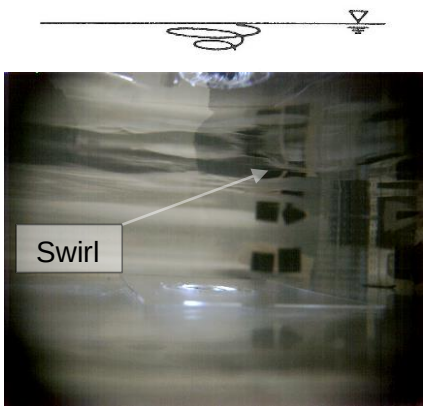

VT1

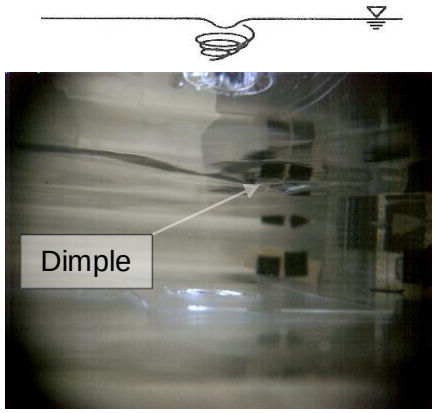

VT2

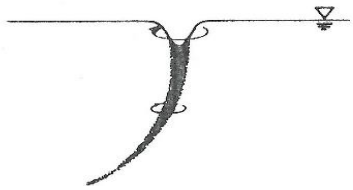

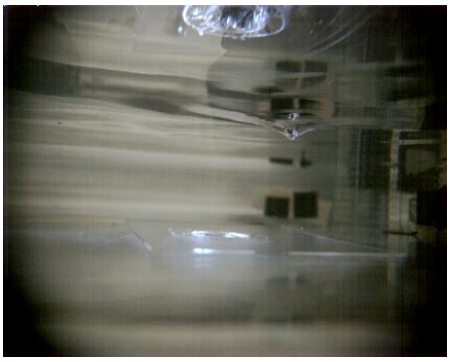

VT3

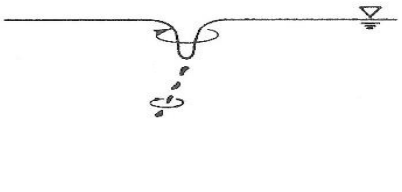

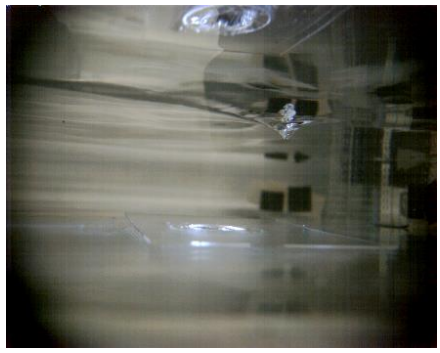

VT4

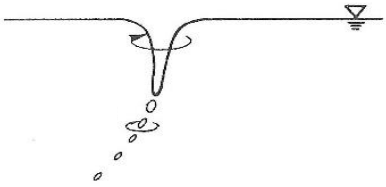

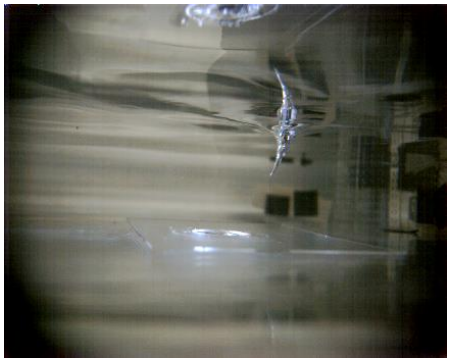

VT5

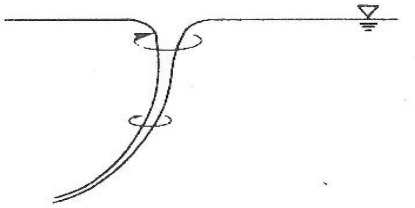

VT6

Figure 2.1: Original ARL vortex type classification system from VT1-VT6 as presented in Knauss (1987) together with laboratory images of the various VT's at the IT Sligo Hydraulics Research laboratory.

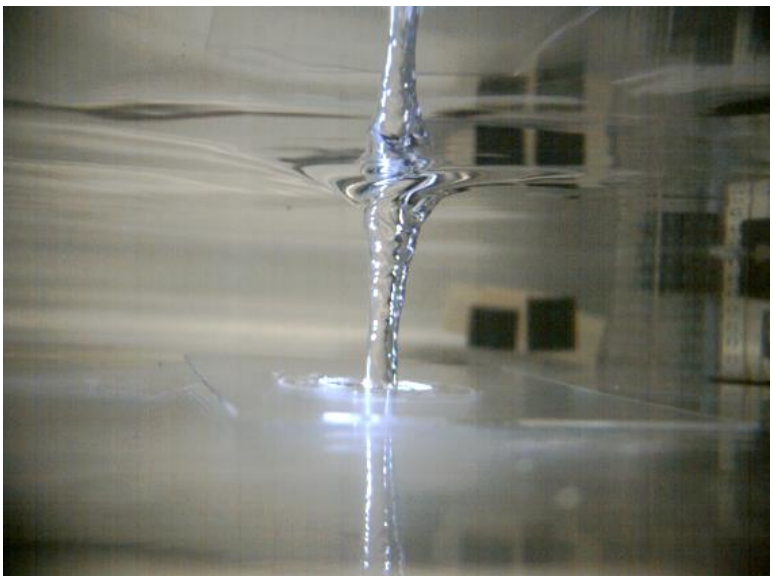

Figure 2.2: The 'strong' stable vortex labelled as VT7 for completeness.

2.2. Sources and Formation of Vortices

The basic explanation for the formation of a free-surface vortex can be described by the conservation of angular momentum (Rouse, 1943; Klimenko, 1998). A particle of fluid moving radially towards an intake only needs a small amount of pre-swirl or vorticity to generate a significant vortex structure in the vicinity of the intake. Say for example, the particle is positioned at a radius of 500 mm from in the intake centreline. If only a small amount of pre-swirl exists (say tangential velocity v_θ = 3 mm/s), the speed must increase inversely proportional to the radius in order to preserve its momentum. Therefore, for the current example, at a radial distance of only 50 mm, the tangential velocity will have increased 10 fold to 30 mm/s resulting in a 100 fold increase in angular velocity. As a consequence, the pressure and hence, the free-surface, decreases with the radius. Then the fundamental question to resolving the source of formation of vortices is related to the soruce of the residual swirl or vorticity. In the following sections a number of sources of pre-swirl and vorticity production are described.

2.2.1. Coriolis Effect and the Rossby Number

The Coriolis Effect is a deflection of moving objects when the motion is described relative to a rotating reference frame (Möller, 2013). It has long been misconceived that the Coriolis Effect resulting from the earth's rotation has an acute effect on the formation and direction of rotation for even small scale vortices at intakes and drains (Shapiro, 1962). However, by observation of the Rossby number (ratio of inertial to Coriolis forces), this statement can be shown to be inexact (Sibulkin, 1983; Möller, 2013). For small scale domains, the ratio of the inertial forces to the length scale tend to be much larger than the Coriolis number due to the earth's rotation (Shapiro, 1962). For example, at a typical hydropower plant (l = 20 m and v_θ = 2 m/s), the local Rossby number was calculated by Möller (2013) to be Ro ≅ 700. Furthermore, in a strong vortex intake structure the length and velocity scales amount to l = 6 m and v_θ = 2.5 m/s (Jain and Kennedy, 1983) which therefore yields a Rossby number in the region of Ro ≅ 18,000. Therefore, it can be assumed that these systems are unaffected by the rotation of the earth in the greater majority of cases.

However, it is important to note that when the local inertial influences (i.e. residual velocity, vorticity, thermal gradients and other perturbations) are kept minimal, the Coriolis forces have indeed shown to influence the preferred rotation of a draining vortex in both hemispheres of the globe (Shapiro, 1962; Binnie, 1964; Trefethen et al., 1965). Marris (1967) later performed theoretical study of this phenomenon where he neglected the radial and axial convective terms in favour of a time derivative in his governing equations to approximate the analysis. Here it was found that residual vorticity and vorticity as a result of the earth's rotation each grow exponentially with time.

2.2.2. Shearing, Vorticity and Axial Stretching

It is also noted that the so called 'organisation time' plays an important role (Quick, 1970) where the vorticity accumulates and continuously increases the strength of a fundamental concentrated vortex structure over time. The unsteady production of vorticity in the approaching flow can originate as a result of a number of processes (Knauss, 1972; Durgin and Hecker, 1978) which are outlined in Figure 2.3. Shear flow vorticity may generate in (a) the boundary layer of an intake channel's lateral walls as a result of a

moment imbalance (Suerich-Gulick, 2013). Vorticity can also attribute to (b) a non-uniformity of the velocity profile generated by far-field asymmetric boundary conditions or commonly as a result of wind action. Pre-swirl can also arise from (c) flow separation or detachment of nearby obstacles such as offsets, piers or dividing walls (Suerich-Gulick, 2013) which is called obstruction.

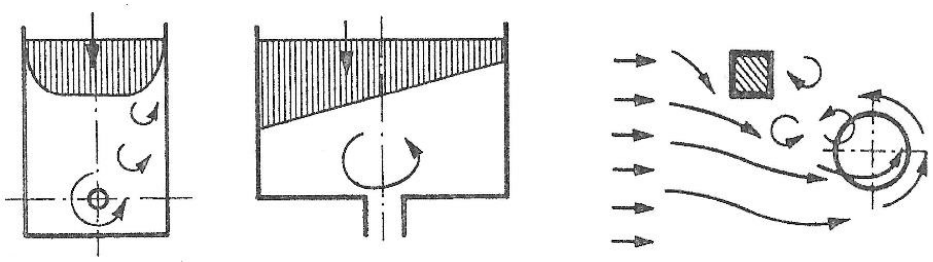

(a) (b) (c)

Figure 2.3: Unsteady production of vorticity in the approach flow: (a) Boundary layer vorticity generation, (b) asymmetric approach flow and (c) Flow separation resulting from an obstruction (Knauss, 1972, Durgin and Hecker, 1978)

These vortices may be generated at a considerable distance upstream from an intake structure. However, as they are advected with the flow they may collect and become concentrated at the intake structures to form a point vortex (Suerich-Gulick, 2013). According to Helmholtz's[10] first law (discussed in Section 2.3.3) (Helmholtz, 1858), when a vortex filament is stretched, the tangential velocity increases proportionally due to an increase of vorticity of the filament. Its implications can be severe in the vicinity of an intake. Carriveau (2009) further postulated two distinct types of vortex formation at an intake. The first of which requires a constant supplied vorticity and an intake rate which is called a non-purely stretching sustained (NPSS) vortex. On the contrary, a purely stretching sustained (PSS) vortex can form without a constant influx of vorticity due to a natural formation at low water depths or because of minor flow asymmetries.

[10] Hermann Ludwig Ferdinand von Helmholtz was a German physician and physicist who made significant contributions to several widely varied areas of modern science.

2.2.3. Effects of the Approach Flow Geometry

Contrary to an unsteady production of vorticity, the opposing case is a steady supply of vorticity or circulation which results in a steady or stable vortex structure with a full air core. A steady production of circulation usually attributes to the asymmetry of the surrounding approach flow geometry and is thus of chief interest to this work. Some conditions for asymmetries in approach flow structures have been described by Durgin and Hecker (1978) and Anwar (1968a) and are portrayed in Figure 2.4(a) and (b).

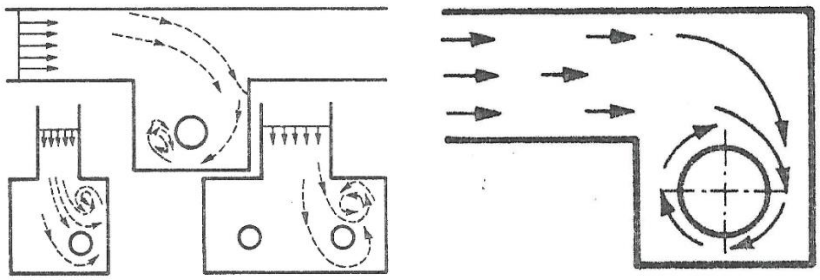

(a) (b)

Figure 2.4: Some typical examples of a steady production of circulation in the approach flow as a result of an asymmetric approach flow boundary conditions (Anwar, 1968a; Knauss, 1972; Durgin and Hecker, 1978).

This situation is commonly termed 'induced circulation' and has a strong influence on the vortices critical depth, flow mechanics and depth/discharge curve (Knauss, 1987). The first test evaluating the dependence of the critical submergence on the induced circulation was provided by Berge (1966). In four extensive investigations an approximate linear relationship between the critical submergence and the induced circulation has been shown to exist (Daggett and Keulegan, 1974; Jain et al., 1978; Anwar and Amimilett; 1980) which is summarised by Knauss (1987). Further examinations of the depth/discharge relationships have been shown to exhibit similar properties (Ackers and Crump, 1960; Mulligan and Hull, 2010). The linear relationship is said to be as a result of the governing circulation constant or swirl parameter given by:

$$\left(\frac{h}{d}\right)_{cr}, \left(\frac{h}{d}\right) = k\frac{c}{\sqrt{g}d^{\frac{3}{2}}} = k\mathsf{NcFr} \qquad (2.2)$$

where k is a proportional factor, $c = v_\theta r$ is the constant vortex strength, where v_θ is the tangential velocity at radius r, d is outlet diameter, Nc is the swirl parameter and Fr is

the Froude number. k is generally a function of the intake direction and c is an intrinsic function of the approach flow geometry or angle denoted by α_a. c may further be denoted by c_a for conditions where the circulation is primarily a hydraulic consequence of the approach flow geometry Knauss (1987). Figure 2.5 summarises the details of the approach flow angle α_a as provided by Amphlett (1978).

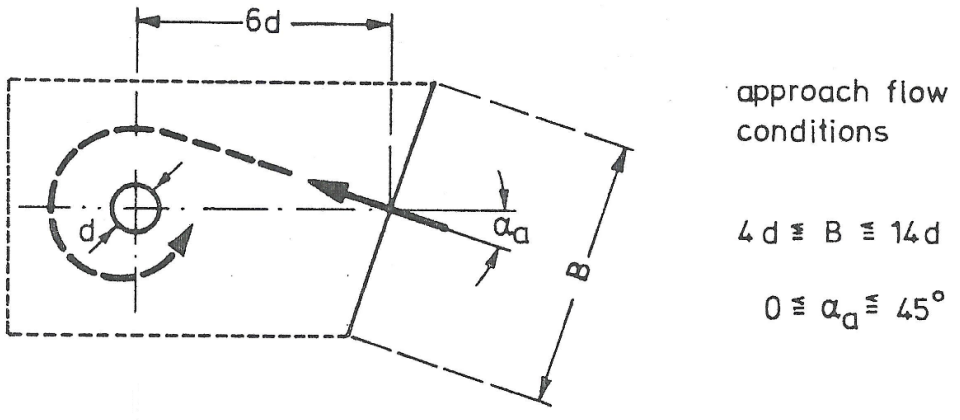

Figure 2.5: Details of the approach flow angle $\boldsymbol{\alpha_a}$ in a vertically inverted intake as presented by Amphlett (1978) highlighting the approach flow angle and wall clearance effect on the critical submergence.

2.3. Kinematics of Vortices

2.3.1. Irrotational and Rotational Flows: The Presence of Vorticity

Using the Cauchy-Stokes decomposition introduced in the previous section, fluid motion can be resolved at each point into a (a) rotation, (b) uniform translation and/or (c) shear deformation as is illustrated in Figure 2.6 (Mihalas and Weibel-Mihalas, 1999). Therefore, for an arbitrary velocity field $\vec{u}$, that the sum of the velocity fields is:

$$\vec{u} = \vec{u}_r + \vec{u}_t + \vec{u}_d \qquad (2.3)$$

where $\vec{u}_r$ is the purely rotational (solenoidal) character of the flow, $\vec{u}_t$ is the translational or potential field and $\vec{u}_d$ is the deformation field induced by irrotational dilation. A flow in which the fluid does not rotate (zero vorticity) throughout the flow field is called an irrotational or potential flow (Rouse, 1963; Shapiro, 1969). Strictly speaking, irrotational flows do not exist in nature but can be considered to be irrotational in an approximate fashion (Shapiro, 1969).

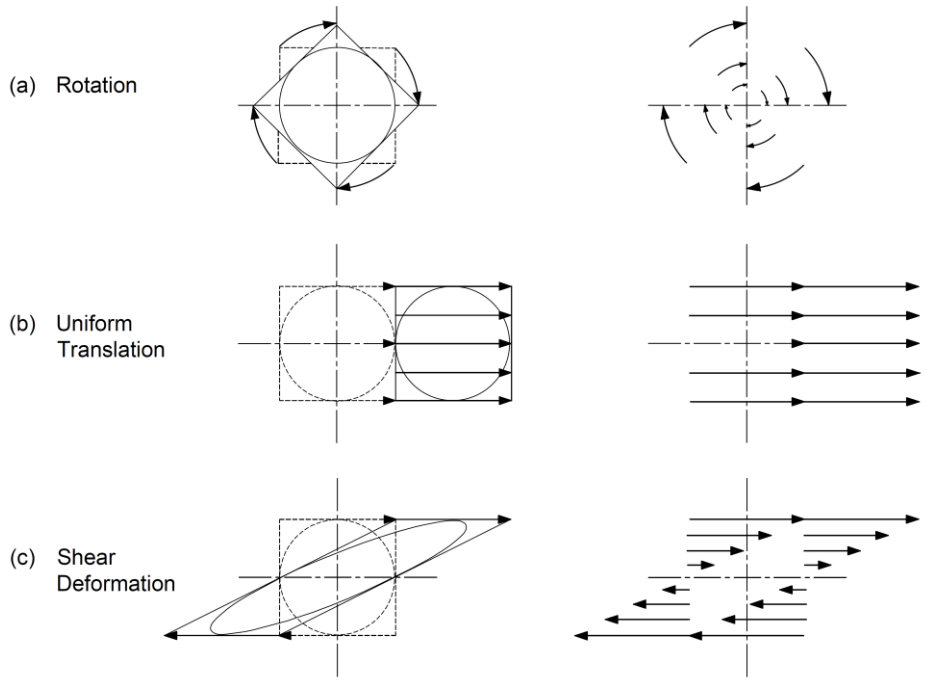

Figure 2.6: Schematic description for the individual field components of the Cauchy-Stokes decomposition and its effect on a fluid particle: (a) rotation, (b) uniform translation and (c) shear deformation.

The rotational component of the flow is a direct consequence of vorticity which can be shown in the Biot-Savart Law[11] (Green, 1995). Vorticity is then the fundamental concept which defines the local spin of a fluid element and is expressed as a vector quantity which is mathematically defined in Cartesian coordinates as:

$$\vec{\Omega} = \nabla \times \vec{v} = \left(\frac{\partial}{\partial x}, \frac{\partial}{\partial y}, \frac{\partial}{\partial z}\right) \times (u, v, w) = \begin{bmatrix} \frac{\partial w}{\partial y} - \frac{\partial v}{\partial z} \\ \frac{\partial u}{\partial z} - \frac{\partial w}{\partial x} \\ \frac{\partial v}{\partial x} - \frac{\partial u}{\partial y} \end{bmatrix} = \begin{bmatrix} \Omega_x \\ \Omega_y \\ \Omega_z \end{bmatrix} \qquad (2.4)$$

where $\vec{\Omega}$ is the vorticity vector, which equals the curl of the total velocity vector comprising of the components u, v and w in the x, y and z directions respectively. Partly or fully rotational flow fields are then generated when $\vec{\Omega}$ is non-zero across the field. The observable effect of vorticity is then the tendency of a cubical fluid element to rotate and

[11] The Biot-Savart law was originally used in physics as a fundamental quantitative relationship between an electric current and the magnetic field it produces. It has also found application in fluid mechanics in the description of rotational flows.

deform as a result of a non-uniform velocity distribution (Shapiro, 1969). Each vorticity component represents the average angular velocity of two orthogonal axes of the elements in their coordinate planes (Rouse, 1963). For a fluid mass rotating as a solid body in an axisymmetric fashion around say, the $z-$axis, the vorticity at all points is equal to twice the angular velocity:

$$\Omega_z = \frac{\partial v}{\partial x} - \frac{\partial u}{\partial y} = 2\omega_z \tag{2.5}$$

where ω_z denotes the rotation around the z-axis. However when both deformation rates of the fluid element equal, and there is no net vorticity in the element $\frac{\partial v}{\partial x} = \frac{\partial u}{\partial y}$ and Ω_z will equal zero signifying irrotational flow. Irrotational flow may be briefly described as flow in which each element of the fluid suffers no net rotation from one instant to the next with respect to a given frame of reference. Therefore, in a fully irrotational flow it holds for an x, y plane that:

$$\Omega_z = \frac{\partial v}{\partial x} - \frac{\partial u}{\partial y} = 0 \tag{2.6}$$

2.3.2. Circulation

If a curve *L* of arbitrary shape bounds a region of vorticity, the product of the area *A* inside the curve and the vorticity is known as circulation Γ (Rouse, 1963). The circulation is mathematically defined as the line integral of the tangential component of the velocity on the line *L* given by:

$$\Gamma = \oint v_L \, dL \tag{2.7}$$

The vorticity component at a point is thus the limit approached by the circulation per unit normal area as the area approaches zero given by:

$$\Omega_A = \lim_{A \to 0} \frac{\Gamma}{A} \tag{2.8}$$

This states that the average vorticity in any region is defined as the circulation per unit of enclosed area (Rouse, 1963). The fundamental variable of circulation is therefore vorticity and any periphery bounded by the curve *L* possessing a definite quantity of circulation must also acquire a magnitude of vorticity. Considering a region of fluid flow,

when the circulation is zero in all curves considered, the region must be entirely free of vorticity (Shapiro, 1969). Thus by employing the concept of circulation, the infinitesimal measure of vorticity is summated to present a global measure of rotation of the flow field.

2.3.3. Helmholtz and Kelvin

In general, vorticity is a function of both space and time in an Eulerian frame of reference. Each point of the fluid possesses a vector vorticity and the whole fluid space may be thought of as being threaded by vortex lines connecting tangents to local vorticity vectors; where the vortex lines represent the local axis of spin of the fluid particle at each point (Rouse, 1963; Shapiro, 1969). If a number of vortex lines are concentrated in a region they form what is then called a vortex tube or filament (Rosue, 1963). This, together with the previously discussed theories on circulation were introduced by Herman von Helmholtz (1858) who devoted considerable work to the mathematics of vorticity (Helmholtz, 1858). Helmholtz's ideas were later refined by Kelvin[12] (1869). In their seminal work, Helmholtz (1858) and Kelvin (1869) established renowned theorems for inviscid fluid flow in the vicinity of vortex filaments. The theorems are summarised from Rouse (1963) and Shapiro (1969) as follows:

1. The strength of the vortex filament is constant along its length.
2. A Vortex filament cannot end in a fluid; it must extend to the boundaries of the fluid or form a closed loop and the circulation is the same for every contour enclosing the vortex line.
3. On a vortex line of fixed identity, the ratio of the vorticity to the product of the fluid density with the length of the line remains constant as time proceeds ($\Omega/\rho l$ =const). Thus, if the vortex line is stretched, the vorticty increases (this is commonly known as axial stretching and was described earlier in Section 2.2.2).
4. In the absence of rotational external forces, a fluid that is initially irrotational remains irrotational forever.

[12] William Thomson, 1st Baron Kelvin was a British mathematical physicist and engineer who did pioneering work on mathematical analysis of electricity and thermodynamics.

2.3.4. Concentrated Ideal Vortices: Free, Forced and Combined Vortices

A concentrated vortex is one where the vorticity is concentrated into a small region which can be treated ideally as a line vortex (Aboelkassem, 2003). Considering a line vortex such as that depicted in Figure 2.7 which is centred about the origin o and rotation of virtual concentric streamlines are about the $z-$axis. It is convenient to describe the system in terms of the cylindrical co-ordinates r, θ, z using a total velocity vector $\overrightarrow{V}$ comprising of v_r, v_θ, v_z corresponding to the radial r, tangential (azimuthal) θ, and axial z velocity components respectively. In a real fluid, each velocity component is a function of space (r, θ, z) and time (t) therefore:

$$\overrightarrow{V} = f(v_r(r, \theta, z, t), v_\theta(r, \theta, z, t), v_z(r, \theta, z, t)) \tag{2.9}$$

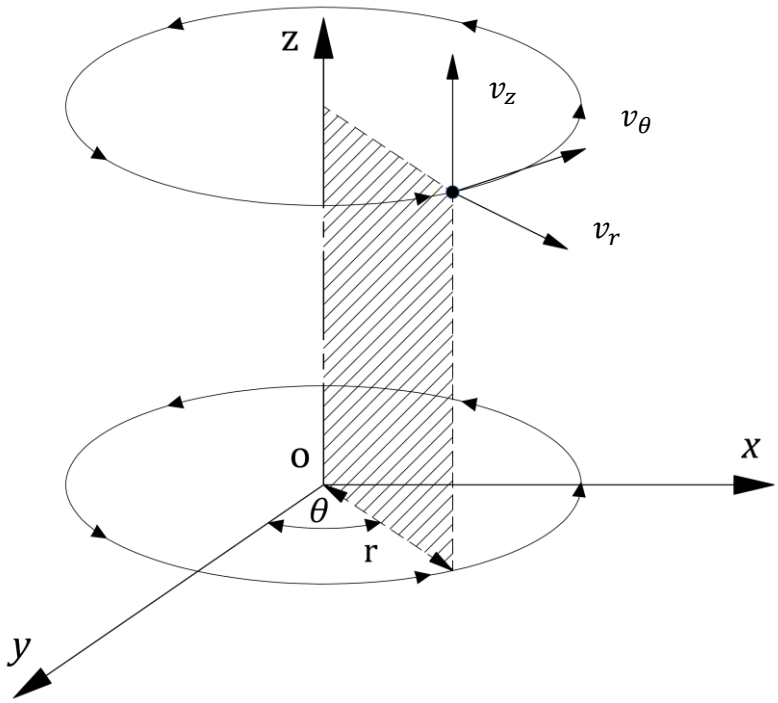

Figure 2.7: Schematic of a line vortex centred at the origin ***o*** rotating around the ***z*** − axis. The illustration depicts the arrangement of the cylindrical coordinate system superimposed on the Cartesian system.

The equations of motion (Navier-Stokes[13] N-S Equations) for an incompressible, isothermal Newtonian flow (density $\rho =$ const., dynamic viscosity $\mu =$ const. and temperature T = const.) are then given by the continuity equation:

$$\frac{1}{r}\frac{\partial(rv_r)}{\partial r}+\frac{1}{r}\frac{\partial v_\theta}{\partial \theta}+\frac{\partial v_z}{\partial z}=0 \tag{2.10}$$

and the three momentum equations (radial, tangential and axial momentum respectively) given by:

$$\rho\left(\frac{\partial v_r}{\partial t}+v_r\frac{\partial v_r}{\partial r}+\frac{v_\theta}{r}\frac{\partial v_r}{\partial \theta}-\frac{{v_\theta}^2}{r}+v_z\frac{\partial v_r}{\partial z}\right)=-\frac{\partial p}{\partial r}+\mu\left[\frac{1}{r}\frac{\partial}{\partial r}\left(r\frac{\partial v_r}{\partial r}\right)-\frac{v_r}{r^2}+\frac{1}{r^2}\frac{\partial^2 v_r}{\partial \theta^2}-\frac{2}{r^2}\frac{\partial v_\theta}{\partial \theta}+\frac{\partial^2 v_r}{\partial z^2}\right] \tag{2.11}$$

$$\rho\left(\frac{\partial v_\theta}{\partial t}+v_r\frac{\partial v_\theta}{\partial r}+\frac{v_\theta}{r}\frac{\partial v_\theta}{\partial \theta}+\frac{v_\theta v_r}{r}+v_z\frac{\partial v_\theta}{\partial z}\right)=-\frac{1}{r}\frac{\partial p}{\partial \theta}+\mu\left[\frac{1}{r}\frac{\partial}{\partial r}\left(r\frac{\partial v_\theta}{\partial r}\right)-\frac{v_\theta}{r^2}+\frac{1}{r^2}\frac{\partial^2 v_\theta}{\partial \theta^2}-\frac{2}{r^2}\frac{\partial v_r}{\partial \theta}+\frac{\partial^2 v_\theta}{\partial z^2}\right] \tag{2.12}$$

$$\rho\left(\frac{\partial v_z}{\partial t}+v_r\frac{\partial v_z}{\partial r}+\frac{v_\theta}{r}\frac{\partial v_z}{\partial \theta}+v_z\frac{\partial v_z}{\partial z}\right)=-\frac{\partial p}{\partial z}+\rho g+\mu\left[\frac{1}{r}\frac{\partial}{\partial r}\left(r\frac{\partial v_z}{\partial r}\right)+\frac{1}{r^2}\frac{\partial^2 v_z}{\partial \theta^2}+\frac{\partial^2 v_z}{\partial z^2}\right] \tag{2.13}$$

where p is denoted as the pressure (Hall, 1966). The above equations are coupled to form a highly non-linear system and therefore they cannot be solved without extreme approximation. An approach that renders appreciable results is that of the quasi-cylindrical approximation (Hall, 1966).

[13] Claude-Louis Navier was a French engineer and physicist who specialised in mechanics of fluids

In the quasi-cylindrical approximation approach the following assumptions are made (Hall, 1966) for an ideal inviscid (Einstein and Li, 1955; Rouse, 1963) case:

1) The flow is steady ($\partial/\partial t = 0$).
2) The system is axisymmetric, thus all derivatives of mean values with respect to θ are neglected ($\partial/\partial\theta = 0$).
3) The derivatives in the axial direction are taken to be small compared to variations in the radial direction ($\partial/\partial z \approx 0$).
4) In an ideal fluid the viscosity is non-existent ($\mu \approx 0$).

Therefore, from an order of magnitude analysis and without significant mathematical effort, it can be shown that the tangential momentum Equation (2.12) of the Navier-Stokes equations simplifies to become:

$$v_r\left(\frac{\partial v_\theta}{\partial r}\right) + \frac{v_r v_\theta}{r} = 0 \tag{2.14}$$

and integrated to yield (Einstein and Li, 1951):

$$v_\theta r = \text{const.} \tag{2.15}$$

where the constant equals $\Gamma/2\pi$ in physically relative terms[14]. This is the classical free-vortex velocity model for an inviscid fluid which states that there is a conservation of angular momentum everywhere in the flow field. Thus the flow is irrotational (Rouse, 1963). Normally, according to previous definitions (Shapiro, 1969), the circulation around a closed curve in an irrotational fluid is zero. However, there exist cases where if such a curve surrounds a singular line vortex such as that in Figure 2.7, the magnitude of the circulation will be the same of the vortex itself. In this case the vortex does not have vorticity outside the singularity and is termed a free or potential vortex.

The complete description of rotation requires the pressure distribution as well as the azimuthal velocity profile. Considering now the radial momentum equation (2.11) and respecting the previous assumptions, the equation can be simplified in the following form:

[14] Obtained through integrating tangential velocity along a concentric streamline encompassing the point vortex.

$$\frac{{v_\theta}^2}{r} = \frac{1}{\rho}\frac{\partial p}{\partial r} = \frac{g\partial h}{\partial r} \tag{2.16}$$

By substitution of Equation (2.15) into Equation (2.16), the actual pressure p would hence vary through an irrotational vortex ranging from a maximum equal to its magnitude p_∞ at infinite radius to a minimum of negative infinity at zero radius by:

$$p_\infty - p = \frac{\rho \Gamma^2}{8\pi^2 r^2} \tag{2.17}$$

or

$$h_\infty = h_r - \frac{\Gamma^2}{8\mathrm{g}\pi^2}\left(\frac{1}{r_\infty} - \frac{1}{r}\right) \tag{2.18}$$

The opposing case is that of a forced vortex, where the fluid is rotating as a solid body. Thus the vorticity is everywhere equal to twice the angular velocity of rotation. Examples of this can be practically observed when a liquid filled container rotates on a turntable. For such a motion the fluid increases linearly with their distance from the centre

$$v_\theta = \omega \mathrm{r} \tag{2.19}$$

where ω denotes fluid rotation about an arbitrary $z-$axis. The ideal irrotational vortex model (Equation 2.15) is a fitting candidate model for analysing a range of fluid vortices. However, the singular conditions at zero radius ($r = 0$) are an extreme that must be eliminated from consideration if the model, as a whole, is to have physical significance. Rankine (1872) proposed the first model to resolve this issue. His elegant solution involved discarding the line vortex at the origin and replacing it with a vortex filament of finite core radius r_c containing a constant vorticity Ω_z. The filament is then surrounded by an irrotational field of the same circulation of the periphery of the vortex filament. The filament of constant vorticity therefore behaves as a solid rotating body. This combined vortex therefore requires work to be done in the core region, where the kinetic energy is dissipated; somewhat simulating the effects of a viscous core. The tangential velocity in this model is then given by:

$$v_\theta(r) = \begin{cases} \frac{\Gamma_\infty r}{2\pi {r_c}^2}, & 0 \leq r \leq r_c \\ \frac{\Gamma_\infty}{2\pi r}, & r_c \leq r \leq \infty \end{cases}, v_r = 0, v_z = 0 \qquad (2.20)$$

and the pressure:

$$p_\infty - p = \begin{cases} \frac{\rho\omega^2 r^2}{8}, & 0 \leq r \leq r_c \\ \frac{\rho {\Gamma_\infty}^2}{8\pi^2 r^2}, & r_c \leq r \leq \infty \end{cases} \qquad (2.21)$$

where the circulation Γ is defined by the field circulation Γ_∞ which will be herein assigned to the assumed irrotational far-field region. The pressure thus decreases according to a second-degree hyperbola from its absolute value to the periphery of the filament where it subsequently decreases parabolically to a minimum finite value at the vortex origin (Rankine, 1872). For a liquid with a free-surface, and assuming that ambient pressure is constant for all surfaces, dividing by the specific gravity of the fluid γ will yield equations for the head or depth distribution in a free-surface vortex.

However, discontinuity that forms at r_c between the rotational and irrotational fields cannot exist as a natural entity in a real viscous fluid. Numerous subsequent models were later developed to relieve this discontinuity and will be discussed in the next section. In the case of a full air core vortex it is assumed that there is a virtual singular vortex line which resides in the centre of the air core. The air core then replaces the viscous core of the previous formulation to relieve the singularity at $r = 0$. The periphery of the irrotational zone then remains at the air water interface of the air core (depicted in Figure 2.4). Therefore the whole of the velocity field in a full air core vortex has been generally treated as fully irrotational (Quick, 1970) according to the theoretical approximation of the quasi-cylindrical approach (Lugt, 1983; Knauss, 1987; Möller, 2013). Both the Rankine vortex and potential vortex for a full air core system are highlighted in Figure 2.8.

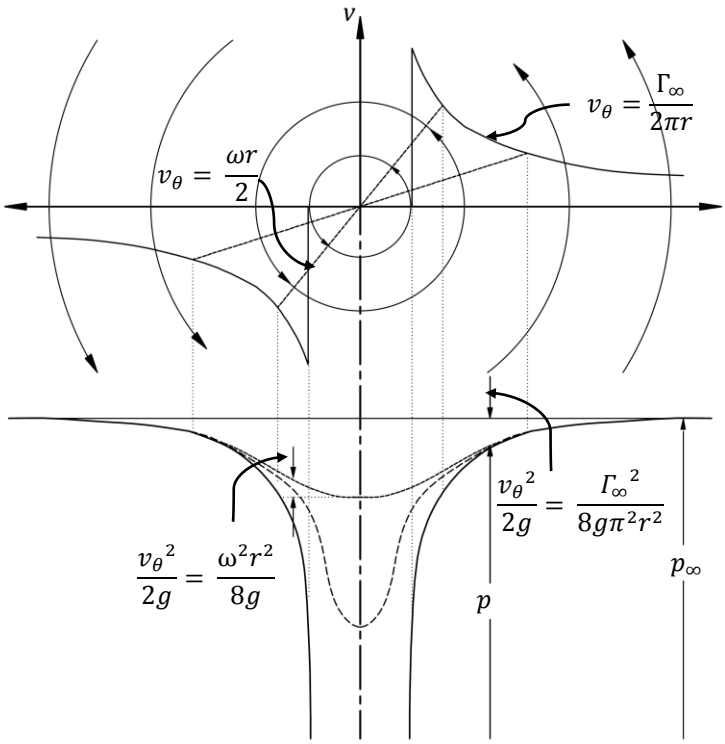

Figure 2.8: The Rankine combined vortex and potential vortex in plan and elevation. Schematic reproduced from (Rouse, 1943).

2.4. The Rankine Vortex Applied to Real Fluids

The Rankine (1872) vortex formulisation (discussed in Section 2.3.4.) will now be discussed for application in a real fluid. Although the vortex Reynolds number $\mathrm{Re}_v = \Gamma_\infty/v$ can be very large, a majority of vortex flows remain laminar and can be treated as inviscid by default for approximation (Klimenko, 1998). Despite the simplicity of the Rankine vortex, it nonetheless suffers the problem of a discontinuity at the viscous core radius r_c when it is applied to a real vortex system (Bhagwat and Leishman, 2002). This discontinuity cannot exist as a natural entity in a real fluid. Efforts have been made (Rosenhead, 1930; Scully, 1975; Vatistas et al., 1991; Odgaard 1986) to relieve this discontinuity at $r \to r_c$ by providing a viscous smearing between the rotational and irrotational regions. These analytical models fall into two categories; time dependent (profiles vary with time) or time independent (steady state models).

2.4.1. Time Dependent Viscous Vortex Models

The Rankine (1872) generalisation can be treated as a time dependent time dependent where features of the vortex mechanics are observed as being evolving (resulting from vorticity accumulation or Coriolis forces) (Klimenko, 1998) or decaying. Vortex decay occurs due to the fact that the Rankine idealisation requires work to be done in order to maintain its motion (Daggett and Keulegan, 1974; Aboelkassem, 2003). If no kinetic energy is supplied to the system in either a steady or unsteady form, the vortex begins to lose energy and decays over time (Aboelkassem, 2003). Oseen (1911) and Lamb (1932) developed a model which is an exact solution to the one-dimensional laminar Navier-Stokes equations. The Lamb-Oseen model is expressed by:

$$v_\theta(r,t) = \frac{\Gamma_\infty}{2\pi r}\left[1 - \exp\left(-\frac{r^2}{4\nu t}\right)\right] \tag{2.22}$$

The viscous core radius is the radial location where the tangential velocity is a maximum $v_{\theta_{max}}$, and can be solved by differentiating Equation. (2.22) with respect to r and equating to zero ($dv_\theta/dr = 0$). The core radius a is then found to grow with time as:

$$r_c(t) = \sqrt{4\varphi\nu t} \tag{2.23}$$

where φ is the Oseen parameter. Further work was carried out by Burgers (1948) who extended to three-dimensional vortex flows. This model includes a tangential velocity profile which is consistent with the Lamb-Oseen model along with a linear distribution of the radial and axial velocity. This implies that a constant axial velocity exists which does not agree with experimental observations. Aboelkassem carried out further theoretical work on the decay of columnar vortices (Aboelkassem, 2003; Aboelkassem et al., 2005). In his work he introduced a novel analytical method to consider the transient decay of the ideal potential vortex (Equation 2.15), the Rankine model (1884) as well as other formulations (Vatistas et al., 1991). His results showed that all the models agreed well accept for differences in the mixed vortex region at the viscous core radius r_c.

2.4.2. Time Independent (Steady State) Viscous Vortex Models

Time independent vortices are ones where kinetic energy is continuously provided to the flow system which would otherwise decay through the shearing and growth of the viscous core (Rouse, 1963; Aboelkassem, 2003) . Typically, this energy is replenished if the system has a radial v_r and axial velocity v_z component (Daggett and Keulegan, 1974; Lugt, 1983) to carry new energy from outside the vortex system. A number of formulations have thereafter been developed to relieve the discontinuing defect of the Rankine velocity profile at the viscous core which would otherwise cause a significant over estimation of the maximum tangential velocity. Originally proposed by (Rosenhead, 1930) the Kaufmann vortex (1962) or better known as the Scully vortex model (Scully, 1975) smoothens the transition between the irrotational and rotational vortex using an algebraic velocity profile of the form:

$$v_\theta(r) = \frac{\Gamma}{2\pi}\left(\frac{r}{{r_c}^2 + r^2}\right) \tag{2.24}$$

Vatistas et al., (1991) subsequently proposed a family of algebraic tangential velocity profiles through the following expression:

$$v_\theta(r) = \frac{\Gamma}{2\pi}\left(\frac{r}{({r_c}^{2n} + r^{2n})^{1/n}}\right) \tag{2.25}$$

where $1 \geq n \geq \infty$. When $n = 1$, Equation (2.25) corresponds to the Scully model whereas if $n \to \infty$ the model corresponds to the Rankine idealisation. For n = 2, the model provides good agreement with measured velocities for a rotor tip vortex (Bhagwat and Leishman, 2002; Aboelkassem, 2003). Efforts were subsequently made to develop the models in three-dimensions. Based on the steady Burgers (1995) formulisation the three-dimensional profiles are given by:

$$v_\theta = f(r),\ v_r = -\xi r,\ v_z = 2\xi z \tag{2.26}$$

where ξ is a positive factor of proportionality for radial flow directed inward toward the $z-$axis. Rott (1958) solved Equation (2.26) for an unknown $v_\theta(r)$ given the other two field distributions to yield:

$$v_\theta(r) = \frac{\Gamma}{2\pi r}(1 - e^{-\xi r^2/2\nu}) \tag{2.27}$$

which is comparable to the Lamb-Oseen unsteady equation Equation (2.22) only "frozen" at a time $t = (2\xi)^{-1}$. A physical interpretation of this is that "*flow carries new circulation from infinity towards the axis*" (Rott, 1958).

For a sink flow, the inflow gradient was found (Rott, 1958) to be:

$$\xi = \frac{Q}{2\pi h^3} \tag{2.28}$$

More recently, Odgaard (1986) arrived at a similar relationship to Rott's (1958) solution when applied to free-surface air core vortex. Gulliver (1988) however added (in his discussion on Odgaards work) that the application has proved to be elusive because it is difficult to predict the "*radius of transition between the free and forced vortex*" in a practical situation.

Mih (1990) and Hite and Mih (1994) provided an alternative model for a three-dimensional free-surface vortex flow based on adapting the Rosenhead (1930) formulation (Equation (2.24)). This is given by:

$$v_\theta = \frac{\Gamma}{2\pi r}\frac{2r}{{r_c}^2 + 2r^2} \tag{2.29}$$

$$v_r = -\nu\frac{8r}{{r_c}^2 + 2r^2} \tag{2.30}$$

$$v_z = -\nu\frac{16{r_c}^2 z}{({r_c}^2 + 2r^2)^2} \tag{2.31}$$

The previous formulations do not express dependence of the solutions on the variable z. Chen et al. (2007) identified this as a potential for uncertainty and revised Hite and Mih's (1994) model to account for the tangential velocity dependency on the z-axis given by:

$$v_\theta = f(r)g(z) \tag{2.32}$$

where the function $g(z)$ denotes the variation of v_θ in the axial direction.

$$v_\theta = \frac{\Gamma}{2\pi r}\frac{2r}{(r_c{}^2 + 2r^2)}(1 + \xi z) \tag{2.33}$$

By substitution of Equation (2.33) into the Navier-Stokes equations v_r and v_z are solved to give:

$$v_r = -\nu\frac{8r}{(r_c{}^2 + 2r^2)}[1 + \ln(1 + \xi z)] \tag{2.34}$$

and

$$v_z = -\nu\frac{16{r_c}^2 z}{(r_c{}^2 + 2r^2)^2}\left[\frac{(1 + \xi z)}{\xi} + \ln(1 + \xi z)\right] \tag{2.35}$$

Some validation studies were performed demonstrate the applicability of these models over the standard Rankine formulation (Hite Jr and Mih, 1994; Aboelkassem, 2003; Cristofano et al., 2014c). Examples of the validations are highlighted in Figure 2.9 (a) (Hite Jr and Mih, 1994) and (b) (Aboelkassem, 2003).

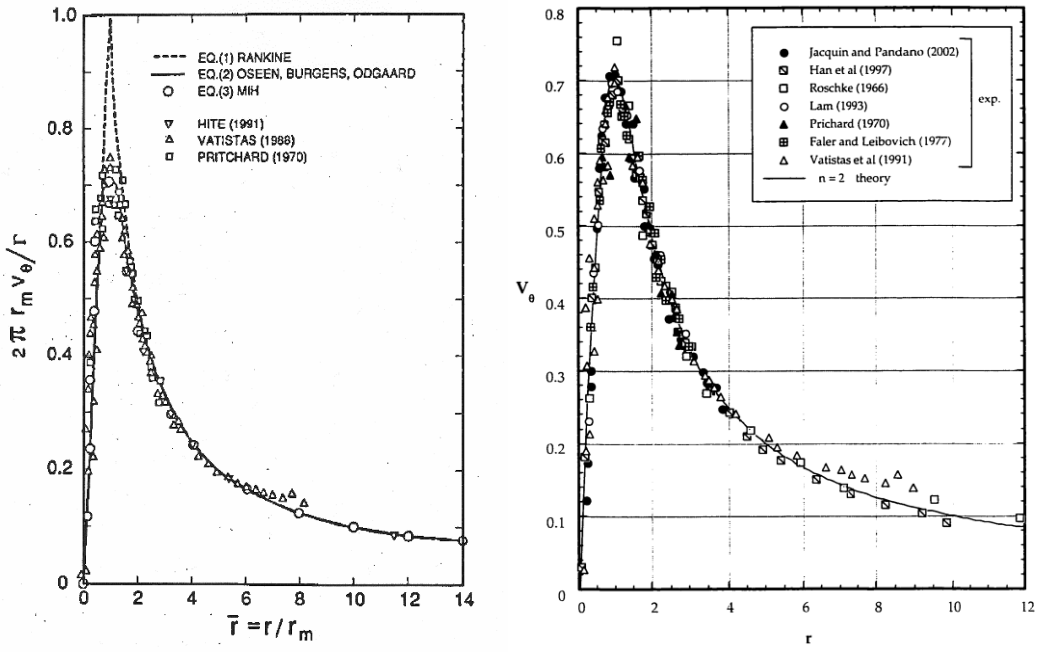

(a) (b)

Figure 2.9: Validation of the tangential velocity profiles with experimental data: (a) Mih's (1990) and Odgaard's (1986) analytical solutions provide a good fit to the experimental and (b) Vatistas $\boldsymbol{n} = 2$ model (Vatistas et al., 1991) provides a good agreement with a range of experiments.

It is interesting to note here that there are few records of alternative tangential velocity profiles to treat the strong full air core vortex scenario. Past studies (Einstein and Li, 1955; Quick, 1961) have often treated the full flow field between r_∞ and the air core diameter a_c as being a potential flow thus the only requirement to compute the flow field is the unknown circulation Γ_∞ using the general principle that $v_\theta \propto 1/r$. Besides Rohan's (1965) indistinct model for $v_\theta = const./r^n$ (as cited in Knauss (1987)), Anwar (1965) presents an alternative model for the tangential velocity defined by:

$$\left(\frac{v_\theta}{v_{\theta_o}}\right)^2 = 1 - 2\frac{1-\sqrt{1-(2n)^2}}{1+\sqrt{1-(2n)^2}} log_e \frac{tan\phi}{tan\phi_o} \tag{2.36}$$

where ϕ is the so called 'angle of conical coordinates' that defines the angle of the tangent to the free-surface on the $r - z$ plane by:

$$\phi = tan^{-1}\frac{r}{z} \tag{2.37}$$

v_{θ_o} then complies with the tangential velocity residing at a conical angle of ϕ_o degrees. The model is derived from the Euler equations and is somewhat difficult to solve as it first requires that the free-surface be resolved in order to compute the angle ϕ which would have to be determined experimentally in order for the model to achieve some level of validity. It is however, interesting to note that the coefficient n of this model represents the ratio of the tangential velocity to the axial velocity and hence *"a coefficient of spiralling streamline flow near the core"* (Anwar, 1965). He later evaluates a value for n = 0.498.

2.5. Turbulent Vortex Flows

The previous formulations (Odgaard, 1986; Hite and Mih, 1994; Chen et al. 2007) have provided reasonable solutions to real laminar flow applications when the circulation Γ is relatively low in comparison to the viscous effects and the assumption of a laminar viscous core is reasonable. Until now, shearing was assumed to be transmitted according to the Newtonian equation for curving flow (Rouse, 1943) by:

$$\tau_l = \mu\left(\frac{\partial v_\theta}{\partial r} - \frac{v_\theta}{r}\right) \tag{2.38}$$

where the local laminar shear stress τ_l is proportional to the velocity gradient multiplied by the kinematic viscosity μ. Further analytical work was carried out by Einstein and Li (1951) and Anwar (1969) who derived a term for the flow field:

$$A_o = \frac{Q_o}{2\pi h\nu} \tag{2.39}$$

where Q_o is the radial flow through the core radius r_o ($Q_o = -2\pi r_o h v_r$). Equation (2.39) describes the effect of which increasing the viscosity has on the vortex. A_o is effectively a form of radial Reynolds number Rr and when $A_o = 0$ and $A_o = \infty$ the vortex corresponds to solid body rotation and an ideal free vortex respectively (i.e. Rankines generalisation).

When the circulation, and consequently the velocity gradient, is increased; turbulence is generated in the flow as a result of the ratio of inertial forces to viscous forces as well as localised instability of curved flow (Scorer, 1967). All variables then fluctuate around their average value by, for example $v_\theta = \overline{v_\theta} + v_\theta{}'$ (denoted for the tangential velocity field) where $\bar{o}$ signifies the average while o' signifies the fluctuation. The role of this turbulence is then to increase the apparent viscosity through what is known as eddy viscosity ε (turbulent exchange rate). Therefore the viscosity ν transcends to become the effective viscosity by $\nu_e = \nu + \varepsilon$. When Einstein and Li (1951) considered experimental data for validation of their analytical model, values for A_o were found to be much larger than the theoretical values in (2.39). From this, Einstein pondered that the turbulence inherent in the real fluid contributed an additional eddy viscosity in the effective viscosity. In his analytical work he states "*one may conclude that turbulence has an equal effect as viscosity if it varies proportionally with the shear motion"* which is valid according to Prandtl's[15] mixing length theory (Odgaard, 1986) where ε is taken as proportional to $\partial v_\theta/\partial r$ if $\partial v_\theta/\partial r \gg \partial v_r/\partial r$ and $\partial v_z/\partial r$. Therefore the following assumption can be justified:

$$\varepsilon r \frac{\partial}{\partial r}(v_\theta/r) = -(\overline{v_r{}' v_\theta{}'}) \tag{2.40}$$

[15] Ludwig Prandtl was a German engineer who pioneered the development of rigorous systematic mathematical analyses which he used for underlying the science of aerodynamic.

that is constant for the flow field. $\overline{v_r{}'v_\theta{}'}$ is known as the turbulent momentum transfer term or a member of the family of Reynolds stresses. Variations in the axial direction z of mean values with respect to time are negligible compared to variations in the radial direction r which completes the quasi-cylindrical approximation for a real viscous fluid (Hall, 1966). Thus, the constancy of equation (2.40) represents a form of isotropic eddy viscosity model (Boussinesq eddy viscosity approximation[16]). A_o in Equation (2.39) is then modified to form an effective constant A_{oe} of the form:

$$A_{oe} = \frac{Q_o}{2\pi h(\varepsilon + \upsilon)} \tag{2.41}$$

Similarly, ν in Equations (2.27), (2.30), (2.31), (2.34), (2.35) is replaced by the effective viscosity v_e (Odgaard, 1986; Hite Jr and Mih, 1994) in order to form the turbulent vortex models for the tangential velocity field. It is reasonable to therefore assume that proportionality exists between ε and Γ_r (Squire, 1954) (Odgaard, 1986) by:

$$\varepsilon = k\Gamma_r \tag{2.42}$$

where k is a factor of proportionality. Anwar (1969) showed theoretically that the eddy viscosity is constant across the turbulent region which disagrees with Equation (2.42) if the distribution of circulation across this region is to behave as solid body rotation.

2.6. Solutions for the Depth-Discharge Relationship

In the following section, a comprehensive review of previous theoretical efforts to determine the depth-discharge equation for strong vortices with a subcritical approach flow will be outlined. Deriving a solution for the discharge in a subcritical vortex flow is somewhat more difficult than that in a supercritical approach flow where the critical section resides in the inlet channel whereby the flow can be computed using the channel slope conditions and the critical depth (Yu and Lee, 2009; Hager, 2010). In a subcritical approach flow however, the critical section exists at the critical air core diameter just downstream of the intake (Quick, 1961). The critical section is then said to shift between

[16] In 1877 Boussinesq postulated that the momentum transfer caused by turbulent eddies can be modelled with an eddy viscosity.

the intake and the inlet channel depending on the Froude number of the approach flow Fr_i (Yu and Lee, 2007). According to Keller (1995) – "*a hollow-core vortex departs from critical state as the cross-sectional area is increased*". This was termed a B-type vortex (Keller, 1995). Extensive detail on the mechanics of the critical cross-section of vortex flows are described by numerous authors (Benjamin, 1962; Benjamin, 1965; Keller et al., 1987; Mudkavi, 1993; Keller, 1995). In the following analysis, a summary of literature describing how previous authors treated the critical section at the air core in order to derive the depth discharge relationship is made.

2.6.1. Modelling Approach

An ideal schematic for the general flow problem is outlined in Figure 2.10 as applied to a typical subcritical vortex chamber arrangement. An approximate expression for the discharge (Q) as a function of the approach flow depth (h) in a vortex with a full air core can be obtained by making a number of ideal assumptions summarised from Binnie and Hookings (1948) and Ackers and Crump (1960):

1. The fluid is incompressible and inviscid; thus there are no losses of energy E.
2. Concentrated flow enters the domain tangentially at an arbitrary radius r and discharges axially at some smaller radius $r_d = d/2$.
3. The resulting vortex structure is stable due to a steady continuous influx ($dQ/dt = 0$) of energy E to the systems.
4. Rotation is axisymmetric around the $z-$axis.
5. There exists a full air core which extends beyond the critical depth into the intake producing an air core diameter a with the critical section residing at the radius a_c.
6. The whole flow field ($0 \geq r \geq \infty$) is irrotational and the velocity varies inversely with the radius according to Equation (2.15) with a constant field circulation Γ_∞ throughout the flow field. This implies that the flow is fully potential and hydrostatic.

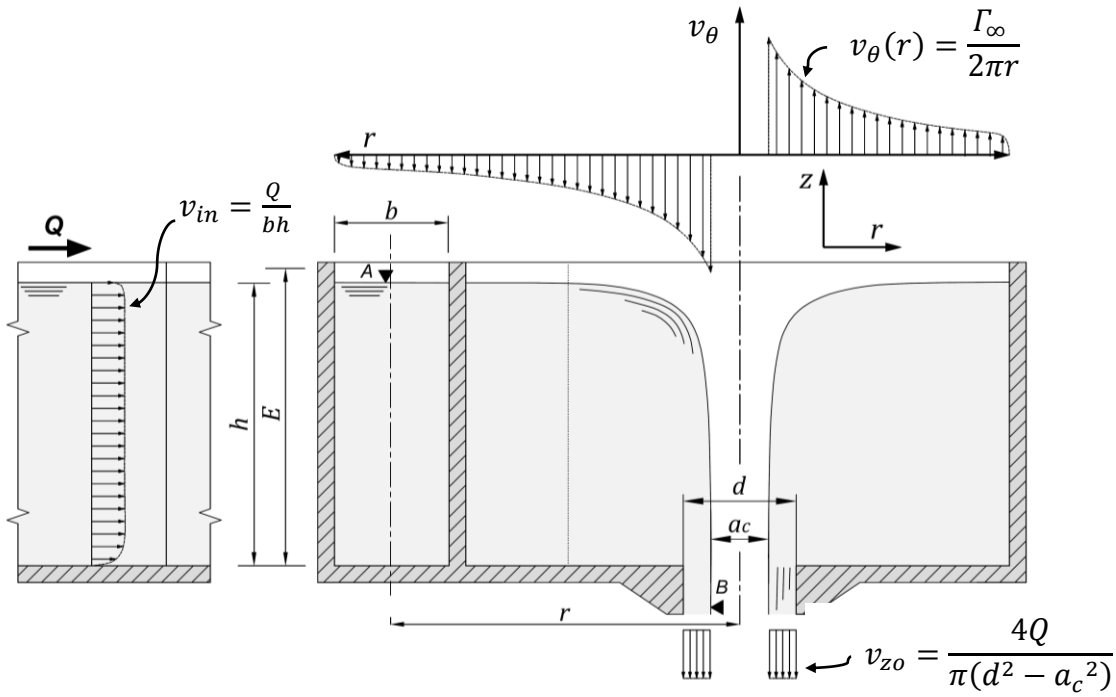

Figure 2.10: Schematic of a typical arrangement for the inlet cross section and elevation of a subcritical vortex chamber highlighting the analytical details of the tangential velocity field and the axial discharge at the critical control section (B).

Based on assumption 5 it can easily be shown that the energy E is everywhere equal to:

$$E = \frac{{v_\theta}^2}{2g} + \frac{{v_z}^2}{2g} + \frac{p}{\rho g} \tag{2.43}$$

Where $p = 0$ at the air water interface. A property of the irrotational flow field is that for all points on a horizontal datum:

$$\frac{{v_\theta}^2}{2g} + \frac{p}{\rho g} = \text{const.} \tag{2.44}$$

Hence, when considering Equation (2.43) across the annulus at the critical section B ($r_d < r < a_c/2$) the axial velocity v_{zo} is found to be constant. Therefore by continuity:

$$Q = \frac{\pi}{4} v_{zo}(d^2 - {a_c}^2) \tag{2.45}$$

Imposing the zero pressure boundary conditions at the air-water interface of diameter a_c, Equation (2.43) then becomes:

$$E = \frac{{\Gamma_\infty}^2}{2g\pi^2{a_c}^2} + \frac{{v_{zo}}^2}{2g} \tag{2.46}$$

Combining Equation (2.45) and Equation (2.46) and solving for Q yields the following expression:

$$Q = \frac{\pi}{4}d^2(1-\lambda)\sqrt{2gE - \frac{{\Gamma_\infty}^2}{\pi^2 d^2 \lambda}} \tag{2.47}$$

where $\lambda = {a_c}^2/d^2$ is the fractional critical air-core cross section. This is the generalised solution for the flow in a free-surface vortex which was first derived by Binnie and Hookings (1948). The equation relates the discharge Q to the total energy E, the circulation Γ_∞ and the critical air core diameter a_c through its fractional quantity λ. Binnie and Hooking's, again in their seminal work on this topic (Binnie and Hookings, 1948), proposed a method to further simplify the solution by applying the principle of maximum discharge. This process determines the size of the air core a_c which permits the greatest discharge Q for a given energy E. Therefore Equation (2.47) is partially differentiated and equated to zero through $\partial Q/\partial\lambda = 0$ to yield a quadratic equation with the solutions:

$$2gE - \frac{{\Gamma_\infty}^2}{\pi^2 d^2 \lambda} = (1-\lambda)\frac{{\Gamma_\infty}^2}{2\pi^2 d^2 \lambda} \tag{2.48}$$

and:

$$gE = \frac{{\Gamma_\infty}^2(1+\lambda)}{4\pi^2 d^2 \lambda} \tag{2.49}$$

Substitution of Equations (2.48) and (2.49) into (2.47) and eliminating Γ_∞ yields:

$$Q = \frac{\pi}{4}d^2\sqrt{\frac{2gE(1-\lambda)^3}{1+\lambda}} \tag{2.50}$$

or alternatively, if E is eliminated from the equation:

$$Q = \frac{d\Gamma_\infty}{8}\sqrt{\frac{2(1-\lambda)^3}{\lambda^2}} \tag{2.51}$$

2.6.2. Theoretical Model for Drop Shaft Arrangements

Equations (2.47), (2.48), (2.49), (2.50) and (2.51) provide the generalised solution for the discharge in a strong free-surface vortex. An immediate application for the equations was made following the development of the vortex drop shaft in 1947 (Drioli, 1947). Thereafter, numerous authors (Viperalli 1950; 1954; Ackers and Crump, 1960; Pica 1968; 1970 and Hager, 1985) adapted the previous solution of Binnie and Hookings (1948) to derive equations suited to the arbitrary approach flow geometry of the drop shaft structure. Ackers and Crump (1960) rewrote the previous solutions in non-dimensional form and simplified the algebra into a system of six equations (see Equation 2.55 in Table 2.1). Two of the equations are a function of the geometry. The solution to solving the equations is a five step iterative process (1960) but only expresses the discharge as a function of the energy E as opposed to the approach flow depth h.

Viperalli (1950; 1954) proposed an alternative tangential velocity distributions for the throat section ($v_\theta \propto r$) and derived a similar equation to before by considering momentum principle and the Bernoulli's theorem. His solution is as follows:

$$Q = \pi d^2\sqrt{2gh}\,C_{\lambda,N_\Gamma} \tag{2.52}$$

which expresses the discharge in terms of a coefficient C_{λ,N_Γ} by:

$$C_{\lambda,N_\Gamma} = \sqrt{1-E_\Gamma} - \frac{a_c}{d}\sqrt{(a_c/d)^2 - E_\Gamma} - E_\Gamma ln\frac{1+\sqrt{1-E_\Gamma}}{\frac{a_c}{d}+\sqrt{(a_c/d)^2-E_\Gamma}} \tag{2.53}$$

where E_Γ is a form of circulation number of the following form:

$$E_\Gamma = \frac{\Gamma^2}{2gEd^2} \tag{2.54}$$

Pica (1968; 1970) further developed Viparelli's (1954) theorem by applying the principle of maximum discharge together with empirical data for the relationship between the discharge coefficient C_{λ,N_Γ} and the air core diameter a_c. The solution (Equation 2.56 in

Table 2.1) is therefore released of dependence on the unknown energy E that was problematic in Ackers and Crump's (1960) solution. The previous analytical solutions are relatively difficult to solve directly as they either require an iterative process or provide an initial guess of the air core size to determine the depth and flow characteristics. Ideally, an equation for the flowrate based purely on the approach flow depth would be advantageous. Hager (1985) remarked on this and applied approximations to Pica's (1970) analytical solution using curve fitting and a non-dimensional approach flow depth y and discharge Q_0 (Hager A (1985) Equation 2.57). Hager (1985) also made assumptions for the criteria of the air core to yield an additional simple equation (Hager B (1985) Equation 2.58) which is dependent only on the geometry and approach flow depth. However this system is strictly linear and therefore will not apply to all cases of vortex flow, particularly where the circulation number N_Γ becomes low.

Table 2.1 The complete analytical/semi-empirical models to determine the depth-discharge relationship in a full air core vortex (Ackers and Crump, 1960, Pica, 1970, Hager, 1985) for a negligible outlet lip Δ.

Author	Solution		Auxiliary Equations	Comments
Ackers and Crump(1959)	$\frac{Q}{\sqrt{g}d^{\frac{5}{2}}} = \mathrm{F}_2\sqrt{\frac{4F_1E}{d}}$	(2.55)	$F_1 = \lambda^2/4(1+\lambda)$ $F_2 = \frac{\pi}{4}\left(\frac{1}{\lambda}-1\right)\sqrt{2(1-\lambda)}$ $G_1 = \ln(r_p/r_D)$ $G_2 = \frac{d^2}{r_p{}^2}\left(\frac{r_p{}^2}{r_D{}^2}-1\right)$ $\frac{E}{d} = \frac{F_2}{(G_1 - F_1G_2)}$	where F_1, F_2, G_1, G_2, are simplifying parameters
Pica (1970)	$Q = \frac{\frac{\pi}{4}d^2\sqrt{2gh}}{\sqrt{\frac{1}{\mu_0{}^2}-\left(\frac{\pi d^2}{4bh}\right)}}$	(2.56)	$C_d = 0.95 - \frac{a_c}{d}$ $h = \frac{\pi r_{in} d}{b}\mu_0$ $\mu_0 = \frac{3}{2}\frac{1-(a_c/d)^2}{1-(a_c/d)^3}\frac{\mu}{\sqrt{1-\frac{\mu}{(1-(a_c/d)^2)^2}}}$	where μ_0 is an ancillary parameter
Hager A (1985)	$Q = \frac{\pi\sqrt{2y}\,Q_0}{\sqrt{\frac{1}{\mu^2}-\left(\frac{\pi d}{y r_{in}}\right)^2}}$	(2.57)	$y = \frac{bh}{r_{in}d}$ $\mu = 0.95 - \left[1-\left(\frac{2y}{9\pi}\right)^{2/3}\right]^2$ $Q_0 = \sqrt{\frac{g r_{in} d^5}{b}}$	where auxillary equations for h and μ_0 in Picas solution are approximated
Hager B (1985)	$Q = h\sqrt{\frac{2gbd^3}{r_{in}}}$	(2.58)	$0 < \frac{a_c}{d} < 0.5*$ $a_c/d > 1/3*$ $0.5 \le y \le 4*$	*Solution is only dependent on geometry for these conditions

2.6.3. Other Models

Other work was carried out by Knapp (1960) but will not be considered in this work because of the relatively poor agreement found when related to experimental data (Ciaravino et al., 1987) compared to that of other models (Ackers and Crump, 1960; Pica, 1970; Hager, 1985). Furthermore, Adami (1967) performed analytical work which is similar in nature to that of Ackers and Crump (1960) and therefore will not be discussed further. Quick (1990) established an analytical solution based on an iterative process of the equations which again were originally proposed by Acker and Crump (1960). More recently, Ciaravino (Ciaravino et al., 1987; Ciaravino and Ciaravino, 2007) applied mild changes to Viparelli's (1954) and Pica's (1970) solutions to establish a solution that permits negative values of pressure in the throat region. The hypothesis of negative pressure was obtained through laboratory observation and the authors (Ciaravino and Ciaravino, 2007) state that incorporating this in the throat section will overcome uncertainties of the previous models. The solution is a system of six relatively complex equations which are closed using experimental parameters. The parameters are determined from ten geometries which conform to Drioli's (1947) standard. Furthermore, Ciaravino et al., 1987 provided a validation of previous models which indicated errors in predicting the depth-discharge relationship within 12 %.

2.7. Summary of Theoretical Literature

An extensive summative review of past research works on theoretical aspects of free-surface vortices with relevance to the current body of work has been presented. The general characteristics of fluid vortices, current types/classification and sources of formation were discussed. This was followed by a review of the kinematics of vortex flows leading to the solutions for the three-dimensional velocity fields. Finally, based on some of the ideal assumptions surrounding the fully potential vortex, the derivation and solutions for the depth discharge relationship in a strong vortex with a subcritical approach flow were presented. It appears that the ARL vortex type classification system gives a qualitative means to categorise the flow of a weak vortex in the context of hydraulic intakes. However there is scope to expand on this classification system in order

to generalise the types of free-surface vortex flows on a full spectrum including strong vortices.

Regarding the three-dimensional velocity field, although it is difficult to solve a complete model for the flow field based on the Navier-Stokes equations, approximations such as the quasi-cylindrical approach have rendered three-dimensional analytical solutions for the flow in a free-surface vortex (Rott, 1958; Odgaard, 1986; Vatistas et al., 1991) on the basis of the effective viscosity hypothesis. The writer question the validity of some parts of this approach as a consequence of neglecting the derivatives with result to the z-axis when deriving the tangential velocity profile which was only accounted for in Chen et al. 's (Chen et al., 2007) approach. These models however are only suitable for application in weak vortices where the air core does not extend into the intake and thus the effects of viscosity or turbulent momentum transfer results in a rotational flow field around the vortex core. Conversely, in a strong vortex flow, besides Anwar's (1965) model, the tangential velocity has been modelled completely on the assumption that the flow field is fully irrotational outside the air core.

A number of important contributions were made on the topic of an analytical solution to the depth-discharge in a strong vortex (Binnie and Hookings, 1948; Viparelli, 1954; Ackers and Crump, 1960). The most significant solutions have been highlighted with regards direct application (Ackers and Crump, 1960; Pica, 1970; Hager, 1985). The models were based on an assumption for the tangential velocity field at the critical section as well as some empirical groundings. The models have been validated in literature (Hager, 1985; Ciaravino et al., 1987) which have shown to be commendable (errors < 12%). However, the writer argues that the solutions that hold the greatest degree of certainty in a real application require a relatively difficult procedure to acquire a solution. In the process of design, a simpler approach to solving the depth-discharge curve would be of advantage in this field.

Chapter 3.

Experimental Literature

SUMMARY

The earliest technical experiments on concentrated vortex flows date back as far as 1937 (Binnie, 1937). At this time the occurrence of swirling flows had been observed as problematic in a wide variety hydraulic structures of differing geometrical configurations. Therefore, in order to supress the effects of irregular, site-specific intake surroundings, early investigations were carried out on relatively simplistic flow geometries such as cylindrical tanks with basic intakes. The results revealed fundamental characteristics of the parameters that govern vortex formation which could then be adapted to more complex flow domains. Since then, research investigations progressed specifically in topics and applications such as that in hydraulic intakes, drop shafts and other industrial flow structures. An investigation of these past experimental investigations are collected and presented in this chapter highlighting notable results on the effect of the approach flow of a vortex. The groundings for hydraulic similarity based on this literature was discussed in detail. It was shown that there was a lack of experimental research carried out on the strong vortex particularly, that with a subcritical approach flow. Furthermore, the subject would benefit from a technical experimental revisit using improved measurement techniques.

3.1. Cylindrical Tank Investigations

Investigations on cylindrical tanks offer a basic, geometrically neutral approach to analysing the triggering mechanisms for the formation of vortex flows. Such experimental configurations were generally designed to have an orifice diameter d to tank diameter D well below a minimum value so as to ensure that the effects of the confining geometry are negligible (Binnie and Hookings, 1948; Quick 1961; Shapiro 1962). Such ideal cases can offer an insight into developing empirical relationships for the fundamental variables such as the discharge, depth and circulation.

The earliest technical experimental investigations date back to those performed by Binnie and Hookings (1948). Extensive work was carried out by the authors on a 1.2 m diameter test tank with a circular orifice 0.125 m diameter orifice. The leading author first published work on the advantages of using bell mouth overflows for large dams (Binnie, 1937) and then proceeded with experimental observations using the test configuration highlighted in Figure 3.1 (a). In this work he demonstrated that the use of radial ribs in the intake were necessary to limit the formation of a vortex which is detrimental to the flow capacity of the outlet. Shortly after, Binnie (1938) investigated a full radial approach flow for intakes of various diameters and geometries by evaluating the relation between the head (depth) h and discharge Q. Here the author presented a detailed qualitative and quantitative description on borda free, borda full, normal rising and vortex flows in addition to the critical depth at which each occur.

Succeeding this, Binnie and Hookings (1948) investigated similar test conditions where the water possessed an induced swirl by a combination of symmetrically radial and tangential approach flows using jet flows. The resulting flow regime caused variations in the critical submergence h_{cr} and the discharge coefficient C_d which were noted. The depth-discharge relationships were determined under various conditions of tangential velocity in order to formulate a correlation between the "swirl" and measured discharge. In this work the author hypothesised on two causes for the reduction of discharge during full air core vortex formation; (a) since a permanent air-core occupies part of the outlet the effective cross-sectional area for water to flow is reduced and; (b) generation of significant swirl diminished the vertical component of flow near the outlet region. In their work, the authors also provide a detailed description for analytical considerations of the flowrate through the vortex with reference to Sir Geoffrey Taylor's[17] suggestions based on Reynolds (1886) that "*at the critical cross section the velocity of streaming is equal to that of a small wave in the fluid*" (Binnie and Hookings, 1948).

[17] Sir Geoffrey Ingram Taylor OM was a British physicist and mathematician, and a major figure in fluid dynamics and wave theory.

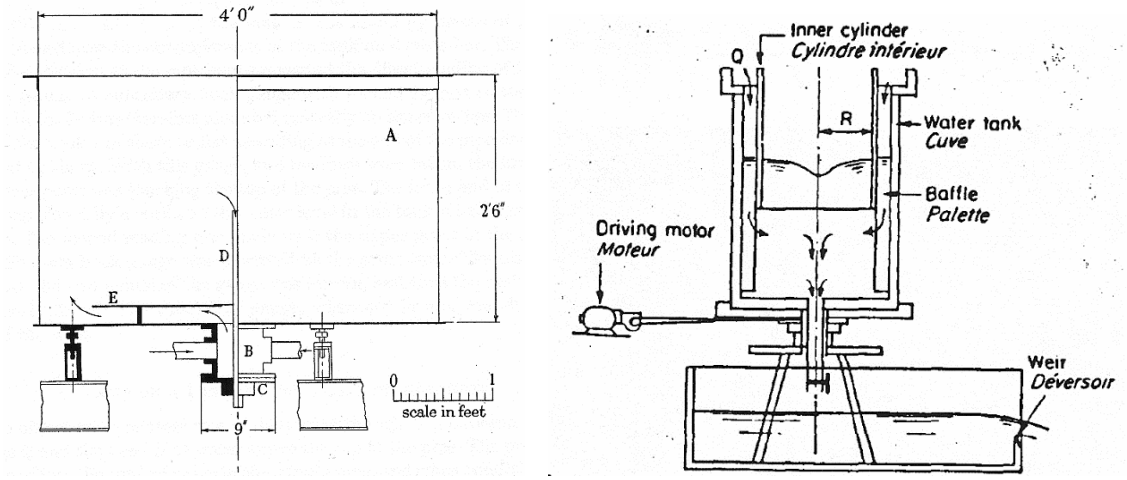

(a) (b)

Figure 3.1: (a) Cross section of Binnie's (Binnie and Hookings, 1948) apparatus and (b) cross section of Einstein and Li's (1951) apparatus.

Kalinske (1940) focused on developing depth-discharge relationships for vortices using vertical pipes of various diameter and lengths. The experiments were conducted in a 6 ft cylindrical tank similar to that used by Binnie and Hookings (1948). However, Kalinske (1940) was also interested in the rate of air flow through the vortex core. Measurement of this additional variable was solved by closing the vessel with an air tight cover and connecting it to a separate air supply. During the experiments, the rate of air flow required to maintain atmospheric pressure inside the tank was justified to be that flowing through the vortex air core. The results of the experiment indicated that the depth-discharge relationship is independent of the pipe length for partly full flow. The author also distinguished between various types of low regimes similar to the work of Binnie (1938). In summary, an empirical relationship that best correlates the data for the rate of water flow through the pipe was derived:

$$Q_w \propto C_d g^{\frac{1}{2}} h^{\frac{1}{2}} d^2 \tag{3.1}$$

where C_d is a dimensionless coefficient of discharge.

Basic experiments were later performed by Posey and Hsu (1950) on a 8 ft cylindrical tank with a 4 inch orifice in order to investigate the circulation dependant coefficient of discharge. Again, the use was made of combined radial and tangential jets (1 inch nozzles) to induce various degrees of circulation. All experiments were carried out under a

constant head of 1.63 ft. Six tests were undertaken for various arrangements of the nozzles and the ratio of tangential to radial flow. It was found that the vortex was not dependent on the number of nozzles but, to a greater extent, on the ratio of the tangential velocity component to the radial velocity component. The results indicate that the coefficient of discharge decreases with θ, the angle the resultant velocity vector makes with the radial axis. This is somewhat related to the angle α_a which was suggested by Amphlett (1978) (see Section 2.2.3).

Einstein and Li (1951) investigated their theoretical solutions (discussed in Section 2.5) on viscous vortex flows by performing experiments in a rotating cylindrical vessel (see Figure 3.1 (b)). The vessel (constructed from glass) is rotated at a definite rate of angular velocity to impose rotation in the fluid. By comparing their results for the shape of the free water surface, it was concluded that the calculated A_o values (parameter dependant on the fluid kinematic viscosity) were much higher than that theoretically anticipated. They therefore conjectured that turbulent momentum transfer otherwise known as the eddy viscosity (ε) may be responsible for the apparent increase in viscosity. Woodford (1964) was later interested in the prediction of the length of the air core when only the circulation and discharge are the system variables. In this case Woodford used an actuator drum with honeycomb perforations to reproduce as much as possible, the ideal boundary conditions of the theoretical model. Like Einstein and Li (1951), Woodford also provided rotation to the drum using a variable speed motor. The drum imparted a moment of momentum to water passing through the perforations which provided a known field circulation, independent of the flow rate. Water was removed from the tank through a central orifice (3 inches in diameter) connected to a suction pipe and pump.

Seminal experimental work was carried out by Quick (1961). In his PhD dissertation, he presented work conducted on the free spiral vortex in two geometrically similar cylindrical tanks to consider conditions for hydraulic similarity. In his work, Quick (1961) determined the dependent dimensionless parameters using Buckingham $\Pi-$theorem (Buckingham, 1915). The small and large tank diameters were 21.25 inches and 7 ft in diameter respectively. An original schematic of Quick's (1961) small tank arrangement is depicted in Figure 3.2(b). In both arrangements, the flow was conveyed to the tank using four supply pipes diametrically opposing each other and spaced evenly throughout

the depth of the tank. A radial flow supply was also permitted at the base of the tank. Measurements of discharge, water surface profile and velocity distribution were made in each test. Velocimetry was performed using an modified stereoscopic imaging technique of particles moving in two vertical planes perpendicular to each other. The results of this work indicated that the non-viscous velocity distribution agrees well with the experimental data but there is a divergence near the vortex core which can amount to a significant error. He states however that "*the assumption of the velocity varying inversely with the radius is accurate to within a small distance from the core surface and even in this region it is still approximately true*" (1961). The results also identify that there is no difference between the agreement of the ideal velocity for weak, medium and strong vortices in the far-field.

Quick (1961) also commented on the radial and axial velocities in detail. He suggested that the radial velocities are too small to be quantified and were therefore considered negligible. However, there exists a band in the flow field near the surface and vessel floor where the radial velocity is large. The axial velocities were found to be immeasurably small in the far-field but nearer the core the velocities became more significant. At the surface, the velocities were always downward and increased with the square of the depth; however, vertical velocities outside the core have been shown to occur in alternate layers of upward and downward flow. A schematic of the secondary flow is highlighted in figure 3.2 (b)). Quick (1961) also highlights that the Reynolds number plays a very minor role and similarity between the model and prototype is obtained by operating at similar Froude numbers in the model and prototype.

Shapiro (1962) undertook renowned work to identify the dependence of vortex formation on the Coriolis Effect (Section 2.2.1). His apparatus consisted of a 6 ft tank and a circular outlet, 3/8 inches in diameter located centrally within the vessel. This work indicated that when all precautions were taken to ensure that the fluid is completely at rest and free from external interference, the vortex does indeed form as a result of the Coriolis force.

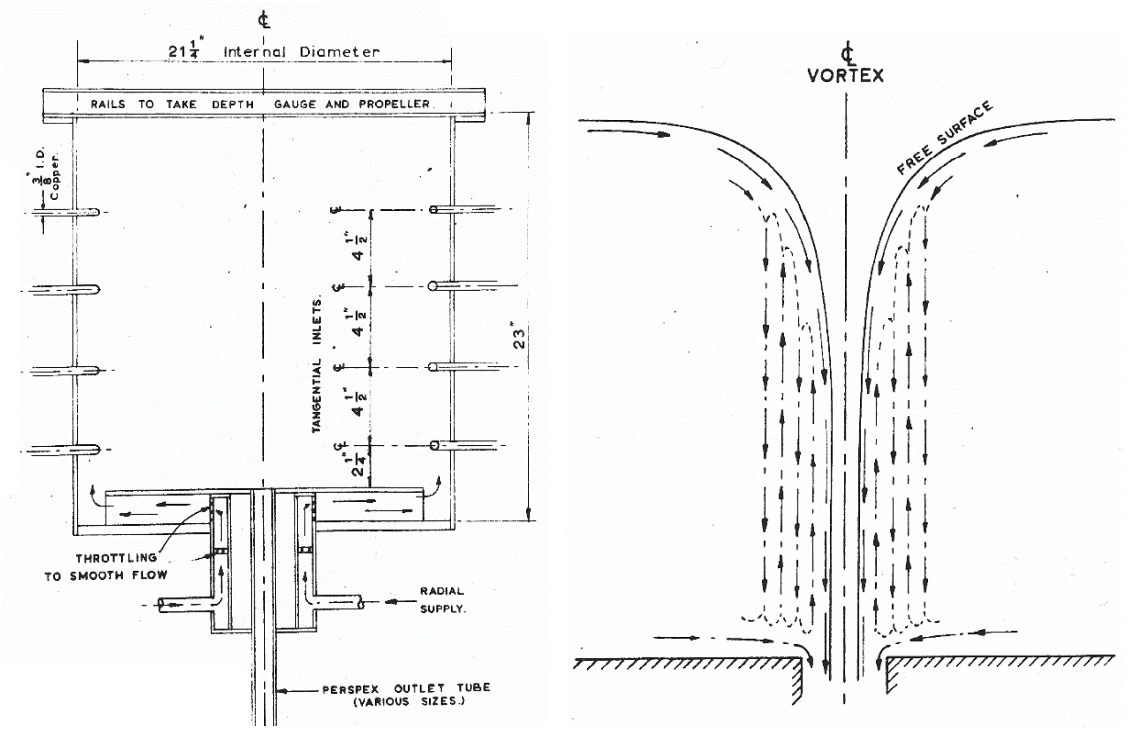

(a) (b)

Figure 3.2: (a) Schematic of Quick's small tank configuration which is constructed from perspex except for the tangential inlets and top rails. (Quick 1961) and (b) Sketch of the observed radial and vertical velocity pattern near-field core region of the vortex (Quick 1961).

Ample research activity was performed by Anwar (1965; 1966; 1968a; 1968b; 1969; 1978; 1980) to investigate the free-surface vortex theoretically and experimentally. Tests were conducted in a transparent plastic tank, 910 mm diameter and 1500 mm deep. The inlet flow configurations were similar to that used by Binnie (1938; 1948), Kalinske (1940), Posey and Hsu (1950) and Quick (1961) with the ability to alternate the tangential and radial supply. In his earliest work (Anwar, 1965) he determined empirical relationships for the coefficient of discharge of three types of flow described by Binnie (1938) for a vertical intake. Anwar (1965) determined the dependent dimensionless parameters using Buckingham Π −theorem (Buckingham, 1915) in a similar fashion to Quick (1961). Successively, his work on vortex flow included theoretical considerations and experimental validation of a number of parameters including limits for hydraulic similarity, coefficient of discharge, water surface and tangential velocity distributions and the effects of turbulence and eddy viscosity.

Determination of the tangential velocity distribution, using an innovative measurement technique described in a later section, resulted in observed discrepancies of the ideal model near the vortex air core, more or less similar to that described by (Quick, 1961). The tangential velocity was shown to be independent of the depth and a high mass flow was recorded to occur in a region close to the top and bottom boundaries (Quick, 1961). In order to reduce this boundary flow an expanded mesh was installed at the boundaries. The streamlines were then taken to be helical in form to produce more turbulent conditions in the core, comparable to conditions described theoretically by Scorer (1967). Anwar (1966) also makes some suggestions regarding hydraulic similarity. He adopts an alternative form of Reynolds number based on the suggestions of Weller (1974) (see section 3.4.2) called the Radial Reynolds number $\mathrm{Rr} = Q/\nu H$. It has been determined (Anwar, 1966) that the circulation number $\mathrm{N_Q} = \Gamma d/Q$ does not depend on this number when $\mathrm{Rr} \geq 10^3$ for vortices with a narrow air core. Anwars experimental work was also used extensively to validate some of the well-established theory on the turbulence in vortex flow and the variation of eddy viscosity in the core region (Anwar, 1969). He also prepared respectable work on the viscous vortex (Anwar, 1968b).

Significant work on the effects of viscosity in vortex flows was presented by Zielinski and Villemonte (1968) using a geometrically similar apparatus tested with oils of various grades of viscosity. The tank used was 6 ft in diameter with an 18 inch slot at the base to accommodate a range of orifices. The tank accommodates an inner boundary ring which permitted the introduction of the test fluid. Zielinski and Villemonte (1968) used dimensional analysis to determine the dependent parameters in their tests. The results showed that as the viscosity increases the circulation decreases from the inlet to the outlet due to increase in viscous shear. In conclusion, the authors found that when $\mathrm{Re}_d > 10{,}000$, the coefficient of discharge can be determined via the following relationship proposed originally by Stevens and Kolf (1959):

$$C_d = 0.686 - 0.218\mathrm{N_v} \qquad (3.2)$$

where $\mathrm{N_v}$ is the vortex number defined later. This finding therefore implied that the effects of viscosity can be neglected for $\mathrm{Re}_d > 10{,}000$.

Dagget and Keulegen (1974) presented a thorough investigation on the conditions of similitude between analogous hydraulic structures that encounter free-surface vortex flows. Experiments were conducted in two cylindrical testing tanks where the flow enters the tank horizontally through set of guide vanes. The larger of the two tanks used was 1.7 m in diameter with the test section inside a 0.9 m diameter ring of 114 guide vanes. Orifices of diameters d = 25 mm, 51 mm, 76 mm and 100 mm were investigated. Baffling and screens produced uniform inlet conditions. The smaller test tank was used to accommodate a smaller volume of glycerine as the test fluid. This was 610 mm square tank with a 343 mm circular test area surrounded by 90 guide vanes. The test orifices used in this model were d = 9.5 mm, 19 mm, 29 mm and 38 mm. To investigate the effects of surface tension and viscosity, mixtures of water, glycerine and various grades of oil were used. The results concluded that when $\mathrm{Re}_d > 5 \times 10^4$ the coefficient of discharge can be obtained with dependency only on the circulation number N_Γ. This was found to be:

$$\begin{aligned} C_d &= 0.921 && \tfrac{1}{2}N_\Gamma \leq 0.1 \\ C_d &= 0.966 - 0.45\tfrac{1}{2}N_\Gamma && \tfrac{1}{2}N_\Gamma > 0.1 \end{aligned} \qquad (3.3)$$

Al'Tshul and Margolin (1968) found a similar relationship in their investigation. For the range of values tested, it was shown that surface tension did not affect vortex formation. Measurements on the tangential and radial velocity components versus depth were also presented demonstrating that the tangential velocity and radial velocity was independent of the depth except for at the boundaries. The radial velocity was found to manifest in the bottom boundary, where a noticeable increase was observed. The variation in velocity was found to be inversely proportional to the radius implying that the effects of boundary roughness are significant; thus confirming the findings of Anwar (1965).

Jain et al. (1978) sought to substantiate on experiments carried out by Anwar (1965; 1966) and Daggett and Keulegen (1974) by examining cases where the intake velocity was independent of submergence depth h/d. Thus, the authors utilised a circular tank with an intake connected to a centrifugal pump to provide independent control of flow and submergence. The small and large tanks were 0.75 m and 1.875 m in diameter respectively. Circulation in the approach flow was provided through adjustable guide vanes in each case. The inflow was homogenised using rectangular conduits packed with

gravel. The effects of viscosity were investigated using carboxy-methly cellulose and water mixture while surface tension was evaluated by adding small quantities of iso-amyl alcohol. Results indicated that the change in surface tension (0.072N/m – 0.044 N/m) exhibits no effect on the critical submergence i.e. when the outlet Weber number We_d was in the range$1.2 \times 10^2 – 3.4\times 10^4$. Freedom from the effects of viscosity were found for values of $Re_d \geq 5 \times 10^4$. A solution to determine the critical submergence was presented with dependence on the circulation number N_Q, outlet Froude number Fr_d and the viscosity.

Echavez and McCann (2002) revisited the three-dimensional flow problem to highlight the importance of separating the secondary radial and axial components of the total outflow. A cylindrical perspex tank of 0.7 m equal diameter and height was used. The flow was conveyed to the tank tangentially using a single horizontal pipe which could be adjusted for a variety of depths h/d. Six different outlets were evaluated. The initial case consisted of a simple 38 mm outlet pipe. The remaining test cases were used to control the secondary flows originating close to the boundary. Circulation was determined using a flotation device which will be addressed further in Section 3.5.1. The general flow pattern was described for various conditions of boundary layer flow to vortex flow with qualitative results presented by flow visualisation. A qualitative model of the general flow pattern with secondary fluid structures were illustrated and compared very well to that described by Quick (1961).

Anderson et al. (2006) studied the bath tub vortex in a rotating cylinder to experimentally validate their theoretical considerations for the velocity and surface shape. Additional consideration for the Ekman boundary layer was included and modelled accordingly. For this experiment, a 20 cm cylindrical perspex tank was mounted inside a square reservoir. A 1 mm radius circular drain hole was made in the metal plate at the centre of the cylinder. The container was rotated at a constant rotation rate about the vertical axis of symmetry. As the rotation rate increased, the air core tip extended and tended towards the tank base. The tip was stable when rotation rates were below a certain value but becomes unsteady with signs of vertical oscillations at higher rotation rates. Air-bubbles were further observed to detach from the tip upon additional rotation. By imaging a laser-induced fluorescence (LIF), the Ekman layer and velocity distribution of the updraft and axial

flow region could be visualised. Velocities were determined from trajectories of small tracer particles which spiral up from the boundary layer and down to the outlet using a vertical laser light sheet. A good agreement was found between the experiment and the linear Ekman theory while the azimuthal velocity profile compared moderately to the test data resulting in a 5 - 10% error.

3.2. Experiments at Hydraulic Intakes

This section summarises the research work conducted on model and prototype studies of hydraulic intakes; namely that of pump sump and hydropower intakes but also in cooling systems of nuclear reactors. As described in Section 1.1, the onset of air entrainment at pump and hydropower intakes can cause considerable reductions in performance efficiencies and detrimental effects to the lifespan of hydraulic machinery. Although Gordon (1970) and Rutschmann et al. (1987) have presented methods and design criteria to avoid vortices at intakes, physical modelling still remains an accurate tool to justify decision making in design processes. Though the subject matter of air entrainment vortices does not directly apply to the focus of this study, it is important to review the experimental methods applied in this context. Furthermore, hydraulic intakes are generally exposed to asymmetrical approach flow conditions which, along with the other governing parameters of depth and discharge, are of vital importance in this study.

Knauss (1987) provided an extensive overview of the work carried out on this topic. A number of authors have investigated the flow field around a pump and hydropower intake in order to present empirical relationships to predict the critical depth. However the results were not well-disposed towards a universal relationship and inclined to be specific to the type of study carried out. A common approach is to evaluate the geometrical arrangement of a system by relating the critical submergence to the intake Froude number by:

$$(h/d)_{cr} = const.\ \mathrm{Fr}_d^{\,n} \qquad (3.4)$$

Various values for the exponent n were suggested e.g. n = 2 (Quick, 1970), n = 1 (Gordon, 1970) and n = 1/2 (Jain et al., 1978) depending on the type of circulation supplied in the system. Further relationships between the critical submergence were determined by Berge (1966), Dagget and Keulegen (1974), Jain et al. (1978), Anwar et

al. (1978), where the general form complies with that of Equation (3.4). Again, the physical meaning of the constant in this equation is interpreted as a function of the intake type (e.g. direction, size, geometric boundaries etc.).

Trivellato and Springhetti (2001), Borghei and Kabiri-Samani (2003), Kabiri-Samani and Borghei (2013) as well as Taghvaei et al. (2012) carried out a comprehensive analysis on the placement of anti-vortex devices to hinder the onset of air-entrainment. In their studies they considered various anti-vortex device designs and the effect they had on supressing vortex flow and consequential effects on the intake characteristics. Martinerie et al, (2008) investigated vortex formation at pump-storage intake structures using physical models where they assessed the risk of frazil ice entrainment using a two-dimensional ultrasonic velocity profiler. Frazil ice entrainment poses the risk of blockage at trash racks and thus solutions to reduce this risk must be considered (Martinerie et al, 2008).

Sarkardeh et al. (2010) performed experimental modelling to investigate the effect of the head wall and trash rack on vortices. Acoustic Doppler Velocimetry was used to determine velocity profiles and circulation. The authors determined a relationship between the vortex strength and type. More recently, Yang et al. (2014) performed dimensional analysis and experimental modelling to determine the effect of the intake-entrance profiles on the critical submergence. The authors tested eight entrance profiles and discovered that the square edge profile produced the highest local head loss. Li et al. (2008) Wang et al. (2010), and Suerick-Gulick et al. (2013) all successfully employed particle image techniques to investigate air core vortices at hydraulic intakes. Carriveau et al. (2009) and Suerick-Gulick et al. (2013; 2014) carried out extensive studies on the mechanisms of free-surface vortex evolution as well as axial stretching. In Carriveau et al.'s (2009) study, the authors investigated NPSS and PSS vortex types. More recently, Möller et al. (2012; 2013) carried out extensive analysis on a number of aspects surrounding the air entrainment vortex. In this work the author presents data on the unsteadiness of the vortex, relationships to determine the critical submergence and specifies guidelines to estimate the air-entrainment rate Q_a.

In recent times, the increasing use of sodium-cooled fast reactors (SFRs) in the nuclear industry has established impetus for the investigation of vortices in such circumstances. SFRs are susceptible to vortex flow gas entrainment as a result of their arrangement thus

posing a threat to the operational safety of the systems. Kimura et al. (2008), Ezure et al. (2011) and Cristofano et al. (2014a) all performed experimental studies on free-surface vortices in a horizontal intake as applied to the SFR's.

3.3. Experiments at Vortex-flow Intakes

In the previous sections of this Chapter, the majority of experimental studies were performed to assess situations where the swirl and free-surface vortex formation was considered undesirable. On the contrary, this section deals with the design of intake structures that produce a controlled and stable vortex flow through geometrically induced circulation. The content of this section is therefore of significant relevance to the overall project. The formation of a strong stable vortex is governed by the approach flow geometry or asymmetry described by the parameter α_a. The majority of the subsequent experiments will be described for that of the drop shaft structure; however, the arrangement is much the same for the aforementioned hydroelectric applications (Dhakal et al., 2015) and other devices such as hydrodynamics flow separators (Vatistas et al., 1986).

In the drop shaft application, flow is conveyed tangentially to the chamber through an inlet of width b with a bottom slope S_o and discharges at some smaller radius through the orifice of diameter d at the base of the tank (Hager, 2010). This sets up a strong steady circulation with a full vortex air core (Jain and Ettema, 1987). Differing from their plunge-flow counterpart, vortex-flow drop structures have an additional circular shaft of diameter d_s which extends vertically for a distance downstream of the orifice (Jain and Kennedy, 1983; Hager, 2010). The vortex air core diameter a initially decreases to the critical section at a_c before increasing again in the drop shaft thereby forming a throat (Jain and Ettema, 1987) and an annular jet. At the critical section just below the orifice (Section 2.6.1), residual centrifugal forces in the annular jet force the fluid to cling or "hug" the drop shaft walls for a considerable distance vertically downstream (Jain and Kennedy, 1983). This is a key aspect that dictates the level of dissipation in the drop shaft through turbulence, shearing and frictional energy losses (Jeanpierre and Lachal, 1966). The experimental studies performed on these types of arrangements will be subsequently discussed in detail.

3.3.1. Types of Vortex Intake

Prior to the review of experiments in vortex intake structures, it is important to comment on the types of vortex intake that are used in industry. There exists two general types: a subcritical inlet and a supercritical inlet. Subcritical inlet structures ($Fr_i < 1$) are ones where the inertial forces in the inlet channel are dominated by the gravitational forces (Jain and Ettema, 1987). The subcritical approach flow can be considered stable for $Fr_i < 0.7$ (Hager, 2010). These are generalised by bottom slope $S_o = 0$. The opposite case is that of a supercritical approach flow ($Fr_i > 1$) where the inertial forces at the inlet dominate. In this case, high velocities are usually introduced by a bottom slope S_o and a streamwise bottom slope S_{oe} where values between 10 - 20% are optimum and the maximum $S_{oe} < 30\%$ (Hager, 2010). The approach flow can also be made supercritical via a pressure flow inlet (Motzet and Valentin, 2002).

There are several configurations for drop shaft structures and vortex chambers alike which are classified into five broad categories (Jain and Kennedy, 1983; Jain and Ettema, 1987) which are summarised as follows:

a) Circular: The most simplistic approach flow configuration is that of a circular inlet where the side of the intake is concentric with the dropshaft and the floor is horizontal ($S_o = 0$). Therefore, subcritical approach flow conditions prevail for the majority of applications (Laushey and Mavis, 1952; Zotloeterer, 2009). They can be further modified by adding a guide vane to increase the discharge capacity of the chamber for a given approach flow depth (h/d).

b) Scroll: Drioli's (1969) scroll inlet is the most commonly used form of vortex intake and further increases the discharge capacity in comparison to the circular shaft by spiralling the sides of the intake towards the drop shaft or orifice. The floor in a scroll shaft is horizontal.

c) Spiral: The spiral inlet has a scrolling formulation similar to b) and it has a sloping floor ($S_o > 0$) (Drioli, 1947). The approach flow conditions are then generally of the supercritical type. These can also be modified to have a banked approaching channel.

d) Tangential: The tangential inlet (Jain, 1984) is a form of supercritical circular inlet. The flow is conveyed tangentially to the circular chamber in a sloping channel. The drop shaft diameter d_s equals the orfice diameter d and decreases in diameter with the contraction angle.

e) Slot: The vertical slot vortex chamber (Quick, 1990) is composed of a vertical pipe with a 90º rectangular slot cut into its top. A vertical guide wall conveys flow into the slot in a form of weir flow where its critical section is now near the inlet. Although the depth discharge of this type of structure is similar to that of the spiral design, the unit saves on space being more compact in its design (suitable for underground installations).

f) Confined: The confined chamber is any combination of the previous configurations, however in this arrangement, a lid is secured over the chamber in order to allow the approach flow to become pressurised on increased depth-discharge. The top lid can be with or without an air vent to allow an air core to form inside the unit. Applications for confined chambers range from hydrodynamic flow separation (Vatistas et al., 1986) to vortex throttling devices (Conway, 1971; Brombach, 1982).

g) Siphonic: The intake consists of a series of siphons located around the edge of the intake. These types are less commonly used and therefore will not be discussed in further detail. (Jevdjevich and Levin, 1953).

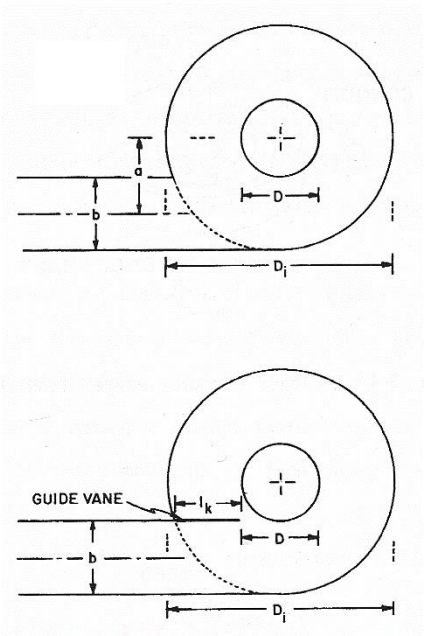
a
b
D
D_i
GUIDE VANE
l_k

(a)

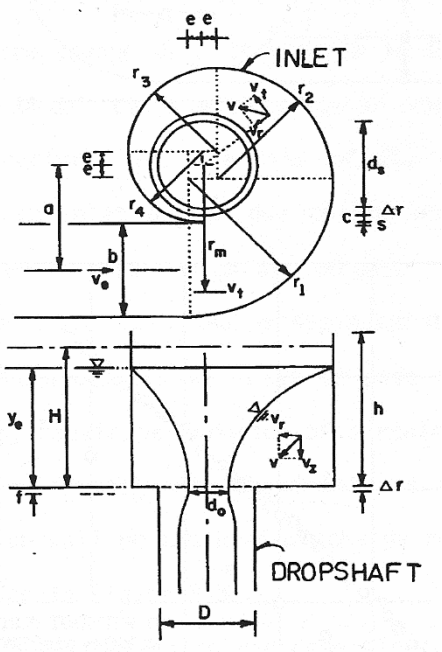
INLET
r_1
r_2
r_3
r_4
r_m
d_s
d_o
H
h
DROPSHAFT
D

(b)

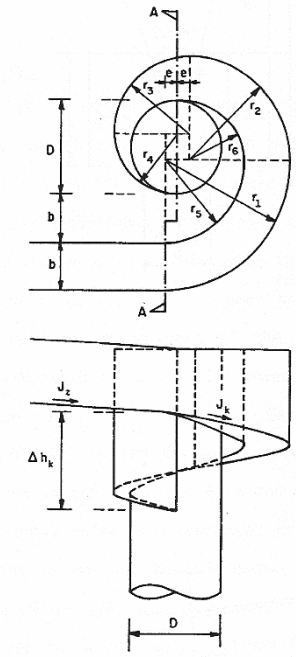
A
D
b
J_z
J_k
Δh_k

(c)

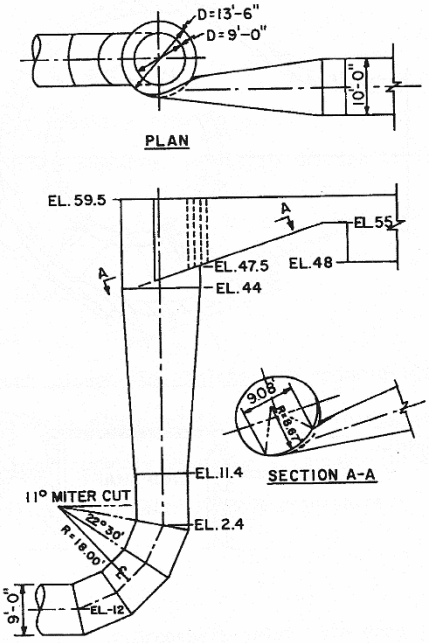
D=13'-6"
D=9'-0"
PLAN
EL. 59.5
EL. 55
EL. 48
EL. 47.5
EL. 44
EL. 11.4
EL. 2.4
EL. 12
11° MITER CUT
SECTION A-A

(d)

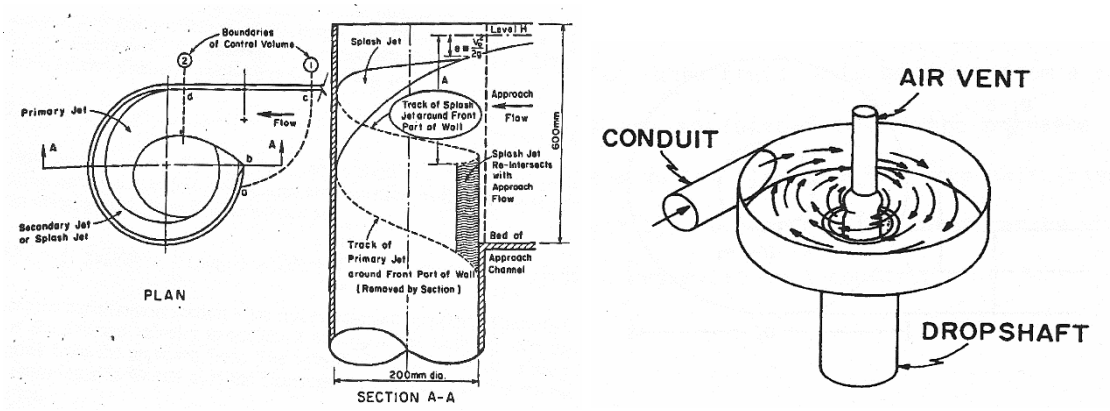

(e) (f)

Figure 3.3: Illustrations of vortex chamber configurations: (a) circular and circular with guide wall, (b) scroll, (c) spiral, (d) tangential, (e) slot and (f) confined. The siphonic type discussed in (g) is omitted from the figure. Images from Jain and Kennedy (1983) and Quick (Quick, 1990).

3.3.2. Experiments on Subcritical Approach Flows

Laushey and Mavis (1952) and Laushey (1953) investigated the circular inlet configuration as a means to safely drop storm-sewer flows for the Algheny County Sanitary District of Pittsburgh. In this work the authors carried out physical model studies to determine the discharge characteristics, air entrainment, pressures and dissipation of energy. The experiments were conducted in a 6 ” diameter pipe having a Lucite section of about 4ft in length at the top. Velocities were measured using a pitot tube. Further experimental model studies of prototypes were conducted by the Anderson (1961) carried out further work on the circular orifice by analysing three tank-diameter/orifice-diameter d/D ratios. The author rejected this design due to failure to comply with design requirements as well as the costs associated with construction. Kleinschroth and Wirth (1981) modified the geometry with the previously described guide-wall which solves the problem by decreasing the discharge capacity. Mulligan and Casserly (2010) performed numerous physical model studies on the circular inlet for the purpose of hydropower generation. In their work, the authors commented on the lack of verticality of the vortex core which would inflict imbalanced forces in the proposed turbine runner. This defect was found to be as a result of the asymmetric tangential velocity distribution caused by the circular approach flow geometry. The problem was resolved through the design of a scroll type vortex chamber. The scroll inlet was subsequently investigated by the authors

(Mulligan and Casserly, 2010) using experimental techniques to resolve the free-surface and velocity distribution across the vortex chamber. The data was used subsequently to validate analytical models. In their findings (Mulligan and Casserly, 2010) it was found that the free-surface analytical model compared reasonably well with the experimental data.

Early experimental investigations on the scroll type vortex chamber were presented by Drioli (1969), Pica (1968; 1970), Viparelli (1950, 1954), Knapp (1960), Ackers and Crump (1960). The ETH VAW Switzerland (ETH, 1977) also performed some model studies for prototypes. Stevens and Kolf (1959) conducted physical model studies on a vortex chamber based on results from dimensional analysis (Buckingham, 1915) on the dependent variables. Stevens and Kolf (1959) considered four varying orifice diameters and arrived at Equation (3.2) which describes a linear regression between the coefficient of discharge and the circulation number for values of $0 > N_v > \pi$.

3.3.3. Experiments on Supercritical Approach Flows

Drioli (1947) was the first to perform experimental analysis on drop shaft structures which were typically that of the spiral inlet design. Kleinscroth and Wirth (1981) as well as Kellenberger (1988) introduced design procedures as well as results on physical model experiments for spiral inlets. Small and large scale model studies were performed by Jain and Kennedy (1983) and suggestions were made on similarity and optimum length of the de-aeration chamber. Jain (1984) conducted a laboratory study to develop and test tangential-inlet drop structures for an in-line storage system proposed by the Milwaukee Metropolitan Sewerage District. The experimental data was used to predict analytical models proposed by the author. Subsequent work was carried out by Jain (1988) to assess air transport in the annular jet of a vortex drop shaft. Hager (1990) optimised the spiral inlet based on data collected from various inlet geometries. The surface profile along the outer guiding wall was analysed. It was found that the Froude number Fr_i of the approach flow and the radius of the outer inlet wall influence the maximum standing wave height.

More recently, Motzet and Valentin (2002) assessed the efficiency of a horizontal bottom vortex chamber (scroll type) when used to convey a supercritical approach flow. Here they used a pressure conduit to convey flow at the inlet and concluded that conventional

supercritical flow equations can be used to predict shock waves for low discharges but disagreements were found for higher discharges. Yu and Lee (2007; 2009) carried out extensive experimental work in order to progress towards general and robust design criteria which are not available for supercritical drop shafts. It was found that the flow in the sloping and tapering section of the inlet is strongly dependent on the geometry of the inlet and drop shaft. Fifteen experimental models are investigated and the observations agree excellently with the theoretical prediction.

3.4. Similarity of Modelling Criteria

Dimensional analysis implemented on vortex flow by previous authors (Stevens and Kolf, 1959; Quick, 1961; Anwar, 1965) highlight that the flow field is always, in some way, dependent on the geometry and the dimensionless numbers: Froude number Fr, Reynolds number Re and the Weber number We owing to the effects of the gravity, viscosity and surface tension in the local scale respectively. Quick (1961) mentioned that dynamic similarity will exist between geometrically similar systems when they are operated at an identical Froude number for a sufficiently large scale. It is well known that when performing experimental modelling using scaled models, it is exceptionally difficult, if not impossible, to ensure that complete hydraulic similarity is conserved in the model (Heller, 2011). This is because it is problematic to attain equality for Fr, Re and We concurrently between the model and prototype.

The general consensus arising from the majority of experimental studies carried out to date (Quick, 1961; Knauss, 1987) is that Froude number Fr is the principal parameter that influences free-surface vortex flows. Therefore, it has been customary (Stevens and Kolf, 1959; Anwar, 1965) to base the model study of vortex flow on Froude similitude provided that physical models are sized to a sufficient scale. Based on past literature, the criteria for suitable model scales that satisfy Froude similarity are discussed in the following sections.

3.4.1. Influence of the Weber Number

The Weber number We is a dimensionless number that gives a measure of the relative importance of a fluids inertia compared to its surface tension. This number is particularly

important in multiphase flows with strongly curved free-surfaces. The Weber number is defined mathematically by:

$$\mathrm{We} = \frac{\rho v^2 l}{\sigma} \tag{3.5}$$

where v is given here as the chracteristic velocity and l is the characteristic length. A number of relevant experimental investigations have been performed to study the dependence of vortex flows on the Weber number. Here the Weber number is derived as the outlet Weber number We_d given by:

$$\mathrm{We}_d = \frac{\rho \widetilde{v_z}^2 d}{\sigma} \tag{3.6}$$

The first examination for the model scale dependence on the outlet Weber number We_d was performed by Daggett and Keulegen (1974). In their work, the authors conducted a thorough review of the effects of the Weber number on incipient conditions, shape and size of a free-surface vortex using two fluids of varying surface tension. The fluids were water-glycerine mixtures and two geometrically similar model scales were assessed. This work displayed that the surface tension does not appear to affect the vortex flow. In his discussion on the previous work (1974), Hughes (1975) contended that, from a theoretical perspective, air entrainment in vortex flows should somewhat depend on the surface tension. However, Yilidrim and Jain (1981) also performed an analytical study and argued in favour of neglecting surface tension for most systems with exception to low circulation cases.

Anwar et al., (1978) subsequently investigated the effect of the Weber number and concluded that the flow in an air-entraining vortex was unaffected by surface tension when the approach flow depth h/d is low, and the Circulation number, Weber number and the radial Reynolds numbers were high. The previous, indeterminate qualitative criteria were later enhanced by Jain et al. (1978) who performed a comprehensive investigation on the surface tension by adding iso-amyl alcohol at the free-surface which did not affect the viscosity of the test fluid (clean water in this case). This concluded that there was no influence of surface tension on the critical submergence when the intake Weber number $\mathrm{We}_d \geq 120$. Anwar and Amphlett (1980) performed an analysis on a

vertically inverted intake and concluded that surface tension has no effect when the radial Reynolds number $Rr \geq 3 \times 10^4$. Based on his theory and data available from previous authors, Odgaard (1986) reported that the surface tension becomes negligible for typical intake model conditions when $We_d > 720 Fr_d^{1/2} N_\Gamma^{-3/2} Re_d^{-1/4}$. More recently Taştan and Yilidrim (2010) investigated the effects of the dimensionless parameters in order to identify the limiting effects of We_d on the critical depth. Suerich-Gulick (2014) showed that the effects of surface tension are different depending on whether the shape of the depression was a funnel or a dimple.

3.4.2. Influence of the Reynolds Number

The influence of the Reynolds number has undergone conflicting opinions following a number of investigations in this area. Haindl (1959) postulated that the Reynolds number between the model and prototype is essential for similitude in vortex flows (Reynolds law). However, many others argue in favour of the Froude similarity with specifications for the minimum outlet Reynolds number.

$$Re_d = \frac{\widetilde{v_z} d}{\nu} \tag{3.7}$$

Zielinski and Villemonte (1968) tested various oil mixtures and reported that Froude similitude can be employed for estimating the coefficient of discharge using the Kolf Number when $Re_d > 10^5$. Dagget and Keulegen (1974) however showed that viscous effects become unimportant for a much smaller outlet Reynolds number $Re_d > 2.5 \times 10^4$.

In the case of full air core vortices, Weller (1974) justly underlined that the use of the radial Reynolds number $Rr = Q/\nu h$ was preferable to the outlet Reynolds number Re_d which is based on a fully submerged orifice. Based on this value, other authors have adopted this value in their studies (Anwar and Amimilett, 1980). It was shown that N_Γ was unaffected when; $Rr > 10^3$ in the case of vortex flow in a cylindrical tank (1965; 1966) and $Rr > 4 \times 10^4$ for vertically inverted intakes (Anwar and Amimilett, 1980). Another limiting value Re_d/Fr_i was suggested by Jain et al. (1978) to be $Re_d/Fr_i > 5 \times 10^4$. Because this value is derived from the outlet Reynolds number Re_d its validity was questioned by Amphlett (1978). Odgaard (1986) based on his theory and data available from previous authors further reported that the viscosity becomes negligible for typical

intake model conditions when $\mathrm{Re}_d > 1.1 \times 10^3 \left(\frac{h}{d}\right)^2 \frac{gd^3}{\Gamma^2}$.

3.4.3. Other Criteria

Denny (1956) suggested that for hydraulic similarity to be maintained, the velocity in the model must equal the velocity in the prototype in a so called 'equal-velocity' criterion. However, Dhillon (1979) later showed that models constructed according to Anwar's criterion (Anwar et al., 1978) exhibited good conformity with prototype investigation as opposed to the equal velocity criterion. Denny's (1956) method also called for relatively large scales and unrealistic approach flow conditions and was thus considered to be profligate in physical model studies (Knauss, 1987). In addition to Anwar's (1965) Criterion, Anwar (1965) also stated a more general yet conservative limit for model scales:

"a reasonably large scale, say 1/20, and be of sufficient extent to reproduce the sum total of circulation about the intake, or the curved flow pattern in the vicinity of the intake must be artificially reproduced".

Padmanabhan and Hecker (1984) performed experimental work on hydraulic models (1:2 and 1:4) of a full size sump and observed no scaling effects when using Froude similarity. The approach flow Reynolds number was in the range of $2 \times 10^3 - 2 \times 10^4$, radial Reynolds number 1.5×10^2 - 4.4×10^4 and the Weber number 6×10^2 - 2×10^3. A detailed model-prototype comparison for a range of projects was presented by Hecker (1981). This confirmed that hydraulic models operated in conformance with Froude similitude are sufficient when predicting vortex intensity. However, no quantitative limits to either the Reynolds number or the Weber number have been specified. Laushey and Mavis (1952) recommend a scale factor l_m/l_p of between $1/4 - 1/6$. Jain and Kennedy (1983) later suggested that scale effects are negligible when the flow in the vortex is in a fully turbulent regime. When modelling the vortex chamber, Pica (1968) reported no scaling effects between two scale models (d = 100mm and 50mm). However, in his discussion on this work, McCorquodale (1961) states that because some values for the Reynolds number in his study are less than 10^5 (Zielinski and Villemonte, 1968), some small viscous scale effects might be expected.

3.4.4. Conclusion on Similarity of Vortex Flows

The availability of theoretical and experimental evidence to support various criteria for hydraulic similarity between the model and prototype is extensive. The Reynolds similarity (Haindl, 1959) and the equal-velocity criterion (Denny, 1956) appear to be unjustifiable and unsuitable in the light of Dhillon's (1979) work. Therefore, Froude similarity is deemed to be appropriate when the Reynolds number and Weber number are kept above the minimum specified values in the model. In order to avoid the effects of surface tension when scaling the model in this fashion, it would be good practice to maintain outlet Weber numbers We_d in excess of 120 according to Jain et al.'s (1978) findings. Odgaard's (1986) condition for the outlet Weber number We_d also appears to be relevant in the case of a strong free-surface vortex.

The effects of viscosity and hence, the Reynolds number, however appears to have not yet gained a general consensus. The type of Reynolds number that is to be monitored in the physical model seems to be dependent on the type of vortex flow under consideration. It is noted that most of the aforementioned studies are validated for situations where the velocity at the intake is independent of the approach flow depth (i.e. pump intakes). Induced or artificial circulation in these models are typically quite low and the vortices tend to be of the 'weak' type. With exception to the criteria specified by Zielinski and Villemonte (1968) and Daggett and Keulegen (1974), investigations on the scale effects in strong vortices with a full air core are relatively limited. Here the previous authors based their limiting criteria on the submerged Reynolds number Re_d (Quick, 1961; Odgaard, 1986) as opposed to the radial Reynolds number which is suggested by Weller (1975). The writers are of the opinion that further work is needed to investigate the scale effects in strong vortices based on the methods specified by previous authors using the radial Reynolds number. A form of tangential Reynolds number (similar to the vortex or Taylor number) may also be of some benefit here having the following form:

$$Re_v = \frac{\Gamma_\infty}{\nu} \tag{3.8}$$

However, in the present study, Anwar's (1966) criteria for the minimum radial Reynolds number of 10^3 in the model will be adhered to. The criteria specified by Jain and Kennedy (1983) for a fully turbulent flow will also be monitored during experimentation.

3.5. Measurement Techniques

So far it can be gathered from the experimental review that the success of testing is governed by accurate determination of the following dimensionless flow parameters:

$$\mathrm{Fr}_{in} = \frac{\widetilde{v_{in}}}{\sqrt{gh}} \quad \text{(inlet Froude number)} \quad (3.9)$$

$$\mathrm{Fr}_{d} = \frac{4Q}{\pi d^2\sqrt{gd}} \quad \text{(intake Froude number)} \quad (3.10)$$

$$\mathrm{K} = \frac{\Gamma_\infty}{\widetilde{v_z}d} = \frac{\pi}{4}\mathrm{Nr} \quad \text{(circulation number)} \quad (3.11)$$

$$\mathrm{N_v} = \frac{\Gamma_\infty}{d\sqrt{2gh}} \quad \text{(vortex number)} \quad (3.12)$$

$$\mathrm{Re} = \frac{\widetilde{v_z}d}{\nu} \quad \text{(intake Reynolds number)} \quad (3.13)$$

$$\mathrm{Rr} = \frac{Q}{\nu h} \quad \text{(radial Reynolds number)} \quad (3.14)$$

$$\mathrm{We}_d = \widetilde{v_z}\sqrt{\frac{\rho d}{\sigma}} \quad \text{(Weber number)} \quad (3.15)$$

$$h/d \quad \text{(relative intake submergence or approach flow depth)} \quad (3.16)$$

$$C_d = \frac{4Q}{\pi d^2\sqrt{2gh}} \quad \text{(discharge coefficient)} \quad (3.17)$$

in addition to the velocity fields v_r, v_θ, v_z and pressure (free-surface) fields p in the radial direction. The repeating experimental variables in the above equations are Γ_∞ (resulting from determination of v_θ at position r), v_z, Q and h by treating the fluid characteristics (ν, ρ and σ) as being constant. The nature of the free-surface vortex makes it a formidable task to obtain accurate measurements of the repeating variables particularly when reliable quantitative conclusions are to be drawn from the results. In this section, further detail with regards to the instrumentation and methods of the previous investigations are presented.

3.5.1. Measurements of Fluid Velocity and Circulation

Although numerous authors (Quick, 1961; Anwar, 1965; Odgaard, 1986; Echavez and McCann, 2002) have made a respectable effort to assess the tangential velocity distribution $v_\theta(r)$ and circulation $\Gamma_r(r)$ distribution, there is little evidence of investigations of this nature carried out on strong vortex flows at vortex intakes. Furthermore, the additional velocity components $v_r(r)$ and $v_z(r)$ are necessary to gather a complete three-dimensional perspective of the flow overall flow field (Anwar, 1969; Daggett and Keulegan, 1974). The use of a pitot tube has been made by numerous authors (Laushey and Mavis; 1952, Borghei and Kabiri Samani, 2003; Mulligan and Casserly, 2010) however the accuracy of the velocity measurements using this device can be uncertain due to its intrusive effect on the flow field (Quick, 1961; Mulligan and Casserly, 2010). Moreover, the pitot tube is a one-dimensional velocimetry device which further downgrades its performance when employed in three-dimensional flows. Vatistas at al. (1986) however made use of a rotating pitot-probe to determine multi-dimensional velocities; however, the method appears to be time intensive and is subject to human error as a consequence of its manual operation.

Echavez and McCann (2002) adopted a floatation device held lightly in place on the water surface to measure the tangential velocity at a particular radius to compute the far-field circulation Γ_∞. Although the technique was somewhat viable for strong vortices, its presence on the free-surface of weaker vortex flows may have hindered their formation and the vortices steady state development.

Early experimental data for the fluid speeds in a full air core vortex using non-intrusive techniques was provided by Anwar (1965; 1966; 1968b; 1969). In these studies, Anwar devised an optical apparatus (original schematic displayed in Figure 3.4) to measure the velocity components. Particles normally present in the water were illuminated by a high intensity light source which were seen as bright flashes when viewed through a telescope at a particular radial position. The movement of these particles appeared to be arrested when viewed through a parallel-sided glass prism set between the tank and the telescope which was rotated at a speed directly related to the fluid speed. Therefore, sensitive measurements of the fluids velocity could be extracted from the flow field in plane with the light source. All three components of the velocity field were extracted from the

measurements. Field circulation Γ_∞ and circulation distribution Γ_r can easily be computed subsequently from the tangential velocity data by $\Gamma = 2\pi v_\theta r$.

Berge (1966) derived another simple, non-intrusive technique to determine the field circulation in a vortex called the refracted ray method. When a parallel beam of light was directed onto the free-surface where a weak full air core vortex is present, the light was refracted within the surface depression casting a circular shadow on the base of the tank. An extensive theoretical analysis of this phenomena was presented by Aboelkassem and Vatistas (2007). Berge (1966) found that the field circulation was correlated with the diameter of the shadow produced and the water depth h by the following empirical formula:

$$\Gamma_\infty = g^{\frac{1}{2}}(0.424d)^{1.942}h^{-0.442} \tag{3.18}$$

where, d is the shadow of the diameter, g is the gravitational constant and h is the total water depth or the water depth at the edge of the free-surface depression. Details of the experimental arrangement is highlighted in Figure 3.5.

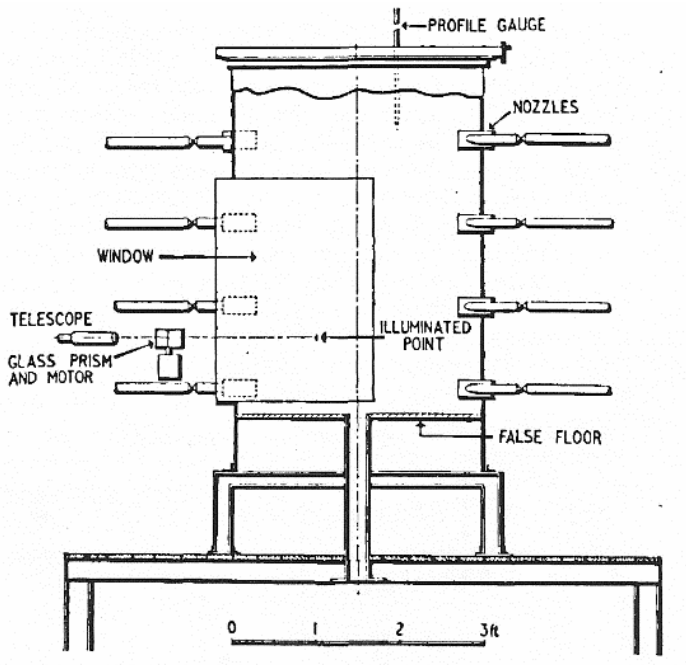

Figure 3.4: Anwar's apparatus highlighting the test tank from a side view including the inlet nozzles, depth gauge, telescope, glass prism and illumination point (Anwar, 1965).

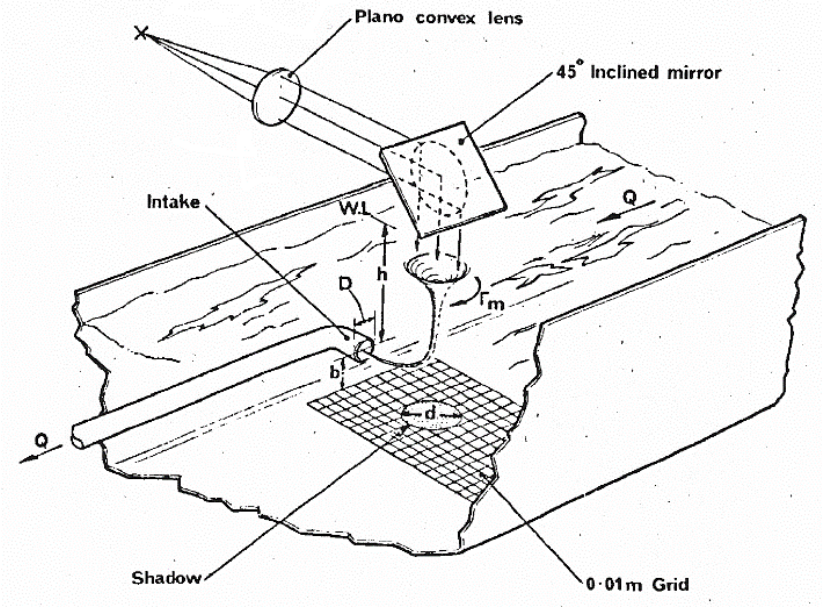

Figure 3.5: Illustration of the refracted ray method highlighting the source of light, plano-convex lens, 45° mirror and the incident light at the free-surface of the vortex. The shadow is cast on the floor of diameter $\boldsymbol{d}$ which is used in equation 3.15 to determine the field circulation Γ_∞ (Anwar et al., 1977).

Further non-intrusive velocity measurements were made by Quick (1961). The author performed particle streak velocimetry (PSV) by adding small neutrally buoyant pellets to the flow in the vortex which were then recorded as a streak on a photograph using a camera with a predetermined shutter speed. The camera was orientated perpendicular to the $z-$axis and which imaged the $x-z$ and $y-z$ plane synchronously using a perpendicular mirror arrangement. This stereoscopic technique enabled velocities to be determined in the tangential, radial and axial directions for a range or arbitrary radii over time. Quick (1961) also accounted for the effects of weak lensing (magnification of the image) through the tank curvature by adapting the tank with a planar vessel filled with the test fluid.

The laser doppler anemometer (LDA) or laser doppler velocimetry (LDV) technique was later employed by Hite and Mih (1994). This non-intrusive technique uses the doppler shift in a laser beam to measure the three components of the velocity at a point in space. This was achieved by crossing two laser beams at their waists (the focal point of a laser beam) in order to generate a set of fringes. As naturally occurring or seeded particles in the fluid passed through the fringes they reflected light that was focused onto a photo

detector. If the sensor was aligned to the flow such that the fringes are perpendicular to the flow direction the electrical signal from the photo detector will be proportional to the velocity of the entrained particle.

More recently, particle tracking velocmitery[18] (PTV) was applied by Wang et al. (2010) on the free-surface to quantify vortex formation for a model of the Xiluodo hydropower project. Trivellato (2010) also used PTV to investigate sub-surface[19] velocity profiles using an argon laser light sheet (1 mm thick) to illuminate the artificially particle laden flow (2 μm particles). More recently, Suerich-Gulick et al., (2013; 2013b; 2014) used PTV to quantify the near-field tangential, radial and axial velocities profiles close to a pump intake. The test configuration was similar to that employed by Quick (1961). An extensive review of this method is outlined in the authors PhD thesis (Suerich-Gulick, 2013). Very few authors (Rajendran et al., 1999; Li et al., 2008; Möller, 2013) have adopted the method of Particle Image Velocimetry (PIV) in the study of vortex flows. This method differs from the previously discussed PTV technique in that the fluid is seeded to a high density (25 particles per interrogation region) and strictly computes the instantaneous Eulerian velocity field using cross correlation methods in successive image pairs. Further technical details of both the PTV and PIV technique will be addressed in a later section.

A number of other vortex flow investigations (Sarkardeh et al., 2010; Suerich-Gulick, 2013) have utilised the acoustic doppler velocimetry (ADV) and technology which operates on the principle of doppler shift. The ADV probe measures the instantaneous fluid velocities for a volume of fluid in three-dimensions. Again, this technique suffers the drawback of interfering with the flow field which it inhabits along with being confined to a point-by-point system of measurements.

[18] The particle tracking technique measures the velocity of the fluid based on the displacement of particles observed on an image sensor.

[19] The subsurface is herein defined as any position below the free-surface of the primary fluid i.e. water in the current study.

3.5.2. Surface Profiles

In order to capture the radial position of the free-surface, two general methods have been employed in past investigations. Einstein and Li (1951) determined the location of the free water surface for an axial symmetric vortex through calibrated images of the air water interface. The images were photographed from outside the vessel but no detail was provided on correction for the weak lensing effects caused by the curvature of the tank interface. This was accounted for in Quick's (1961) work. Numerous authors (Anwar, 1966; Zielinski and Villemonte, 1968; Hite Jr and Mih, 1994; Yu and Lee, 2007; Trivellato, 2010) have instead been inclined to use a simple depth gauging technique to physically track the location of the free water surface at discrete radii. This method, albeit being a timely process, is only subject to human and instrumentation error which are easily quantified as opposed to possible unknown uncertainty in the prescribed optical imaging techniques. In the work presented by previous authors, the general arrangement consists of a point or hook gauge mounted on a moveable bridge which transverses the flow field in one or two dimensions. Other methods to determine the water surface profile in unmanageable areas such as at the vortex core were presented by (Viparelli, 1950; Ciaravino and Ciaravino, 2007). Here the authors installed manometer tubes in the orifice to directly measure the pressure head in poorly accessible regions.

3.6. Summary of Experimental Modelling of Vortices

The previous review emphasises that significant experimental work has been carried out on the topic of free-surface vortices. The work has led to many discoveries in the field both qualitative and empirical in nature. In the experimental studies of vortex intakes, there is a respectable record of research work carried out on the supercritical approach flow type vortex chamber (Jain, 1984; Kellenberger, 1988; Hager, 1990; Motzet and Valentin, 2002; Zhao et al., 2006; Del Giudice et al., 2009; Yu and Lee, 2009). In contrast, only a small number of experimental studies relating to subcritical approach flow geometries have been performed (Stevens and Kolf, 1959; Pica, 1968) and focus mainly on site specific geometries and/or analytical validation.

Commercial hydraulic investigations have been made only on a prescribed geometry or on a site specific basis (Drioli, 1947; Laushey and Mavis, 1952; 1962; Jain and Kennedy,

1983; Echávez and Ruiz, 2008). For this reason, current design work is generally based on the experience gained from the success of preceding projects without establishing a generic design procedure. Despite the previous advances made on strong vortex flows, it is clear that this area of research would benefit substantially from a comprehensive and systematic experimental investigation of the effect of the approach flow geometry. This research gap was also highlighted by Jain and Ettema (1987), Knauss (1987) and further addressed by Quick (1990). Furthermore, additional work is required to determine the dependence of circulation Γ_∞ on the approach flow geometry for a subcritical system - *"Bypassing the problem of a direct determination of induced circulation, similar research may be of some advantage for design practice"* (Knauss, 1987). Furthermore, any prior studies implemented on strong vortex flows, particularly those in vortex chambers, have not included a thorough investigation of the three-dimensional velocity fields. With increasing availability of accurate velocimetry techniques in this field, it is necessary for this area to be revisited in order to assist establishing proper design practices.

The topic of hydraulic similarity has been covered in detail and it was decided that it should be appropriate to maintain Froude similitude for model-prototype scaling so long as the criteria established by previous authors (Daggett and Keulegan, 1974; Anwar et al., 1978) is adhered to (see summary in Section 3.4.4).

Chapter 4.

Numerical Modelling Literature

SUMMARY

In recent years, numerical modelling has become a preferable form of analysis due to the relatively low cost and time associated with preparing models, performing simulations and extraction of results. The ease of parameterisation also renders this form of fluid analysis attractive for commercial projects in industry. In this chapter, a review of the literature with respect to numerical modelling of vortex flows using computational fluid dynamics is presented. It will be shown from this review that there are a scarce number of numerical modelling studies on vortex flows that retain sufficient validity. This is generally due to the three-dimensional complexity of the vortex near-field as a result of anisotropic turbulence and a failure to properly consider the multiphase nature of the flow. It will also be exposed that there has been little or no research implemented on the topic of strong vortex flows. Moreover, multiphase flow analysis as well as a comprehensive review of the appropriate turbulence closure methods are currently absent from literature in this particular topic. Finally, the capabilities of the ANSYS CFX numerical code will be presented by carrying out an extensive comparison between the numerical and experimental data.

4.1. Early Numerical Analysis

Early work on numerical modelling of vortex flows was presented by Binnie and Davidson (1949) who applied a finite difference approximation to the free-surface problem. Later, finite element method (FEM) modelling of circulation in vortices was employed using the two-dimensional depth integrated conservation of mass and momentum equations. Once the velocities were known at any time, the circulation could be computed along a closed path around an intake. Brocard et al. (1983) applied this method by formulating the conservation equations for turbulent flow through replacing the Reynolds stresses using the turbulent eddy viscosity approach. The choice of eddy

viscosity ε used in the FEM was crucial to the solution and was found to vary depending on the actual flow conditions. The most reasonable reproduction of circulation for flow in a circular tank was determined from analytical models. This optimum value was presented by Brocard et al. (1983) by the following relationship:

$$\frac{2\pi\varepsilon h}{Q} = 0.5 \tag{4.1}$$

When Brocard et al. (1983) applied the solution to an idealised intake, the results did not agree with the actual experimental circulation due to instabilities in the flow and the use of low values of eddy viscosity. Furthermore, the model was sensitive to the grid selection and bottom friction. Trivellato and Ferrari (1997) later adopted a different approach based on Cassulli and Cheng's (1992) finite difference model formulated from the hydrostatic shallow water equations and solved using the Euler-Lagrange approach. The model demonstrated capabilities in simulating the flow field circulation and the radial jet or radial band near the vessel floor. The work was comparable to that of Dagget and Keulegen's (1974) experiments. However, based on the impetus to solve more complicated, three-dimensional intake flows, Trivellato et al. (1999) advanced on the foregoing work by performing finite volume method (FVM) analysis of free-surface draining vortices. In this analysis Trivellato et al. (1999) uses a semi-implicit numerical scheme through a staggered mesh configuration. The terms controlling diffusion and pressure are solved implicitly while the convective terms are approximated using an Euler-Lagrangian approach. When compared to the experimental data provided by Dagget and Keulegen's (1974) results, the model was understood to be capable of predicting the two distinctive features of vortex flow; the tangential velocity field and the radial jet near the bottom boundary.

4.2. Commercial Code Investigations

With commercial computational fluid dynamics codes becoming more readily available, numerous authors (Tokyay and Constantinescu, 2005; Okamura, 2007; Suerich-Gulick et al., 2006), have presented benchmark studies on intake vortices for various codes. So far, the majority of these investigations have been stimulated by requirement to predict the critical submergence $(h/d)_{cr}$ at HPP and pump and SFR intakes. Commercial codes (i.e.

ANSYS Fluent, ANSYS CFX, Flow-3D, OpenFOAM) tend to be all-inclusive regarding modelling capabilities stratified or separated flows, steady or transient and a range of numerical schemes, turbulence closure preferences with numerous orders of solving accuracy). On this basis, some research in numerical modelling studies on vortex flows (Suerich-Gulick et al., 2013; Sarkardeh et al. 2014; Škerlavaj et al. (2014), in a relatively broad sense, progressed through validation studies in order to recognise, in a timely and efficient manner, the advantages and disadvantages of the various modelling approaches in commercial CFD codes.

4.2.1. Free-Surface Modelling

A number of numerical investigations (Rajendran et al., 1999; Ansar et al., 2002; Nakayama and Jiao 2001; Li et al. 2004) have been performed by assuming that the flow is single phase and treating the free water surface as a fixed, free-slip surface. This is often referred to as a 'fixed lid boundary condition'. Rajendran et al. (1999) performed numerical modelling in such a case using the Reynolds averaged Navier-Stokes equations using a near-wall turbulence model. Significant discrepancies were observed and the author suggests that this was as a result of natural unsteadiness of the flow and inadequacy of the available turbulence model. Similar studies were undertaken by Ansar et al. (2002) based on the method developed by Constantinescu and Patel (1997) assuming that the fluid was inviscid. The model provided a good qualitative description of the flow field with fair agreements found when compared to the available quantitative data set. Nakayama and Jiao (2001), Li et al. (2004), Tokyay and Constantinescu (2005), Okamura (2007), Li and Chen (2008), Desmukh and Gahlot (2010), Škerlavaj et al. (2014), Tang et al. (2011) , Chen et al. and Dhakal et al. (2015), all performed numerical simulations for a fixed lid boundary condition. The general conclusion realised using this approach was that through bypassing a complex interface modelling process, reasonable qualitative flow information could be extracted at a low computational expense. However, validity of the quantitative data was limited particularly in strong vortex flows where the water surface was strongly curved.

In multiphase approaches, the volume-of-fluid (VOF) method was the most commonly used interface capturing process for deforming free-surface flows. The VOF method

models the flow as a two-phase system separated by a clearly defined interface. A new parameter was then introduced called the fluid volume fraction ϕ_k which was a scalar quantity that defines the amount of fluid k that was present within individual cells. This quantity has values ranging from $\phi_k = 1$ (cell is completely full of fluid k) and $\phi_k = 0$ (cell is completely empty of fluid k). The free-surface interface was then located at approximately 0.5. This method will be discussed in further detail in subsequent sections. So far only a few studies have been carried out on vortex flows using the VOF method. Suerich-Gulick et al. (2006), Sarkardeh et al. (2014), Cristofano et al., (2014b) carried out multiphase analysis using the VOF approach to capture the free-surface interface. Apart from the work carried out by Gang et al. (2011), Shi et al. (2012), Shabara et al. (2015) very few multiphase models were implemented on vortex intakes that can be regarded as conclusive. It was noted (Suerich-Gulick et al., 2006) that most of the preceding work on the deformation of the free-surface has only been modelled qualitatively and more quantitative work is needed. In the majority of the previous studies (Gang et al., 2011; Škerlavaj et al., 2014; Dhakal et al., 2015), a mass flow or velocity normal to inlet and an average static pressure outlet was assigned for cases considering vortex flow chambers.

4.2.2. Turbulence Modelling

Due to the inherent presence of strong streamline curvature (Shur et al., 2000) and the associated highly anisotropic turbulent conditions inherent in vortex dominated flows (Scorer, 1967; Dyakowski and Williams, 1993), numerical modelling of these systems tends to be problematic. Previous studies appear to suggest (Tokyay and Constantinescu, 2005; Suerich-Gulick et al., 2006; Stephens and Mohanarangam, 2010; Chen et al., 2012) that numerical modelling of curving flows is strongly dependant on the type of turbulence model employed. Despite such findings, there are a number of recent CFD studies that have continued to disregard a careful consideration for the choice of turbulence model (Gang et al., 2011; Dhakal et al., 2015). Overlooking this problem can have a detrimental effect on the accuracy of results used in engineering applications. Early CFD research for the evaluation of vortices at pump-intake structures (Constantinescu and Patel, 1997; Rajendran et al., 1999) using the standard eddy viscosity

models (e.g. $k-\varepsilon$, $k-\omega$) suggested that the model would be enhanced when anisotropic turbulence and unsteadiness is considered. A first comparison between the $k-\varepsilon$ and the $k-\omega$ models was carried out by Constantinescu and Patel (2000). Both models showed no major differences in the results (Constantinescu and Patel, 2000).

The shear stress transport (SST) model (Menter, 1994) was later applied by Tokyay and Constantinescu (2005) which proved to be inadequate when compared to the more complex Large Eddy Simulation (LES). It has been concluded that the eddy viscosity models significantly overestimate the turbulence in the vortex core which is suspected to be as a result of rotation (Tokyay and Constantinescu, 2005; Suerich-Gulick et al., 2006; Chen et al., 2012). Shur et al. (2000) states that "*conventional linear eddy-viscosity turbulence models fail to predict this effect accurately, or even fails to predict it at all"*. Alterations can be made to the eddy-viscosity models to account for system rotation and curvature by applying a curvature correction (CC) to the RANS equations (Spalart and Shur, 1997). The curvature correction reduces the production of turbulent kinetic energy and increases its rate of dissipation in regions of streamline curvature. So far the CC principle has only been tested for a small range of free-surface (multiphase) vortex flow applications (Škerlavaj et al., 2011; Stephens and Mohanarangam, 2010; Škerlavaj et al., 2014) with no direct studies on the topic of the CC approach in multiphase vortex simulations. The results showed that CC process significantly improved the simulation with no substantial increase in the computational cost.

The SST scale adaptive simulation (SAS) model was investigated by Skerlavaj et al. (2011), Skerlavaj et al. (2014) and Cristofano (2014b) with and without CC. The SAS model is an improved unsteady Reynolds averaged Navier-Stokes (URANS) (transient) formulation which resolves turbulence based on the von Karman length-scale[20]. This enables the development of a turbulence spectrum in unsteady regions which exhibits LES-like behaviour. Skerlavaj et al. (2011) observed that the SAS with CC was in good agreement with the LES model. Full Reynolds stress models (RSM) have a fundamental

[20] The length scale formulated by Theodore von Kármán, is a physical quantity describing the size of the large energy-containing eddies in a turbulent flow. Theodore von Kármán was a Hungarian-American mathematician, aerospace engineer and physicist who was active primarily in the fields of aeronautics and astronautics.

advantage over simpler eddy viscosity models due to the explicit appearance of rotation and curvature terms in the turbulence equations (Spalart and Shur, 1997; Wilcox, 1998). Previous investigations using various formulations of the RSM (Škerlavaj et al., 2011) have proven to be very accurate but at the cost of being computationally intensive (approximately $5 - 9$ times the CPU time for the SST model) (Škerlavaj et al., 2011).

It is worth noting that, as far as the writer is aware, Škerlavaj et al.'s (2014) numerical modelling work is the only study available in the literature whereby the author performed a detailed investigation of turbulence models in a vortex chamber type testing scenario. Although his results were compared to those of a previous author (Monji et al., 2010) and the flow was treated as a single phase, Škerlavaj et al. (2014) was able to draw significant conclusions on the validity of the various turbulence models by comparing the gas core length, axial (downward) and tangential (circumferential) velocity profiles. Škerlavaj et al. (2014) determined that when a CC operation was not included in the standard RANS formulisations, a wide vortical structure was obtained. He stated that the CC option decreases the eddy viscosity resulting in a 'narrower' more realistic core. Škerlavaj et al. (2014) also found that for low approach flows, the numerical data from the SST-CC and SAS-CC agreed well with Monji et al.'s (2010) experimental data. When the approach flow was increased, the discrepancy grew. The maximum tangential velocity was significantly overestimated by a percentage error of 35 % and the core radius was larger than that of the experimental data for higher approach flows. Both the SST-CC and SAS-CC were shown to adequately predict the axial velocity distribution in both approach flow settings. He also explained that the SST-CC and SAS-CC models were capable of predicting the gas core length for short cores but for long cores the length was under predicted. The author (Škerlavaj et al., 2014) also makes an attempt to model surface tension which was shown to improve the accuracy in predicting the gas core length.

4.3. Summary of Numerical Modelling Literature

A complete review of research efforts in the area of numerical modelling of vortex flows has been presented. Very little work on the topic of multiphase vortex flow modelling has been performed that provides sufficient evidence of validity for direct industrial application. There have been numerous studies where CFD codes were used in industrial

applications without an understanding for the uncertainty involved in modelling this complex flow phenomena (i.e. considerations for false diffusion, free-surface deformation, curvature, unsteadiness and turbulence etc.).

Although some research works have addressed this gap, the investigations have failed to tackle a comprehensive validation for the effect of mesh structure, refinement, time-step analysis, steady state/transient modelling. Moreover, the topic of turbulence modelling does not seem to be thoroughly investigated, particularly in vortex drop shaft structures. In some cases, the single phase numerical model can present reasonable results for vortex detection at intakes. However, when strong vortices with large free-surface deformations are considered, the single phase solution will no longer be valid. Thus, there is a necessity to investigate this gap using a multiphase flow technique such as the homogeneous Eulerian-Eulerian method. Another likely problem in previous studies is the lack of experimental results immediately available to the authors performing code validation studies. Many authors have based their validation on the results obtained/requested from other studies. Clearly, it would be of benefit to the numericist if they had direct access to their own experimental data set from a physical model.

Chapter 5.

Experimental Modelling

SUMMARY

This section will provide an overview of the experimental methodology undertaken in the project to address the problems and gaps in the current literature. Initial consideration for dimensional analysis was made as well as the design of the physical models and test rig configuration. Specific detail is then presented on the velocimetry techniques of particle tracking velocimetry and particle streak velocimetry which were formulated based on whether experimentation is being performed in the far-field or near-field of the vortex respectively. The technique of planar laser-induced fluorescence is also described which was used to visualise turbulence and the secondary flow fields of the vortex. The testing procedures for measuring the effects of the approach flow geometry, free-surface profiles, critical air core diameter, velocity fields and flow visualisation are documented. Finally, qualitative and quantitative notes on the relative uncertainty of the experimental data that should be expected are discussed.

5.1. Overview

With reference to Figures 5.1 and 5.2, the following parameters of the flow were explored as part of the overall experimental program:

- General Hydraulic Variables: approach flow depth h, critical air core diameter a_c, bulk discharge Q and field circulation Γ_∞.
- Dependent hydraulic parameters h/d, a_c/d, C_d, N_Q, Fr_i, Fr_o, Re_i, Re_o, Re_v, N_Γ as a function for the flow geometry.
- Distribution of the water surface profiles h_r.
- Distribution of the tangential v_θ, radial v_r and axial v_z velocities.
- A visual investigation of the turbulence and secondary flow fields.

A scroll type vortex chamber with a relatively sharp orifice was adopted as a test case for the experimental program. This system ensures that the approach flow is subcritical and the critical section should always remain just below the orifice section (Quick, 1961). In this way, parametrisation of the approach flow in the vortex chamber could be exclusively evaluated. A scroll type vortex chamber also provides good scope for adaptation to other forms of vortex flows with a subcritical approach condition e.g. intake vortices (Knauss, 1987). The test program was separated into two phases: (1) effects of the approach flow geometry, (2) investigation of the mean three-dimensional velocity fields and the secondary flows. Each phase is briefly discussed in the following sections.

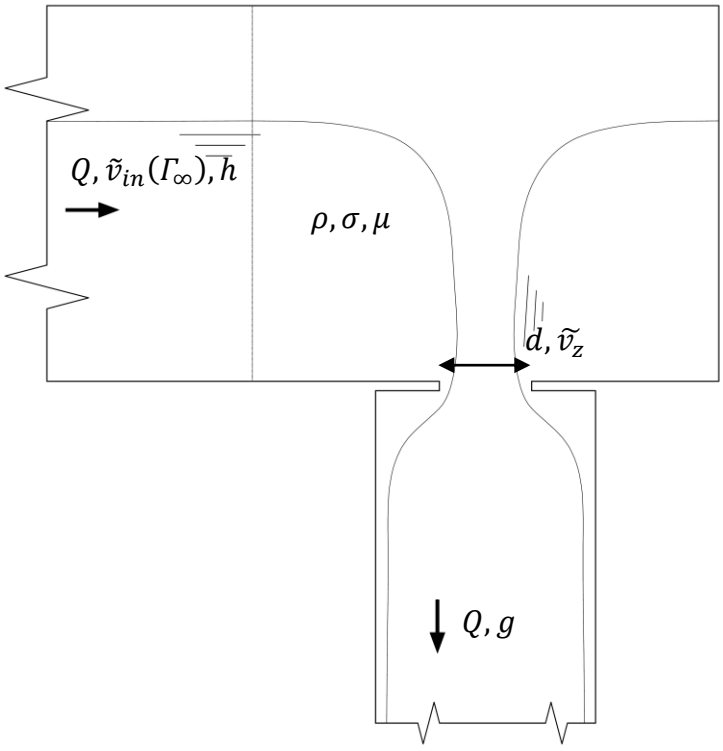

Figure 5.1: Fig. 1. (a) Plan and; (b) Elevation of the scroll type vortex chamber where $\boldsymbol{r_p}$ is the chamber radius at an angle $\boldsymbol{\theta_p}$, $\boldsymbol{d_s}$ is the lower drop shaft diameter.

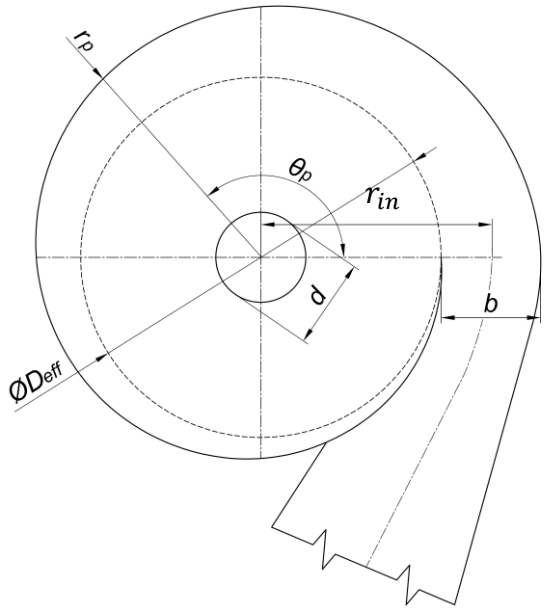

Figure 5.2: (a) Plan and; (b) Elevation of the scroll type vortex chamber where $\boldsymbol{r_p}$ is the chamber radius at an angle θ_p, d_s is the lower drop shaft diameter.

5.1.1. Investigation of the Effects of Geometry

The ability to predict the discharge Q based on the approach flow conditions is important for hydraulics design projects (Ackers and Crump, 1959; Hager, 1985). The discharge is a generalised hydraulic parameter which permits the direct evaluation of a range of other more specific parameters (i.e. velocities, circulation, pressure, turbulence etc.) and therefore the ability to forecast this parameter is of significant importance. In Section 2.6 a number of seminal analytical investigations to predict this parameter have been presented. In this phase, an alternative empirical formula to predict the depth-discharge relationship which may serve as a simpler alternative to previous formulations (Ackers and Crump, 1959; Pica, 1970) is explored. In the process, valuable data on the approach flow conditions and how the circulation varies as a function of the parametric variation of the approach flow geometry is available to explore. The problem of predicting the effect of the approach flow and the determination of the field circulation in free-surface vortices has been remarked upon regularly throughout the monograph presented by Knauss (1987). It is intended that the comprehensive findings resulting from this experimental program will address some of the gaps highlighted in the state-of-the-art.

5.1.2. Investigation of the Mean Velocity Profiles and Secondary Flows

In section 2.3 - 2.6, a number of theoretical models devised to predict the tangential, radial and axial velocity profiles in a free-surface vortex have been presented. The models presented so far (Rankine, 1873; Rosenhead, 1930; Vatistas et al., 1991) are applicable only for weak or dissipating vortices where the air core has not fully extended through the intake. Therefore the core region in these models consists of a highly turbulent region defined by the core radius r_c (Einstein and Li, 1955; Odgaard, 1986). In a strong full air core vortex however, there is no evidence in the literature to suggest that the turbulent core radius is in existence. Instead, Quick (1961) and Anwar (1965) successfully applied the ideal irrotational model across the full radial extent of the strong vortex The ideal model agreed well in the far-field but a significant discrepancy was observed close to the air core region (near-field) in both studies (Quick, 1961; Anwar, 1965). The aim of this section is then to investigate the tangential velocity profile throughout the strong vortex to fully investigate the phenomenon that was reported in these studies. Furthermore, the radial and axial velocity profiles are also investigated along with the free-surface distribution across the vortex chamber. In addition, an investigation into the secondary flows reported by previous authors (Al'tshul and Margolin, 1968; Daggett and Keulegan, 1974) is carried out using planar laser-induced fluorescence. In this section, the turbulence of the flow field will also be qualitatively studied in addition to the sources and behaviour of flow instabilities.

5.2. Dimensional Analysis

Dimensional analysis is a method commonly used in experimental research to determine the key influential parameters that govern a physical study. It serves to simplify the experimental program by reducing the number of known and unknown dimensional variables into a smaller number of dimensionless Π-groups. As shown in previous studies, a number of authors (Kolf and Zielinski, 1959; Stevens and Kolf, 1959; Quick, 1961; Anwar, 1968a; Zielinski and Villemonte, 1968; Taştan and Yildirim, 2010) implemented dimensional analysis on free-surface vortices to determine the primary non-dimensional parameters that affect the critical depth to prioritise experimental investigations accordingly. The following dimensional analysis will however be provided with respect

to the discharge Q in the vortex. The Buckingham Π-theorem (Buckingham, 1915) is employed to identify the dimensionless groups with respect to Figure 5.1and 5.2. Assuming that the dropshaft size d_s is large enough, so as not to effect the primary flow field, the outlet effectively becomes a sharp edged orifice[21]. In this way it was assumed then that the flow at the outlet from the vessel is in the critical flow regime. This was described by Quick (1961) as follows:

"*The flow at the outlet of such a tank is in the critical flow condition and the entry to the Perspex tube acts as a control section. Therefore, provided the annular hydraulic jump occurs below the pipe entry, the outflows from the vortex tank will be constant*"

The functional relationship for the dependent parameters in a strong free-surface vortex is then given by:

$$f_1\left(\Gamma_\infty, \widetilde{v_z}, \rho, \sigma, \mu, g, b, D_{eff}, h, d\right) = 0 \tag{5.1}$$

where σ is the surface tension, μ the dynamic viscosity, b is the inlet width and D_{eff} is the effective diameter and h is the approach flow depth. Applying Buckingham Pi-Theorem, Equation (5.1) can be re-written as:

$$f_2\left(\frac{\Gamma_\infty}{v_z d}, \frac{v_z}{\sqrt{gd}}, \frac{v_z d}{\nu}, \frac{{v_z}^2 d\rho}{\sigma}, \frac{b}{d}, \frac{D_{eff}}{d}, \frac{h}{d}\right) = 0 \tag{5.2}$$

This relationship can also be obtained from the Navier-Stokes equations and a similar relationship was derived by Dagget and Keulegen (1974). Introducing the bulk discharge Q via $\widetilde{v_z} = 4Q/\pi d^2$ the following simplifications can be deduced:

$$\frac{\pi}{4}\frac{\Gamma_\infty d}{Q} = \frac{\pi}{4}\mathrm{N\Gamma} = \mathrm{K} \tag{5.3}$$

$$\mathrm{N_Q} = \frac{Q}{\sqrt{g} d^{5/2}} \tag{5.4}$$

$$\mathrm{Re}_d = \frac{\widetilde{v_z} d}{\nu} \tag{5.5}$$

$$\mathrm{We}_d = \frac{\widetilde{v_z}^2 d\rho}{\sigma} \tag{5.6}$$

[21] A horizontal sharp edged orifice ensures free-discharge of flow.

where N_Γ is the circulation number, K is the Kolf Number, N_Q is the discharge number, Re_d is the outlet Reynolds number and We_d is the Weber number. It is interesting to note that the discharge number and the outlet Froude number are interchangeable. The remaining parameters of Equation (5.2) are related to the approach flow geometry and depth. In order to further simplify Equation (5.2), b/d and D_{eff}/d are collected and grouped together to define a new dimensionless number α which designates the ratio of the inlet radius from the shaft centre r_{in} to the inlet width b by:

$$\alpha = \frac{\frac{b}{2d} + \frac{D_{eff}}{2d}}{b/d} = \frac{r_{in}}{b} \tag{5.7}$$

Equation (5.2) can thus be written in terms of the discharge number by:

$$N_Q = f_3\,(K,\, Re_d,\, We_d,\, \frac{h}{d},\, \alpha) \tag{5.8}$$

Following the formalism of Quick (1961), the effects of viscosity and surface tension on free-surface vortex flow are generally considered to be negligible if certain predefined hydraulic conditions can be met (discussed in Chapter 3.5). If the limiting conditions can be adhered to, both Re_d and We_d can be omitted from Equation (5.8) implying that surface tension and viscosity do not affect circulation and discharge thus allowing the results to be scaled using the complete Froude model (Quick, 1961; Knauss, 1987). This is then given by the following equation:

$$N_Q = f_4\,(K, \frac{h}{d}, \alpha) \tag{5.9}$$

The latter two dimensionless variables can therefore be investigated using a systematic experimental program to determine their effects on the circulation and consequently the discharge number.

5.3. Model Design and Construction

From the previous section it has been established that the discharge number is strongly dependent on the Kolf number K and the approach flow geometry α and depth h/d. In order to gain a complete understanding of the effect of these parameters, a comprehensive physical modelling program was carried out on twelve models of the vortex chamber. In many past studies, the orifice diameter was varied in addition to other geometric

parameters to monitor the change in the flow field. However, this was considered to be a profligate method. As discussed by Quick (1961) and others (Binnie and Hookings, 1948; Ackers and Crump, 1960) because the critical section generally resides at the orifice, its diameter d forms the controlling section of the flow. Furthermore, it is a continuously used as a repeating system variable in Equation (5.2). It was the opinion of the writer in this study that by altering this parameter this would have the same effect as scaling the model. Thus, in this methodology, d was kept constant and the α parameter was varied by discretely altering r_{in} and b thus simplifying the experimental process significantly. Furthermore, the model was then easily scalable for a geometrically similar prototype by the details of the outlet or orifice at the control section $d_p = d_m l_{scale}$. The scroll type vortex chamber with a spiral peripheral wall was to be designed as a function of the values r_{in} and b. Drioli (1969) presents a method to determine the periphery of the spiral chamber. However, in the current study, the periphery of the chamber was designed simply based on the geometry of the logarithmic spiral which was found to be typical of vortex streamlines in nature (Ogawa, 1992) and furthermore validated by an initial spiral arm visualisation of the flow in a weak free-surface vortex in this study (Figure 5.3) using planar-laser induced fluorescence. Furthermore, the logarithmic spiral vortex chamber was observed to be suitable to maintain the verticality and central position of the vortex air core over the orifice in a previous investigation (Mulligan and Casserly, 2010).

Figure 5.3: Logarithmic spiral arm of the free-surface vortex. Image captured during an initial planar laser-induced fluorescence analysis at the IT Sligo Hydraulics Research Laboratory.

The radial position of the casing perimeter therefore takes the form of $r(\theta) = ce^d$ where $r(\theta)$ is the radial dimension at angle θ to the inlet (as shown in Figure 5.2) and c and d are geometric constants based on r_{in} and b. c and d can easily be acquired for a specific geometry using the following conditions for the inlet:

$$\text{for } \theta = 0^o, \quad r = D_{eff}/2$$
$$\text{and for } \theta = 360^o, \quad r = D_{eff}/2 + b$$

and hence, c and d can be solved simultaneously and subsequently used to plot the periphery of the casing.

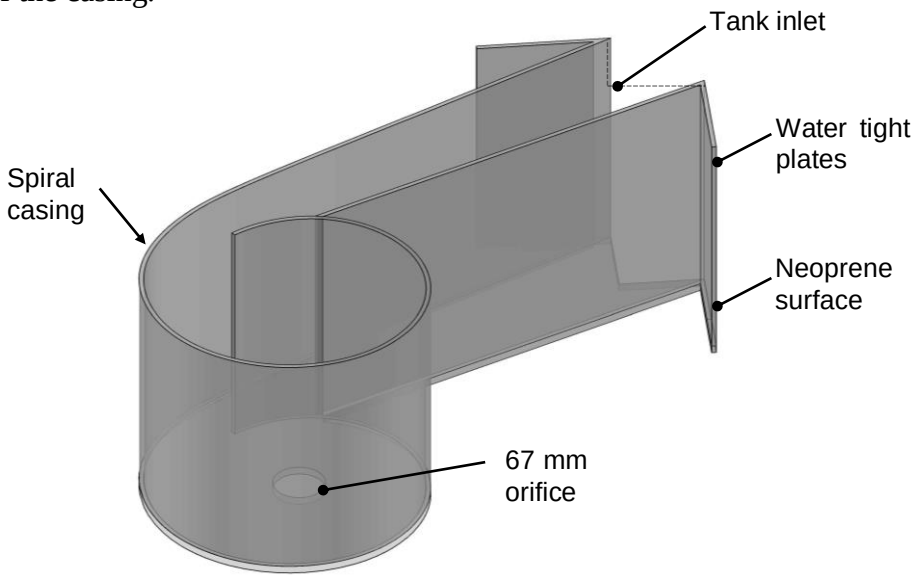

Figure 5.4: Auto CAD representation of the vortex chamber model geometry.

The primary tangential velocity field resides in the horizontal plane of a gravitational vortex and therefore it was necessary to only design the models planimetrically i.e. no variation in the horizontal geometry in the $z-$axis. Thus, the effects of the horizontal geometry could be evaluated independently. Twelve variations of the geometry were investigated in order to cover a wide spectrum of α values. A [3 × 4] geometric matrix was derived containing three equally varying effective diameters, D_{eff} and four equally varying inlet widths b. The details of the geometries are presented in Table 5.1. To coincide with the form of Equation (5.9), the repeating variable d was used as the universal constant for the experimental program and thus, D_{eff} and b were expressed as a function of this value accordingly. The individual geometries were then named

according to #[D_{eff}][b] e.g. #3.0d0.5d is the first casing in Table 5.1 with D_{eff} = 201 mm, b = 33.5 mm and α = 3.278. Preliminary analysis was carried out to propose a sufficient size for d. By conservatively estimating this value from the Froude scaling criteria suggested by previous authors (Anwar, 1965; Jain et al., 1978), values for d were found to range from 0.05 m to 0.15 m. Due to availability of space as well as expense of fabrication outside the projects budget, the size of d was limited to 0.067 m. Diameters of typical scroll type drop shaft structures range from 0.3 m – 7 m (Jain and Kennedy 1983) and so this scale did not comply with the additional 1/20 scale criteria specified by Anwar (1966).

Table 5.1 Geometric matrix of tested models. Individual geometries are named according to #[D_{eff}][b] e.g. #3.0d0.5d is the first casing in the table with D_{eff} = 201 mm, b = 33.5 mm and α = 3.278

	$b = 0.5d$	$b = 1.0d$	$b = 1.5d$	$b = 2.0d$
$D_{eff} = 3.0d$	$\alpha = 3.278$ D_{eff} =201 mm b =33.5 mm	$\alpha = 2.095$ D_{eff} =201 mm b =67 mm	$\alpha = 1.495$ D_{eff} =201 mm b =100.5 mm	$\alpha = 1.301$ D_{eff} =201 mm b =134 mm
$D_{eff} = 4.0d$	$\alpha = 4.875$ D_{eff} =268 mm b =33.5 mm	$\alpha = 2.688$ D_{eff} =268 mm b =67 mm	$\alpha = 1.956$ D_{eff} =268 mm b =100.5 mm	$\alpha = 1.577$ D_{eff} =268 mm b =134 mm
$D_{eff} = 5.0d$	$\alpha = 6.220$ D_{eff} =335 mm b =33.5 mm	$\alpha = 3.129$ D_{eff} =335 mm b =67 mm	$\alpha = 2.267$ D_{eff} =335 mm b =100.5 mm	$\alpha = 1.805$ D_{eff} = 335 mm b =134 mm

Note: α values are corrected slightly for fabrication imperfection

The twelve models were designed and constructed by the writer to within a measured geometric accuracy of $\pm$ 4 %. Images as well as the fabrication process are presented in Appendix A1 for further design information. Three examples of the geometries are depicted in Figure 5.5.

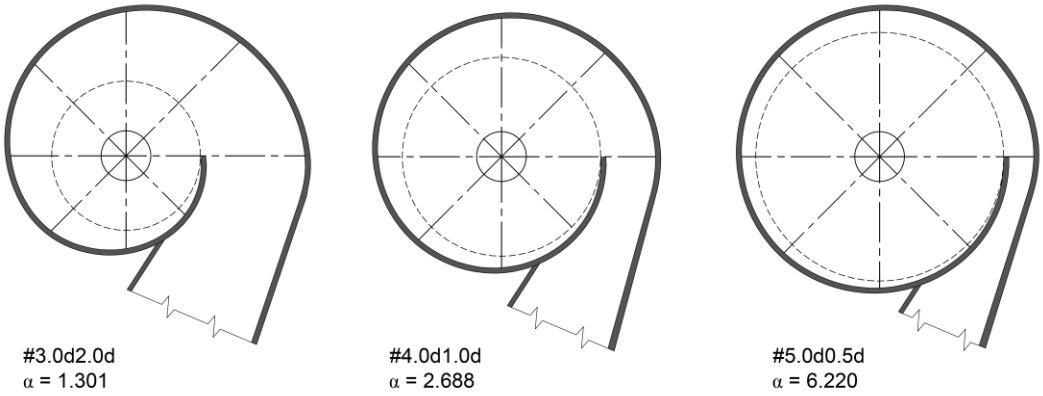

Figure 5.5: Examples of three vortex chamber geometries.

In order to benchmark the data, a single radial flow model was also investigated. The radial flow in the chamber was easily arranged by designing a model to ensure a strong uniform flow. This was achieved using flow in radial jets that inhibit the development of natural or induced circulation or vorticity (Posey and Hsu, 1950; Quick, 1961). A model was designed for this purpose which consisted of a 0.4 m diameter acrylic cylinders perforated with 16 mm holes spanning the perimeter of the model at 25 mm horizontal centres. The Radial flow model is highlighted in Figure 5.6.

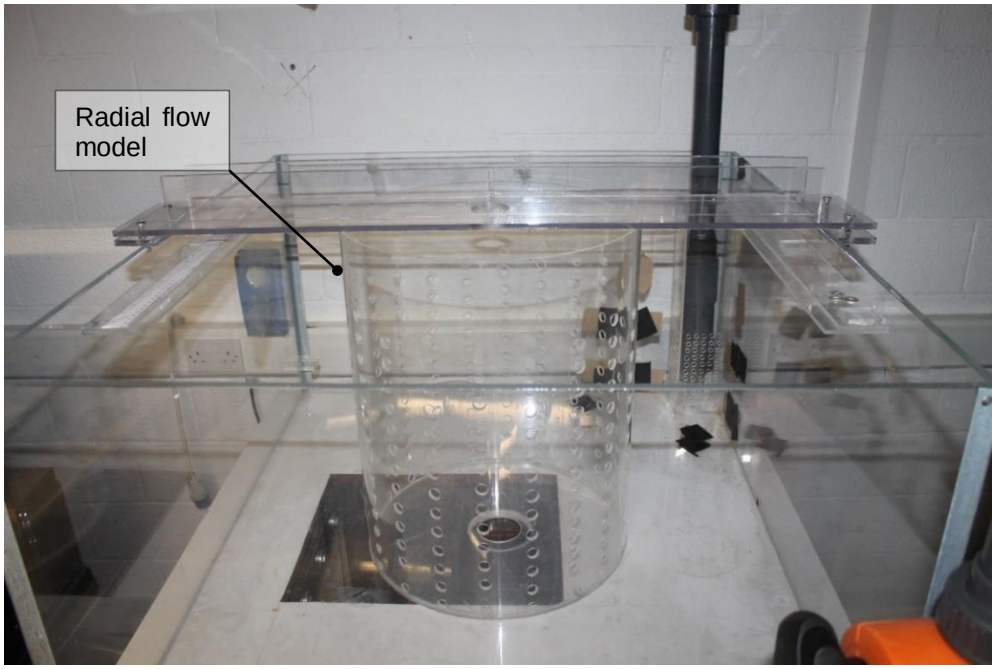

Figure 5.6: Radial flow model. Note: the geometrically staggered position of the perforations.

5.4. Test Rig Configuration

Three-dimensional AutoCAD models of the overall test rig are displayed in Figures 5.7, 5.8 an 5.9. The test geometries are analysed in an open tank 0.5 m high and 0.85 m wide and 0.95 m long. The walls of the tank are 10 mm thick. A 0.1 m circular orifice was centrally located in the base of the tank and rested on a steel platform over the storage reservoir which had a capacity of 565 litres. The steel platform was adapted for connecting various instruments (e.g. camera enclosure which will subsequently be discussed). Water was conveyed into the tank at its corner through a bell mouth pipe exit and was passed through flow straightening plates in order to homogenise the approach flow and minimise turbulence intensity. Upon discharge through the orifice, the flow enters a rectangular drop shaft that conveys the test fluid to the lower reservoir. The flow was circulated from the reservoir through the system using a centrifugal pump supplied by *Serfilco* (range between 0 – 3.5 l/s) and was regulated using two control valves. The flow was monitored using a magnetic flow meter supplied by *MagMeters*.

The aforementioned tank arrangement serves two purposes (a) to allow for a permanent fixture whereby geometric models can be mounted and analysed and (b) to permit imaging of flow bearing particles through planar interfaces in order to avoid the aforementioned weak lensing and distortion effects generated from the model curvature (see Sections 3.1 and 3.5.1) and water surfaces respectively. The length of the inlet channel ranged from $8d$ - $10d$. A moveable depth gauge system was used to traverse the flow field in both $x-$ and $y-$directions to capture the approach flow depth h and water surface profile h_r accordingly. During testing, the lower reservoir was filled and emptied using the laboratory supply and waste facilities. The tank was generally cleaned every two-three weeks. The temperature variation of the tank water was monitored to investigate potential influence of pump to fluid heating. Over the maximum pump operation time of one hour, no changes in temperature were observed that could affect the fluid properties during testing. Uncertainty of the various instruments will be discussed in Section 5.9.

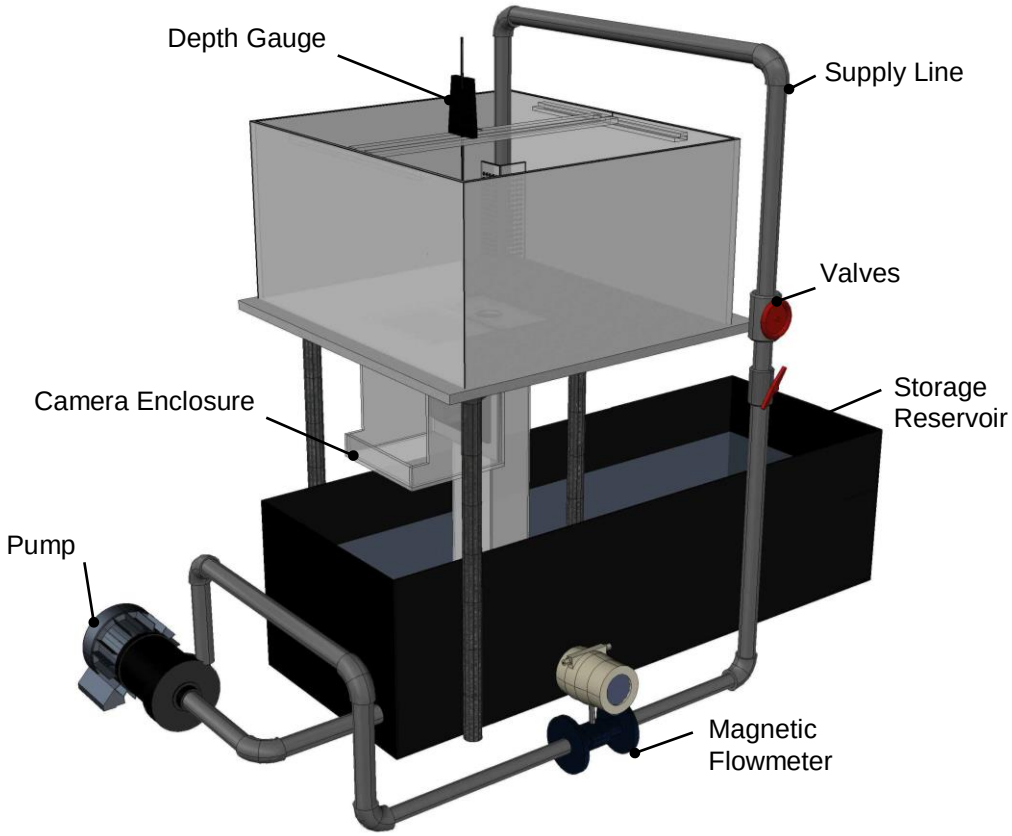

Figure 5.7: Three-dimensional perspective view of the test facility labelled accordingly.

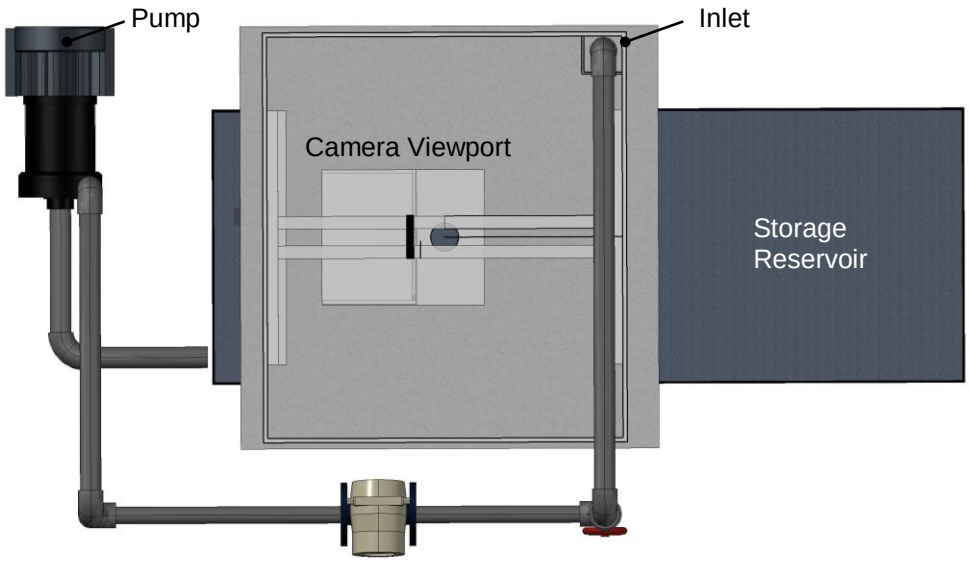

Figure 5.8: Plan of test facility labelled accordingly.

Figure 5.9: Test Rig configuration: (a) end view of test rig in an AutoCAD model and (b) Test rig during experimentation highlighting the flow in the model.

5.5. Velocimetry and Circulation

A number of velocimetry methods were identified in Section 3.5.1 with particular emphasis paid to determining the tangential velocity v_θ and the field circulation Γ_∞. It was revealed that determination of these variables in a free-surface vortex was a difficult process and was highly subject to uncertainty; particularly when the method was intrusive. Due to the nature of the strong vortex and the requirement to determine the field velocities as opposed to a point-by-point method, 2D Particle Tracking Velocimetry (PTV) was used. The merits and successful application of similar PTV and PIV techniques is highlighted by Quick (1961) and Suerich-Gulick (2013).

Displacements are observed by imaging the particle locations successively using a high-speed camera. Two variations of PTV were devised to consider (a) far-field tangential and radial velocities and (b) near-field axial velocity distributions in the non-hydrostatic core region. In the far-field a planar PTV method was adopted while in the near-field, a modified particle streak velocimetry (PSV) method was used. Both methods are discussed

in detail next. For all methods it was assumed that the vortex centre was steady maintained position at exactly 0,0 (the centre of the outlet) which was based on the observations made by Mulligan and Casserly (2010). This assumption permits ease when computing the field circulation in the vortex chamber. In a weak vortex structure which is known to 'wander' in the flow, PTV analysis would require a continuous tracking of the vortex centre due to the transient wandering nature of their structures (Möller, 2013).

5.6. Planar Particle Tracking Velocimetry (PTV)

Planar (pulsed-light) particle tracking velocimetry was applied in the far-field of the vortex to calculate the tangential and radial velocity profiles across the field-of-view (FOV). This was achieved by successively illuminating a thin slice of the flow using a high energy laser passed through light sheet optics. The scattered light observed on an image sensor locates the precise positions of individual particles inherent in the flow which are then tracked in a Lagrangian reference frame. PTV uses a low mean particle concentration which ensures that the probability of two particles overlapping was small. Therefore it is sometimes also called low particle number density (or low image density) particle image velocimetry (PIV) (Adrian, 1991; Dracos, 1996) and differs significantly from the traditional PIV. This method was fitting for use in the current study in that individual particles could be readily identified and located between successive images. This was particularly suited to the low pulse repetition rate of the available laser system.

A requirement for planar PTV is that there is a small out-of-plane velocity component (Adrian and Westerweel, 2011). When the out-of-plane velocity component is excessively large, this can enhance the loss of particle image pairs in successive image frames. In the case of the current study, the out of plane velocity component corresponds to the axial velocity component due to the horizontal arrangement of the light sheet. Quick (1962) however states that the axial velocity in the far-field of a vortex is small (where v_θ and v_r are dominant in-plane components) and therefore the problem of out-of-plane velocities could be considered to be negligible. Out-of-plane can however be responsible for significant error in PTV measurements. The uncertainties surrounding this will be discussed subsequently in Section 5.9. The standard elements of the planar PTV configuration are highlighted in Figure 5.10.

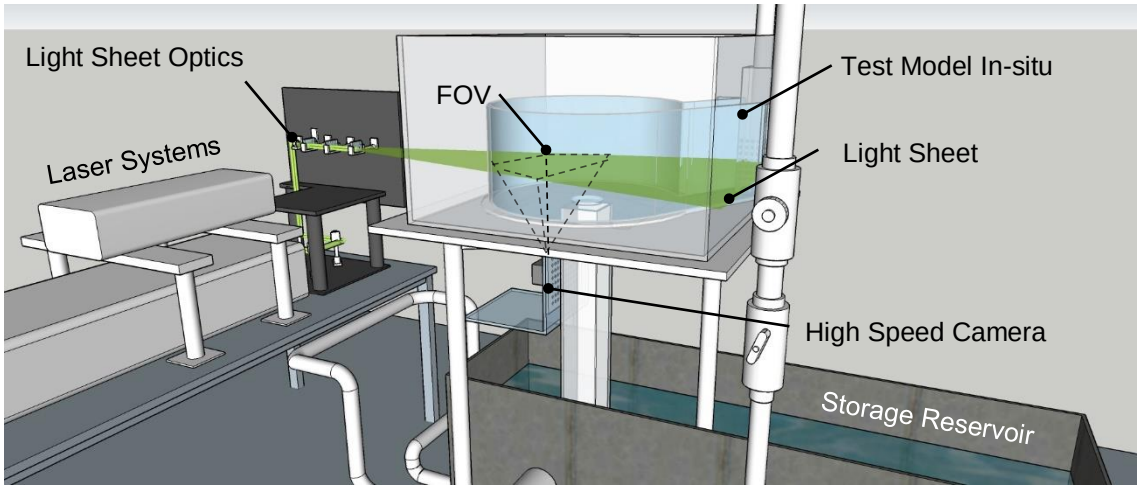

Figure 5.10: Particle tracking velocimetry (PTV) configuration (image by Gerry Foley).

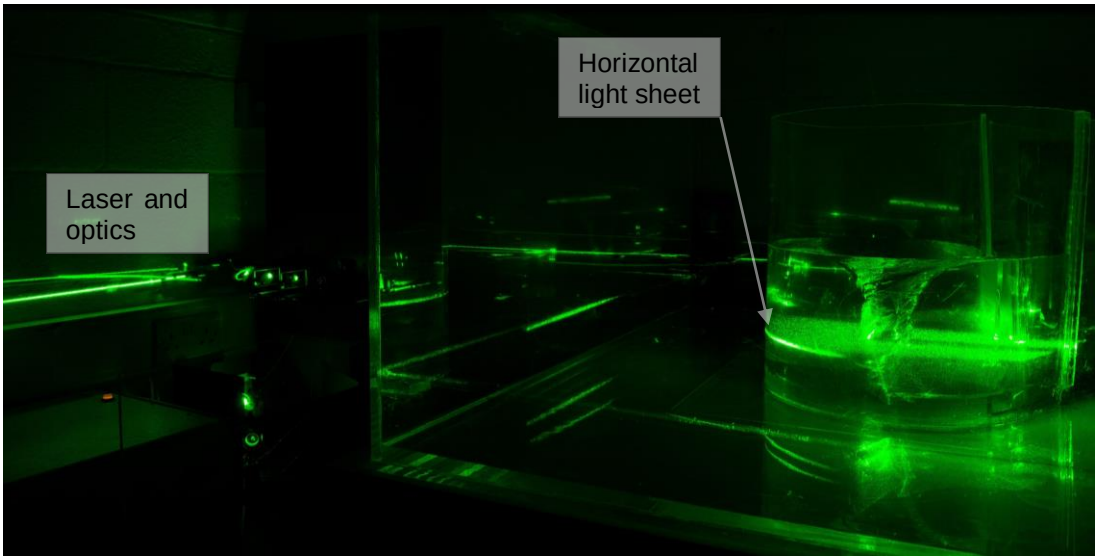

Figure 5.11: Laser light sheet during an experimental test. The 2D PTV technique is used to determine the field circulation Γ_∞ and tangential velocity profiles $v_\theta(r)$ at a sub-surface depth corresponding to a datum at h_{PTV}.

5.6.1. Illumination Plane

Illumination was achieved using a Nd:YAG laser system (*Spectron SL404*) with pulse repetition rates ranging from 10 - 30 Hz and a maximum pulse energy of 250 mJ. The laser was housed on a bench and directed towards an optical arrangement which was located adjacent to the test rig. The laser emitted a 6 mm diameter circular beam profile which was transported to a vertical breadboard using mirrors. The optical breadboard housed a mirror that directs the beam through light sheet optics into the area-of-interest (AOI). The light sheet optics comprised of two vertically focusing cylindrical lenses that

compressed the beam to 2 mm and one horizontal diverging cylindrical lens which fanned the beam. A number of diverging lenses were available to adjust the fan angle of the light sheet to vary the illumination intensity and the AOI. It was possible to adjust the optical configuration for a range of collimations in order to position the relative height of the light sheet h_{PTV} to probe various sub-surface depths of the vortex h_{PTV} = 0 – 500 mm. To avoid excessive motion blur or streaking of particles, the pulse width δt of the illumination source must be small enough to virtually "freeze" the position of the particle in the image. The criteria of $\delta t/\Delta t < 0.1$ was suggested (Adrian and Westerweel, 2011). The pulse width of the Spectron SL404 laser system was δt = 7 ns and therefore was well below this requirement.

5.6.2. Imaging

The positioning of the image sensor for this application was crucial. It is advised not to obtain PTV images through curved interfaces or at oblique angles unless steps are taken to minimise refraction (Adrian and Westerweel, 2011). Imaging the light sheet from a top down view would require imaging through the hyperbolic and unsteady wavy free-surface of the vortex. Examples of problems related to considerable distortion introduced by imaging in this way were highlighted by Adrian and Westerweel (2011) and a technical discussion was provided by Aboelkassem and Vatistas (2007). Instead, the camera was housed on the underside of the tank within a compartment which images the light sheet from a bottom-up view. This was similar in practice to Möller's (2013) configuration; however, in this case it was only possible to view half of the whole vortex chamber due to the eccentric position of the camera enclosure. To alleviate this problem and improve optical accessibility, Möller (2013) considered tilting the camera with respect to the perpendicular view. The tests showed that the effort involved in tilting and correcting images was too large in return for a small benefit in optical accessibility.

Due to the axisymmetric behaviour of the vortex flow field, the half flow field optical access was deemed to be sufficient. The high speed camera (*MotionBLITZ EoSens mini*) was installed in a compartment (Figure 5.9, 5.10 and 5.12) on a vertical mount and views the AOI at distances of 400−800 mm through a planar viewport on the tanks underside. The lens used was a 16 mm fixed focal length objective with a maximum

distortion/aberration of less than 0.1 % at a 300 mm minimum viewing distance. The laser energy was maintained at a constant value for all tests but the $f-$stop[22] (or f-number) $f_{\#}$ was varied according to h_{PTV} as well as the approach flow depth h/d. As the laser light sheet approached the free water surface, large reflections would cause the image sensor to become dangerously saturated as well causing poor visualisation of tracer particles. Therefore the aperture had to be modified between test conditions to cater for this risk. Too large an aperture creates an excessive depth of field. The optimum range of $f_{\#}$ used during tests varied from 3 - 8. The h_{PTV} was imaged at subsurface depths ranging between 0 and 235 mm which resulted in magnifications of $M_o = 0.035 - 0.066$. Each particle occupied approximately 36 pixels.

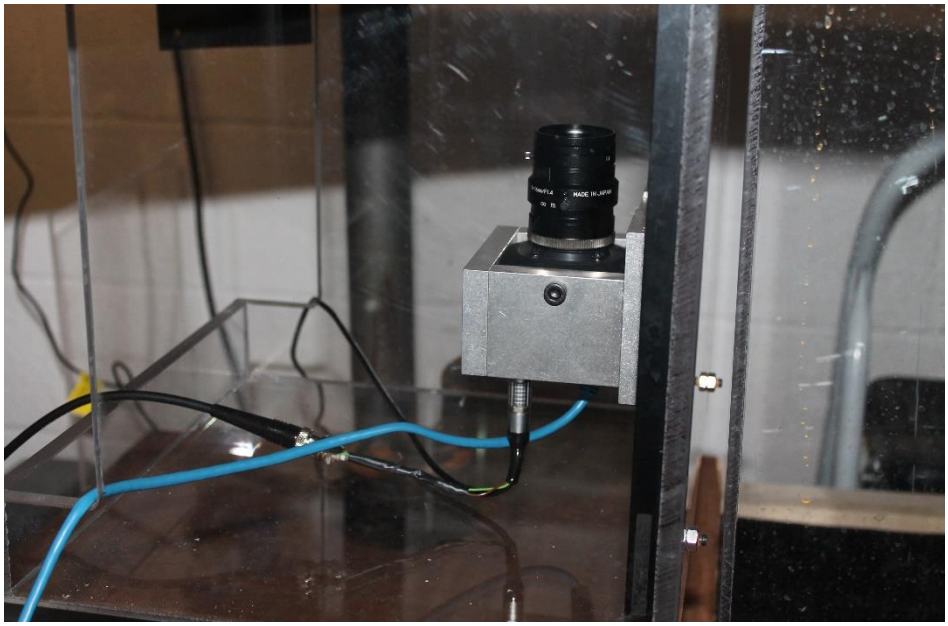

Figure 5.12: High speed camera installed in camera enclosure. The camera images vertically through a viewport on the underside of the tank.

5.6.3. Seeding Particles

The flow should be seeded with particles that are small enough to follow the fluid acceleration but of a sufficient size to scatter light to form bright particle images. Illuminated particles have the advantage in this application in that they are effectively

[22] In optics, the f-number (sometimes called focal ratio, f-ratio, f-stop, or relative aperture) of an optical system is the ratio of the lens's focal length to the diameter of the entrance pupil.

point sources which sample the fluid position with a relatively small uncertainty (Adrian and Westerweel, 2011) in comparison to the optical error. In this PTV application, polyethylene microspheres supplied by *Cospheric* were used. The density of the particles ranged from 0.99 g/cc-1.01g/cc and possessed a mean particle diameter $d_p = 800$ μm. This particle size produces a diffracted particle image diameter d_τ according to Raffel et al. (2013) of:

$$d_\tau = \sqrt{(M_o d_p)^2 + d_{diff}^2} \tag{5.10}$$

where d_{diff} is the diffraction limited image diameter given by :

$$d_{diff} = 2.44 f_\#(M_o + 1)\lambda_l \tag{5.11}$$

where λ_l is the illumination wavelength. For the range of magnifications, the particle image diameter was found to be in the range of 6 pixels on the image sensor. Therefore the chosen particles satisfied the requirement whereby the recorded particle image diameters are to be larger than 1 pixel (Adrian and Westerweel, 2011; Raffel et al. 2013). The particles were seeded manually in the inlet channel of the chamber by slowly pouring a glass beaker filled with a mixture of particles and the test fluid at a distance of approximately $8d$ upstream of the vortex chamber. An example of the particle images at the inlet region is highlighted in Figures 5.13 and 5.14 which depicts their homogenous arrangement in the flow on the approach to the inlet. A 500 μm sieve, located at the bottom of the drop shaft chute was used to collect the particles after testing to avoid wastage.

5.6.4. Image Acquisition and Analysis

Particle displacements within each pulse were recorded by acquiring successive images of the particle as it moved through the illuminated section (Figure 5.14 and 5.15). Images were acquired using the *MotionBlitz Studio* frame grabber. Due to the small thickness of the light sheet, particles only remain in examination plane for a short time resulting in only 3 - 6 successive particle images. An illustration of the PTV imaging analysis and notation is highlighted in Figure 5.15. For simplicity, the spatial field for displacement determination is described using x for the circumferential displacement and y for the

radial displacement. The Eulerian velocity at point x, $u(x,t)$ is, by definition, the limit as $\Delta t \to 0$ of the displacement of the point of fluid mass that passes through x at time t divided by Δt. The image velocities are determined from particle image displacements $(\Delta X_p, \Delta Y_p)$ or Lagrangian trajectories by measuring the finite particle displacements $(\Delta x_p, \Delta y_p)$ using the following equation:

$$(v_{px}, v_{py}) \cong \frac{(\Delta x_p, \Delta y_p)}{\Delta t} = \frac{(\Delta X_p, \Delta Y_p)}{M_o \Delta t} \tag{5.12}$$

Then the Eulerian velocity is equated to the Lagrangian particle velocity by:

$$u[x_p(t), t], = v_{px}(t) \tag{5.13}$$

which assumes that the particle slip and finite-difference error associated with the finite time seperation Δt are negligible (Adrian and Westerweel, 2011). A significant reduction of the finite-difference error can be achieved by interpreting Δx_p through a central difference method (Adrian, 1991). At least three successive particle images were required to determine the Eulerian velocity vector using a central difference method and two particle images were required for a forward difference method. For the central difference method, Δx_p is determined by:

$$\Delta x_p = \frac{x_p(t - \Delta t) - x_p(t + \Delta t)}{2} = \frac{x_1 + x_2}{2} \tag{5.14}$$

and for forward difference:

$$\Delta x_p = x_p(t + \Delta t) - x_p(t) \tag{5.15}$$

The locations of and displacements of particle x_p, y_p were manually obtained using a cubic spline to model the trajectories between particle images as shown in Figure 5.15 in *AutoCAD*. The components of x_p, y_p are extracted from this data. Δt was assumed small enough as to ensure that that the magnitude of acceleration along x_p, y_p was negligible. The cubic spline method was third order accurate. Spatial calibration was ensured by imaging a submerged grid plate that is orientated at a particular radius from the orifice prior to each test.

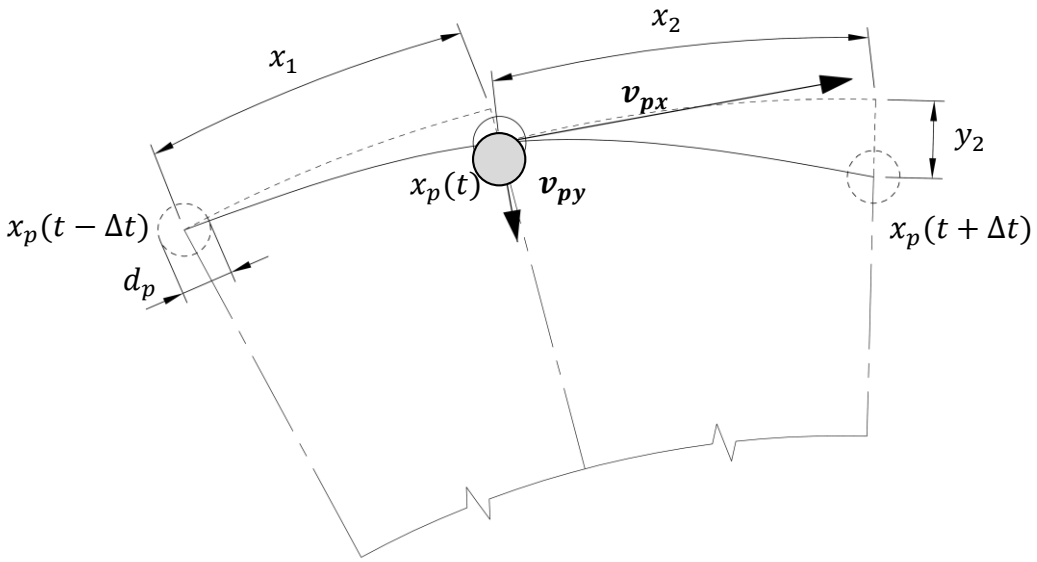

Figure 5.13: Schematic of the particle displacement analysis using a central difference approach.

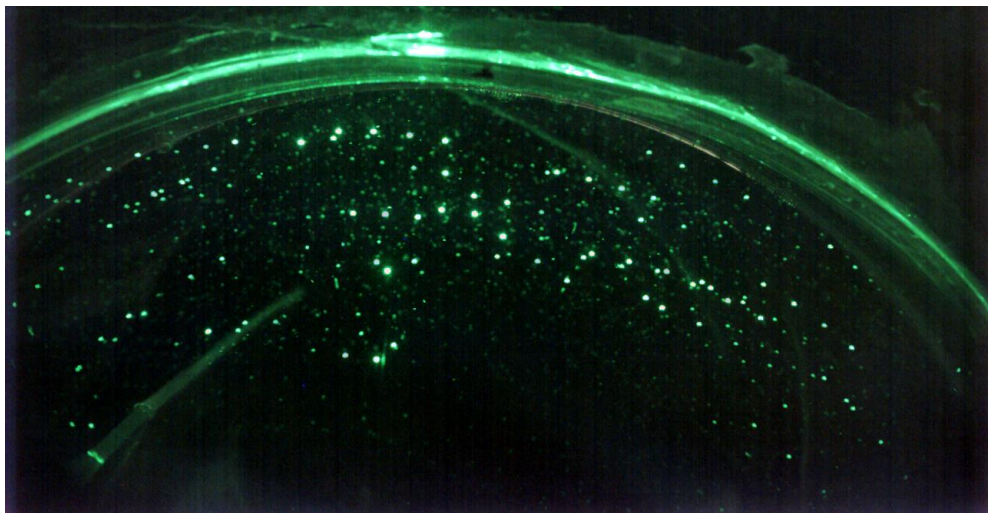

Figure 5.14: FOV containing illuminated particles for four over layed particle images (model #4.0d1.0d - $h_{PTV} = 15$ mm, $h/d = 1.0$).

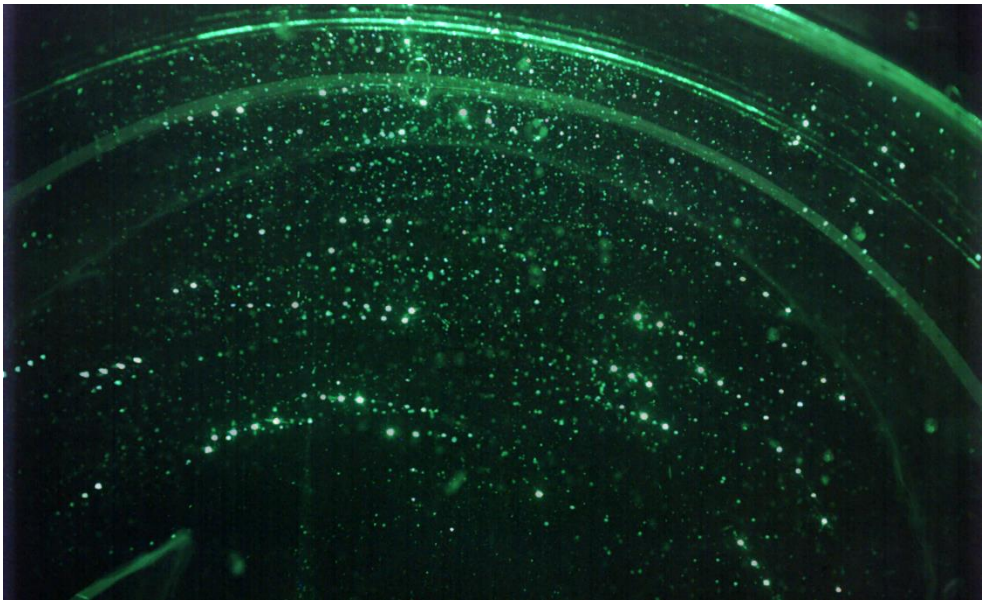

Figure 5.15: FOV containing illuminated particles for four overlayed particle images (model #5.0d2.0d - $h_{PTV} = 55$ mm, $h/d = 2.0$).

5.7. Near-Field Particle Streak Velocimetry

The drawback with the abovementioned two-dimensional PTV method is that it only acquires the tangential and radial velocity profiles on an arbitrary horizontal plane of the flow field. Furthermore, there existed a 'blind spot' on all images close to the vortex core due to optical obstruction from the tank support structure which then only permitted velocity measurements in the far- to mid-field of the vortex $3.5 \geq r/d \geq 1$. An alternative simple technique was devised to solve this problem which was a modified form of Quicks (1961) procedure. In order to obtain an unobstructed view of particles in the core region, images were acquired on a small cylindrical control volume using a PSV method. By illuminating the core region and imaging the vertical $x - z$ plain it was possible to extract both tangential and axial velocity data from the near-field.

5.7.1. Illumination

In this case, illumination was provided by a continuous light emitting diode (LED) array suspended above the tank. The light source illuminates an approximate cylindrical volume, 100 mm in diameter around the vortex core. In this way, particles orbiting the core could be observed (see figure 5.16 (a) and (b)). Due to the low energy of the light

source compared to the previous laser setup, larger particles were to be used. The particles were 1 mm polyethylene beads supplied by *Cospheric*. The particles possessed a specific gravity of 1.1 and a mean particle diameter $d_p = 1$ mm. Initial observation showed that the particles were clearly visible as bright specks in the illuminated volume and therefore their size was deemed to be sufficient.

Figure 5.16: Particle images using the PSV method for (a) h/d = 2 and (b) h/d = 3.5 in model #4.0d1.5d and #5.0d2.0d respectively. Figure 5.17(b) shows the particle streaks when aligned with the $x_0 - z_0$ plane as discussed in section 5.7.2.

5.7.2. Imaging and Analysis

The concept behind the PSV approach is simple. If one views a particle orbiting the air core from above, they will observe the particles moving almost concentrically. However, if viewed perpendicular to the $z-$axis, one will then observe the particle to essentially oscillate on the horizontal plane with a quantity of downward movement due to the axial velocity. This oscillation can be represented as a sinusoidal curve for the function between the angle of rotation and displacement. Hence, when $dx/d\theta$ = 0, the particle is located at its maximum in-plane horizontal radius. Thus, by observing the locations where the particle appears not to move in the $x-$direction it depicts the spatial position when the motion is perpendicular or tangential to $x_0 - z_0$ allowing the observer to determine the radii r_l and r_r with relative precision (see Figure 5.17). Tangential and axial particle displacements are then determined from the image streaks as the particle moves along the $x_1 - z_1$ plane at $x_1 = 0$. Its velocity can then be resolved from the exposure time of the image and the streak geometric components $\Delta x_p, \Delta z_p$. The position of the x_1- z_1 plane is

obtained by an estimation of the particles radial position Δr_p which is taken to be an average of positions r_l and r_r which reside on the x_0- z_0 plane. This assumption assumed that the particle is moving along an Archimedes spiral trajectory which may be considered valid for small radii (< 50 mm). The particle images were again calibrated by imaging a grid plate positioned on the $x_0 - z_0$ plane when the tank was full of the test fluid. Using the particle radius $(r_l + r_r)/2$, the magnification of the x_1-z_1 plane $M_{0x_1-z_1}$could subsequently be computed. The streaks were measured using a cubic spline and the position of the displacement vector was assumed to be in the mid-point of the streak (central difference approach). The two dimensional velocity vectors were then obtained using:

$$\left(v_{px}, v_{pz}\right) \cong \frac{\left(\Delta x_p, \Delta z_p\right)}{\Delta t} = \frac{\left(\Delta X_p, \Delta Z_p\right)}{M_{0x_1-z_1}\Delta t} \tag{5.16}$$

where Δt is now the exposure time of the image frame. The high-speed camera was aligned perpendicular to the x, z axis and images were obtained of the illuminated volume through the tanks planar surface. In order to avoid weak lensing effects introduced by the curvature of the model wall, the tank was filled with the test fluid thus reducing the refraction across the model interface (Quick, 1961). In this case, the images were obtained at frequencies of between 50 and 75 Hz due to the large velocities in this region ($[v, w] >$ 1 m/s). One may pose the question about the axial velocity in the far-field outside $r =$ 0.05 m where only the tangential and radial velocity profiles are obtained. However, previous research (Quick, 1961) showed that the axial velocity was very small in the far-field and can be considered negligible. Hence it was only important to obtain axial velocity data in the near-field using this technique.

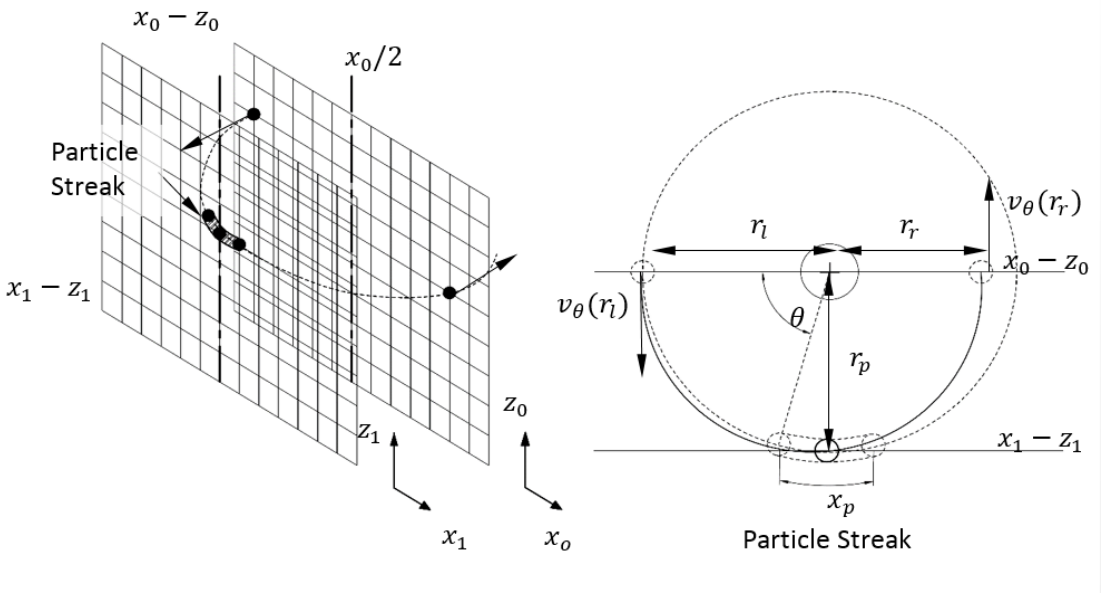

Figure 5.17: Schematic of the particle displacement analysis using the PSV method to determine the tangential component and axial velocity component.

5.8. Testing Procedures

To recap, the objective of the experimental program was to (1) implement a systematic investigation of the governing dimensionless parameters for each of the geometries, (2) investigate the near and far-field mean three-dimensional velocity profiles in the vortex and (3) observe the secondary flow processes in the strong free-surface vortex. Undertaking all three assignments for the full range of models would be a timely process. Other authors (Quick, 1961; Anwar, 1965; Daggett and Keulegan, 1974) have before now revealed that the tangential velocity is independent of the subsurface depth except close to the boundaries and water surface. Therefore some data required, for example, to obtain the dimensionless parameters in the approach flow geometry investigation, can be curtailed by only analysing a single light sheet setting h_{PTV} similar to the assumptions made by Möller (2013).

5.8.1. Approach Flow Geometry Investigation

In Section 5.2, dimensional analysis revealed that the flow in a strong free-surface vortex was dependent on five dimensionless parameters through Equation (5.2) . In order to fully explore the effects of each parameter, it was proposed that twelve geometries be

investigated. α was pre-calculated for each geometry and h/d, N_Q, Re_d and We_d were determined for a range of approach flows using the available instrumentation. The Kolf number K was measured using the prescribed PTV technique for each approach flow depth h/d by analysing the far field tangential velocity and hence, the field circulation Γ_∞. The far-field PTV technique was used to acquire the field circulation for a small portion at the inlet for one subsurface depth of each approach flow ($z/h \approx 0.5$). The field circulation was taken to be a mean of the measured values by:

$$\Gamma_\infty = \frac{1}{n}\sum_{i=1}^{n}\Gamma_i = \frac{2\pi}{n}\sum_{i=1}^{n} v_{\theta\,i} \times r_i \qquad (5.17)$$

where n is the number of samples. The PTV measurements were obtained over a time of five minutes and therefore the results could be regarded as a time average field circulation to consider a steady flow field. For each geometry, the depth discharge relationship was obtained by determining the approach flow depth and corresponding discharge for a range of incremental depths. Data to determine the dimensionless parameters were obtained for six approach flow conditions in each geometry (a_c, h/d, Q, and Γ_∞) summarised in Table 5.2. The free-surface profile was also measured for each approach flow depth.

Table 5.2 Experimental program performed within this study for the approach flow geometry investigation highlighting the geometry, the approach flow depths h/d, discharge Q, measured circulation Γ_∞ air core diameter $\boldsymbol{a_c/d}$ and inlet Froude number Fr_i

Test (no.)	Model (-)	α (-)	h/d (-)	Q (m^3/s) $\times 10^{-3}$	$\Gamma_{\infty(PTV)}$ (m^2/s)	N_Γ (-)	a_c/d (m)	Fr_i (-)
1	#3.0d0.5d	3.279	0.50	0.280	0.169	31.61	0.925	0.633
2	#3.0d0.5d	3.279	1.00	0.640	0.200	16.55	0.836	0.682
3	#3.0d0.5d	3.279	1.50	1.040	0.249	12.58	0.731	0.748
4	#3.0d0.5d	3.279	2.00	1.500	0.270	9.46	0.612	0.817
5	#3.0d0.5d	3.279	2.50	1.920	0.274	7.51	0.537	0.838
6	#3.0d0.5d	3.279	3.00	2.330	0.279	6.30	0.478	0.848
7	#3.0d1.0d	2.097	0.50	0.360	0.125	18.31	0.866	0.388
8	#3.0d1.0d	2.097	1.00	0.925	0.186	10.57	0.761	0.446
9	#3.0d1.0d	2.097	1.50	1.480	0.201	7.14	0.672	0.459
10	#3.0d1.0d	2.097	2.00	2.020	0.201	5.23	0.537	0.462
11	#3.0d1.0d	2.097	2.50	2.505	0.210	4.41	0.463	0.450
12	#3.0d1.0d	2.097	3.00	3.090	0.207	3.52	0.388	0.459
13	#3.0d1.5d	1.495	0.50	0.490	0.149	15.99	0.791	0.298
14	#3.0d1.5d	1.495	1.00	1.070	0.163	8.02	0.649	0.273

Test (no.)	Model (-)	α (-)	h/d (-)	Q (m^3/s) $\times 10^{-3}$	$\Gamma_{\infty(PTV)}$ (m^2/s)	N_Γ (-)	a_c/d (m)	Fr_i (-)
15	#3.0d1.5d	1.495	1.50	1.765	0.173	5.15	0.537	0.279
16	#3.0d1.5d	1.495	2.00	2.415	0.179	3.91	0.463	0.276
17	#3.0d1.5d	1.495	2.50	3.070	0.180	3.08	0.403	0.273
18	#3.0d1.5d	1.495	3.00	3.560	0.179	2.65	0.299	0.263
19	#3.0d2.0d	1.301	0.50	0.515	0.125	12.77	0.701	0.235
20	#3.0d2.0d	1.301	1.00	1.146	0.137	6.27	0.582	0.216
21	#3.0d2.0d	1.301	1.50	1.890	0.154	4.28	0.507	0.219
22	#3.0d2.0d	1.301	2.00	2.500	0.162	3.42	0.427	0.208
23	#3.0d2.0d	1.301	2.50	3.175	0.162	2.68	0.321	0.205
24	#3.0d2.0d	1.301	3.00	3.670	0.165	2.36	0.269	0.195
25	#4.0d0.5d	4.875	0.50	0.240	0.211	46.15	0.940	0.700
26	#4.0d0.5d	4.875	1.00	0.515	0.213	21.80	0.828	0.721
27	#4.0d0.5d	4.875	1.50	0.880	0.260	15.51	0.754	0.816
28	#4.0d0.5d	4.875	2.00	1.285	0.268	10.98	0.642	0.882
29	#4.0d0.5d	4.875	2.50	1.700	0.315	9.76	0.597	0.905
30	#4.0d0.5d	4.875	3.00	2.130	0.339	8.36	0.552	0.912
31	#4.0d1.0d	2.688	0.50	0.310	0.150	25.53	0.866	0.365
32	#4.0d1.0d	2.688	1.00	0.700	0.170	12.77	0.746	0.357
33	#4.0d1.0d	2.688	1.50	1.150	0.186	8.51	0.597	0.368
34	#4.0d1.0d	2.688	2.00	1.700	0.206	6.38	0.507	0.393
35	#4.0d1.0d	2.688	2.50	2.190	0.212	5.09	0.463	0.395
36	#4.0d1.0d	2.688	3.00	2.600	0.211	4.28	0.448	0.387
37	#4.0d1.0d	2.688	3.50	3.100	-	3.73	-	-
38	#4.0d1.5d	1.956	0.50	0.390	0.149	20.09	0.821	0.276
39	#4.0d1.5d	1.956	1.00	0.886	0.179	10.62	0.709	0.263
40	#4.0d1.5d	1.956	1.50	1.460	0.188	6.77	0.567	0.268
41	#4.0d1.5d	1.956	2.00	2.050	0.189	4.86	0.478	0.270
42	#4.0d1.5d	1.956	2.50	2.605	0.189	3.82	0.394	0.266
43	#4.0d1.5d	1.956	3.00	3.140	0.197	3.30	0.351	0.265
44	#4.0d2.0d	1.577	0.50	0.515	0.149	15.21	0.791	0.254
45	#4.0d2.0d	1.577	1.00	1.180	0.160	7.12	0.687	0.239
46	#4.0d2.0d	1.577	1.50	1.845	0.168	4.80	0.537	0.228
47	#4.0d2.0d	1.577	2.00	2.485	0.199	4.21	0.418	0.219
48	#4.0d2.0d	1.577	2.50	3.110	0.197	3.34	0.313	0.212
49	#4.0d2.0d	1.577	3.00	3.635	0.200	2.90	0.284	0.203
50	#5.0d0.5d	6.220	0.50	0.220	0.216	51.55	0.940	0.670
51	#5.0d0.5d	6.220	1.00	0.425	0.236	29.16	0.828	0.600
52	#5.0d0.5d	6.220	1.50	0.700	0.253	19.02	0.746	0.643
53	#5.0d0.5d	6.220	2.00	1.000	0.305	16.03	0.709	0.681
54	#5.0d0.5d	6.220	2.50	1.320	0.329	13.12	0.679	0.712
55	#5.0d0.5d	6.220	3.00	1.650	0.343	10.92	0.657	0.742
56	#5.0d1.0d	3.129	0.50	0.300	0.177	31.03	0.881	0.340
57	#5.0d1.0d	3.129	1.00	0.635	0.203	16.83	0.739	0.311
58	#5.0d1.0d	3.129	1.50	1.100	0.218	10.40	0.649	0.337

Test (no.)	Model (-)	α (-)	h/d (-)	Q (m^3/s) $\times 10^{-3}$	$\Gamma_{\infty(PTV)}$ (m^2/s)	N_Γ (-)	a_c/d (m)	Fr_i (-)
59	#5.0d1.0d	3.129	2.00	1.500	0.221	7.77	0.597	0.332
60	#5.0d1.0d	3.129	2.50	1.985	0.228	6.05	0.537	0.342
61	#5.0d1.0d	3.129	3.00	2.400	0.265	5.82	0.522	0.342
62	#5.0d1.5d	2.267	0.50	0.330	0.167	26.60	0.851	0.223
63	#5.0d1.5d	2.267	1.00	0.760	0.193	13.35	0.724	0.217
64	#5.0d1.5d	2.267	1.50	1.265	0.202	8.38	0.657	0.225
65	#5.0d1.5d	2.267	2.00	1.800	0.205	5.98	0.575	0.231
66	#5.0d1.5d	2.267	2.50	2.370	0.205	4.55	0.493	0.238
67	#5.0d1.5d	2.267	3.00	2.820	0.209	3.90	0.455	0.234
68	#5.0d2.0d	1.805	0.50	0.385	0.159	21.67	0.760	0.188
69	#5.0d2.0d	1.805	1.00	0.895	0.164	9.63	0.694	0.178
70	#5.0d2.0d	1.805	1.50	1.450	0.183	6.63	0.597	0.175
71	#5.0d2.0d	1.805	2.00	2.105	0.194	4.86	0.463	0.180
72	#5.0d2.0d	1.805	2.50	2.650	0.202	4.01	0.388	0.173
73	#5.0d2.0d	1.805	3.00	3.140	0.202	3.38	0.358	0.167
74	Radial	-	2.00	1.274	-	-	0.000	-
75	Radial	-	1.00	2.548	-	-	0.000	-
76	Radial	-	0.67	3.158	-	-	0.075	-
77	Radial	-	0.50	3.626	-	-	0.179	-
78	Radial	-	0.47	3.674	-	-	0.343	-

The radial flow cylinder was analysed additionally to benchmark the data obtained from each vortex chamber. To further eliminate vortex formation, a vane was used to supress vortex formation for low h/d in this model. The dimensionless parameters were acquired in a similar fashion to the vortex chamber geometries. In total, 390 examinations were performed in the course of the approach flow geometry program.

5.8.2. Free-Surface Profiles

The free-surface profiles were monitored for each approach flow depth h/d. The depth gauge spanned the flow field in the $x-y$ plane and the tip was dropped through z to locate the position of free-surface. Initial observations displayed that for the majority of the tests, the free-surface profile was approximately axisymmetric. To reduce experimental effort, the water surface profile was therefore only mapped for a single radial section of the vortex. This section was chosen to span from the inlet through the orifice extending to the opposite side of the vortex chamber. The depth gauge was calibrated for each model by measuring the position of the chamber walls and orifice. The

water surface was mapped at 10 mm radial increments in the far-field reducing to 5 - 2.5 mm increments in the near-field. Instabilities on the core of the free-surface rendered it difficult to achieve the position of the free-surface close to the vortex throat i.e. the critical air core diameter a_c. The diameter of this critical section was measured using an alternative technique specified below.

5.8.3. Critical Air Core Diameter

The difficulty in determining the air core diameter a_c of the critical throat section using the depth gauge apparatus was discussed in the previous section. An alternatively photographic technique was adopted for this purpose. Here, the camera was suspended above the tank on the camera mount and centred over the orifice. The camera was focused onto a calibration plate resting on the orifice prior to testing. The air core was then imaged for each approach flow depth h/d. The surface of the critical section of the air core was clearly visible on the image where a distinct interface was made between the black background of the lower reservoir and the illuminated vortex core. The transient diameter of the vortex core was time averaged by measuring the diameter for an image obtained every 0.2 seconds.

5.8.4. Three-Dimensional Velocity Profiles

The tangential, radial and axial velocity profiles were fully explored in the radial and axial extents. Three approach flow conditions were examined for a single model of the vortex chamber $h/d = 1.0$, 2.0 and 3.5. The #4.0d1.0d model was chosen as it produces a moderate circulation field ($\alpha = 2.688$). From figure 5.14 and 5.15, it was observable that the whole-field PTV method outlined in Section 5.6 can only be applied on a field-of-view which is approximately half that of the chamber due to the eccentrically positioned camera enclosure. The assumption was therefore made that the flow is axisymmetric around the *z*-axis. Thus it was only necessary to analyse the velocity profiles for a radial portion of the flow spanning from the inlet to the orifice and assuming repeatability the velocity profiles in the azimuthal direction. The AOI is highlighted in Figure 5.18 (a). The far-field PTV method was applied for a range of subsurface depths z/h for each approach flow condition. The subsurface depths considered were typically at 15, 30, 50,

75, 100, 150, 175, 200, 215 and 233 mm depending on the type of approach flow being considered. This was achieved by varying the collimation of the light sheet optics in small increments and refocusing the camera onto the test plane in each case. A submerged gridded plate (see Figure 5.18 (b)) was imaged additionally for calibration purposes. PTV was also applied at the free-surface by tracking buoyant beads in a similar fashion to the pre-described PTV technique. In this case the high speed camera is suspended above the tank on a bridge and focused onto the water surface for each approach flow depth. The PSV technique (Section 5.7) was implemented for each approach flow depth to assemble the tangential and axial velocity fields around the vortex core. In this case, the particles axial positions were random due to illumination of the flow volume as opposed to a specified plane in the PTV technique. Each particles radial and axial position was however recorded during displacement analysis. The flow fields were imaged for approximately five minutes in both the PSV and PTV techniques and therefore the correlation of the data will be representative of a time averaged velocity field.

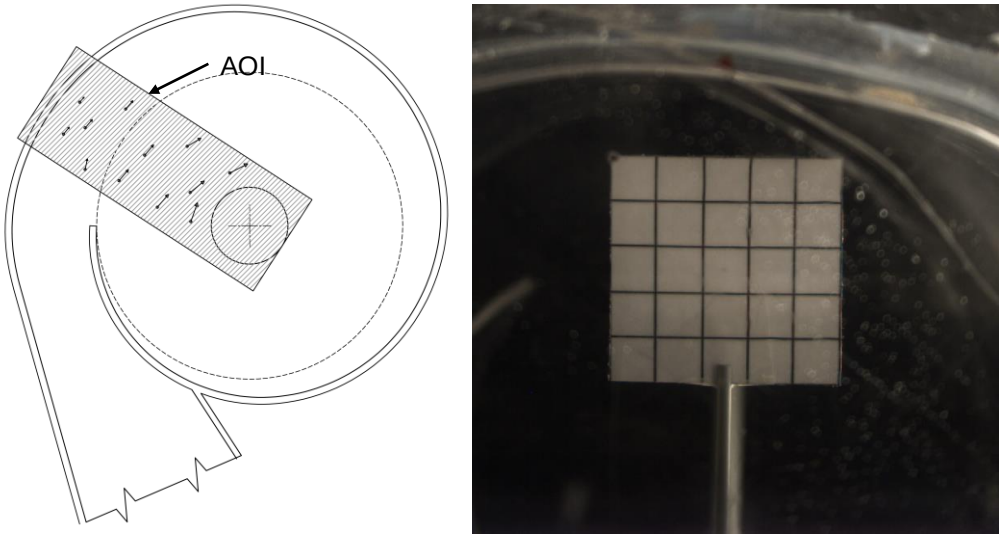

Figure 5.18: (a) Plan schematic of vortex chamber model highlighting the AOI and (b) example image of calibration plate in the vortex chamber.

5.8.5. Planar Laser-Induced Fluorescence (PLIF)

In order to supplement the quantitative data obtainable through the procedures set out in Section 5.8.4, a qualitative analysis by visual observation of the flow field was achieved through the planar laser-induced fluorescence (PLIF) technique. PLIF is an optical flow

visualisation technique used to observe the advection and diffusion of a fluorescent dye in the flow. In this way it was a suitable method to observe the macro turbulent flow structures of the whole-flow field. Typically, PLIF uses a laser light source to excite a fluorescein material which emits light to distinctly appear different to that of the host fluid. This fluorescence process was molecular in nature and can be described as the return of an electron to the energy ground state with light emission being a product of the event. In this way, the fluorescence can be image on a CCD sensor aligned perpendicular to the light sheet in a similar fashion to that of the previously described PTV technique. The PLIF process is outlined in Figure 5.19 as applied to both visual and quantitative flow analysis.

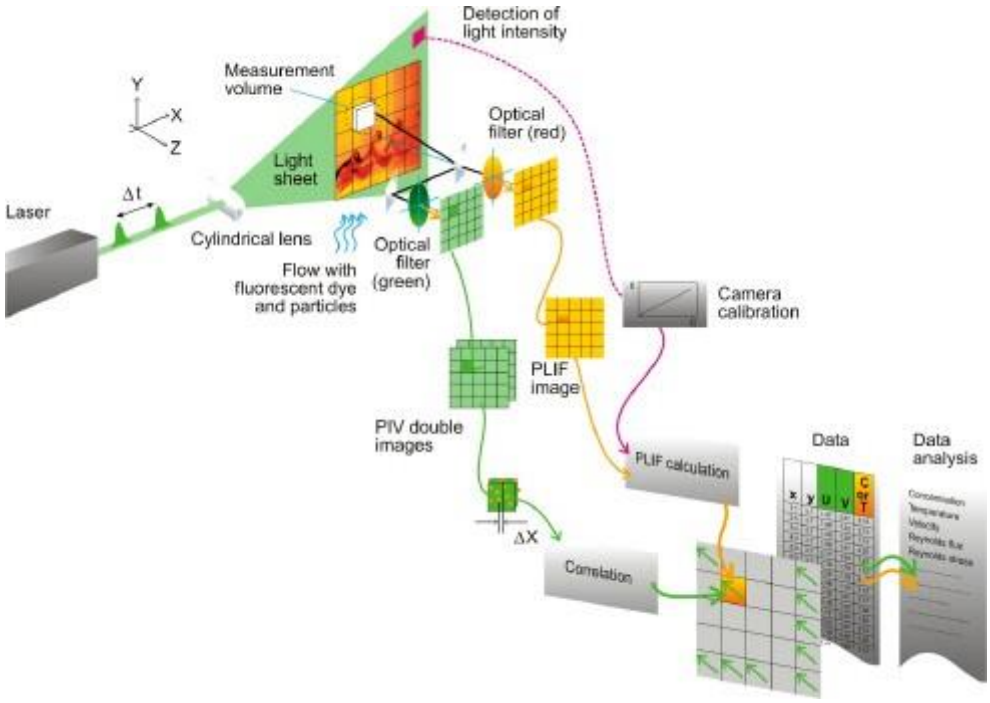

Figure 5.19: Planar laser-induced fluorescence technique as applied to both qualitative and quantitate flow analysis.

In the current application, the 532 nm Nd:YAG laser light was used in conjunction with the Rhodamine B fluorescein. Rhodamine B fluoresces with a yellow (590 nm) wavelength under the absorption of 532 nm light. Because of its low molecular diffusivity

and high Schmidt[23] number it renders it very suitable for turbulent mixing studies (Lima et al., 2002). The PLIF technique was employed for two visual investigations; (1) turbulent flow structures on a horizontal plane and (2) to investigate the secondary flow fields of the vortex. In (1) the laser light sheet and imaging arrangement was similar to that of the PTV method. A small quantity of Rhodamine B dissolved in water was injected above the light sheet just upstream of the inlet using a pipette.

The secondary flow field exists as radial and axial flow processes to ensure continuity of flow in the vortex. Thus, to analyses these flows in (2), the light sheet is instead arranged to highlight the $z - x$ axis passing directly through the centre of the orifice. The camera is positioned perpendicular to the light sheet arrangement as shown below in Figure 5.20 (a). Figure 5.20 (b) further depicts the nature of the fluorescent emission observed from outside the tank during PLIF analysis. In (2) the Rhodamine B is injected at two separate locations just upstream of the vertical lights sheet; at (a) the vessel floor and (b) at the water surface. These two locations are highly suspected as the main secondary flow regions according to previous reports (Quick, 1961; Anwar, 1965; Daggett and Keulegan, 1974). The light sheet and transport of the fluorescein in each observation was imaged at a fixed pulse repetition and frame rate of 30 Hz.

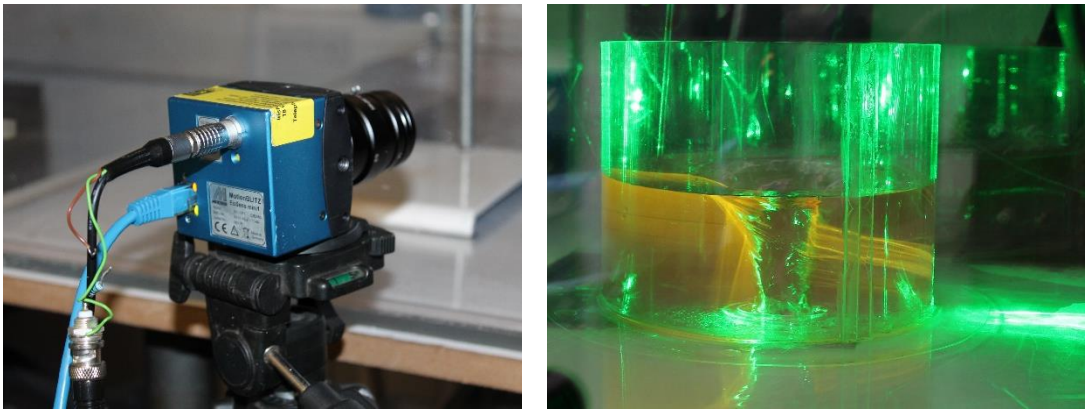

Figure 5.20: (a) Image of camera arrangement and (b) example of fluorescent light emission as viewed from outside the tank.

[23] Schmidt number (Sc) is a dimensionless number defined as the ratio of momentum diffusivity (viscosity) and mass diffusivity, and is used to characterize fluid flows in which there are simultaneous momentum and mass diffusion convection processes. It was named after the German engineer Ernst Heinrich Wilhelm Schmidt (1892-1975).

A summary of the research program for Sections 5.8.2 – 5.8.5 for the mean three-dimensional velocity investigation using both PTV and PSV as well as free-surface examinations and laser induced fluorescence investigations is summarised in Table 5.3.

Table 5.3 Experimental program performed within this study for mean three-dimensional velocity investigation highlighting the geometry, the approach flow depths h/d, discharge Q, subsurface depth above the orifice h_{PTV} and whether or not particle streak velocimetry (PSV), free-surface profiling (FSP) or laser induced fluorescence (LIF) was performed and where WS denotes when water surface measurements were performed.

Test (no.)	Model (-)	α (-)	h/d (-)	Q (m^3/s) $\times 10^{-3}$	h_{PTV} (m)	PSV (y/n)	FSP (y/n)	LIF (y/n)
1	#4.0d1.0d	3.279	1.0	0.725	0.015	y	y	n
2	#4.0d1.0d	3.279	1.0	0.725	0.035	y	y	n
3	#4.0d1.0d	3.279	1.0	0.725	0.050	y	y	n
4	#4.0d1.0d	3.279	1.0	0.725	WS	y	y	n
5	#4.0d1.0d	3.279	2.0	1.677	0.015	y	y	y
6	#4.0d1.0d	3.279	2.0	1.677	0.035	y	y	y
7	#4.0d1.0d	3.279	2.0	1.677	0.050	y	y	y
8	#4.0d1.0d	3.279	2.0	1.677	0.075	y	y	y
9	#4.0d1.0d	3.279	2.0	1.677	0.100	y	y	y
10	#4.0d1.0d	3.279	2.0	1.677	0.125	y	y	y
11	#4.0d1.0d	3.279	2.0	1.677	WS	y	y	y
12	#4.0d1.0d	3.279	3.5	3.111	0.015	y	y	y
13	#4.0d1.0d	3.279	3.5	3.111	0.035	y	y	y
14	#4.0d1.0d	3.279	3.5	3.111	0.075	y	y	y
15	#4.0d1.0d	3.279	3.5	3.111	0.125	y	y	y
16	#4.0d1.0d	3.279	3.5	3.111	0.150	y	y	y
17	#4.0d1.0d	3.279	3.5	3.111	0.175	y	y	y
18	#4.0d1.0d	3.279	3.5	3.111	0.215	y	y	y
19	#4.0d1.0d	3.279	3.5	3.111	0.225	y	y	y
20	#4.0d1.0d	3.279	3.5	3.111	WS	y	y	y

5.9. Uncertainty

Uncertainty is a major factor in experimental programs in hydraulics and fluid mechanics. This can be as a result of known and unknown or unquantifiable error sources. Failure to account for uncertainty can be detrimental to the reliability of the results, particularly if they are to be used in prototype scaling and subsequent decision making. A detailed qualitative and quantitative analysis on the uncertainty of the aforementioned test programs will now be discussed.

5.9.1. General Instrumentation

The depth gauge possessed a graduation error rating of $\pm$ 0.01 mm for vertical readings and $\pm$ 0.05 mm in the radial position. The flow meter measurement error is $\pm$ 0.1 % with a reading standard deviation of $\pm$ 0.0015 l/s. This corresponded to error bars for intake Froude and radial Reynolds numbers of $\mathrm{Fr}_i = \pm 0.019$ and $\mathrm{Rr} = \pm 34$ respectively. Values of this magnitude were considered to be insignificant in comparison to the experimental range. Location of the vortex centre at the orifice using the calibration plate was found to cause an error in locating the particles radial position by $\pm$ 4 mm.

5.9.2. Water Surface Profiles

Measurement of the free water surface in the far-field was virtually free of error due to the small instrument inaccuracy of $\pm$ 0.01 mm as it accounts for only 0.03 % of the smallest approach flow depth. On approaching the vortex core, uncertainty was amplified significantly due to the oscillating nature of the free-surface. In the worst case, these oscillations were observed to be approximately $\pm$ 4 mm. The uncertainty of locating the depth and the radial position in the near-field was estimated to be approximately $\pm$ 1.21 mm and $\pm$ 7 mm respectively. Measurements of the critical air core a_c using the imaging technique were estimated to be approximately $\pm$ 1.5 mm.

5.9.3. Temporal and Optical Error

Pulse trains, such as that in the laser system exhibit some deviations with respect to their temporal pulse positions from those in a perfectly periodic pulse train. This phenomenon is called the timing or pulse jitter. If the pulse jitter is excessive, it may cause uncertainty in the temporal accuracy of the measured physical process by an increase or decrease of the actual time separation between laser pulses (i.e. $\Delta t_{act} = \Delta t \pm \delta t$). δt is therefore the standard deviation of the temporal pulse positions with respect to the average pulse positions. The pulse jitter was measured for the laser system accordingly. A photo-diode (supplied by *Thor Labs*) was positioned in the laser emission zone which converts the pulsing laser light into a measureable current. This signal was sent to a storage oscilloscope which computes the average pulse repetition rate and standard deviation by sampling the peak of the input signals. The jitter was found to be $\pm$ 0.033 µs which was

insignificant when compared to the average pulse separation of 0.1 - 0.033 s.

Optical errors tend to be the principal form of error in PTV and PIV analysis. Generally, most of the problems associated with optical uncertainty are removed by calibrating the image sensor in the field using a grid plate or other such methods. This effort helps to remove significant refraction errors influenced by imaging the AOI through mediums of varying refractive index[24]. However, other errors can arise as a result of using optical methods. In planar methods, it is assumed that the light sheet is nominally small such that $t_{PTV} = 0$ and therefore conventional mapping can be employed. In reality, the light sheet thickness was finite ($\cong 2$ mm) and thus implies that there was a variation of the magnification depending on the particles position in the light sheet cross section. This perspective error as a result of the varying particle magnification was found to be in the range of ± 0.1 - ± 0.2 % and can lead to an error in the calculation of the in-plane displacement components. Other optical errors include poor alignment of the laser light sheet through the AOI, resulting in further magnification uncertainty, barrel distortion of the particle image in the far-fields, residual calibration and unaccounted refraction errors.

5.9.4. Particle Dynamics

The disadvantages of particles in PTV are that they must slip with respect to the fluid to generate the drag force needed to follow fluid acceleration. It is also well known (Adrian, 1991) that particles with specific gravity different from that of the fluid can lag or drift in flows where large local accelerations are experienced. The acceleration applies a force to the particle of mass:

$$m_p = \frac{\pi}{6}\rho_p d_p^3 \tag{5.18}$$

which possesses a density ρ_p different to that of the fluid which it occupies (Adrian, 1991). Accelerations are experienced due to gravitational forces in low inertial flows or close to the vortex core where both tangential normal components of acceleration are sizeable. The effects of the uncertainty associated with particle slip will be analysed here for the worst case of maximum vortex chamber flow. The finite particle slip Reynolds

[24] The refractive index determines how much light is bent, or refracted, when entering a material

number is given by:

$$\mathrm{Re}_p = \frac{|u - v_p| d_p}{\nu_f} \tag{5.19}$$

where the slip velocity v_p in a fluid system is then given by:

$$v_p - u = \frac{\bar{\rho} - 1}{\bar{\rho}} a_{cc} \tau_0 / \phi \tag{5.20}$$

and $\bar{\rho} = \rho_\rho / \rho_f$, a_{cc} is the local acceleration, ϕ is a modification factor initially assumed (ϕ = 1) and τ_0 is the time constant that comes from the balance between the inertia of the particle and the quasi-steady viscous drag force given by:

$$\tau_0 = \frac{\rho_p d_p^2}{18 \nu_f \rho_f} \tag{5.21}$$

(Adrian and Westerweel, 2011). Using Equation 5.20, and treating a_{cc} as the gravitational acceleration, the particle settling behaviour of the 0.8 mm and 1.0 mm particles are estimated to be in the order of 1×10^{-5} m/s which is considered to have a negligible effect on the PTV error. Particles tend to be more subjective to local fluid accelerations in the field (Adrian and Westerweel, 2011). In flows with strong streamline curvature such as vortex flows, particles can drift inward or outward radially depending on their specific gravity relative to the test fluid. This drift velocity was determined by Equation 5.20 where a_{cc} was treated as the centrifugal acceleration ${v_\theta}^2/r$. By assuming that the whole flow field was fully irrotational, the centrifugal acceleration can be calculated radially using $v_\theta = \Gamma_\infty / 2\pi r$. This analysis revealed that for the highest circulation field in the model, the maximum slip near the vortex core $v_p - u$ = 0.96 mm/s corresponding to a finite particle slip Reynolds number Re_p = 0.75. This local slip velocity was several orders of magnitude smaller than the local fluid velocity (0.2 – 1.2 m/s) being measured and therefore could be considered negligible.

5.9.5. Geometry Errors

The details of the vortex chamber design and construction are highlighted in Section 6.2. Further details on the design and construction carried out by the lead author for the thirteen models can be found in Appendix A. During fabrication, each unit was subjected to small imperfections in the workshop. The completed models were individually

reassessed for verticality, peripheral imperfection, orifice size and inlet geometry. The α parameter was modified from its theoretical value to account for small imperfections observed at the inlet. Maximum defects in the horizontal position of the spiral periphery were found to be in the region of $\pm$ 4 % which were considered to be reasonable.

A summary of typical errors generated from instrumentation and measurement techniques that was estimated in previous sections (Section 5.9.1-5.9.5) is presented in Table 5.4. The error given was the maximum calculated error and is presented as a function of the mean measurement that was undertaken. The estimated errors generated in the measurements were quite small and compare to be within a reasonably safe limit when compared to another study (Möller, 2013).

Table 5.4 Maximum potential errors generated in instrumentation and measurement technique

Instrumentation and Measurement Technique	**Range**	**Reading Standard Deviation**	**Error Generated**
Pump	0-3.9 l/s	-	-
Magnetic Flow Meter	0-8 l/s	$\pm$ 0.0015 l/s.	$\pm$ 0.1 % (of flow reading)
Depth Gauge	-	-	$\pm$ 0.01 mm $\pm$ 0.05mm (vertical and horizontal free-surface position)
Calibration Plate Position	-	-	$\pm$ 4 mm (from vortex core)
Laser Pulse Jitter	-	$\pm$ 0.033 µs	≈0
Camera Distortion	-	-	$\pm$ 0.1 % (of measured particle position)
Misaligned Light Sheet	-	-	$\pm$ 1.3 % (of measured particle position)
Resolution of Image correction	-	-	$\pm$ 3.0 % (of measured particle position)
Perspective Error	-	-	$\pm$ 0.1 - 0.2 % (of measured particle position)
Residual Refraction	-	-	$\pm$ 2.0 % (of measured particle position)
Seeding Particle Lag	-	-	0.005% (of minimum velocity)
Seeding Particle Drift	-	-	0.128 % (of velocity in the core region)
Model Manufacturing Errors	-	-	$\pm$ 4 mm

5.10. Summary of Experimental Modelling

This chapter presented a complete overview of the experimental methodology that was employed throughout the physical modelling investigation. The chapter begins by introducing the three phases of experimental inquiry comprising of investigations on (a) the effects of the approach flow geometry, (b) the three-dimensional velocity profiles and (c) secondary flow fields. Dimensional analysis was subsequently performed which reveals that the flow, expressed through the discharge number N_Q in the strong free-surface vortex is dependent on five dimensionless parameters which can be narrowed down to only three parameters provided that conditions for Froude similitude can be adhered to (Anwar, 1965; Jain et al. 1978). The governing geometric parameter was found to be α which designates the ratio of the effective diameter to the inlet width in order to represent the horizontal flow geometry.

Upon identifying the governing parameters, an experimental program is developed based on the hydraulic analysis of these parameters in twelve vortex chamber geometries. The design of the models as well as a description of the test configuration was presented. It was noted that accurate determination of the tangential velocity field and hence the field circulation tends to be difficult in experimental modelling. Particle tracking methods (PTV and PSV) are adopted to measure the flow field fluid velocities. The various measurement techniques as well as the laser illumination and image acquisition methods were then discussed. To observe the secondary flow processes, planar laser induced fluorescence was employed and described within the text.

Based on the configuration of the laboratory apparatus and instrumentation, a description of the testing processes was described for each experimental investigation which include: approach flow geometry, investigation, free-surface profiles, critical air core diameter, three-dimensional velocity profiles, planar laser-induced fluorescence. Finally, the relative uncertainty surrounding these techniques were noted and integrated into the analysis.

Chapter 6.

Experimental Results and Discussion

SUMMARY

The results of the overall experimental program are presented and critically discussed in this section. It will be shown that the conditions of the approach flow in each model satisfy the criteria for the outlet Reynolds number in order to be scaled through Froude similitude. However, four of the approach flows did not achieve the criteria for the outlet Weber number. Subsequent analysis of the data indicate that the circulation and hence the Kolf number (K) is strongly dependant on the approach flow geometry which is characterised by a non-dimensional approach flow factor, y_α. The discharge number (N_Q) varies inversely with K for each geometry by intrinsic relationships governed by two further empirical parameters: the constant k_α and exponent n_α. Empirical models for the auxiliary terms are presented. These findings collectively deliver an alternative, simple model to determine the depth-discharge relationship in a vortex. Validation of the newly proposed depth-discharge model is made based on the data for two prototype systems reported in the literature. Errors were reported to be less than 15 %. The 3D velocimetry data indicate that the tangential velocity profile is independent of the subsurface depth. Based on findings for the axial velocity field, an alternative analytical model to predict the near-field tangential velocity field is presented. An improved prediction of the near-field tangential velocity profile by approximately 30 % is achievable using this model. The third contribution of the experimental work is the evaluation of the secondary flow fields using the planar laser induced fluorescence technique. Here it is found that the secondary flow fields consists of a banded motion where the radial velocity is concentrated at the vessel floor and free-surface and the axial velocity at the tank periphery and air core.

6.1. Similarity

In Section 3.4, a discussion was made regarding similarity and the conditions for employing Froude based similitude founded on the criteria of Anwar (1965) and Jain et al. (1978). It was deemed necessary to also include Odgaard's conditions for Froude similitude based on his work (Odgaard, 1986). The capacity of the physical models to meet these criteria is presented in Table 6.1. The minimum and maximum approach flow conditions are reported for each model together with the minimum and maximum measured experimental Weber and Reynolds numbers (both the radial and submerged Reynolds numbers) as well as their calculated minimum limits. It is observed here that there are only a few cases where the surface tension may have an effect on the model vortex flow ($3.0d2.0d$, $4.0d1.0d$, $4.0d1.5d$ and $5.0d1.5d$) due to $\mathrm{We}_d < 120$. For all higher approach flows tested in these models the intake Weber number exceeded the required limit. The radial Reynolds numbers for all model tests were greater than the limiting condition ($\mathrm{Rr} > 10^3$) (Anwar, 1965) and in a number of cases also exceeded the secondary condition ($\mathrm{Rr} > 10^4$) (Anwar and Amphlett, 1980). The lower bound condition was deemed appropriate for the current test program as the flow was through a horizontal orifice. The intake Reynolds number Re_d exceeded Odgaard's (1986) limiting factor in all cases by an order of two. Based on the radial Reynolds number in all tests it was assumed that the effects of viscosity are negligible and Froude similarity can be exercised with caution.

Table 6.1 Results of dependent dimensionless numbers for assessment of criteria for Froude similitude. *Note*: values highlighted as **red** are ones which do not achieve conditions for Froude similitude. Note Exp. Are to be greater than calculated for [b] and [e] criteria.

Model #		N_Q	h/d	We_d [(a)]	We_d [(b)]		Rr [(c & d)]	Re_d [(e)] $\times 10^3$	
					Exp.	Calc.	$\times 10^3$	Exp.	Calc.
3*d*0.5*d*	Min	0.077	0.5	288.4	288.4	0.107	6.6	4.188	0.027
	Max	0.640	3.0	682.1	682.1	2.118	9.1	34.609	0.376
3*d*1.0*d*	Min	0.099	0.5	154.5	154.5	7.373	8.4	5.347	0.051
	Max	0.849	3.0	990.7	990.7	25.128	12.0	45.899	0.674
3*d*1.5*d*	Min	0.135	0.5	128.3	128.3	8.280	11.4	7.278	0.036
	Max	0.978	3.0	1143.4	1143.4	36.600	13.9	52.880	0.898
3*d*2.0*d*	Min	0.142	0.5	**77.0**	77.0	10.000	12.0	7.650	0.052
	Max	1.008	3.0	1171.3	1171.3	45.200	14.3	54.514	1.065
4*d*0.5*d*	Min	0.066	0.5	321.3	321.3	3.200	5.6	3.564	0.018
	Max	0.585	3.0	703.1	703.1	11.300	8.3	31.639	0.252
4*d*1.0*d*	Min	0.085	0.5	**114.5**	114.5	5.800	7.2	4.604	0.036
	Max	0.852	3.0	791.7	791.7	23.400	10.2	38.621	0.647
4*d*1.5*d*	Min	0.107	0.5	**107.1**	107.1	7.100	9.1	5.793	0.037
	Max	0.863	3.0	959.7	959.7	29.400	12.3	46.641	0.746
4*d*2.0*d*	Min	0.142	0.5	141.8	141.8	7.000	12.0	7.650	0.037
	Max	0.999	3.0	1169.7	1169.7	33.400	14.2	53.995	0.721
5*d*0.5*d*	Min	0.061	0.5	270.0	270.0	2.600	5.1	7.650	0.017
	Max	0.453	3.0	630.1	630.1	11.300	6.4	53.995	0.246
5*d*1.0*d*	Min	0.082	0.5	133.6	133.6	4.800	7.0	4.456	0.026
	Max	0.660	3.0	815.6	815.6	17.500	9.4	35.650	0.411
5*d*1.5*d*	Min	0.091	0.5	**106.8**	106.8	7.200	7.7	4.902	0.029
	Max	0.775	3.0	947.3	947.3	26.300	11.0	41.888	0.662
5*d*2.0*d*	Min	0.106	0.5	163.6	163.6	8.000	9.0	5.719	0.032
	Max	0.863	3.0	481.0	481.0	33.500	12.3	46.200	0.711

[a] We_d	$= v_z\, d\rho/\sigma$	> 120	Jain et al. (1978)
[b] We_d	$= v_z{}^2 d\rho/\sigma$	$> 720 Fr^{1/2} N_\Gamma^{-3/2} Re^{-1/4}$	Odgaard (1986)
[c] Rr	$= Q/\nu h$	$> 10^3$	Anwar (1965)
[d] Rr	$= Q/\nu h$	$> 10^4$	Anwar and Amphlett (1980)
[e] Re_d	$= v_z\, d/\nu$	$> 1.1 \times 10^3 \left(\frac{h}{d}\right)^2 \frac{g d^3}{\Gamma^2}$.	Odgaard (1986)

6.2. General Hydraulics Results

6.2.1. Initial Observations

A range of stably subcritical (Froude number $Fr_i < 0.7$) (Hager, 2010) and transitionally subcritical ($0.7 < Fr_i < 1.0$) approach flows were observed. Transitionally subcritical is defined here as the intermediate phase prior to supercritical flow development where a small submerged hydraulic jump develops downstream of the inlet in the vortex chamber. This results in a mild free-surface instability however the air core remains relatively steady. In all twelve models of the vortex chamber, a full air core vortex was observed. An example of both a moderate strength and weak vortex structure is presented in Figure 6.1 for large and low approach flow depths respectively. The vortices appeared to be strong and turbulent in nature but sustained a relatively steady approach flow depth. When the models with a low α value were examined it was noted that the vortex core becomes relatively unstable and oscillated vigorously when the approach flow depth was increased (see #3d2.0d for h/d = 3.0 in figure 6.1). The low α parameter refers to a weak circulation field and so the increase in head causes axial velocities at the core to become more dominant resulting eventually in the collapse of the vortex at h_c. The conditions of critical submergence could not be observed in this examination because of the testing limitations. The nature of the stability of the vortex based on experimental observations is discussed in a later section.

It is noticed that for low discharges, the flow in the base of the tank was a Borda type plug flow similar to that described by Binnie (1948). This was as a result of the bottom friction overcoming the tangential momentum at the inlet and so the streamlines pursue an easier radial route to discharge. The Froude numbers ranged from 0.195 - 0.912 for the inlet and 0.077 - 1.285 for the outlet. Although no supercritical inlet conditions were experienced in the tested models, a small submerged hydraulic jump ($\sim 4-6$mm) formed just downstream of the inlet in large α value models (see Figure 6.2).

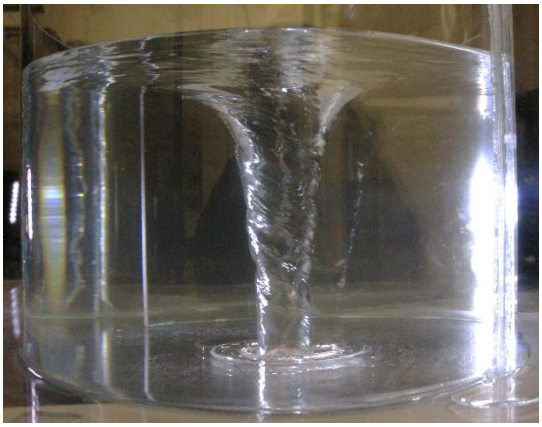

Model #4d1.0d: h/d = 3.0, K = 4.277

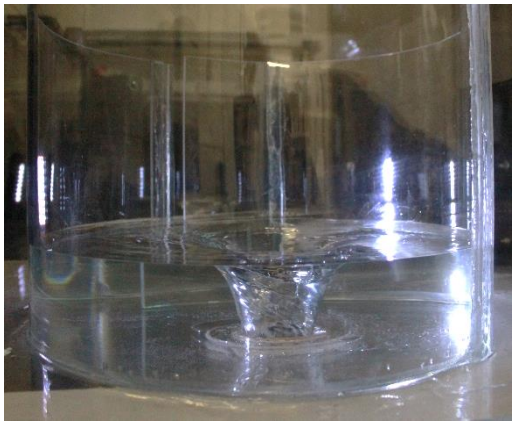

Model #4d1.0d: h/d = 1.0, K = 12.766

Model #3d2.0d: h/d = 3.0, K = 2.362

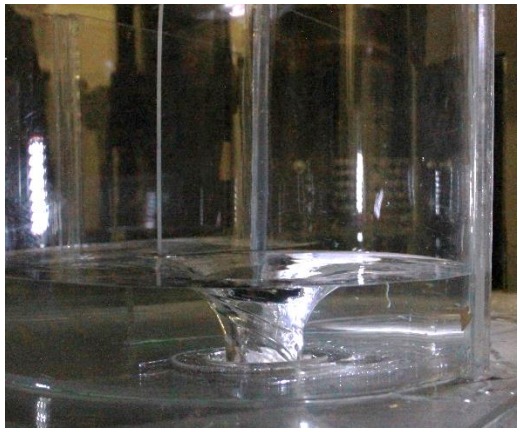

Model #3d1.0d: h/d = 1.0, K = 6.274

Figure 6.1: Images of the free-surface vortex structure for $\boldsymbol{\alpha}$ = 2.688 and $\boldsymbol{\alpha}$ = 1.301 for approach flow depths $\boldsymbol{h/d}$ = 3.0 and $\boldsymbol{h/d}$ = 1.0 respectively.

The radial flow model had the effect of dampening the tangential velocity field through strong radial jets around the periphery of the 0.4 m cylindrical vessel. A small head difference, probably due to accumulated shock losses at the individual perforations, was recorded between the outside and the inside of the vessel for each approach flow depth. The depth-discharge was recorded in the model with and without the vortex suppression vane. For low h/d, a vortex still formed with an air core observable behind each vane arm as presented in Figure 6.3. The suppression vane had no noticeable effect on the depth discharge relationship which will be presented quantitatively in Figure 6.4 (Section 6.2.2).

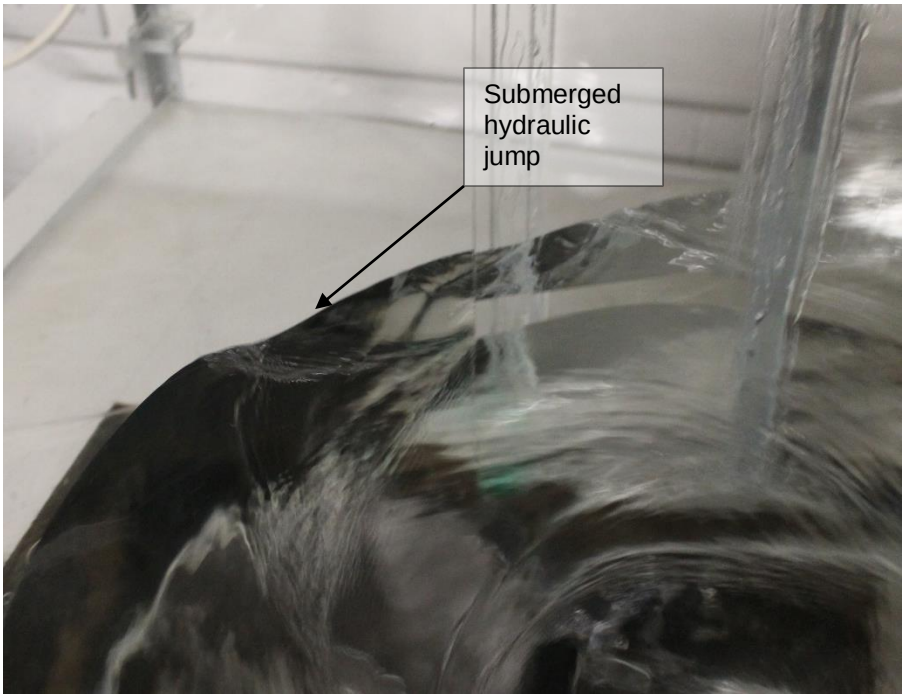

Figure 6.2: Small submerged hydraulic jump forming in model with $\alpha = 6.220$.

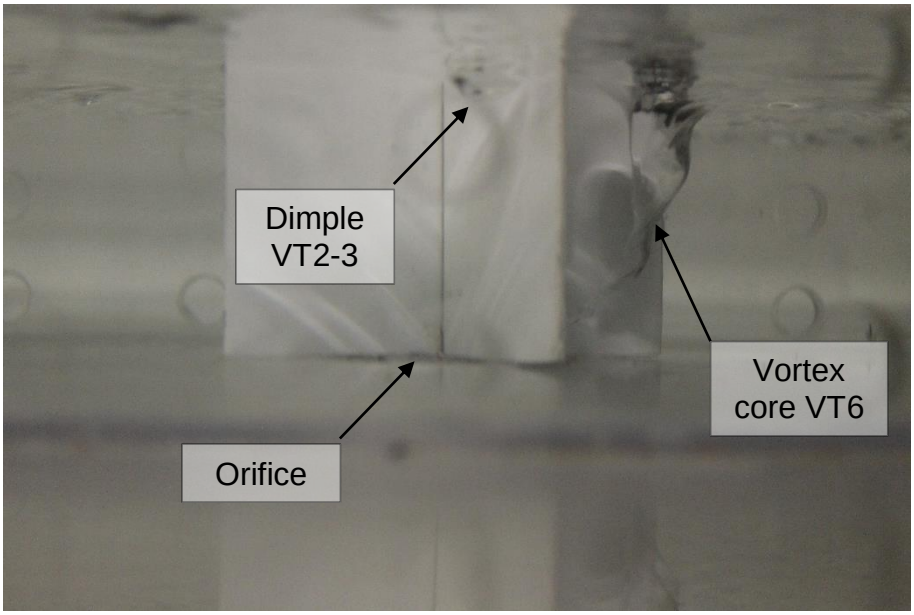

Figure 6.3: Vortex air core forming behind the vortex suppression vane in the radial flow model.

6.2.2. Depth-Discharge Relationship

Figure 6.4 presents the depth-discharge curves for five model vortex chambers including the radial flow model with and without the suppression vane. Only five models are presented here to maintain clarity in the presentation. A graphical presentation with the 12 approach flows is presented in Appendix C. In Figure 6.4 it is shown that the relative slope of each curve increased with the geometric factor α which is a hydraulic consequence of the approach flow circulation (Knauss, 1987). It can be observed that the head varies linearly with discharge for moderate α values ($2.095 < \alpha < 2.688$). When α is large (> 2.688), the depth varies with discharge by $Q \propto h^n$ where $n > 1$. For these conditions, the control section was naturally gradually shifted from the outlet to the inlet channel. When α was small, the exponent n tends to 0.5 and the vortex becomes weak and unstable. This depth-discharge relationship is apparent for the results of the radial model in Figure 6.4. It is also noted that there is virtually no difference in the depth-discharge relationship for the radial flow model with and without the vortex suppressing vane.

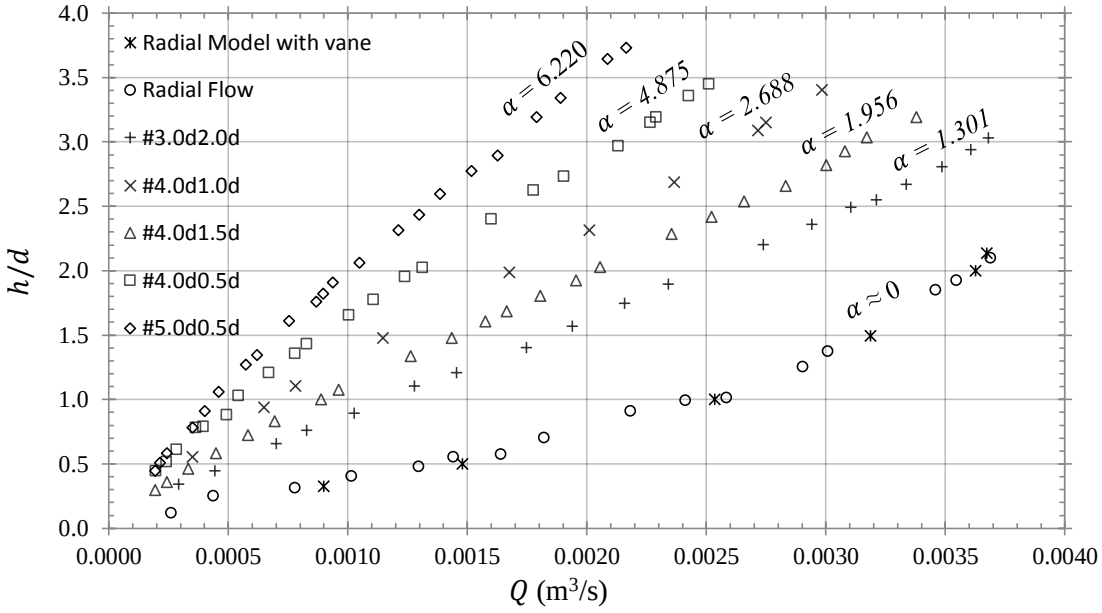

Figure 6.4: Depth-discharge curves for five geometries and the radial flow model.

6.2.3. Depth-Circulation Relationship

The almost linear relationship found between h and Q for moderate values of α in Figure 6.4 suggests that the velocity in the inlet channel and hence, the circulation will not vary significantly for the range of approach flow depths under examination. To verify this property, the bulk circulation, given by:

$$\tilde{\Gamma} = 2\pi r_{in} \frac{Q}{bh} \tag{6.1}$$

is plotted against the approach flow depth h/d in Figure 6.5. Here it was assumed that the depth across the inlet cross-section was constant. For low to medium α values ($1.301 < \alpha < 3.291$) the bulk circulation $\tilde{\Gamma}$ increased with the approach flow depth h/d to become relatively constant value for $h/d > 1.5$ which was similar to that observed by Ackers and Crump (1960). Here the authors (Ackers and Crump, 1960) used the discharge number N_Q instead of h/d. For $\alpha > 3.129$, constancy of the bulk circulation was almost achieved for larger approach flow depths of which could not be fully examined due to restriction of the model height.

For α = 4.875, the bulk circulation appears to reduce after $h/d > 3.0$. This relationship becomes a linear one for α = 6.220 with lower values of circulation achieved. It was suspected that this was primarily a result of the hydraulic jump that occurs for the transitionally subcritical approach flows. The results of the non-dimensional approach flow circulation $\tilde{\Gamma}/\tilde{\Gamma}_{max}$ for geometries in the range of $1.301 < \alpha < 3.129$ was presented in Figure 6.5 and indicates that there exists a characteristic relationship between these two parameters for stably subcritical approach flows. The general decrease in bulk circulation for $h/d < 1.5$ suggested that the radial flow became more dominant which agreed with visual observations made in the laboratory of radial flow patterns under the same approach flow conditions.

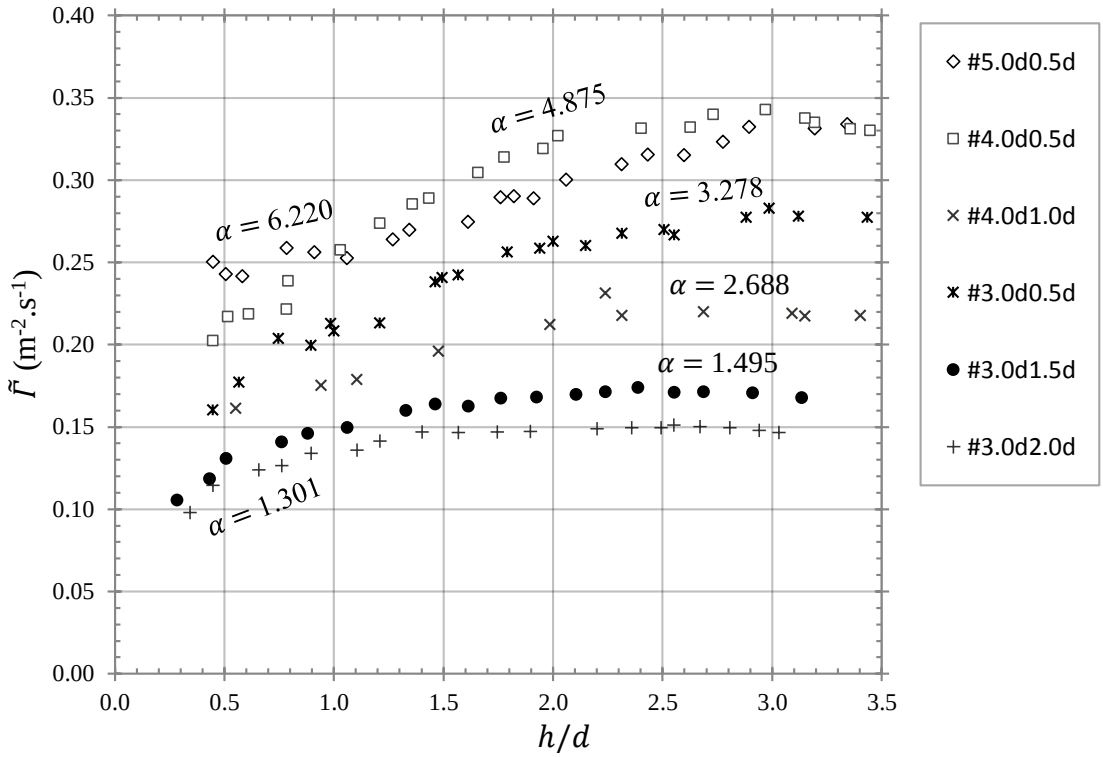

Figure 6.5: Bulk circulation Equation (6.1) versus approach flow depth h/d for six of the models.

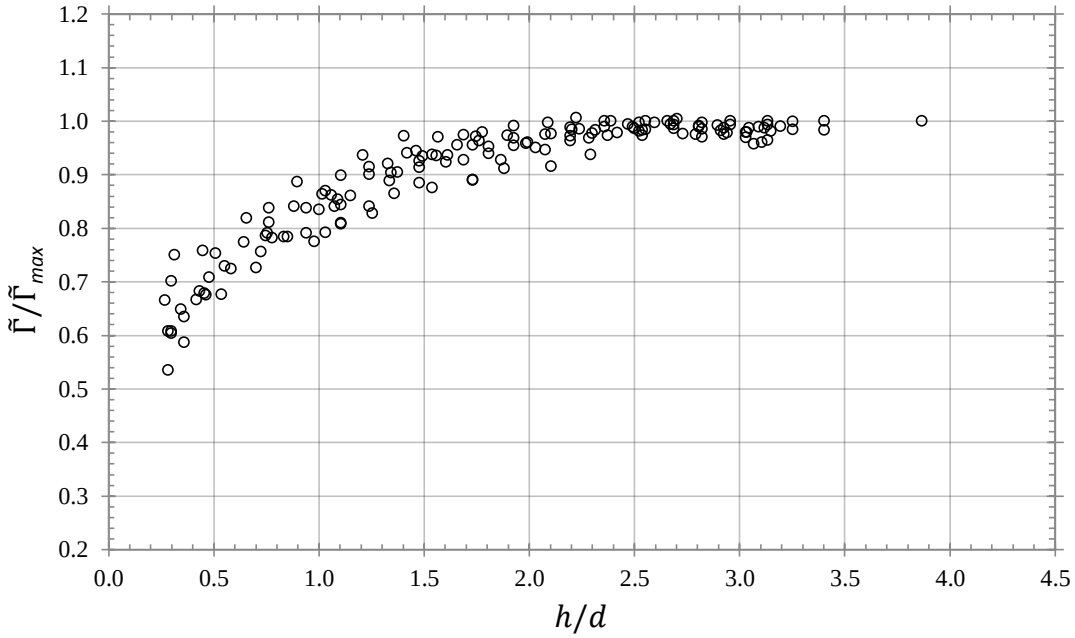

Figure 6.6: Non-dimensional bulk circulation $\tilde{\Gamma}/\tilde{\Gamma}_{max}$ versus the approach flow depth for all model data. The curves indicate the trends of the measurements.

Ackers and Crump (1960) state that the mean velocity across the inlet cross section should approximate closely to the velocity in the inlet channel and hence the field circulation Γ_∞. This assumption was made in other studies where the field circulation is determined by the mean velocity at the inlet (Stevens and Kolf, 1959; Hager 1985; Ciaravino and Ciaravino 2007; Dhakal et al., 2015). The writer deemed it necessary to investigate this by comparing the far-field PTV determination of the field circulation Γ_∞ to the bulk circulation $\tilde{\Gamma}$, the results of which are displayed in Figure 6.6 for five approach flow geometries. In each case the experimental field circulation agreed with the calculated bulk circulation to within a maximum deviation of $\pm$ 9 %. It is therefore reliable to calculate the field circulation of a free-surface vortex on the basis of the mean velocity through the inlet.

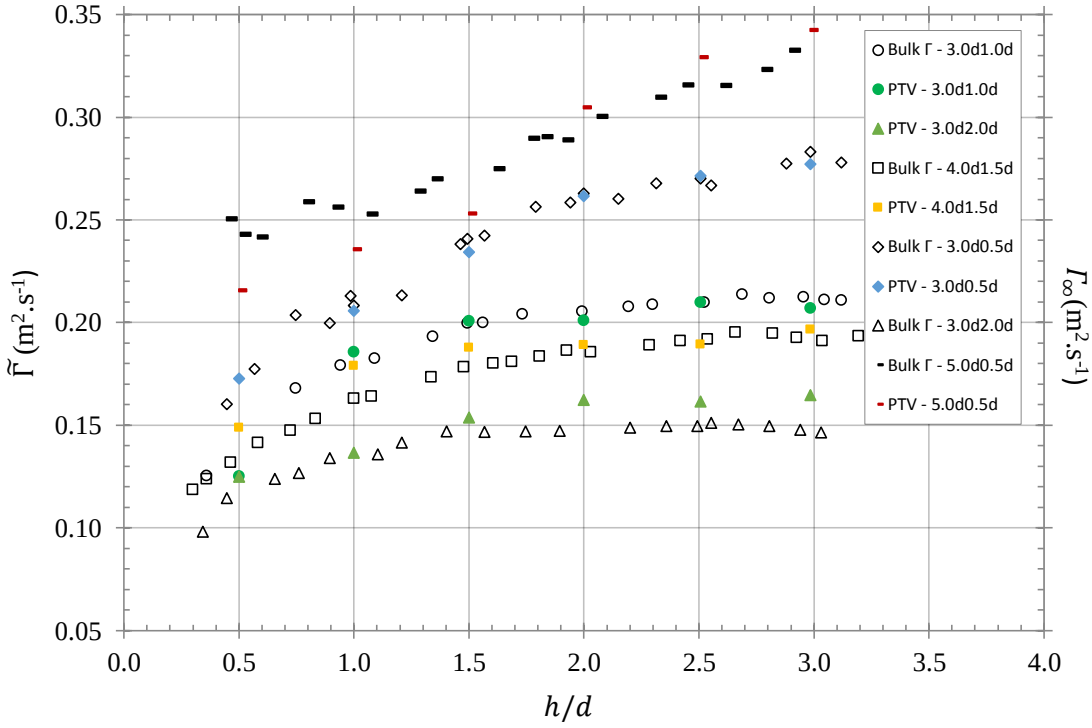

Figure 6.7: Bulk circulation $\tilde{\Gamma}$ versus the approach flow depth for all models compared to the field circulation Γ_∞ obtained in PTV analysis.

6.2.4. Air Core Diameter

The air core diameter is a significant parameter that has been incorporated in many previous analytical and experimental investigations (Ackers and Crump; 1960, Pica, 1970; Viparelli, 1950; Viparelli, 1954; Hager, 1985) and is the contributing factor for the

reduction of discharge (Posey and Hsu, 1950). Figures 6.8 and 6.9 depict the general trend between the air core diameter a_c/d and the approach flow depth h/d. As h/d increases, a_c/d decreases and tends towards $a_c/d = 0$ when $h/d \to h_c$. For low values of α, the relationship was almost linear for the observed values (Figure 6.7). For larger values of α, the relationship was found to be curved as is observed in Figure 6.9.

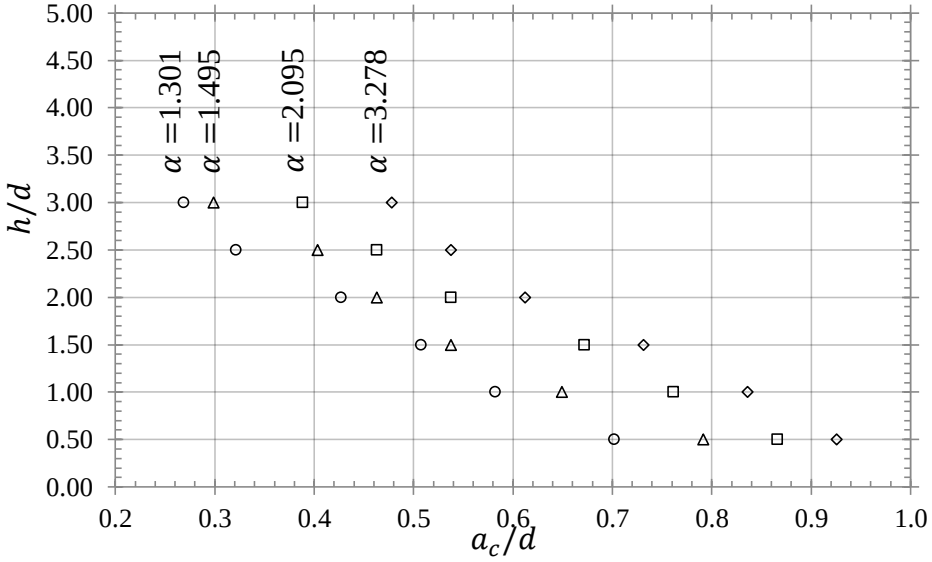

Figure 6.8: Approach flow depth h/d versus air core diameter a_c/d for the $D_{eff} = 3.0d$ model series.

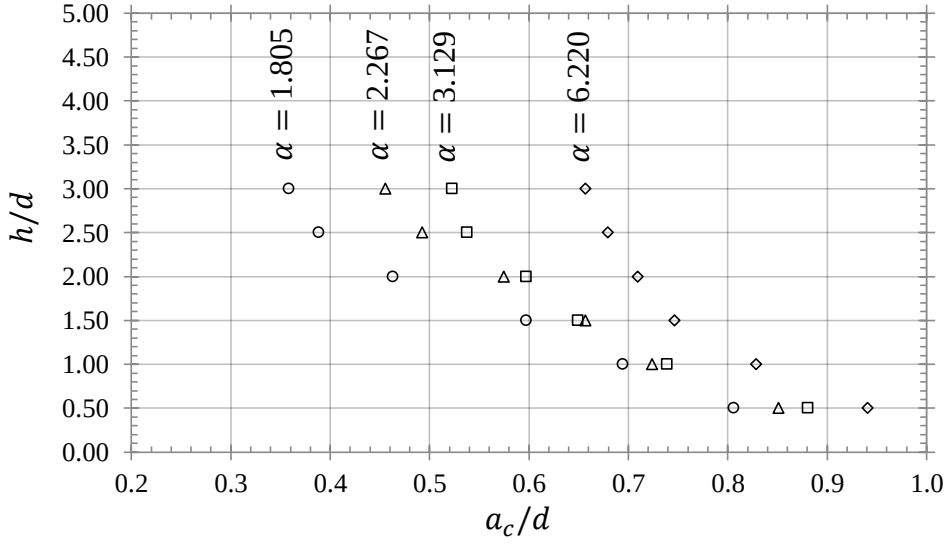

Figure 6.9: Approach flow depth h/d versus air core diameter a_c/d for the $D_{eff} = 5.0d$ model series.

As defined by previous authors (Anwar, 1965; Quick, 1961) the discharge number (or coefficient of discharge in some studies) in a vortex is strongly dependant on the circulation. This can explained through observation of the measured experimental relationship between the Kolf number K and the air core diameter a_c/d in Figure 6.10 on a semi-log plot. Here the trend suggests that the air core diameter increases according to the Kolf number resulting from large near-field tangential velocities. The increase in air core diameter resulted in a smaller annular cross section which restricted the discharge Q.

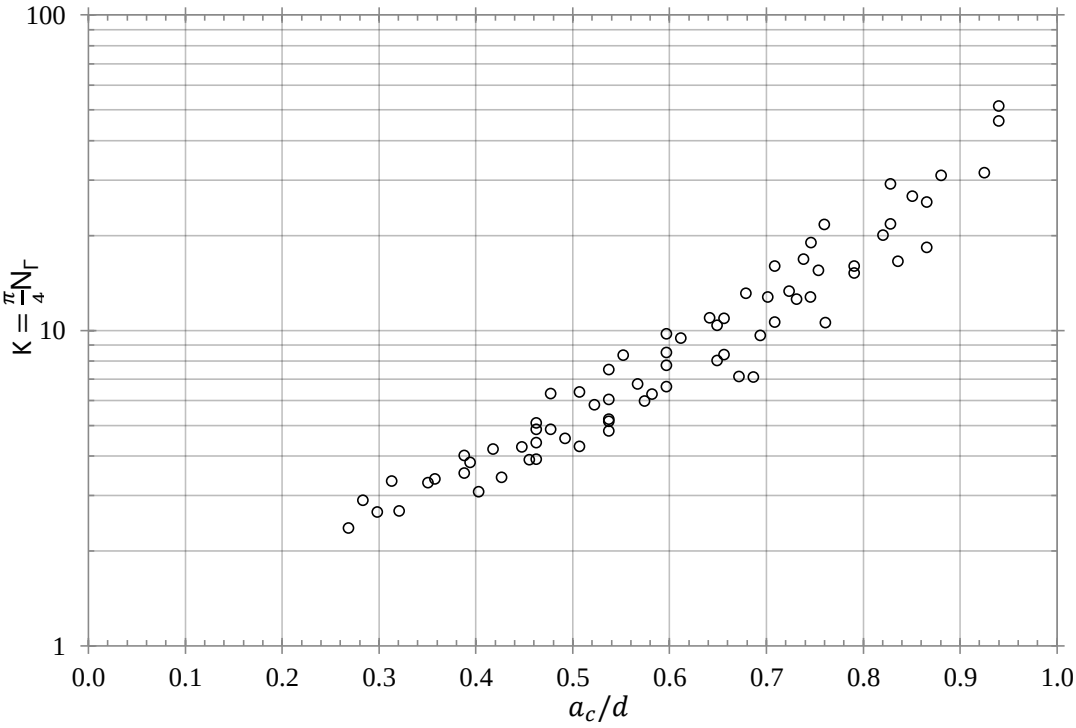

Figure 6.10: Semi-log plot of the Kolf number K versus the air core diameter a_c/d.

The dependence of the discharge on the air core diameter was evident in Equation (2.47), and was included extensively in modelling the coefficient of discharge C_d by Viparelli (1954) in Equation (2.52) through the circulation number $N_{\Gamma/E}$ defined in Equation (2.53). Pica (1970) recommended an empirical relationship as a replacement to Equation 6.2:

$$C_d = 0.95 - a_c/d \tag{6.2}$$

in order to simplify the model. The relationship was reinvestigated using the current data. The relationship between coefficient of discharge C_d for the results of this study are

presented in Figure 6.11 in comparison with Picas (1970) linear relationship Equation (6.2) as well as for plots of $N_{\Gamma/E} = 0$ and $N_{\Gamma/E} = (\ a_c/d\ )^2$. The data appears to correlate well with Picas (1970) data for $a_c/d\ > 0.7$ but diverges for $a_c/d\ < 0.7$ according to the linear relationship:

$$C_d = 0.7 - 0.68 a_c/d \tag{6.3}$$

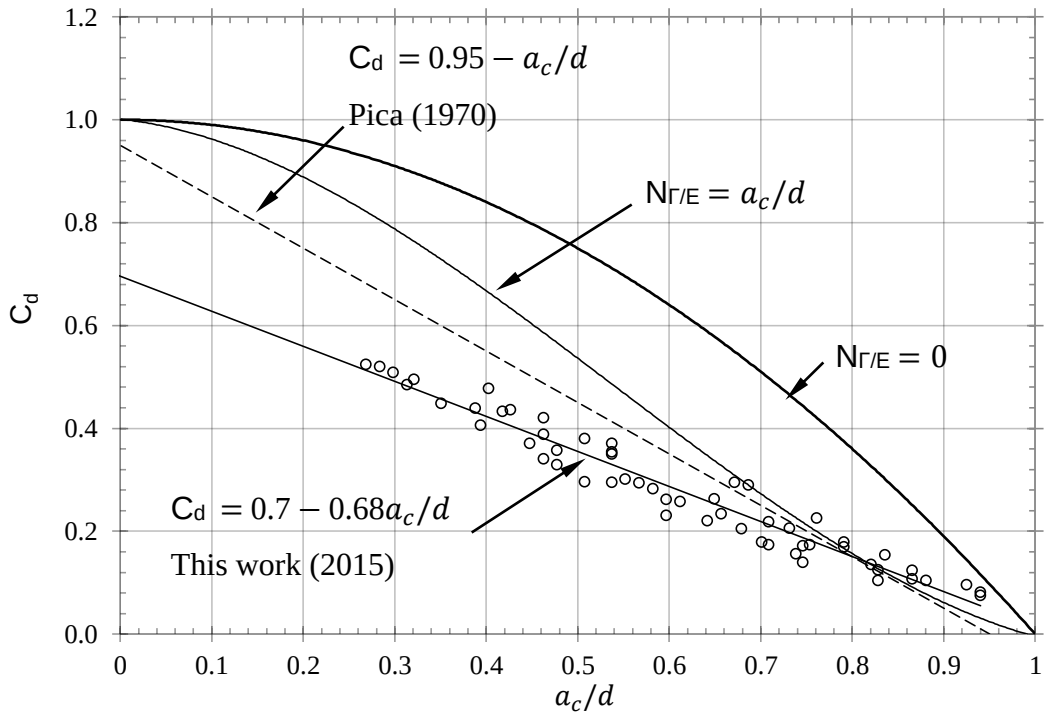

Figure 6.11: Comparison between the current data and Pica's experimental data set for the relationship between the coefficient of discharge C_d and the air core diameter a_c/d.

The observable difference was thought to be due to the fact that the energy E in Pica's (1970) physical models comprises the geometry of the 'lip' on the outlet. In the current study, geometric consideration for a 'lip' which facilitates a greater drop of energy head E at this position is omitted. The lip at the base of structure should have the effect of increasing the coefficient of discharge and thus might explain the discrepancy in the data. However, it may also be possible that scale effects influenced the current data.

6.2.5. Other Trends

If the flow in a full air core vortex is compared to that of a fully submerged orifice free of swirl, the discharge difference ΔQ as a result of free-surface vortex formation is then given by:

$$\Delta Q = \frac{\left(\frac{\pi}{4}\,\mathrm{d}^2\sqrt{2gE} - Q_{vortex}\right)}{\frac{\pi}{4}\,\mathrm{d}^2\sqrt{2gE}} \tag{6.4}$$

This should be intrinsically related to the circulation field Γ_∞. This was investigated for all test data by plotting the discharge difference against the circulation number N_Γ in Figure 6.12. The relationship confirms that as the circulation number increased the discharge difference induced by the vortex increased. The discharge difference ranged from 50 to 90 % of the theoretical discharge. This characteristic described the advantages of using vortex flows for discharge retention/attenuation.

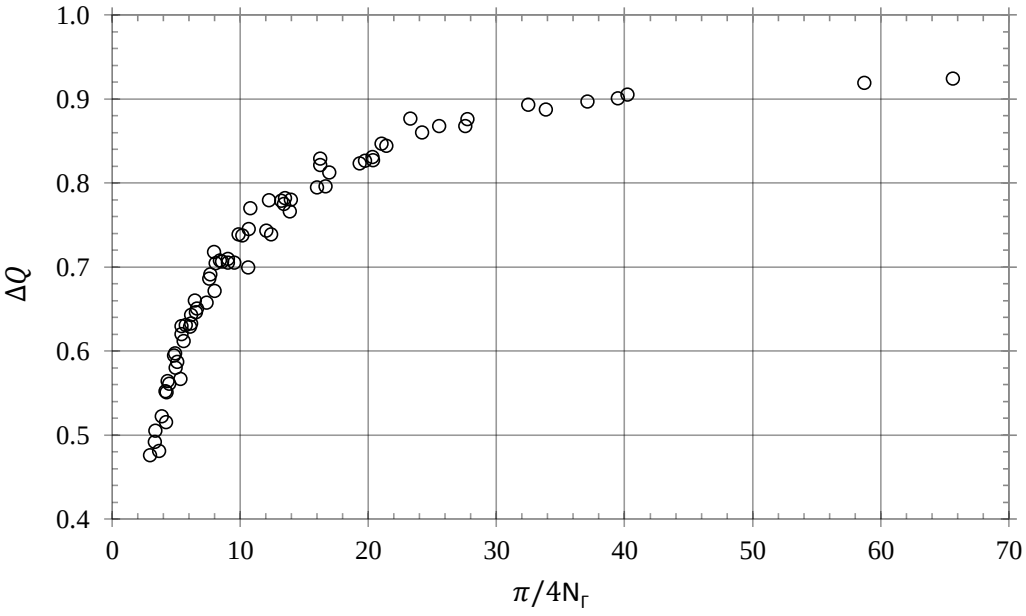

Figure 6.12: Discharge difference as a result of the free-surface vortex ΔQ versus the circulation number $\frac{\pi}{4}\mathrm{N}_\Gamma$ for all experimental data.

Stevens and Kolf (1959) showed that through defining the vortex number N_V by:

$$N_V = \frac{\Gamma}{d\sqrt{2gh}} = \frac{2\pi r\sqrt{2gh_r}}{d\sqrt{2gh}} \tag{6.5}$$

and when $r = d/2$ the relationship becomes:

$$N_V = \frac{\pi\sqrt{h_d}}{\sqrt{h}} \tag{6.6}$$

where h_d is the difference between the water level at the inlet to that at the edge of the orifice. This shows analytically that, when the difference $h_d = h$, i.e. the air core interface resides at the orifice perimeter, the vortex number is limited to π. In their test data (Stevens and Kolf, 1959), the correlation obtained between the coefficient of discharge C_d and N_V supported this by revealing a straight line equation which tends towards $N_V = \pi$ by:

$$C_d = 0.686 - 0.218N_V \tag{6.7}$$

However, Stevens and Kolf's (1959) data only extended to vortex numbers in the region of 2.8. By imposing the limit of $N_V = \pi$ in Equation (6.7), this would imply that negative values for the discharge coefficient are obtainable for $N_V > \pi$ and so according to Knauss (1987) "*there must be a limit to their validity*". In physically realistic terms, an air core diameter a_c approaching or residing on the orifice diameter d would suggest that, for a real viscous fluid, the discharge should tend to zero ($\therefore Q \rightarrow 0$) thus implying that a steady state equilibrium for the approach flow can never be achieved. Thus, h and h_d can never be equal. Therefore, Equation (6.7) proposed by Stevens and Kolf (1959) is to be further developed for values of $N_V > \pi$. In the current study, values for N_V range from 0 to 4.7 and therefore values for $N_V > \pi$ could be further explored. Figure 6.13 shows the relationship between the coefficient of discharge and the vortex number N_V in comparison to the straight line equation of Stevens and Kolf (1959). The experimental data compares reasonably well with empirical relationship of Equation (6.7). The data exhibited a straight line relationship for observed values of vortex number for $1.0 < N_V < 2.75$ similar to that observed by Stevens and Kolf's (1959). After $N_V > 2.75$, the discharge coefficient appeared to become mildly independent of N_V with values found in the region

of $1.0 < C_d < 2.75$. This observation opposes the previous postulation made by Stevens and Kolf (1959). The writer therefore suggest replacing the original linear equation for the discharge coefficient by a piecewise linear relationship given by:

$$C_d = 0.8 - 0.25\ N_V \qquad \text{for } 1.0 < N_V < 2.75 \tag{6.8}$$

and

$$C_d = 0.16 - 0.018\ N_V \qquad \text{for } N_V > 2.75 \tag{6.9}$$

which is a more realistic model for the coefficient of discharge for large values of vortex number N_V. It can further be addressed that the close resemblance between Stevens and Kolf's (1959) data and the experimental data of the current study may suggest that scaling issues are negligible.

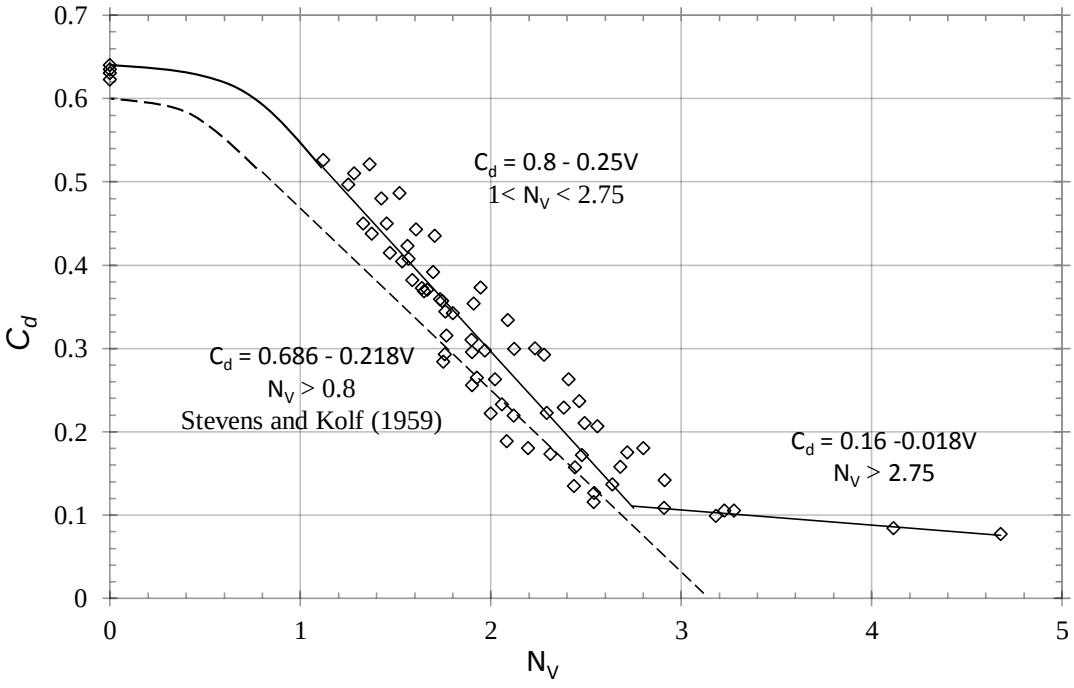

Figure 6.13: Piecewise linear relationship between the coefficient of discharge C_d and the vortex number N_V compared to the relationship proposed by Stevens and Kolf (1959).

6.3. Relationships for Dependant Parameters

6.3.1. Effects of Geometry on Approach Flow Circulation

The absolute field circulation Γ_∞ and the bulk discharge Q were used to determine the circulation number N_Γ which was expressed in terms of the Kolf number K in the present study. The relationship between the Kolf number and approach flow depth was presented in Figure 6.14 for six tested models for equally spread α values (see Appendix B for remaining model relationships). The trends confirm that the circulation number decreased as the approach flow depth increased (when $h \rightarrow h_c$, $v_z \gg v$ and $C_d \rightarrow 1$). Comparable reports were made by previous authors (Posey and Hsu, 1950; Anwar, 1965). Similarly, the circulation decreased with the value of α. When α was large, the variation between the maximum and minimum K values were found to be correspondingly large. By combining α with h/d in the form of $y_\alpha = h/\alpha d$, a new parameter was derived called the non-dimensional approach flow factor which merges both parametric effects. The relationship between the circulation number $\frac{\pi}{4}N_\Gamma$ and this parameter y_α is highlighted in Figure 6.15 where all the model data is unified into a single curve as presented. The curve has the following mathematical relationship:

$$K = \frac{\pi}{4}N_\Gamma = \frac{5.1952}{{y_\alpha}^{0.965}} \cong \frac{5\alpha d}{h} \text{ for } h/d \geq 0.5 \qquad (6.10)$$

Below h/d = 0.5 it was probable that the Kolf number in Figure 6.15 was limited due to friction at the vessel floor and reduces to zero as the depth tends to zero. In this case, radial flow effects at the orifice would begin to predominate. A probable extrapolation for these low values of h/d is also highlighted in Figure 6.15.

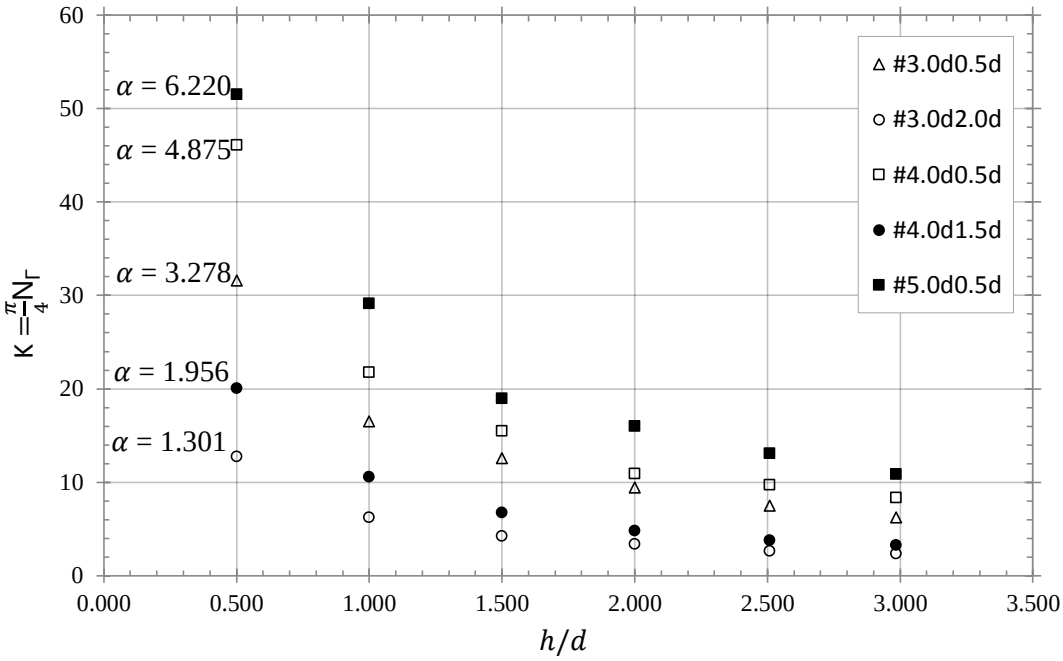

Figure 6.14: Relationship between the Kolf number K and the approach flow depth h/d for six geometries.

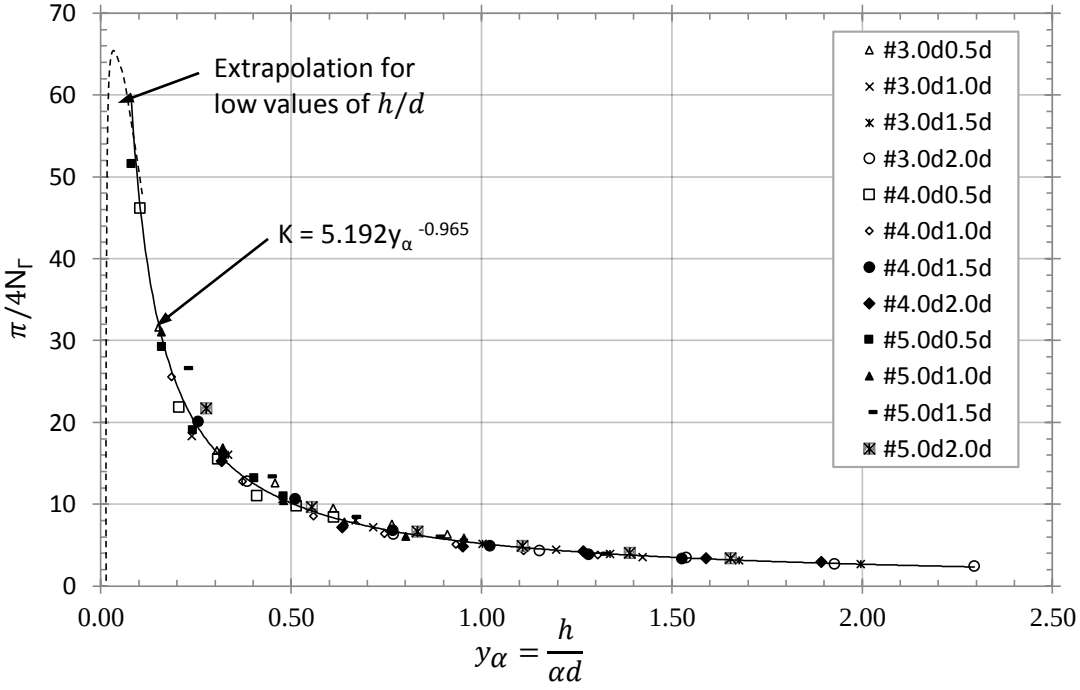

Figure 6.15: Relationship between K and non-dimensional approach flow factor y_α including the line of best fit $K = 5.192 y_\alpha^{-0.965}$.

6.3.2. Effects of Approach Flow Circulation on the Discharge

The discharge number (or coefficient of discharge in some studies) in a vortex is strongly dependant on the circulation (Quick, 1961; Anwar, 1965). This was elucidated through observation of the relationship between the Kolf number K and air core diameter a_c/d in Figure 6.10. In Section 6.3.1 it was further shown that the circulation itself was dependent on the approach flow geometric parameter y_α through a definite relationship. Therefore, Equation (5.9) can be rewritten as:

$$\mathrm{N_Q} = f_5\,(\mathrm{K}) \tag{6.11}$$

where K in this intrinsic relationship can be replaced by:

$$\mathrm{K} = f_6\left(\frac{H_{in}}{d}, \alpha\right) = \frac{5\alpha d}{h} \tag{6.12}$$

which can be directly measured from the hydraulic geometry. The relationship between the discharge number and the circulation number was presented in Figure 6.16. Here only five of the models are displayed with the remaining model results obtainable in Appendix B. For each approach flow geometry, there exists an exclusive correlation between the two variables given by Equation 6.13 where k_α is a coefficient related to the vortex strength and n_α is an exponent describing the slope of the depth-discharge curve.

$$\mathrm{N_Q} = \frac{k_\alpha}{\mathrm{K}^{n_\alpha}} \tag{6.13}$$

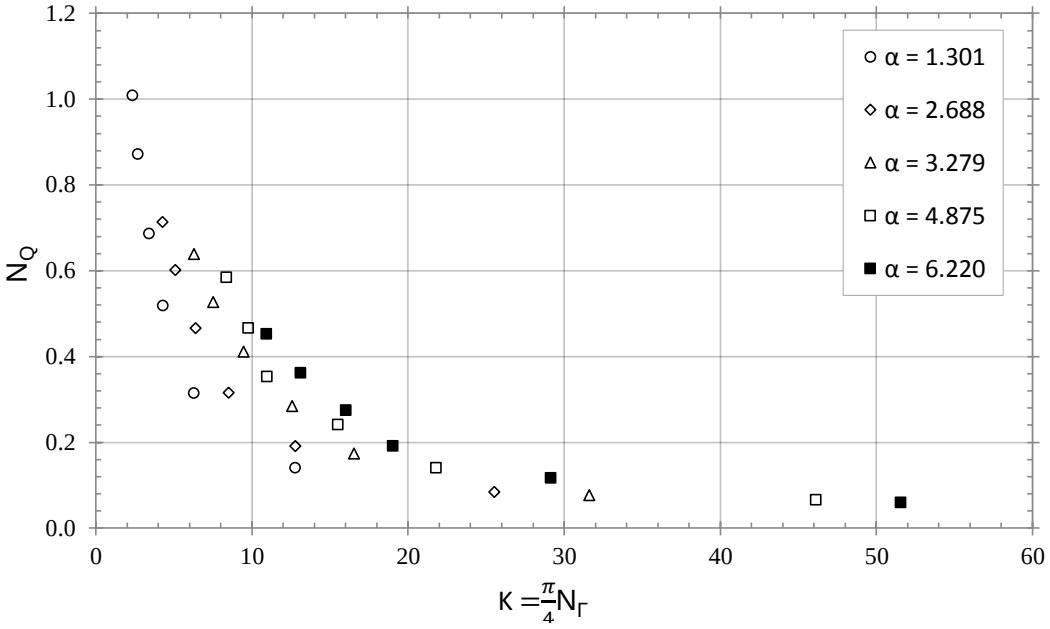

Figure 6.16: Relationship between the discharge number and $K = \frac{\pi}{4} N_\Gamma$ for five geometries.

6.3.3. Empirical Solution for the Depth-Discharge Relationship

Figure 6.16 further displays that the two auxiliary parameters n_α and k_α can be directly correlated to α. Both auxiliary terms reach a peak value and begin to diminish when α exceeds a definite value. The maximum value for each parameter lies in the region of $3.8 < \alpha < 5$. Further analysis for discrete values of α are required in this region to resolve the location of the maximum values of each of the terms. For α (and thus r/b) to increase to limits beyond which the auxiliary parameters diminish the following two environments are likely:

1. The inlet width b becomes excessively small that viscous effects limit the inlet velocity or the velocity increases towards supercritical values resulting in energy dissipation through a hydraulic jump downstream of the inlet.
2. The inlet radius r becomes excessively large that the local tangential velocity in the far-field is dissipated and fails to influence the near-field.

The distribution of the auxiliary parameters n_α and k_α are modelled using third order and second order polynomials which have the following form:

$$k_\alpha = -0.12\alpha^3 + 0.79\alpha^2 - 0.62\alpha + 0.36 \qquad \text{for } 0 < \alpha < 6 \qquad (6.14)$$

$$n_\alpha = 0.05\alpha^2 - 0.39\alpha - 0.55 \qquad \text{for } 0 < \alpha < 6 \qquad (6.15)$$

which are valid for $1.3 > \alpha > 6.22$ (examined in this study) but cover a wide range of geometric arrangements.

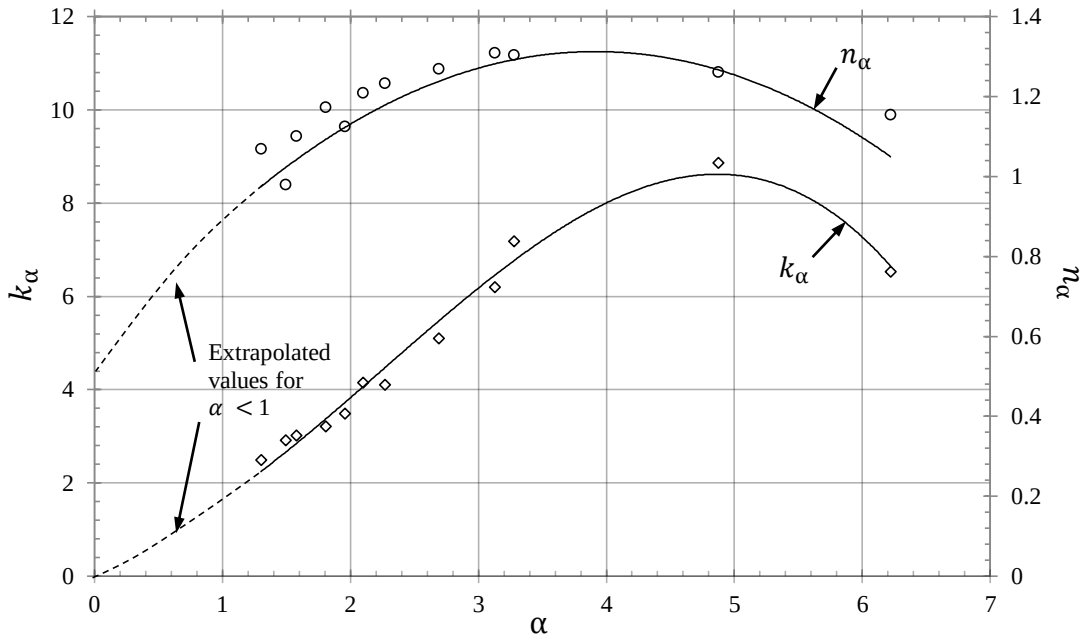

Figure 6.17: Experimentally determined values of k_α and n_α for varying values of α. The curves are empirical fits to the data using Eqs. (6.12) and (6.13). The curves are extrapolated to indicate a possible trend for values of $\alpha < 1$.

It is important to emphasise that the equations (Equation 6.14 and 6.15) are only certain for $0 < \alpha < 6$ after which the polynomial expressions become invalid. The discharge in a strong free-surface vortex can thus be calculated from the approach flow geometry using the following Equation (6.16) in addition to Equations (6.14) and (6.15).

$$Q = \frac{k_\alpha}{\left(\frac{5\alpha d}{h}\right)^{n_\alpha}} \sqrt{g} d^{\frac{5}{2}} \qquad (6.16)$$

It is interesting to note that when $\alpha = 0$, extrapolation of Equations (6.14) and (6.15) in Figure 6.17 indicates that k_α tends to a small non-zero number and $n_\alpha \rightarrow 0.5$. Despite the risks inherent in extrapolations, when these boundary conditions were imposed, Equation (6.16) reduces to that of flow in a free jet discharging through a fully submerged orifice

(Equation 6.17). Further experimental work for values of α in the model between 0 and 1 are required to confirm this hypothesis.

$$Q = Cd\frac{\pi d^2}{4}\sqrt{2gh} \tag{6.17}$$

Equations (6.14) – (6.16) are the complete empirical solution for flow in a free-surface vortex. This formula maintains simplicity over previous analytical models due to its dependency only on the approach flow geometry. Furthermore, it captures the detail of the curvature/linearity of the head discharge relationship. The following solution for the flow in a free-surface vortex is then given by the following procedure which can be adapted for design purposes:

1. $\alpha = r/b$ is calculated based on the approach flow geometry.
2. Using α, the auxiliary terms n_α and k_α can be calculated using Equations (6.14) and (6.15).
3. The design discharge Q for a particular approach flow depth or a range of approach flow depths are computed using Equation (6.16). The discharge can be used to determine if the flow is stably subcritical or transitionally subcritical through the inlet Froude number.

In order to validate this solution, two scaled test cases were examined. The first validation was on the depth-discharge data from a scaled up laboratory model as reported by Ackers and Crump (1960) ($L_p/L_m \approx 2.5$) which has a rounded lip at the entry to the drop shaft (where L_p/L_m is the scale ratio of the prototype to model). The second validation was implemented on data presented by Drioli (1969) on the depth-discharge relationship for the "Impianto di Monte Argento" energy dissipation structure. The orifice diameter of the prototype is 5.5 m thus $L_p/L_m \approx 82$. Data for the depth-discharge was in the form of scaled model results and in-situ prototype measurements by Società Terni. The validation is presented in comparison to the equations proposed by Ackers and Crump (1960), Pica (1970) and Hager (1985). The results of the first validation case (Figure 6.18) confirm that the model agrees reasonably well with the experimental data. A maximum error of approximately 15 % was observable for low discharges. In this region, the flow in the

physical model was controlled by the lip which "*may dominate as a weir*" (Ackers and Crump, 1960) thus causing the increased discharge capacity when compared to the proposed vortex model. In comparison to other models, Pica's (1970) solution appears to give a good prediction of the depth-discharge relationship. However, the drawback of this model was that it failed to directly predict the discharge based on a given approach flow depth, i.e. the solution required trial values for the air core by $f = a_c/d$ to obtain the curve. Furthermore, this process required solving four equations sequentially. Hager's (1985) (B) solution was also creditable for the range observed but again this model was based on solving four equations.

The second validation was presented in Figure 6.19. The proposed model appears to agree well with the experimental and in-situ data (to within a 10% error range) for discharges up to 60 m^3/s before it began to diverge. Contrary to the results observed in the Ackers and Crump (1960) comparison, Pica's (1970) model appeared to agree less favourably with the experimental data. The slope of Pica's (1970) and Ackers and Crump (1960) models regress unexpectedly for the prototype geometry which has a relatively small α =1.1. The proposed model of this work predicted a curve regressing more realistically with the exponent $n < 1$. Therefore it can be said that the proposed model provided a more realistic description of the curvature/linearity of the depth discharge curve as it was derived empirically. To close the discussion, both validations have shown that the proposed depth-discharge model agrees consistently well with the real data to within 15%.

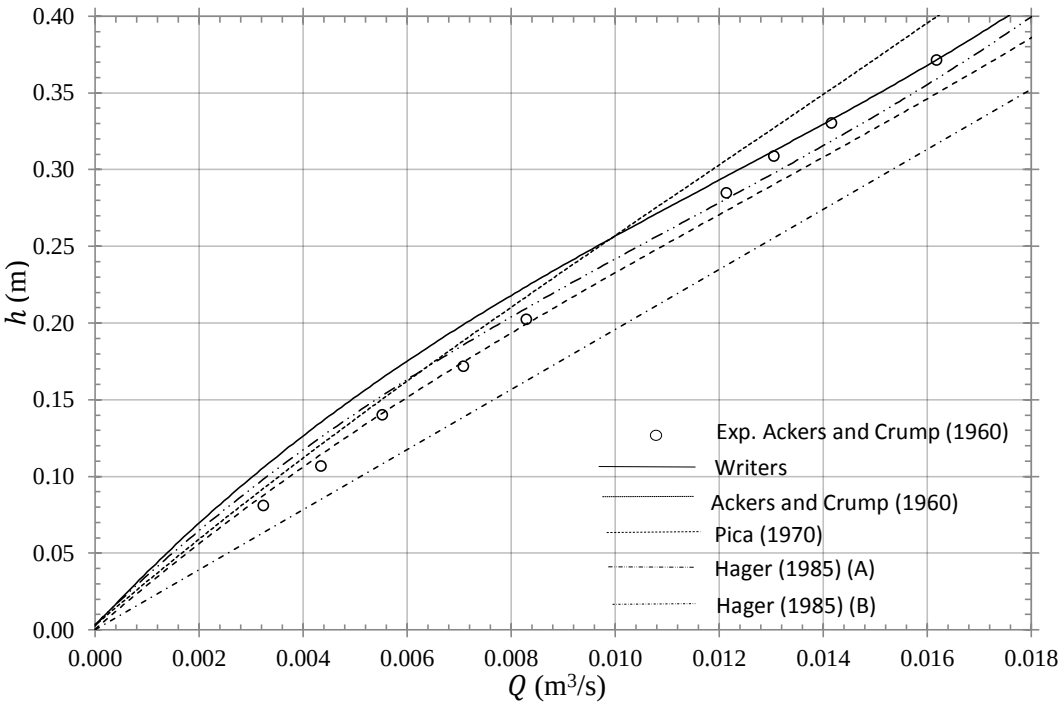

Figure 6.18: Comparison between the experimental results from Ackers and Crump (1960) experimental model, existing analytical models and the newly proposed empirical model (author).

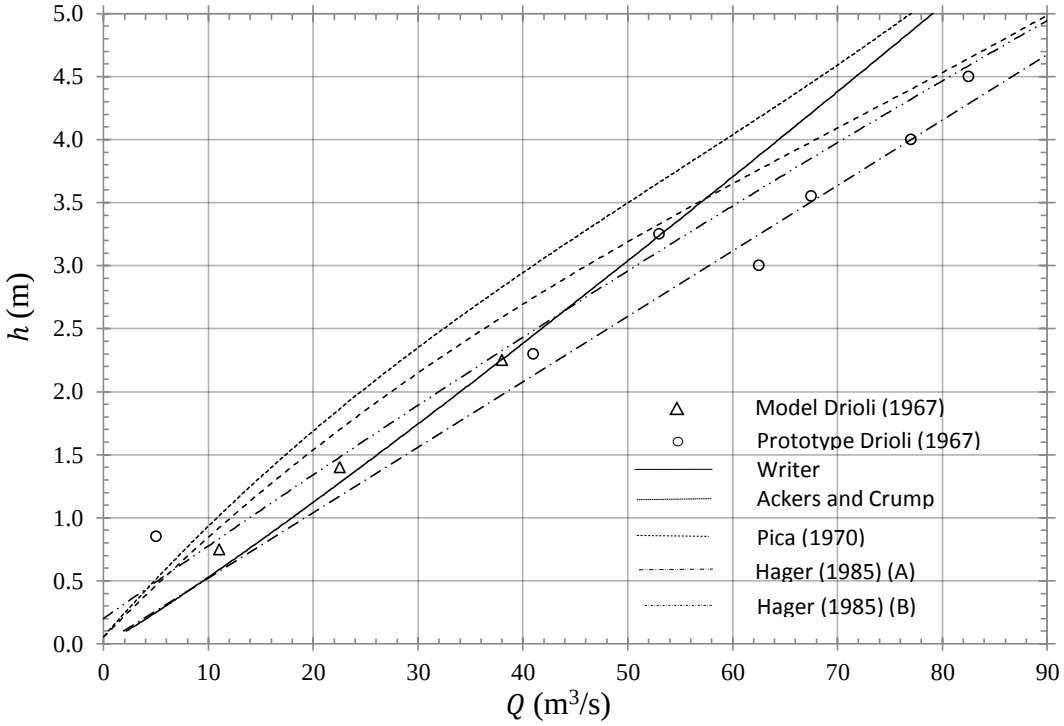

Figure 6.19: Comparison between experimental and prototype results from Drioli (1969), existing analytical models and the newly proposed empirical model (author).

6.3.4. Depth-Discharge Chart

The validation of Equations (6.14) – (6.16) confirmed the practicality of the proposed depth-discharge model as applied to prototypes installations. In order to provide a convenient format for the model, characteristic curves resulting from the equations are presented in chart form in Figure 6.20. The user requires only α and the approach flow depth h/d to achieve a quick estimation of the discharge number and hence the discharge rate for a given vortex chamber. The data for the radial flow model was used to compute the chart depth-discharge relationship for $\alpha \approx 0$ which is represented by the dashed line. Similarly, the curve for theoretical jet flow is also presented. The chart can be divided into four uniquely identified zones of vortex flow. Stably subcritical flows ($Fr_i < 0.7$) (Hager, 2010) refers to low approach flow depths and large α wherein the vortex core remains relatively steady. Unstably subcritical flow occurs when the approach flow depth increases and or the α value becomes relatively small therein causing the vortex core to wobble transiently and/or undergo repetitive collapse and re-formation. The transitionally subcritical ($0.7 < Fr_i < 1$) phase occurs when the flow at the inlet approaches the supercritical values ($Fr_i \rightarrow 1$) resulting in the formation of small standing waves just downstream of the inlet. In the transitional phase, energy is lost in the hydraulic jump which limits the subcritical induced circulation that can be applied at the inlet hence a reduction in n_α and k_α with α. The fully supressed vortex region occurs when rotation in the flow field diminishes and the vortex air core seizes to form. This occurs for values of $\alpha \approx 0$ and for approach flow depths above the critical depth h_c.

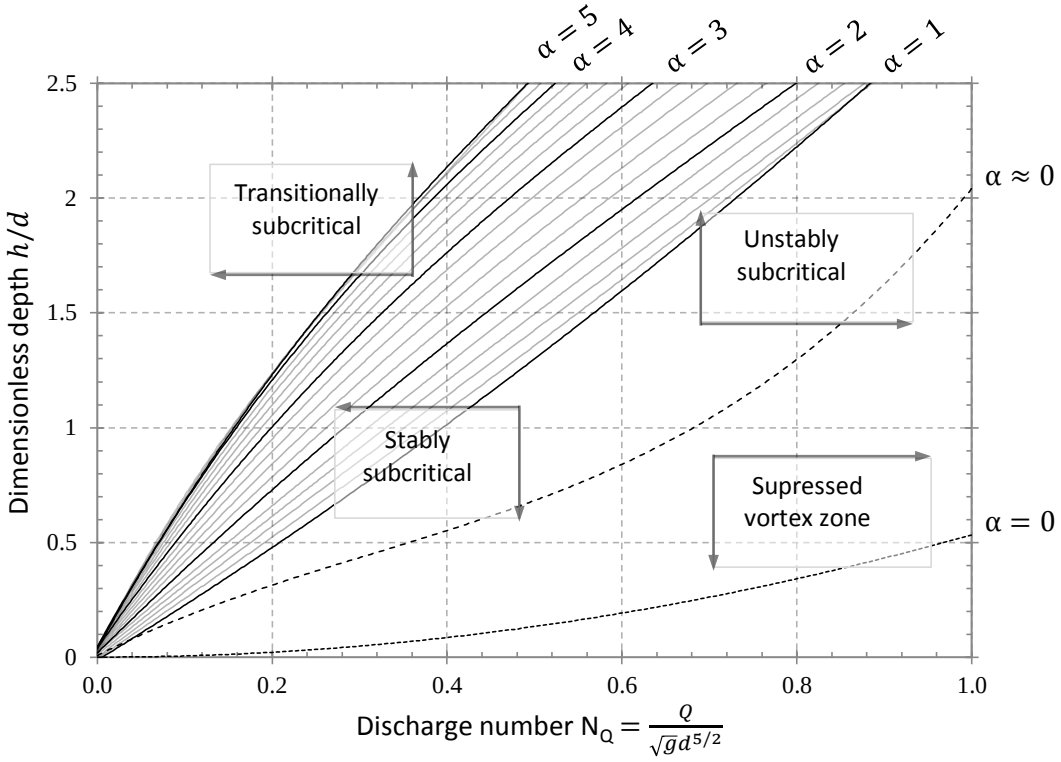

Figure 6.20: Universal depth-discharge chart for strong free-surface vortex flows based on the model proposed in this study (note - zones of flow only highlight their approximate position).

6.4. Velocity Distributions

6.4.1. Tangential Velocity and Circulation

In Section 2.4 and 2.5, analytical models for predicting the tangential velocity in laminar and turbulent free-surface vortices were presented. In a weak vortex, the velocity field resembles a profile similar to that of the classical Rankine vortex model with smoothing of the transition between the rotational and irrotational regions. In a strong vortex, due to the existence of a substantial air core diameter, the tangential velocity was found vary inversely with the radius throughout the full radial field; however, it is limited at the air water interface where the superficial velocity terminates. The real velocity field was found to vary in accordance with the ideal velocity distribution in the far-field but departs from this theoretical solution in the near-field (Quick, 1961). It was hypothesised that this departure resulted from a generation of the eddy viscosity in the turbulent core region which increases the "*apparent viscosity*" of the fluid (Einstein and Li, 1951; Anwar, 1969,

Odgaard, 1986). The tangential velocity profile is revisited in this section to determine if similar discrepancies are observed in the near-field region of a strong vortex.

The tangential velocity field determined from PTV and PSV analysis is presented for each approach flow in Figures 6.21, 6.23 and 6.25. Each figure presents the combined tangential velocity profile for the range of sub-surface depths z/h. There were no variations in the velocity field for each sub-surface depth except at their individual termination points due to contact with the air core interface which differs according to each subsurface h_{PTV} collimation under consideration. From this it was concluded that the tangential velocity was independent of the sub-surface depth in a strong free-surface vortex for subsurface depths away from the tank bottom boundary and free-surface for a distance of at least $z/d > 0.22$. This is consistent with observations made by (Al'tshul and Margolin, 1968; Daggett and Keulegan, 1974). For h/d = 1.0 the distribution of circulation Γ_r (Figure 6.22) was found to be constant throughout the observed field approximating closely to the field Γ_∞ and bulk circulation $\tilde{\Gamma}$. This observation indicated that the flow was fully irrotational (complying with a potential flow discussed in 2.3.1). However, in the larger approach flows, (h/d = 2.0 and 3.5) the circulation field was shown to decrease on approaching the vortex core for values of r/d < 1.0. The reduction was larger for h/d = 3.5 (Figures 6.24 and 6.26).

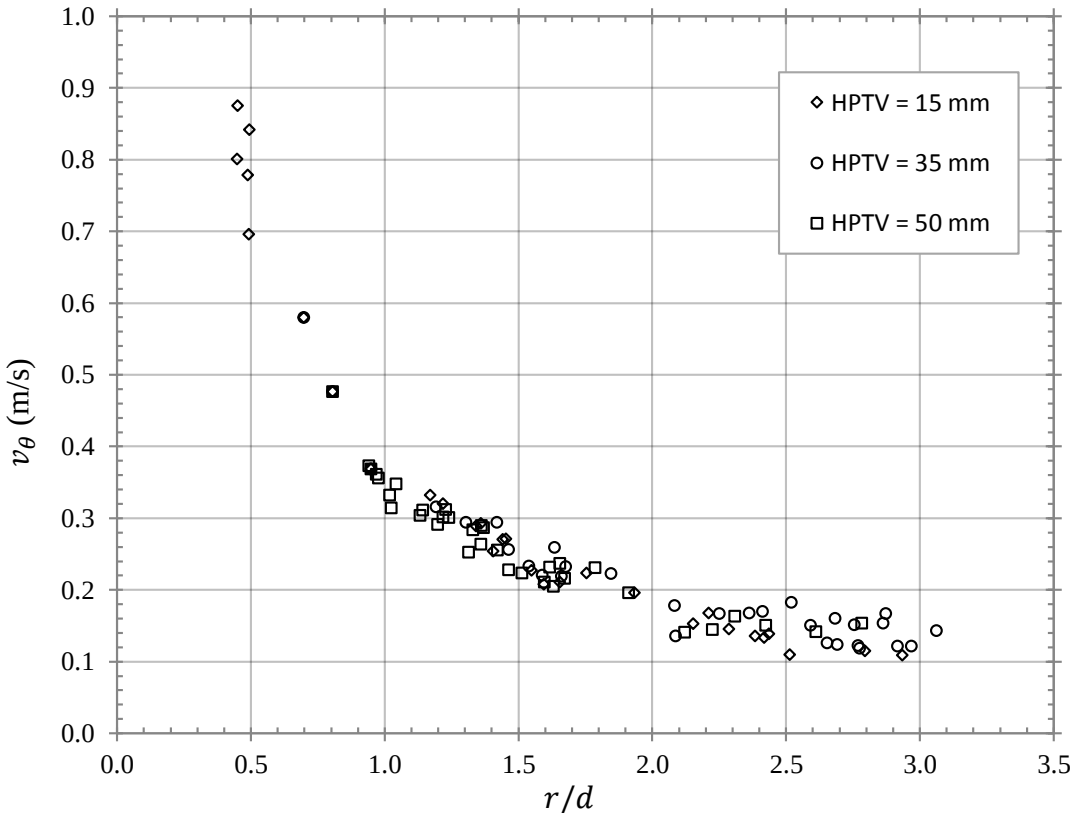

Figure 6.21: Tangential velocity distribution in model #4d1.0d ($\alpha = 2.688$) for $h/d = 1.0$, $\tilde{\Gamma} = 0.178$ m^2/s, Rr = 8162, $N_\Gamma = 12.766$ and $N_Q = 0.1923$.

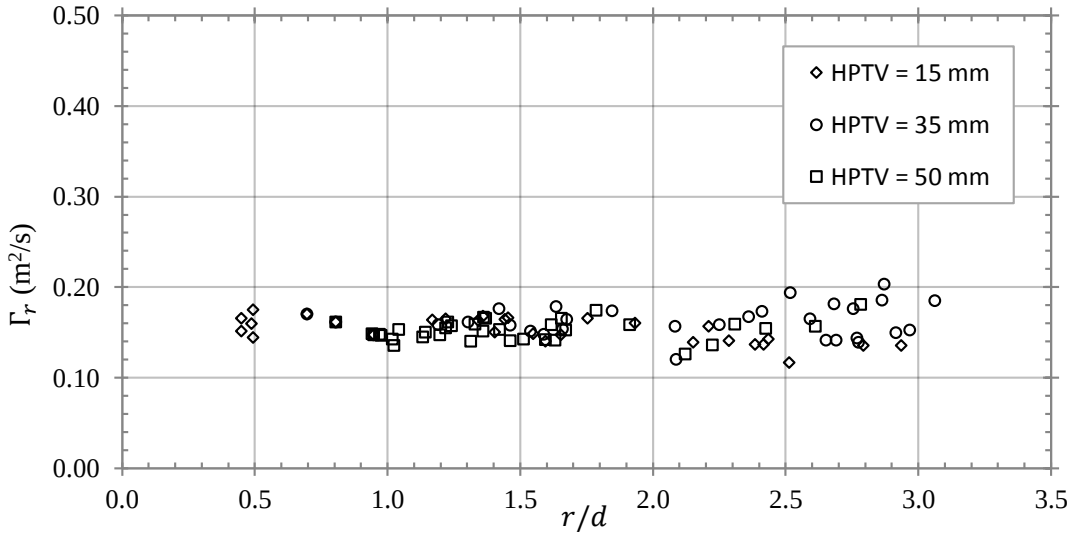

Figure 6.22: Circulation Γ_r distribution in model #4d1.0d ($\alpha = 2.688$) for $h/d = 1.0$, $\tilde{\Gamma} = 0.178$ m^2/s, Rr = 8162, $N_\Gamma = 12.766$ and $N_Q = 0.1923$.

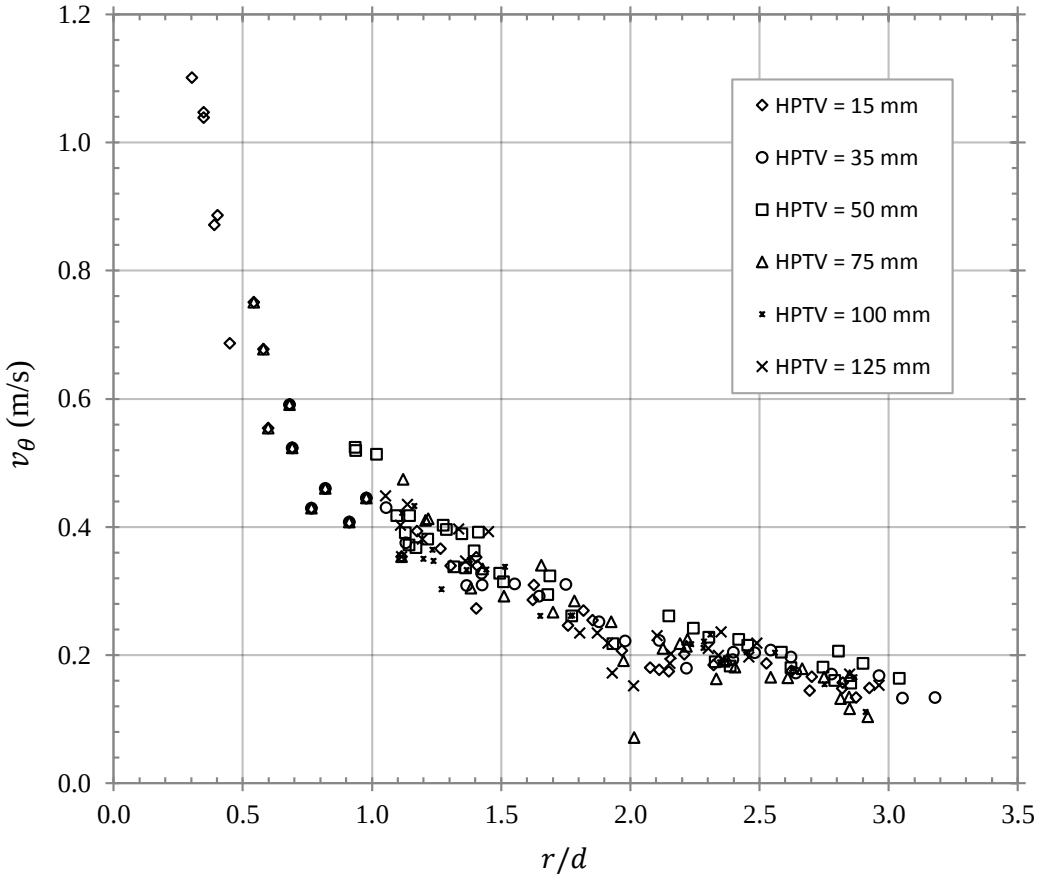

Figure 6.23: Tangential velocity distribution in model #4d1.0d ($\alpha = 2.688$) for $h/d = 2.0$, $\tilde{\Gamma} = 0.214$ m^2/s, Rr = 9911, N$_\Gamma$ = 6.383 and N$_Q$ = 0.467.

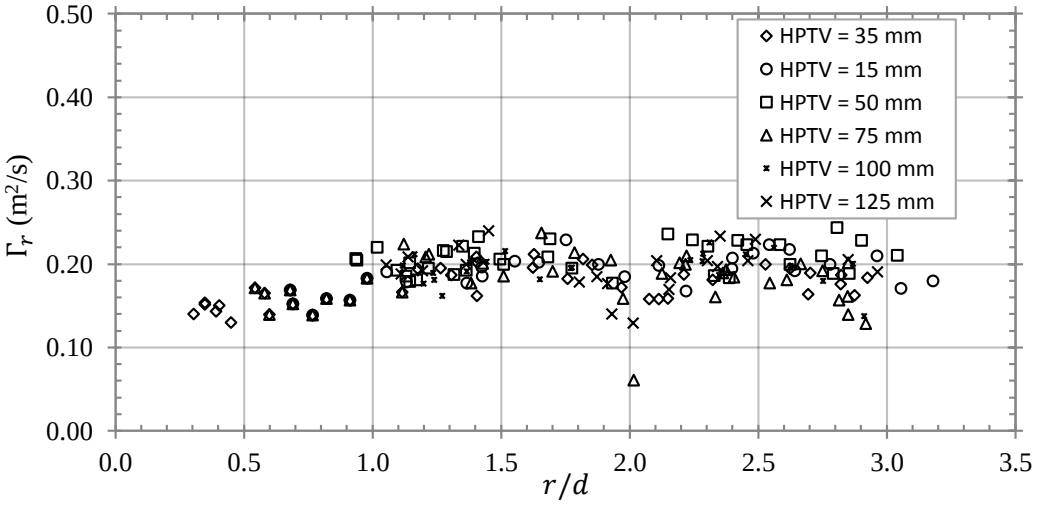

Figure 6.24: Circulation Γ_r distribution in model #4d1.0d ($\alpha = 2.688$) for $h/d = 2.0$, $\tilde{\Gamma} = 0.214$ m^2/s, Rr = 9911, N$_\Gamma$ = 6.383 and N$_Q$ = 0.467.

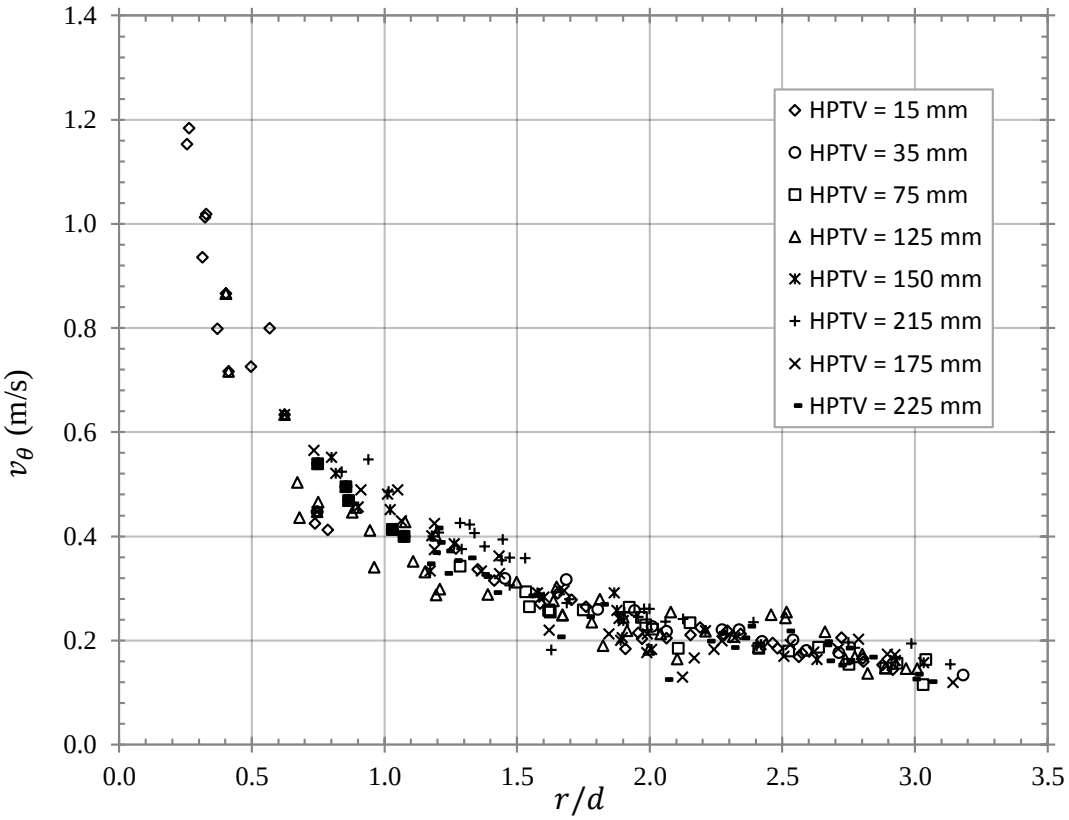

Figure 6.25: Tangential velocity distribution in model #4d1.0d ($\alpha = 2.688$) for $h/d = 3.5$, $\tilde{\Gamma} = 0.220$ m^2/s, Rr = 10305, Nr = 3.7261 and $N_Q = 0.852$.

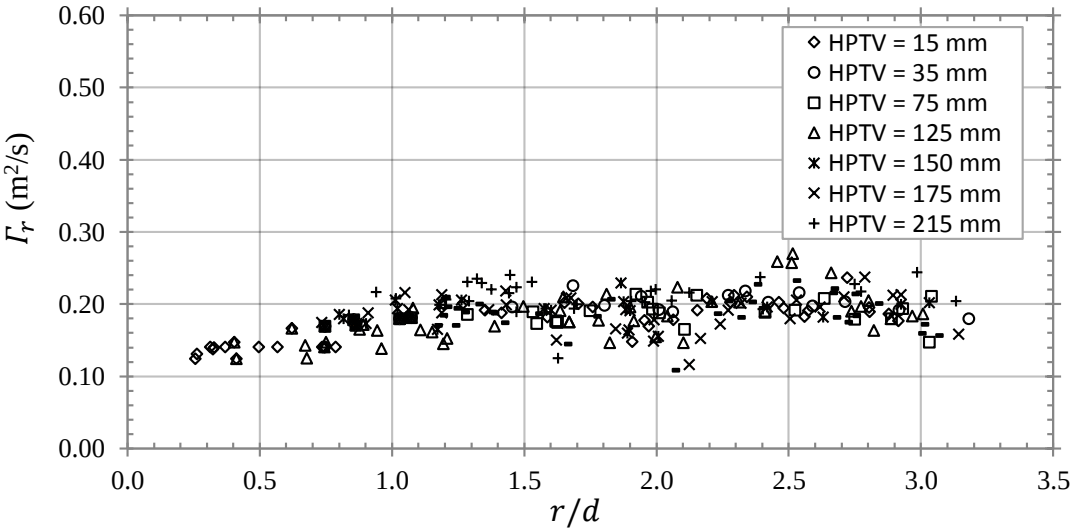

Figure 6.26: Circulation Γ_r distribution in model #4d1.0d ($\alpha = 2.688$) for $h/d = 3.5$, $\tilde{\Gamma} = 0.220$ m^2/s, Rr = 10305, Nr = 3.7261 and $N_Q = 0.852$.

Unlike in the $h/d = 1.0$ case, the reduction in the circulation field Γ_r close to the vortex core for $h/d = 2.0$ for $h/d = 3.5$ indicated that differences are to be expected when the data is compared to the ideal irrotational flow model. The results of the tangential velocity data complying to a subsurface depth residing at $h_{PTV} = 15$ mm in each approach flow is presented in Figure 6.27 together with the ideal velocity distribution. The ideal velocity was in good agreement with the experimental data for $h/d = 1.0$. However, for $h/d = 2.0$ and 3.5 the expected discrepancy was observed in each case and was similar in nature to the observations made by Anwar (1965), Quick (1961) and Rohan (1965) (as cited in Knauss (1987)). It can therefore be said that the ideal tangential and free-surface profiles agree well with the experimental data in the far- to mid-field for $1 \leq r/d \leq 3$. For $r/d \leq 1$, the ideal analytical solution, derived from the quasi-cylindrical approach (Equation 2.15), began to diverge from the experimental data. This divergence was observed to worsen with the approach flow depth with little discrepancy recognised for $h/d = 1.0$. A distinct departure was recognised for values of $r/d < 1$.

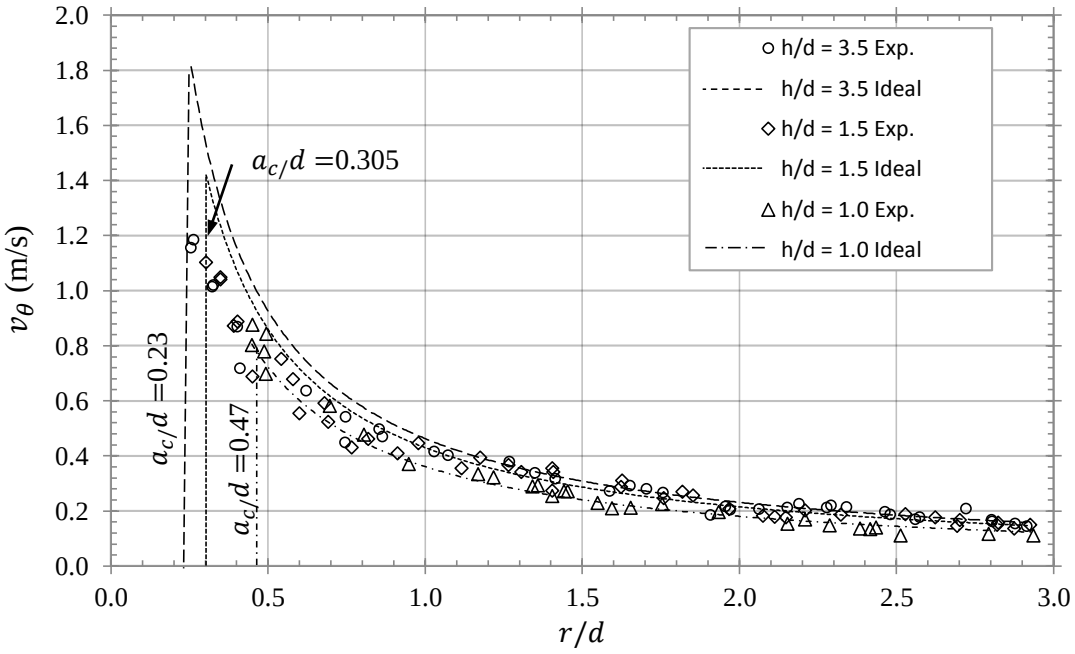

Figure 6.27: Tangential velocity distribution in model #4d1.0d ($\alpha = 2.688$) for $h/d = 3.5d$, 1.5d and 1.0d at an arbitrary sub-surface depth compared to that of their ideal tangential velocity prediction.

Figure 6.28 presents a detailed comparison for the h/d = 3.5 test case with the inclusion of error bars representing potential and worst case uncertainty. From this, it was apparent that no error bars extended across the analytical solution which therefore suggests that the ideal irrotational model was certainly inconsistent with the experimental data in the near-field region.

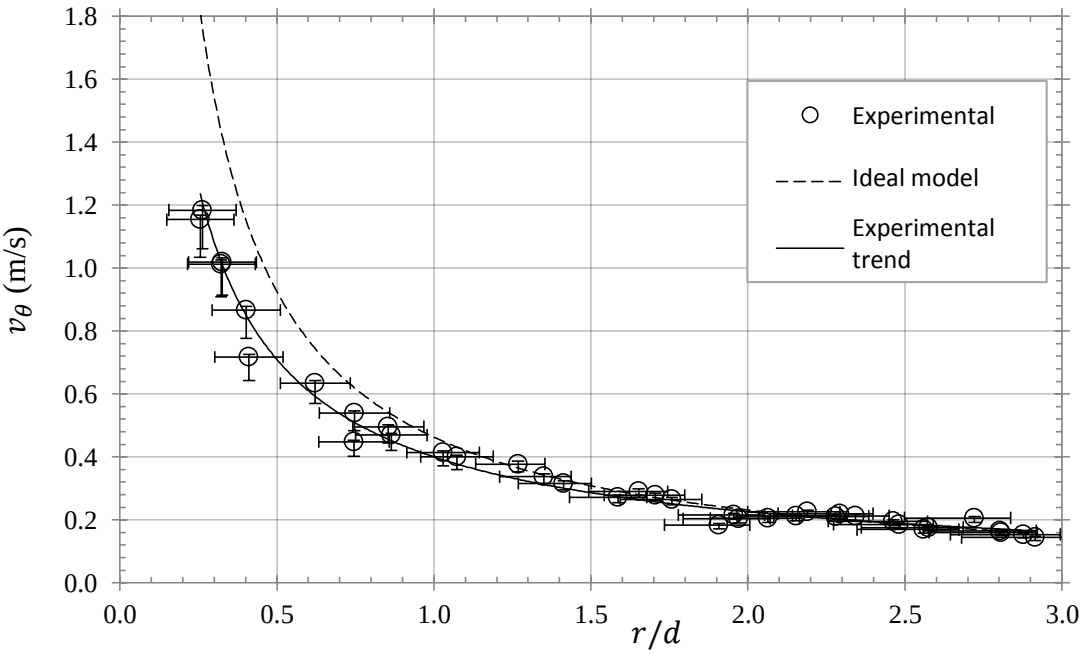

Figure 6.28: Tangential velocity distribution in model #4d1.0d (α = 2.688) for h/d = 3.5, $\tilde{\Gamma}$ = 0.220 m^2/s, Rr = 10305, Nr = 3.7261 and N_Q = 0.852 at h_{PTV} = 15 mm including the maximum potential uncertainty of measurements.

In order to better model the near-field tangential velocity distribution, the viscous analytical vortex models of Rosenhead (1930) (better known as the Scully (1975) vortex model) and Vatistas et al. (1991) were investigated. Here the air core radius $a_c/2$ was treated as the viscous core radius r_c in Equations (2.24) and (2.25). This was to ensure that there was no decrease in the tangential velocity field in the air core region as to appropriately replicate the real data. In addition, the turbulent vortex model of Rott (1958) and Odgaard (1986) was inspected by modelling the core region with an effective viscosity ν_ε using Equation (2.27). The effective viscosity comprised of the modelled eddy viscosity ε plus the constant fluid viscosity ν.

The results of the three analytical models compared to that of the experimental data of approach flow h/d = 3.5 is displayed in Figure 6.29. The Vatistas $n = 2$ model offered very little improvement apart from limiting the near-field velocity profile. Errors in this model were found to be in the region of 39 %. The Scully vortex model improved the solution significantly obtaining a maximum overestimation error of 14.5%. The problem with the former models was that they assume a viscous core exists in the near-field which is probably not a valid assumption for a full air core vortex. Thus, the value for the viscous core radius r_c must be guessed in advance which can be problematic. Here the guess that the viscous core resides at the air core radius was reasonable as this is the position that should experience the maximum tangential velocity $v_{\theta max}$. The results of the turbulent vortex model appeared to agree reasonably with the experimental data in Figure 6.29; however, the turbulent eddy viscosity had to be determined by providing the best fit of Equation (2.27) to the experimental data. Discrepancies of 23% were observed in the near-field and the model failed to predict the location of the maximum tangential velocity. The eddy viscosity for each approach flow depth is displayed in Table 6.2 and were found to be of the order of 10^{-5} which is consistent with that reported by Odgaard (1986).

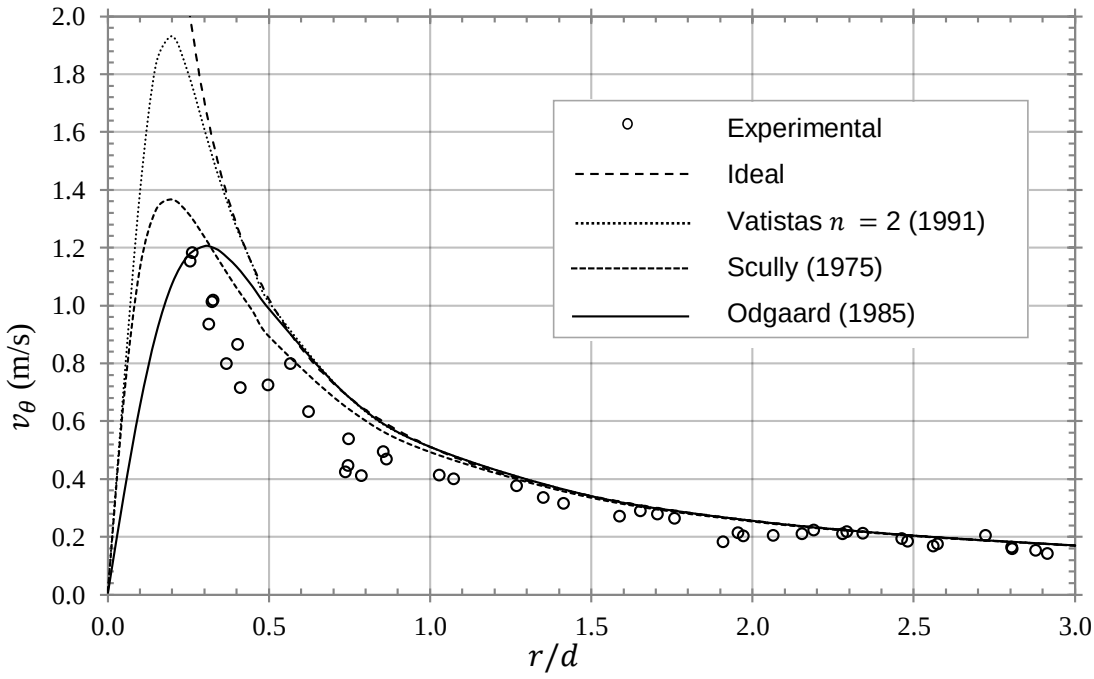

Figure 6.29: Comparison of analytical models for the prediction of the tangential velocity field in a strong full air core vortex. $h/d = 3.5$, $\tilde{\Gamma} = 0.220$ m²/s, Rr = 10305, $N_\Gamma = 3.7261$ and $N_Q = 0.852$ at h_{PTV} = 15 mm.

Table 6.2 Summary of the modelled eddy viscosity ε values in each approach flow

Approach Flow (h/d)	Kolf Number	Eddy Viscosity ε	Viscous Core radius r_c/d	Air core Radius $a_c/2d$
1.0	13.35	6.0 x 10^{-5}	0.33	0.37
2.0	6.62	1.7 x 10^{-5}	0.35	0.25
3.5	3.73	0.5 x 10^{-5}	0.26	0.19

In conclusion, the ideal tangential velocity profile can be employed accurately for $r/d > 1$. Analytical models (Rankine, 1872; Rosenhead, 1930; Vatistas et al., 1991) are available to limit the singular behaviour associated with the ideal vortex model for near-field analysis $r/d < 1$. However, the problem with these models is that they assume a viscous or turbulent vortex core exists in the near-field which is not a valid assumption for a full air core vortex. Thus, the value for r_c or turbulent eddy viscosity ε must be guessed in advance which can be problematic. In a strong vortex with a wide air core, the tangential field increases inversely with the radius everywhere. Therefore, the postulation for the existence of a viscous or turbulent core radius is not valid unless it is assumed to lie at the air core radius. The results of the currently available analytical solutions in Figure 6.29 highlight the necessity for a revised velocity model to be applied in strong vortex flows and will be addressed in an alternative method in a later section (Section 6.6).

6.4.2. Water Surface Profile

The water surface profiles were obtained for each approach flow depth, using the prescribed experimental technique of Section 5.9.2, and were compared to the ideal analytical water surface profile presented in Equation (2.18). Figure 6.30 depicts the comparison between theoretical and experimental free-surfaces for each approach flow depth h/d. The expected disagreement at the vortex core was apparent and was not surprising as this model was mathematically coupled to the ideal tangential velocity profile (as derived in Section 2.3.4). A significant departure was again recognised for $h/d = 1$. The error bars for the water surface profile results were presented in Figure 6.31. All the error bars extend across the ideal water surface profile thus suggesting that

error entrained during measurement may have being large enough to deviate from the ideal model. However, owing to the discrepancies observed in Section 6.4.1 for the tangential velocity profile, in addition to the right hand side positioned bias of experimental free-surface data, it was concluded that this was probably as a result of a defect in the ideal free-surface model. Additionally, errors of the same nature in predicting the free-surface profile have been presented by Quick (1961) and Anwar (1965) – *"The free surface of a strong vortex is thus shown to be hyperbolic up to the point B, but closer to the axis the actual surface departs significantly from the hyperbolic form"* (Anwar, 1965) where B was a definition of the radial point of local departure between the ideal model and the experimental data.

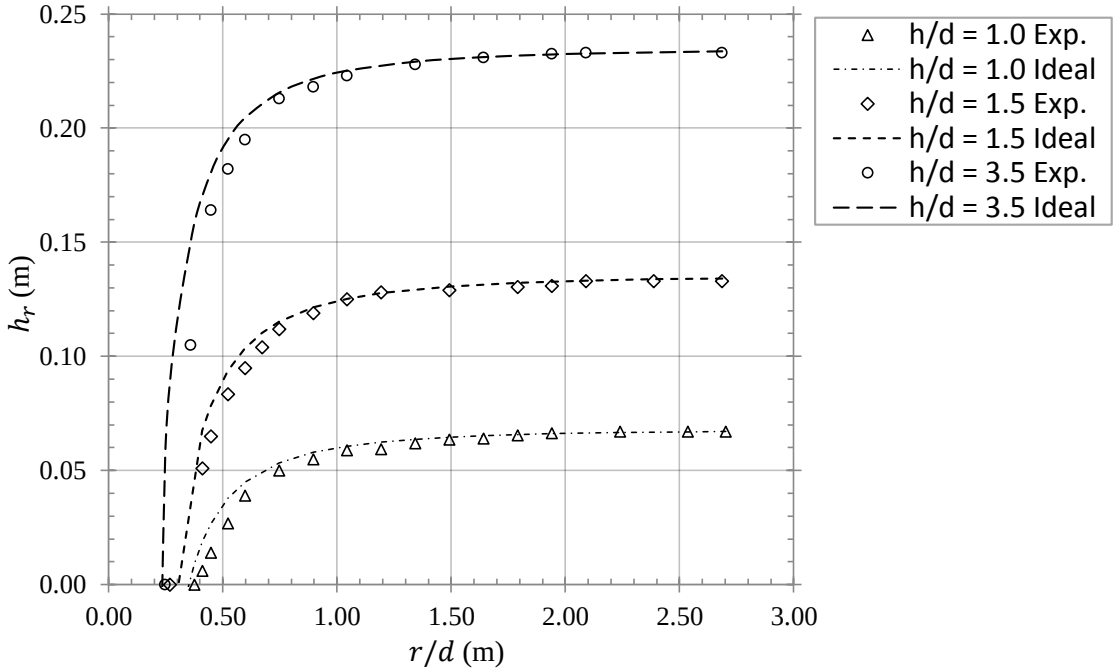

Figure 6.30: Comparison of the ideal and experimental data for the free-surface profile h_r in each approach flow.

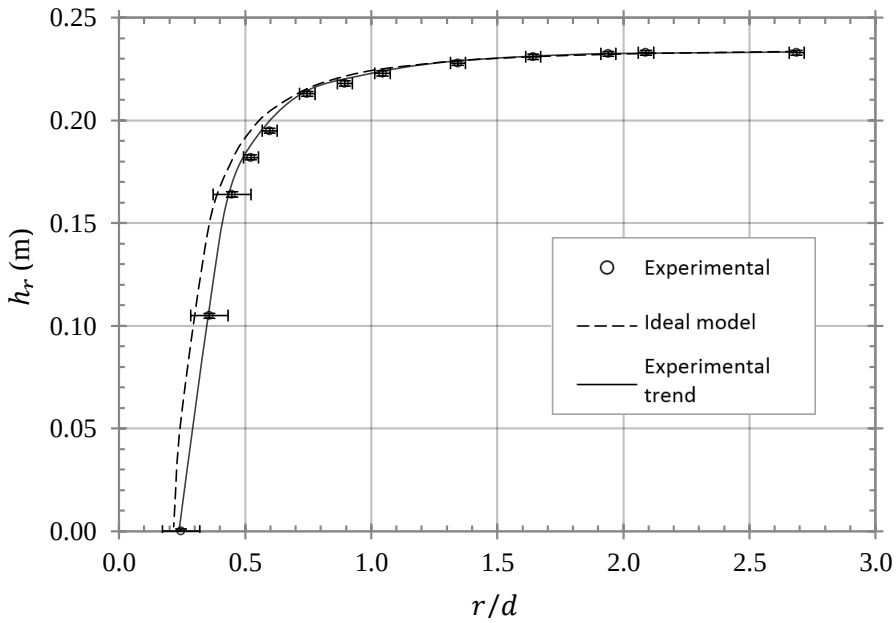

Figure 6.31: Comparison between the experimental data and the ideal free-surface model for $h/d = 3.5$ including the maximum potential uncertainty of measurements $h/d = 3.5$, $\tilde{\Gamma} = 0.220$ m^2/s, Rr = 10305, $N_\Gamma = 3.7261$ and $N_Q = 0.852$.

6.4.3. Radial Velocity Profiles

For the range of sub-surface depths investigated using the planar PTV technique it was difficult to recognise a definite trend in the radial velocity distribution. Displacements were found to be immeasurable or arbitrarily small in comparison to the local tangential velocity field away from the tank boundaries. Both negative and positive radial velocities were also observed. An example of the radial distribution is presented for $h/d = 3.5$ in Figure 6.32. Although the spread of data was extensive, there was however a noticeable increase in the radial velocity v_r as the core of the vortex was approached. In particular, the maximum radial velocity field was observed for $z/h = 0.96$ which was also reported by Dagget and Keulegen (1974). In their work the authors (Dagget and Keulegen, 1974) recognised that continuity is ensured through the formation of a radial jet or band close to the water surface and vessel floor. For the lowest sub-surface depth examined ($z/h = 0.064$) there was no apparent increase in the radial velocity profile to highlight the concentration of the velocity component at the floor.

It may be required that the examination plane be located closer to the base of the vessel. Furthermore, the available PTV configuration did not permit observation of the radial

velocities close to the air core due to obstruction of view. Comments on the existence of this radial band will be discussed in the laser-induced fluorescence experiments in Section 6.5.2. To explain the scattered distribution of the radial velocity field it was hypothesised that the radial component of the flow was highly unsteady and therefore, without substantial amounts of data to perform a time dependent statistical analysis, it was difficult to highlight the precise nature of this flow field using the available technique. The writer suggests that by employing an Eulerian velocimetry method (for example PIV) in a transient experimental analysis, an enhanced improvement in resolving the radial flow fields should be obtainable.

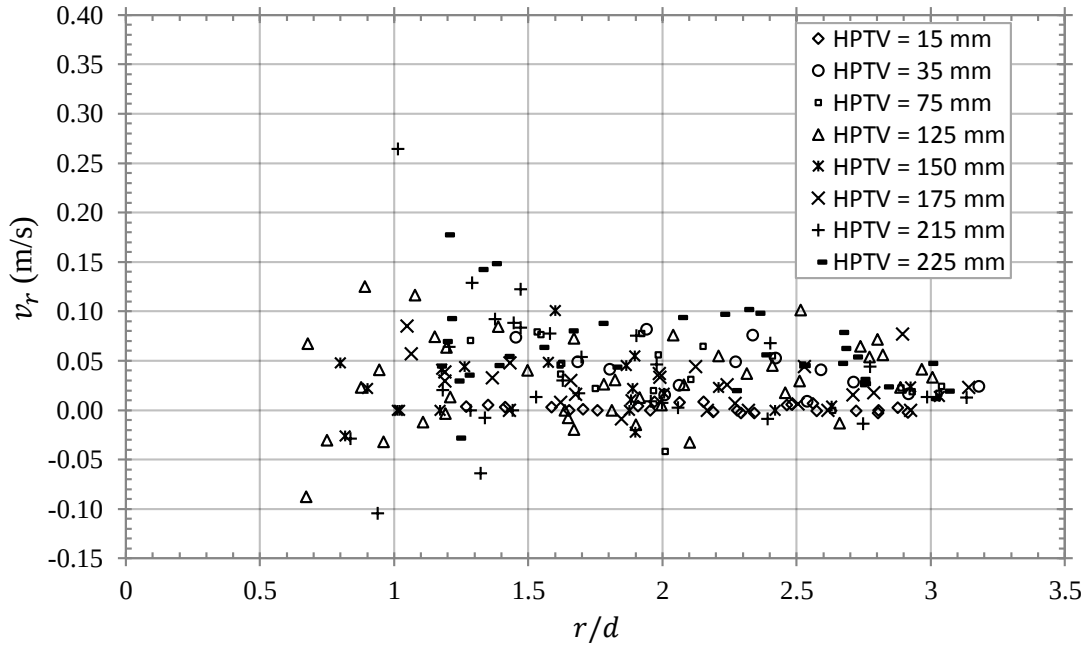

Figure 6.32: Radial velocity v_r measurements at radial positions r/d for $h/d = 3.5$, $\tilde{\Gamma} = 0.220$ m^2/s, Rr = 10305, $N_\Gamma = 3.7261$ and $N_Q = 0.852$.

6.4.4. Axial Velocity Distribution

The axial velocities were obtainable for $r/d < 1$ using the near-field particle streak velocimetry (PSV) technique outlined in Section 5.7. The results for all approach flow depths were displayed in Figure 6.33 where the axial velocity v_z was non-dimensionalised using $\bar{v_z} = v_z/v_{z_{max}}$ where $v_{z_{max}} = \tilde{v}_{z_o} = 4Q/\pi(d^2 - {a_c}^2)$. Each plot, which was representative of the local axial velocity for a range of vertical depths z, generally

highlights that the velocity increased towards $v_{z_{max}}$ when $r \rightarrow a_c$. However, it was very difficult to observe particle displacements at the critical section where $v_z \approx v_{z_{max}}$ because the particles quickly disappear from the field of view. Further work is required using a more definitive technique in the core region for $a_c/2 < r < d/2$.

To establish a relationship between the axial velocity profile $v_z(r)$ and the subsurface depth z the axial velocity gradient $v_z(z) = v_z \pi {r_0}^2/Q\chi$ is plotted against r/d in Figure 6.33 for each approach flow depth where $\chi = z/h$ is the non-dimensional height. A similar comparison was provided by Anwar (1969) and the results show a similar increase in the axial velocity gradient in this region. For each approach flow the axial velocity gradient in the region considered is substantial. Both Hinze (1959) and Scorer (1967) state that when the axial flow and its gradient in the region between the axis of symmetry and the circumference of the outlet r_0 is large, strong turbulence exists which can perturb the flow through instabilities.

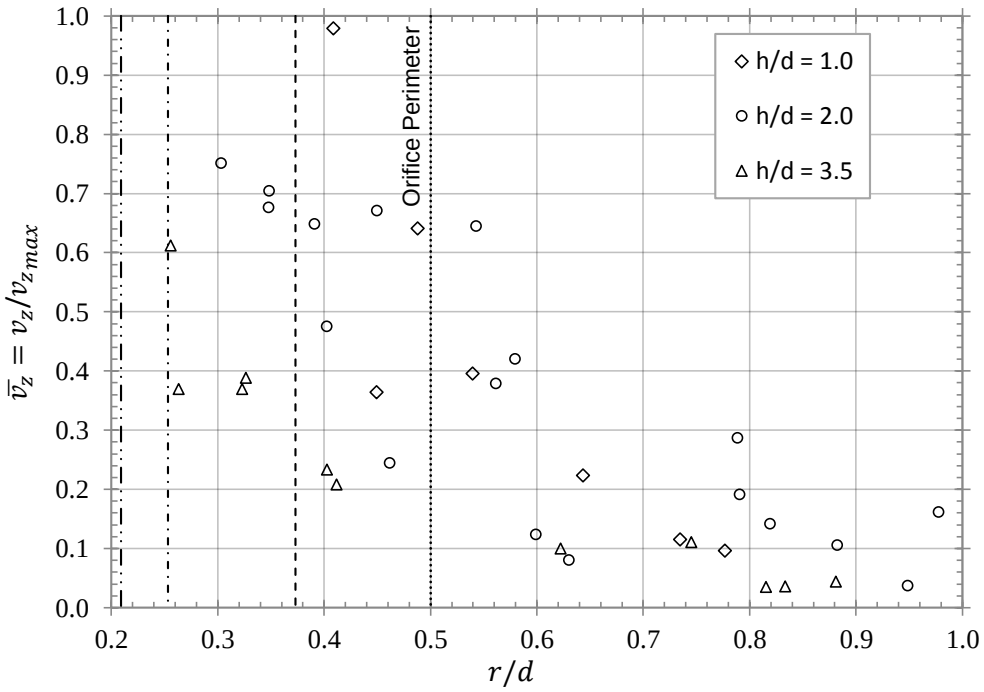

Figure 6.33: Distribution of the axial velocity throughout the core region for r/d< 1 for each approach flow depth in model #4d1.0d (α = 2.688). The curves only indicate the trends of the experimental data. Each vertical line indicates the radial position of the critical air core radius $a_c/2d$.

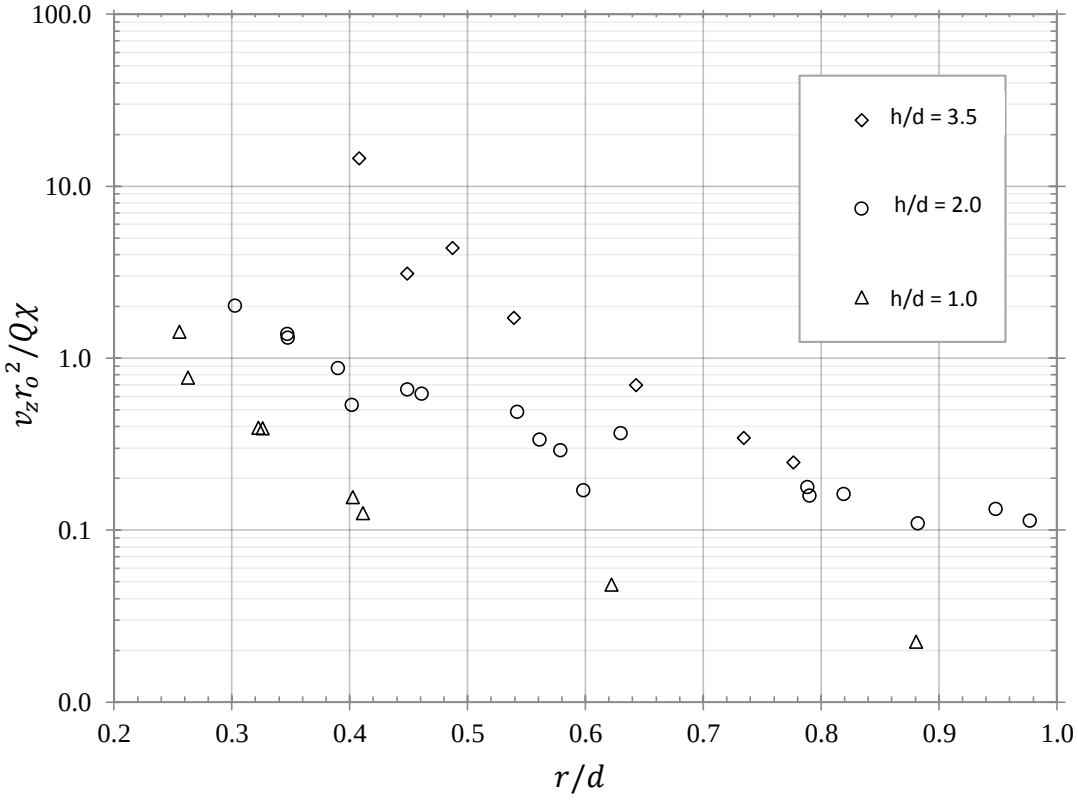

Figure 6.34: Distribution of the axial velocity throughout the core region for $r/d < 1$ for each approach flow depth in model #4d1.0d ($\alpha = 2.688$). The curves only indicate the trends of the experimental data.

6.5. Turbulence and Secondary Flow Fields

In the final section of the experimental results, the planar laser-induced fluorescence (PLIF) secondary flow visualisation is presented. The procedure for the PLIF process is highlighted in Section 5.8.5.

6.5.1. Turbulent Mixing Visualisation

A time-lapse of frozen image frames from $t = 0.000$ s (at the time of the initial injection event) to $t = 4.934$ s is displayed in Figure 6.35 for PLIF imaging on a horizontal plane at h_{PTV} = 150 mm for $h/d = 3.5$. It was evident from an initial observation of the image sequence, that the flow was highly turbulent. After only 5 seconds of the initial injection, the fluorescein was completely mixed throughout the chamber. Between $t = 0.000$ and 1.134 s the dye entered the chamber and appeared to be highly strained with inherent

vortices forming and dissipating. After 2.934 seconds the dye makes one complete revolution in the chamber. A short period after this event ($t \approx 0.6$ s) a rapid diffusion process takes place and the dye was completely mixed throughout the chamber. It was deemed that the eddy viscosity of the fluid was playing a significant role in this mixing process. Although it will not be addressed quantitatively in the experimental analysis, it should be noted that this process can be described mathematically using the turbulent Schmidt number Sc_t. The turbulent Schmidt number is the ratio between the rate of turbulent transport of momentum and the turbulent transport of mass. It is somewhat similar to the turbulent Prandtl number Pr_t which described the ratio of turbulent momentum to the heat transfer eddy diffusivity. The turbulent Schmidt number also plays a significant role in CFD simulations. A further note can be made from these findings applied to hydraulic similarity. Jain and Kennedy (1983) state that if the flow in the model is fully turbulent, then the model can be considered to be free from scaling effects due to viscosity. Therefore, the findings on the turbulent transport of the dye in Figure 6.35 further supporting the findings of Section 6.1.

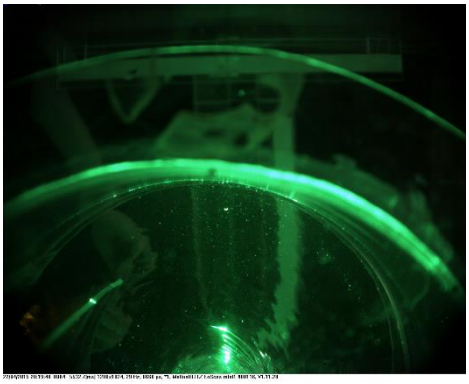

t = 0.000 s

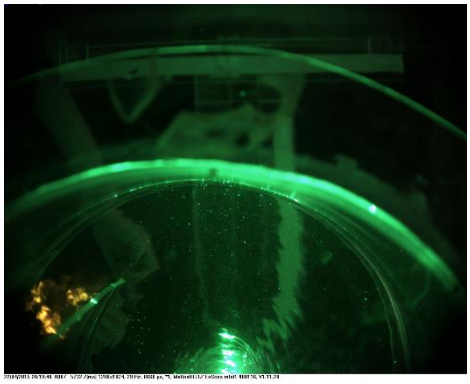

t = 0.200 s

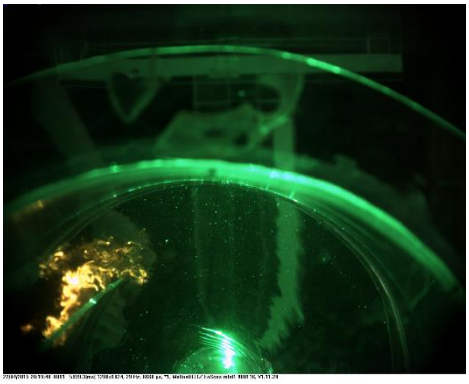

t = 0.467 s

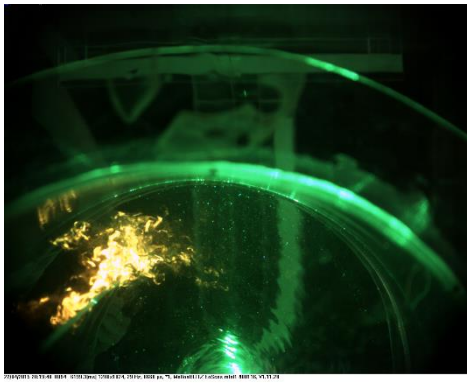

t = 0.667 s

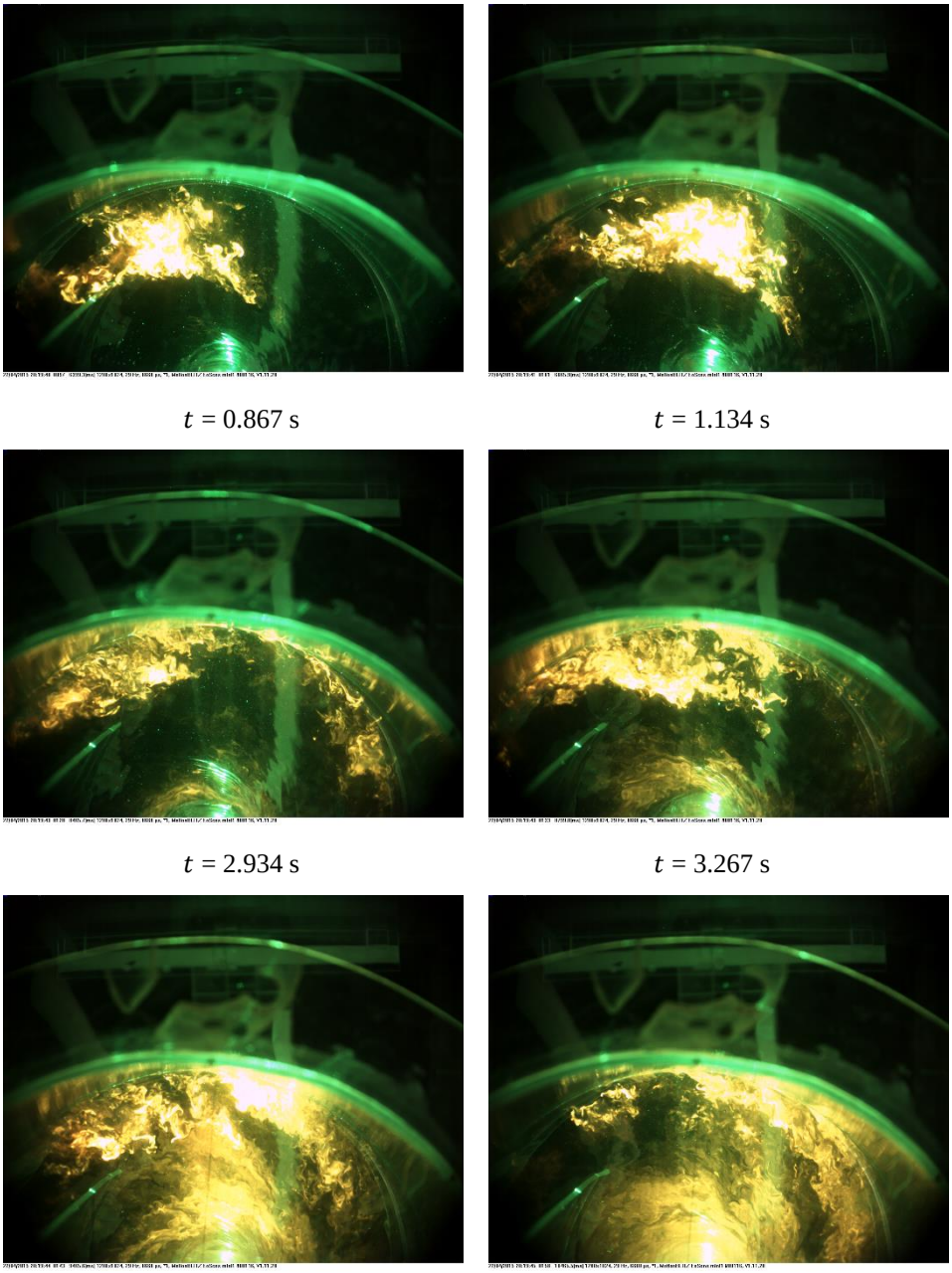

t = 0.867 s t = 1.134 s

t = 2.934 s t = 3.267 s

t = 3.934 s t = 4.934 s

Figure 6.35: Turbulent mixing on a horizontal plane in the vortex chamber visualised using planar laser-induced fluorescence. $h/d = 3.5$, $\tilde{\Gamma} = 0.220$ m^2/s, Rr = 10305, $N_\Gamma = 3.7261$ and $N_Q = 0.852$.

6.5.2. Secondary Flow Visualisation

The PLIF experiments performed for the secondary flows are now presented. Figure 6.36 depicts the typical transport of fluorescein when injected at the vessel floor of the physical model. Although the dye was advected in all three-dimensions in a spiralling pattern

throughout the chamber, the vertical light sheet only permited observation of the dye as it moved radially and axially. It can be seen that just after 1 second the dye reached the orifice through a finite jet at the vessel floor similar to that observed by Anwar (1965) Al'tshul and Margolin (1968) and Dagget and Keulegen (1974). This jet was estimated to be approximately 5 - 7 mm thick ($\Delta t_{radialjet}/d \approx 0.09$) which corresponds to about half of the annular jet thickness. The most remarkable feature determined in this observation was the presence of an 'upward draft' near the chamber periphery at 1.665 s and again on the inside of the left wall in 2.965 s after it made one revolution. This suggested that the flow at the inlet was advected both radially at the base of the tank and along the outside periphery as a result of a local positive axial velocity gradient. After 4 seconds the dye reached the free-surface and was transported along the air core to discharge at the orifice.

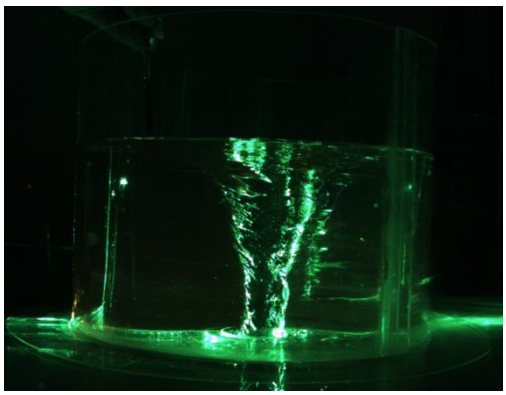

t = 0.000 s

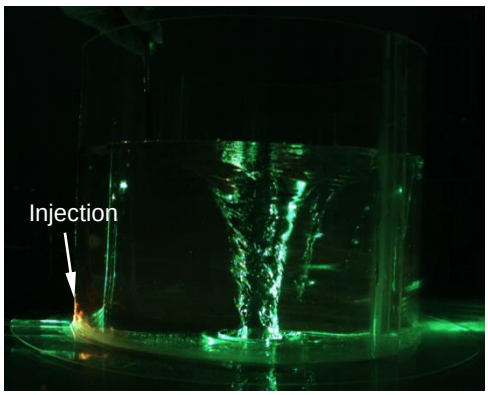

t = 0.333 s

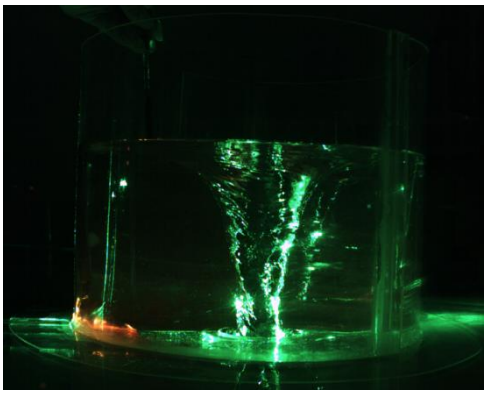

t = 0.666 s

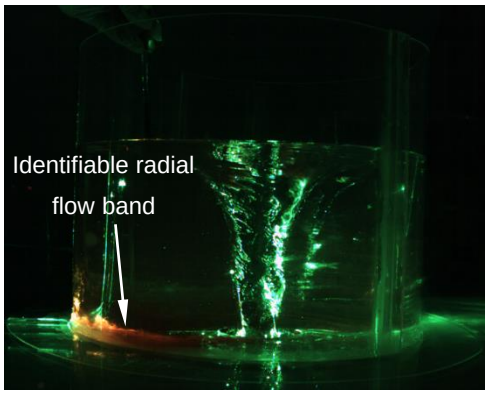

t = 0.999 s

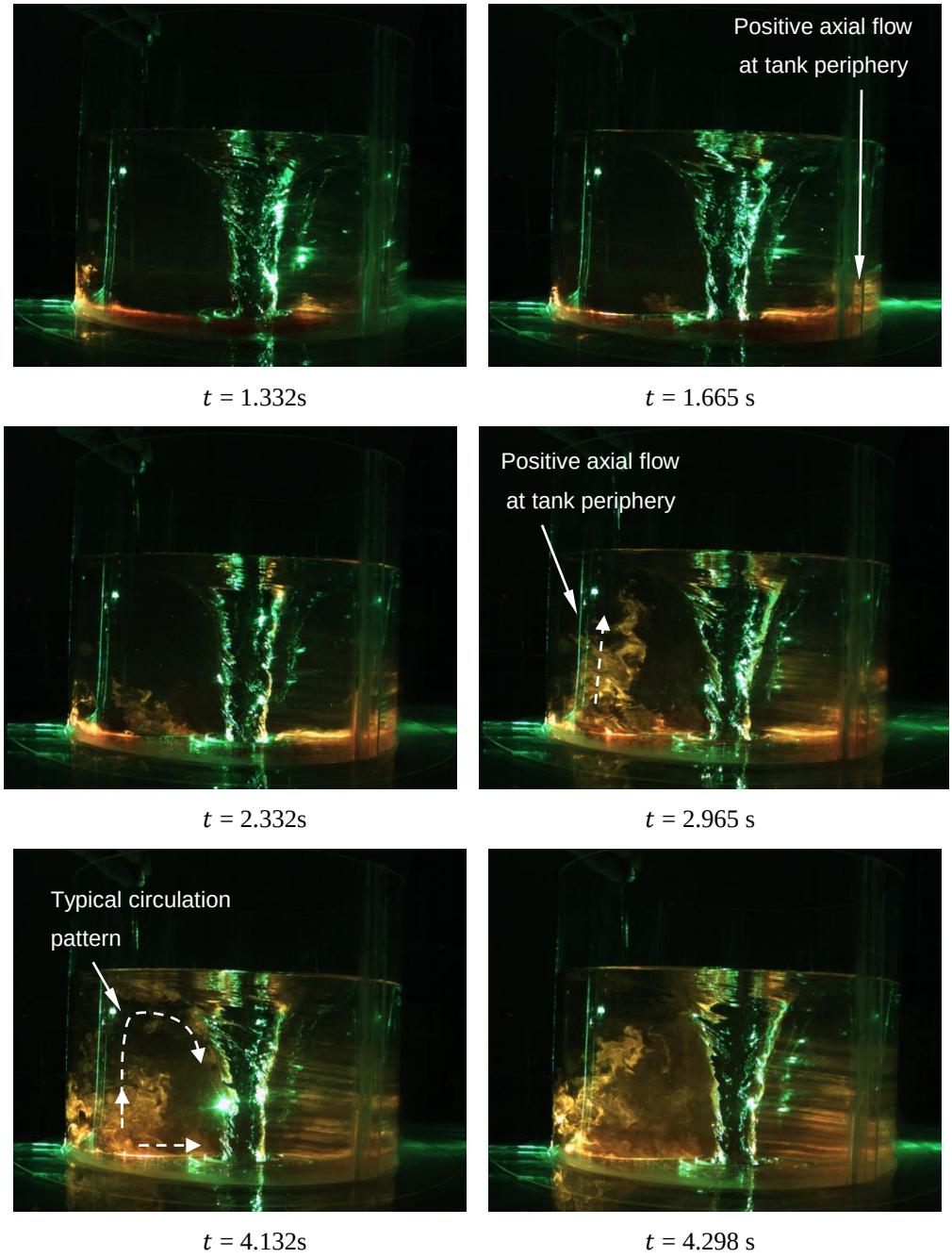

Figure 6.36: Visualisation of turbulent transport of Rhodamine B upon initial injection at the vessel floor using planar laser-induced fluorescence in model #4d1.0d (α = 2.688) for h/d = 2.0, $\tilde{\Gamma}$ = 0.214 m^2/s, Rr = 9911, N_Γ = 6.383 and N_Q = 0.467.

Similar to the previous investigation, the Rhodmaine was injected just below the free-surface upstream of the inlet channel. The results of transport in this secondary flow region is presented in Figure 6.37. It was recognisable that the transport of the dye was at a lower velocity compared to when it was injected at the vessel floor thus indicating that the upper radial band was of lower strength than the lower band. Anwar (1965) suggested that by roughening the vessel floor, the radial velocity will be concentrated in the mid depth and free-surface region thereby increasing the free-surface radial velocity and reducing the strength of the vortex significantly. As the dye was transported with the flow, it was seen to intersect with the vertical light sheet close to the vortex core as it flowed in the vortex. This confirmed that the flow was in fact concentrated in the region of the free-surface in addition to that at the vessel floor. However, a second injection of dye was made just below the free-surface and, instead of being transported along the free-surface it was quickly diffused across the depth of the vortex. This showed that the radial band at the free-surface was delicate and of a relatively shallow thickness. In both of the previous experiments it was confirmed that the secondary flow field consisted of negative radial bands at the vessel floor and free-surface as well as a positive and negative axial velocity gradients close to the vessel periphery and air core respectively. In the mid-depth region, where the tangential velocity field was dominant, there existed a secondary sub-flow process which manifested as fluctuating radial and axial velocity distribution or a multitude of transient vortex cores spanning the circumferential extent of the chamber.

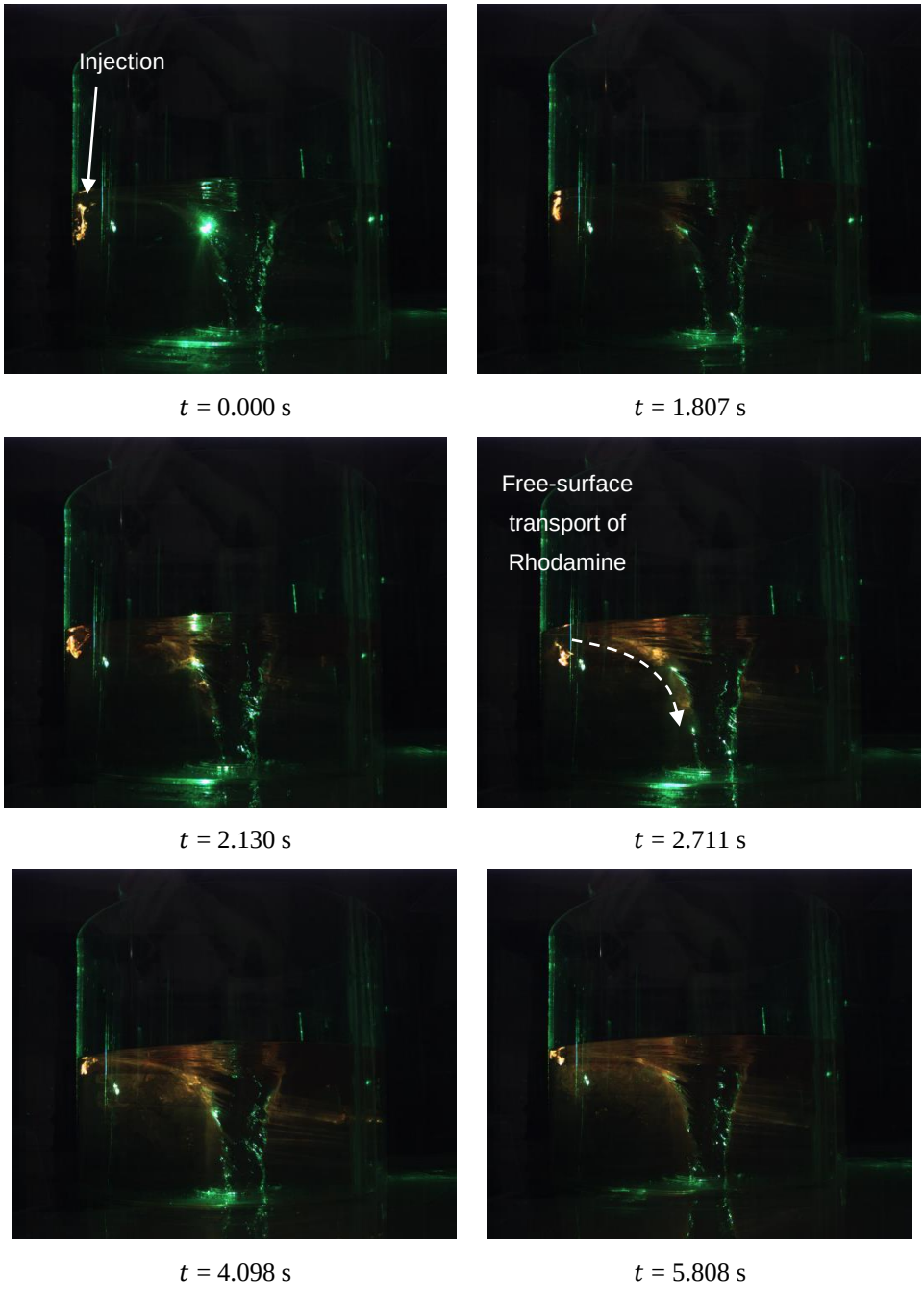

t = 0.000 s t = 1.807 s

t = 2.130 s t = 2.711 s

t = 4.098 s t = 5.808 s

Figure 6.37: Turbulent transport of Rhodamine B upon initial injection at the free-surface using planar laser-induced fluorescence in model #4$\boldsymbol{d}$1.0$\boldsymbol{d}$ ($\boldsymbol{\alpha}$ = 2.688) for $\boldsymbol{h/d}$ = 2.0, $\tilde{\boldsymbol{\Gamma}}$ = 0.214 m^2/s, Rr = 9911, N_Γ = 6.383 and N_Q = 0.467.

6.6. An Alternative Tangential Velocity Profile

In Section 6.4.1 it was shown that the ideal velocity distribution based on the quasi-cylindrical ideal irrotational approach substantially over estimated the near-field experimental tangential velocity profile. Growth of the discrepancy appeared to increase for radial positions of $r/d < 1$. The difference appeared to worsen as the approach flow depth increased. So far, analytical models have been developed (Rankine, 1872; Rosenhead, 1930; Odgaard, 1986; Vatistas et al., 1991) to primarily eliminate the singular nature of the ideal irrotational vortex model, but only apply to a weak vortex with a closed air core where a viscous or turbulent vortex core is in existence. The problems associated with applying the previous analytical models to that of a full air core vortex have been shown in Figure 6.29. In order to address the problem in this study, it was pondered that, before taking into consideration the effects of turbulence in the core region, it might be more pragmatic to question the assumptions in which the quasi-cylindrical approach is founded upon. Daggett and Keulegen, based on the results of their work (Daggett and Keulegan, 1974) stated that:

"*it is apparent from these measurements of the velocity field that using the simplifying assumptions that the vertical velocities are negligible and that radial velocities do not vary in the vertical direction is invalid. Any theoretical solution must consider all three components of the velocities*".

In the new approach, the writer hypothesises that the existence of axial velocities in the near-field in addition to gradients in the axial direction $\partial/\partial z$ may have a significant role to play in breakdown of the validity of the ideal velocity profile. This was further emphasised by experiments performed for the case of a strong, stable full air core vortex, where it was shown that the axial velocity and partly the radial velocity in the near-field region are actually sizeable (Section 6.4.3 and 6.4.4). Assuming that the viscous effects and hence, turbulence, has a negligible roll to play in the tangential velocity distribution of a strong vortex, the Euler equation for the steady, axisymmetric tangential momentum will be presented as follows:

$$v_r \frac{\partial v_\theta}{\partial r} + \frac{v_r v_\theta}{r} + v_z \frac{\partial v_\theta}{\partial z} = 0 \qquad (6.18)$$

It was shown that the validity of the quasi-cylindrical inviscid approach totally relies on the assumption of that $\partial v_\theta/\partial z = 0$ everywhere in the flow field and thus the tangential velocity varies inversely with the radius by $v_\theta \propto 1/r$ (Einstein and Li, 1951). If however that this derivative is non-zero, i.e. $\partial v_\theta/\partial z \neq 0$, the derivation for the tangential velocity would instead take the form of:

$$\frac{\partial v_\theta}{\partial r} + \frac{v_\theta}{r} = -\frac{v_z}{v_r}\frac{\partial v_\theta}{\partial z} \tag{6.19}$$

where the effect of v_z and v_r would be considerable in determining $v_\theta(r)$. The question as to whether $\partial v_\theta/\partial z$ exists in the near-field region will be addressed again in the results of the numerical model (see Chapter 7). For now, it is assumed that $\partial v_\theta/\partial z \neq 0$ and therefore by some brief mathematical manipulation of Equation (6.19) it is possible to show that the term on the right hand side has the effect of reducing the tangential velocity distribution for large values of v_z or v_r.

This was confirmed empirically by examining the relationship between the maximum model discrepancy (of the ideal velocity $\%\Delta v_\theta$ and circulation $\%\Delta\Gamma_\infty$) in Figure 6.38 where the values in the core region depended on the circulation number $\frac{\pi}{4}$Nr. It appears that the maximum discrepancy decreases linearly with increasing circulation number for the available data in Table 6.3 and Figure 6.38. Because the circulation number presents a measure of the competition between the tangential and the axial flow field, it is not surprising therefore that the discrepancies observed in the ideal model would increase with decreasing $\frac{\pi}{4}$Nr (hence as a result of an increasing axial flow field). Thus the circulation number presents a direct empirical measure of the effect that the axial velocity field exhibits on the ideal tangential velocity model in a strong free-surface vortex.

The eddy viscosity appears to vary linearly with the circulation number according to:

$$\varepsilon\ (\times 10^{-5}) = 0.536\mathrm{K} + 1.8772 \tag{6.20}$$

Table 6.3 Values of measured discrepancies obtained between the ideal analytical model and the experimental data.

h/d	$\frac{\pi}{4}N_\Gamma$	$\%\Delta v_\theta$ (m/s)	$\%\Delta\Gamma_\infty$ (m^2/s)
1.0	13.35	0.05	0.0732
2.0	6.62	0.27	0.317
3.5	3.73	0.468	0.3917

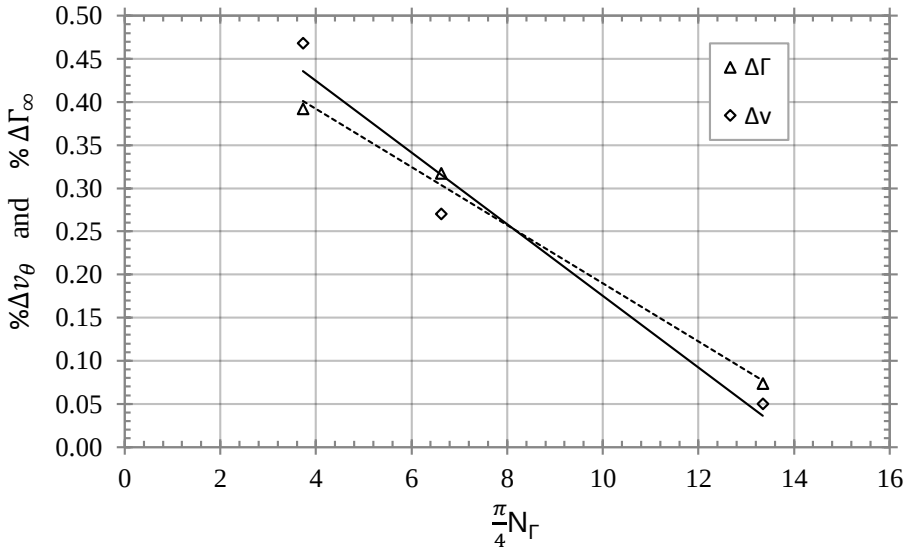

Figure 6.38: Plot of maximum measured discrepancies ($\%\Delta v$ and $\%\Delta\Gamma$) obtained between the ideal analytical model and the experimental data versus the circulation number $\frac{\pi}{4}N_\Gamma$.

To build on this improvement analytically, the functional relationship to determine the tangential velocity field in a two dimensional field of a free-surface vortex is given by:

$$f_1(\tilde{v_z}, \Gamma_\infty, \Gamma_r, r, d, \nu) = 0 \qquad (6.21)$$

where Γ_r is the circulation which varies with radius r. Here the effects of surface tension were considered to be negligible[25]. Through the Buckingham Π theorem, choosing Γ_∞, d, ν as the repeating variables, the following dimensionless parameters can be obtained:

$$f_2\left(\frac{v_z d}{\Gamma_\infty}, \frac{\Gamma_r}{\Gamma_\infty}, \frac{r}{d}, \frac{\nu}{\Gamma_\infty}\right) = 0 \qquad (6.22)$$

[25] Surface tension is omitted from this analysis as it has been found to be a safe assumption in the experimental section.

In effect, ν/Γ_∞ is equal to $\nu/2\pi vr$ which is a form of tangential Reynolds number[26] (Taylor, 1923). A crucial assumption was made in that the viscous effects and hence the turbulence had a negligible effect on the tangential velocity field and was therefore omitted from the current analysis at this point. However, it was included until now for the purpose of demonstrating that a universal tangential velocity model will require the effect of both the axial gradient and the viscous or turbulent vortex core properties. The first term is the circulation number which can be re-written as $1/\frac{\pi}{4}\mathrm{N}\Gamma = \frac{4}{\pi}\frac{Q}{\Gamma_\infty d}$ as an inverse of previous formats used in this thesis. According the writers assumption, this parameter should have the effect of reducing the ideal tangential velocity distribution along the radial field r/d and therefore Equation (6.22) is rewritten as:

$$\frac{\Gamma_r}{\Gamma_\infty} = f_3\left(\frac{4}{\pi N_\Gamma}, \frac{r}{d}\right) \tag{6.23}$$

or

$$v_\theta(r) = \frac{\Gamma_\infty}{2\pi r} f_4\left(\frac{4}{\pi N_\Gamma}, \frac{r}{d}\right) \tag{6.24}$$

In the proposed alternative model, the term in the brackets on the right hand side of Equation (6.24) was treated as a correction factor that should reduce the values of the ideal model $v_\infty = \Gamma_\infty/2\pi r$ along r/d to yield the revised velocity profile $v_\theta(r)$. From observation of the experimental results it was remarked that a noticeable departure with increasing divergence was recognised for values of r/d <1. Similar departures were reported by Quick (1961) and Anwar (1965). Furthermore, it was shown that the deviation between the velocity profiles was linearly proportional to the inverse of the circulation number $1/\frac{\pi}{4}\mathrm{N}\Gamma$. Thus, through insight, a typical model format that would take into account the axial flow and its near-field behaviour would require the correction factor to take the following form:

$$C_\Gamma = f_4\left(\frac{4}{\pi N_\Gamma}, \frac{r}{d}\right) = 1 - \left(\frac{4}{\pi N_\Gamma}\right)^{\frac{mr}{d}} \tag{6.25}$$

[26] The tangential Reynolds number has the same form as the Taylor number (Ta) which will be discussed in a later section.

where m is an empirical exponent. In the revised model, the term $1/\frac{\pi}{4}N_\Gamma$ is always less than unity and therefore mr/d plays a significant role in three critical radial locations as follows:

1. In the far-field, $mr/d \gg 1$ i.e. r/d becomes large, the correction factor remains close to 1. Therefore the irrotational properties of the far-field are modelled correctly by unchanging the ideal tangential velocity model $v_\theta = \Gamma_\infty/2\pi r$.
2. When $mr/d \to 1$, the vortex core is approached and the non-hydrostatic and axial flow properties of the near-field are modelled through the effect of the inverse circulation number.
3. For values of $mr/d < 1$, within the vortex core, the ideal tangential velocity is reduced to more realistic values based as a result of the increasing axial velocity field.

The modified velocity profile in its full form is:

$$v_\theta(r) = \frac{\Gamma_\infty}{2\pi r}\left(1 - \left(\frac{4}{\pi N_\Gamma}\right)^{\frac{mr}{d}}\right) \tag{6.26}$$

Values for the exponent m then provide a family of curves for the tangential velocity distribution. It is interesting to note that when m or $\frac{mr}{d} \to 0$, the tangential velocity gopes to zero $v_\theta(r) \to 0$. Additionally when m or $\frac{mr}{d} \to \infty$, $v_\theta(r) \to \Gamma_\infty/2\pi r$. Therefore the model is bounded and exhibits no singular behaviour.

The performance of the above model was tested and the family of curves for m = 0.5, 1, 2 and 5 were evaluated using the data provided in 6.4.1. The results of the models for each approach flow condition h/d = 1, 2 and 3.5 are displayed in Figures 6.39, 6.40 and 6.41 respectively. The model was shown to be highly dependent on the value of m. When m = 5, the model approaches the ideal solution (or for $m = \infty$). When m is reduced, the tangential velocity field is dampened significantly and the profile appears to flatten. A good fit was found for values for m = 2. By observation of Equation (6.26), it was evident that when m = 2, the exponent mr/d approached 1 when the perimeter of the orifice i.e. $2r = d$. Therefore, the divergence of the tangential velocity profile from its ideal

approximation occurs radially on the approach to the orifice, where the axial velocity field begins to grow in strength. In each approach flow depth it was observed that the curve begins to depart from the ideal model at $r/d = 1$ which agreed with past experimental observations.

For h/d = 3.5 it was recognisable that the model underestimates the tangential velocity at the air core radius by approximately 10%; however, the model was in good agreement with the experimental data up until this point. For $h/d = 2.0$, the corrected model agreed well except for a small region between $0.6 > r/d > 1$. For $h/d = 1.0$ a good agreement was obtained throughout the flow field. It was presumed that the randomness of these discrepancies were probably as a result of the experimental uncertainty (as discussed in Sections 5.9, 6.4.1 and 6.4.2). In conclusion the model increased the accuracy of the analytical solution by approximately 30% throughout the near-field.

In order to provide a closure, it was interesting to note that because the reciprocal of the circulation number is being used, its value can be conveniently replaced with the unifying Equation (6.10) that was obtained in Section 6.3.3, as follows:

$$v_\theta(r) = \frac{\Gamma_\infty}{2\pi r}\left(1 - \left(\frac{h}{5\alpha d}\right)^{\frac{2r}{d}}\right) \tag{6.27}$$

Thus, an expression that defines the tangential velocity field $v_\theta(r)$ in a full air core vortex for a predefined approach flow depth and geometry is presented in Equation 6.27. The model is shown in its $m = 2$ form. Further validation is required however to verify if the $m = 2$ is universal or if m is dependent on another physical process.

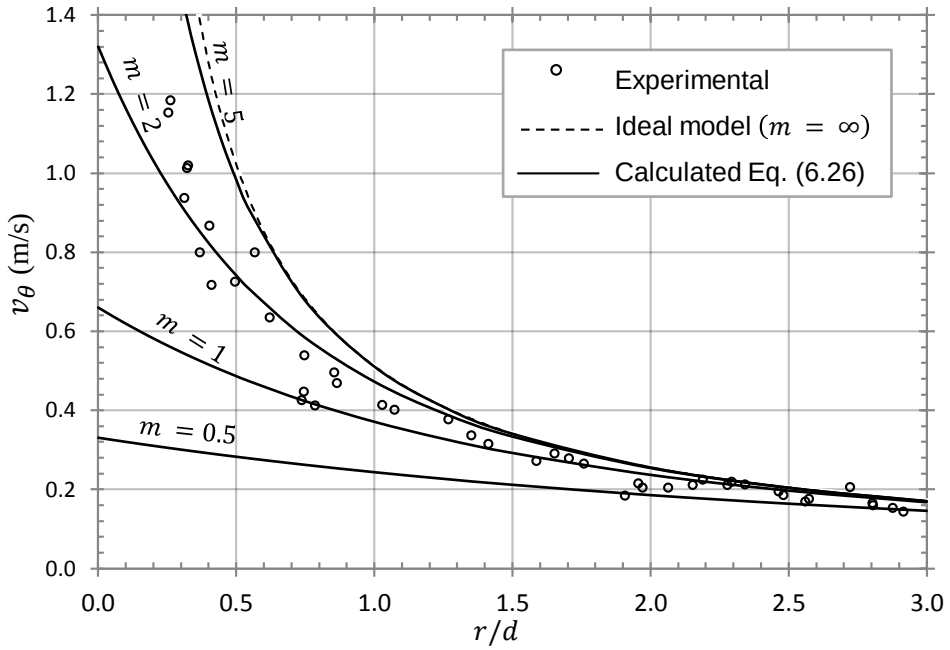

Figure 6.39: Comparison between calculated and measured tangential velocities using Equation 6.26 for various values of m in model #4d1.0d ($\alpha = 2.688$) for $h/d = 3.5$, $\tilde{\Gamma} = 0.220$ m^2/s, Rr = 10305, $N_\Gamma = 3.7261$ and $N_Q = 0.852$.

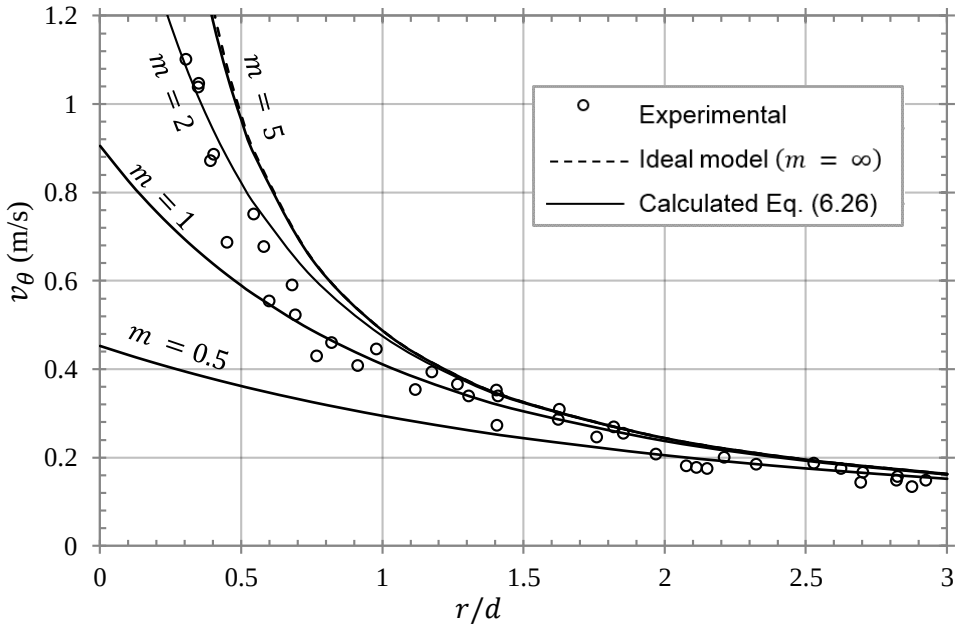

Figure 6.40: Comparison between calculated and measured tangential velocities using Equation 6.26 for various values of m in model #4d1.0d ($\alpha = 2.688$) for $h/d = 2.0$, $\tilde{\Gamma} = 0.214$ m^2/s, Rr = 9911, $N_\Gamma = 6.383$ and $N_Q = 0.467$.

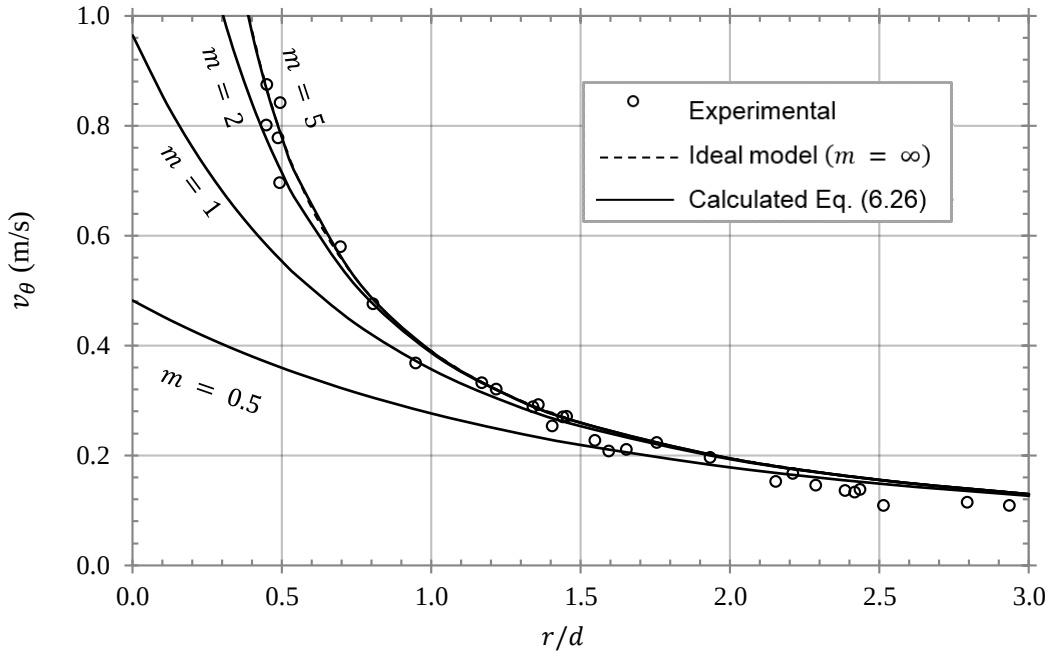

Figure 6.41: Comparison between calculated and measured tangential velocities using Equation 6.26 for various values of m in model #4d1.0d ($\alpha = 2.688$) for $h/d = 1.0$, $\tilde{\Gamma} = 0.178$ m^2/s, Rr = 8162, $N_\Gamma = 12.766$ and $N_Q = 0.1923$.

6.7. Conclusions

The results of the experimental program were presented with in detail. Initial evaluation of the hydraulic similarity exposed that four of seventy two models tested were susceptible to possible effects of surface tension. The general hydraulic results showed initial key trends in the experimental data. Comparisons of the current data to former studies highlighted some interesting conclusions regarding empirical relationships.

The effects of the approach flow geometry on a strong free-surface vortex have been systematically reviewed using experiments on twelve varying vortex chamber geometries. The results indicate that the Kolf number is directly related to a non-dimensional approach flow factor y_α and can be easily computed from the geometry α and the approach flow depth h/d. The intrinsic relationship between the discharge number and the circulation number was investigated for each geometry. It was found that the curves relating the discharge number to the Kolf number can be resolved using the two auxiliary empirical parameters n_α and k_α which were modelled using polynomial equations. The results collectively presented a solution for the depth-discharge equation

in a strong free-surface vortex which can be solved only on the basis of the approach flow geometry. Although it was noted that some caution may need to be exercised when neglecting the effects of surface tension in the physical models, no scale effects have been reported in the experimental results. The proposed model is validated against an up-scaled model and a prototype. Observations depicted a number of phases of vortex flow exist which are characterised by the inlet Froude number and the approach flow geometry. These included stably subcritical, unstably subcritical, transitionally subcritical and fully supressed free-surface vortex flow. The model is presented in chart format together with the approximate regions for the outlined flow phases.

The results from the experimental data on the tangential velocity field indicated that it was independent of the $z-$axis for sub-surface depths away from the vessel floor and free-surface. The results of the radial velocity field showed that they are highly unsteady and immeasurable in most cases using the available technique. The PLIF method highlighted that the radial velocity was confined to bands at the vessel floor and free-surface as was observed in previous studies. The axial velocity data indicated that it was focused as a strong gradient around the vicinity of the vortex air core. The PLIF observations also highlighted that the axial velocity existed as a positive gradient at the vessel periphery.

When the tangential velocity data was compared to that of the ideal model, significant discrepancies were observed in the near-field. Furthermore, it was shown that previous analytical models for predicting the tangential velocity behave poorly in the strong vortex application. In response to this gap in the research, the writer developed an alternative velocity profile for predicting the tangential velocity in the near-field of a strong full air core vortex. The new model operates on the basis of a correction factor applied to the ideal model. The correction factor is based on the inverse circulation number and were found to increase accuracies in predicting the near-field tangential velocity profile by approximately 30 %.

Chapter 7.

Numerical Modelling

SUMMARY

An extensive experimental numerical comparison was performed on the ANSYS CFX computational fluid dynamics code for modelling strong free-surface vortices. The simulations were modelled using the available data from the experimental study in Chapter 6. A multiphase two-fluid (air water) homogeneous Eulerian-Eulerian approach was employed. Solution sensitivity to mesh structure and density, steady and transient turbulence model formulations and time-step refinement was carried out. The results indicate that it was necessary to use a radially structured mesh as opposed to an unstructured tetrahedral mesh in order to avoid the effects of an over generated false diffusion across the vortex chamber. The mesh should be refined at the vortex core region to a size within 1.5 % of the outlet diameter. Furthermore, unsteady flow features in the vortex chamber, namely that of free-surface oscillations at the air core and annular jet interface as well as that in the fluctuating radial flow field, are unable to be resolved by the steady state approach. A significant improvement to the flow field solution in terms of the free-surface and tangential velocity profiles was observed when the flow is modelled transiently. Superior performance was observed using the shear stress transport model with curvature correction as well as the Reynolds stress model. Both models achieved accuracies to within 12 – 15 % in predicting the free water surface and 20 – 26 % in predicting the tangential velocity field, however the Reynolds stress model requires significant computational expense.

7.1. Overview of Multiphase Modelling using ANSYS CFX

Numerical modelling was performed in this project using the commercial CFD software ANSYS CFX (V14.5) which is extensively used in industry for modelling hydro-mechanical engineering problems. Numerous authors have successively employed this

code in the analysis of vortex flows (Suerich-Gulick et al., 2006; Stephens and Mohanarangam, 2010; Škerlavaj et al., 2011; Suerich-Gulick, 2013; Suerich-Gulick et al., 2014; Pandazis and Blömeling, 2014; Škerlavaj et al., 2014). In this section, a complete review of the theoretical literature surrounding the ANSYS CFX solver will be presented with emphasis made on certain approaches that will be employed in the CFD simulations of the strong multiphase vortex flow.

7.1.1. Overview of the Solver

ANSYS CFX uses a hybrid finite-element/finite-volume (finite element based finite volume method) approach to discretising the Navier-Stokes equations. Global conservation is satisfied by enforcing local conservation over the control volumes. The finite element approach is used to determine various surface fluxes and source terms within each element. Advection fluxes are evaluated using a high-resolution scheme that is second-order accurate and bounded. For transient simulations, an implicit second order accurate time differencing scheme is used. CFX utilises a coupled solver to resolve the hydrodynamic equations as a single system. It therefore offers the advantages of being robust, efficient and simple in comparison to its segregated counterpart where the momentum equations are solved using a guessed pressure. The solution is fully implicit at any time step and is thus unconditional of the Courant number[27]. For steady-state solutions, the time step is treated as an acceleration parameter which marches the approximate solutions in a physically based manner to a steady-state solution. In a time-dependant (transient) approach, the solution is solved for the n^{th} time step using coefficient loop criteria. The following flow chart (Figure 7.1) depicts the general solution process that is employed in the CFX-Solver (ANSYS, 2009)

[27] Emphasised in more detail later, the Courant number other wise known as the Courant–Friedrichs–Lewy (CFL) condition is a necessary condition for convergence while solving certain partial differential equations (of the hyperbolic type).

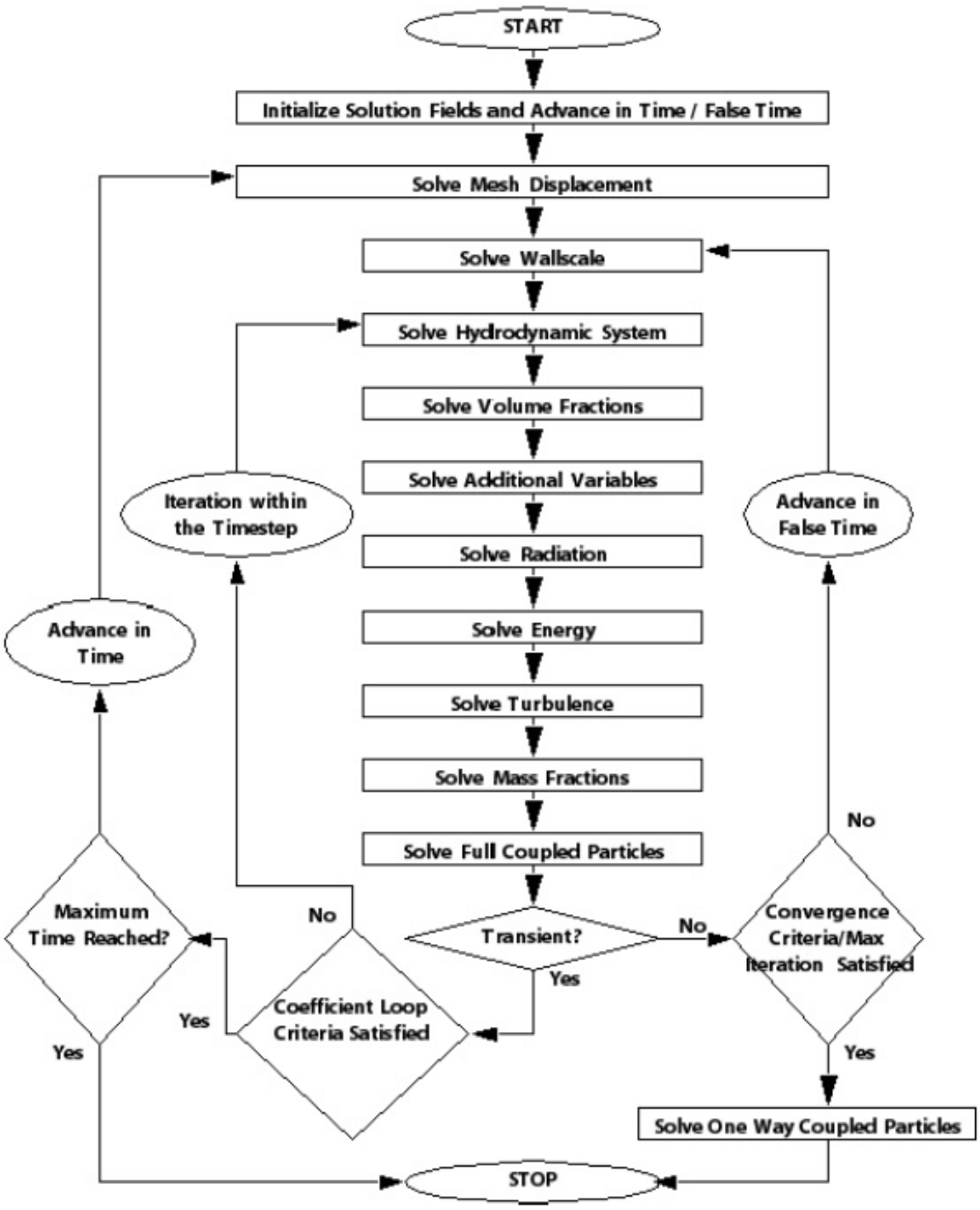

Figure 7.1: Flow chart highlighting the overall ANSYS CFX solver algorithm for both transient and steady state analysis (ANSYS (2009)).

7.1.2. Discretisation

Analytical solutions to the Navier-Stokes equations are extremely difficult to achieve (Hall, 1966). To obtain solutions to real flows, the flow domain is discretised using a mesh and the Navier-Stokes equations are replaced by algebraic approximations. All solution variables are stored at the mesh vertices. The conservation equations for mass, momentum and passive scalar, expressed in Cartesian co-ordinates by:

$$\frac{\partial \rho}{\partial t} + \frac{\partial}{\partial x_j}(\rho U_j) = 0 \tag{7.1}$$

$$\frac{\partial}{\partial t}(\rho U_i) + \frac{\partial}{\partial x_j}(\rho U_j U_i) = -\frac{\partial P}{\partial x_i} + \frac{\partial}{\partial x_j}\left(\mu_e\left(\frac{\partial U_i}{\partial x_j} + \frac{\partial U_j}{\partial x_i}\right)\right) \tag{7.2}$$

$$\frac{\partial}{\partial t}(\rho\varphi) + \frac{\partial}{\partial x_j}(\rho U_j \varphi) = \frac{\partial}{\partial x_i} + \left(\Gamma_{eff}\left(\frac{\partial \varphi}{\partial x_j}\right)\right) + S_\varphi \tag{7.3}$$

where U is the velocity vector, P is the pressure, μ_e is the effective viscosity, φ is the general scalar variable, and Γ_{eff} is the effective diffusivity (ANSYS, 2009). The equations are integrated over each control volume. Gauss' divergence Theorem[28] is applied to convert volume integrals involving divergence and gradient operators to surface integrals. The volume and surface integrals are subsequently discretised in the element control volume and surfaces respectively. Because the surface integrals are equal and opposite for adjacent control volumes, the surface integrals are guaranteed to be locally conservative (ANSYS, 2009).

A series expansion (i.e. Taylor series) is used to approximate the continuous functions. The order of accuracy therefore becomes important and is a function of the exponent on the mesh spacing and time step factor. Such approximations are therefore subjected to truncation error which is defined as *"the difference between the exact analytical solution of the partial differential equation and the exact (round-off-free) solution of the corresponding difference equation"* (Wendt, 2008). Increasing order accuracy of the approximation reduces the truncation error with mesh or time step refinement. However, high-order approximations tend to be less numerically stable. The advection term requires that the scalar variable at integration points φ_{ip} are to be approximated in terms of nodal values by:

$$\varphi_{ip} = \varphi_{up} + \beta\nabla\varphi \cdot \Delta\vec{r} \tag{7.4}$$

[28] Gauss' divergence theorem states that the outward flux of a vector field through a closed surface is equal to the volume integral of the divergence over the region inside the surface.

where φ_{up} is the value at the upwind node and $\vec{r}$ is the vector from the upwind node to the integration point ip. Choices of the blend factor β then yields different numerical schemes. A number of schemes are available in ANSYS CFX. Škerlavaj et al. (2014) implemented a single phase numerical model for a vortex chamber using ANSYS CFX. In their work, the authors concluded that the choice of numerical scheme (through manipulation of β) had no significant effect on the tangential and axial velocity field. They also state that, in order to obtain a proper result for the length of the gas core of free-surface vortices, it was necessary to use a sufficiently small time-step regardless of the type of numerical scheme. In light of these findings, the high resolution scheme was employed in the ongoing analysis which was second-order, uses upwind-biased discretisation and was bounded to avoid unphysical oscillations. This was ensured by limiting the blend factor β. The recipe for β was based on the boundedness principles proposed by Barth and Jasperson (1989), values for φ_{min} and φ_{max} are first computed. Subsequently Equation (7.4) is solved to ensure $\varphi_{min} < \varphi_{ip} < \varphi_{max}$. The nodal value of β was taken to be the minimum value of all integration point values surrounding the node and is not permitted to exceed 1. The control volume gradients were evaluated using a form of Gauss' divergence theorem by:

$$\nabla\varphi = \frac{1}{V}\sum_{ip}(\varphi\Delta\vec{n})_{ip} \tag{7.5}$$

where V is the control volume and $\Delta\vec{n}$ is the outward surface vector at ip. Pressure-velocity coupling was fulfilled using a non-staggered grid layout where the control volumes are identical for all transport equations. To avoid the checkerboard pressure field oscillations, Rhie and Chow (1983) suggested an alternative discretisation using a momentum-based interpolation for the cell face mass fluxes in the continuity equation that closely imitates the staggered practice. Majumdar (1988) further improved the flux interpolation to avoid dependence of the steady-state solution on the time step. A similar strategy was adopted by ANSYS CFX (ANSYS, 2009). The general discrete approximation of the transient term for the n^{th} time step was given by:

$$\frac{\partial}{\partial t}\int \rho\varphi dV \approx V\,\frac{(\rho\varphi)^{n+\frac{1}{2}} - (\rho\varphi)^{n-\frac{1}{2}}}{\Delta t} \tag{7.6}$$

where $n+\frac{1}{2}$ and $n-\frac{1}{2}$ are assigned as superscripts to assign the values at the start and end of the time step. In this study, the first order backward Euler scheme was used where the start and end time step are approximated using the old and current time solution values respectively. The discretisation was robust, bounded, conservative in time, fully implicit and did not have a time step size limitation. In this way, the scheme was unconditional of the Courant–Friedrichs–Lewy[29] (CFL) condition which specifies the Courant number as:

$$\mathrm{C}_x = u\frac{\Delta t}{\Delta x}; \quad \mathrm{C}_y = v\frac{\Delta t}{\Delta y}; \quad \mathrm{C}_z = w\frac{\Delta t}{\Delta z} \tag{7.7}$$

in the x, y and z directions respectively. The stability of an explicit scheme was such that the time step Δt must satisfy an inequality and therefore $\mathrm{C}_{max} = 1$. In an implicit scheme it can be shown (Casulli, 2015) that for any time step Δt the numerical solution obtained possesses the discrete max-min property and consequently the scheme is unconditionally stable.

7.1.3. Multiphase Modelling

Flow in the vortex chamber is a fully segregated multiphase system comprising of water and air. Relative motion between both fluids is assumed to be insignificant which was justified by observations of the physical model. N_P is used to define the number of phases in a multiphase system. Each phase then possesses a separately defined volume fraction ϕ_k of phase k defined by:

$$\phi_k = \frac{\mathrm{V}_k}{V} \tag{7.8}$$

where V_k is the volume of phase k in a cell. The volume fractions for all phases in a cell should sum to unity, that is:

[29] The condition is named after Richard Courant, Kurt Friedrichs, and Hans Lewy who described it in their 1928 paper.

$$0 < \phi_k < 1, \quad \sum_{k=1}^{N_P} \phi_k = 1 \tag{7.9}$$

The two phase fluid domain is modelled using a homogeneous Eulerian-Eulerian multiphase flow model. This is a limiting case of the full Eulerian-Eulerian model which assumes that the interphase momentum transfer is negligible. This is valid for the current test case where the phases are completely stratified and the interface is well defined and interphase mixing is minimal to non-existent. In the homogenous approach, both phases are treated as interpenetrating continua parted by a well-defined interface and share a common velocity, pressure and turbulence field (ANSYS, 2013). Therefore, cells that are located away from the interfacial zone will be representative of either air or water $\phi_k = 1$ and cells in the vicinity of this zone will contain a mixture of both $0 > \phi_k > 1$. Maintaining this sharp interface during fluid simulation is a difficult task in the modelling of interfacial flows (Rider and Kothe, 1998). The homogeneous model assumes that the transported quantities (with the exception of the volume fraction) are the same for all phases. Because of this share in the transported quantities in homogeneous multiphase flow, it is then sufficient to solve only one bulk transport equation rather than solving individual phasic transport equations. The computational effort required to solve free-surface flow problems is then reduced considerably compared to that of the full Eulerian-Eulerian two-phase (inhomogeneous) flow approach. The bulk momentum equation is solved to obtain the shared velocity field by:

$$\frac{\partial(\rho U)}{\partial t} + \nabla.(\rho UU) = -\nabla p + \nabla\left(\mu(\nabla U + (\nabla U)^T)\right) + \rho g + T_\sigma \tag{7.10}$$

where the mixture quantities are:

$$\rho = \sum_{k=1}^{N_P} \phi_k \rho_k \tag{7.11}$$

$$U = \frac{1}{\rho}\sum_{k=1}^{N_P} \phi_k \rho_k \tag{7.12}$$

$$\mu = \sum_{k=1}^{N_P} \phi_k \mu_k \tag{7.13}$$

and T_σ is the surface tension force at the phase interface. Equation (7.10) is essentially a single phase transport equation with variable density and viscosity. The homogeneous volume conservation equation is then:

$$\frac{\partial}{\partial t}\rho + \nabla \cdot (\rho U) = S_{MS} \tag{7.14}$$

The tracking of the interface between the phases is accomplished by solving the volume fraction equation for one of the phases. For free-surface flows, this is based on the Volume of Fluid (VOF) method (Hirt and Nichols, 1981; Hirt, 1992). ANSYS CFX uses an implicit scheme in solving the volume fraction equation (ANSYS, 2013). The CFD code also has capabilities of modelling the free-surface based on the continuum surface force model of Brackbill et al. (1992).

7.1.4. Turbulence Modelling

Turbulence, characterised by high Reynolds number, consists of fluctuations in the flow field in space and time. Analysis of solutions to the Navier-Stokes equations show that turbulence develops as an instability of laminar flow (Wilcox, 1998). For a real fluid, the instabilities arise from the interaction between the non-linear inertial and the viscous terms. The Navier-Stokes equations describe both laminar and turbulent flows and a solution obtainable for industrial flows through direct numerical solution (DNS) is not currently practical. In order to numerically predict turbulence, a number of turbulence models have been established. Wilcox (1998) states that "*an ideal model should introduce the minimum amount of complexity while capturing the essence of the relevant physics*". Turbulence models are generally a modification of the unsteady Navier-Stokes equations by introduction of averaged and fluctuating quantities to yield the Reynolds Averaged Navier-Stokes (RANS) equations by averaging concepts introduced by Reynolds (Reynolds, 1894). For such a flow the instantaneous velocities are expressed by:

$$\begin{gathered} u_i(x,t) = \bar{u}_i(x) + u'_i(x,t),\ v(y,t) = \bar{v}(y) + v'(y,t), \\ w(z,t) = \bar{w}(z) + w'(z,t) \end{gathered} \tag{7.15}$$

where $\bar{u}, \bar{v}, \bar{w}$ represents the mean velocity components and u', v', w' denotes the fluctuating velocity component. In transient flows, the equations are ensemble-averaged terms of an N number of identical calculations. The RANS equations then become known as the Unsteady Reynolds Averaged Navier-Stokes (URANS) equations. Models employing the RANS and URANS equations are known as statistical turbulence models due to the implementation of the statistical averaging process. The RANS and URANS equations have additional turbulent flux terms which are called the Reynolds stresses, contained within the Reynolds stress tensor given by:

$$\tau_{ij} = -\rho\overline{u_i' u_j'} \tag{7.16}$$

which is a symmetric tensor and therefore has six independent components which arise from the nonlinear convective terms of the instantaneous equations. The averaging process was also described in Section 2.5. The combination of the four unknown mean-flow parameters (i.e. pressure and three velocity components) along with the six Reynolds-stress components yields a total of ten unknowns which are not yet closed. Closure forms the basis of the fundamental problem of turbulence in engineering. As well as the laminar model, two general categories of turbulence model are investigated in this work: Eddy viscosity turbulence models and the 2nd order closure model (i.e. Reynolds stress modelling).

The eddy viscosity models are 1st order and are based on the concept of eddy viscosity (also discussed in Section 2.5) which was first introduced by Boussinesq (Boussinesq, 1877; Schmitt, 2007). In this approximation, the Reynolds stresses are assumed to be proportional to the mean velocity gradients and the eddy viscosity μ_t by the gradient diffusion hypothesis:

$$\tau_{ij} = -\rho\overline{u_i' u_j'} = \mu_t\left(\frac{\partial U_i}{\partial x_j} + \frac{\partial U_j}{\partial x_i}\right) - \frac{2}{3}\,\delta_{ij}\left(\rho k + \mu_t \frac{\partial U_k}{\partial x_k}\right) \tag{7.17}$$

where k is the turbulent kinetic energy. The problems associated with eddy viscosity models were discussed in Section 7.1.4. However, some researchers have found merits in some of the models, particularly when by modifying the production term in closure methods such as the Re-Normalisation Group (RNG) (Chen et al., 2012) and Curvature Corrections schemes (Spalart and Shur, 1997; Skerlavaj et al., 2014). The turbulence

models under consideration in this study are now discussed briefly. The author however recommends the ANSYS CFX solver theory guide (ANSYS, 2009) for further technical details on the mathematical composition of each model along with a list of model closing coefficients which are employed in the solver.

The RNG $k-\varepsilon$ model is determined on the basis of Re-Normalisation group analysis (Yakhot et al., 1992) of the Navier-Stokes Equations which attempts to account for the different scales of motion through changes to the production term. This differs significantly from the standard $k-\varepsilon$ model where the eddy viscosity is determined from a single turbulence length scale.

The $k-\omega$ based shear stress transport (SST) by Menter (1993, 1994) provides the advantages of both the $k-\omega$ model (Kolmogorov, 1941; Wilcox, 1988) (in the near wall region) and the $k-\varepsilon$ in the free stream region. Therefore, the model benefits from using a low-Reynolds number near the wall without extra damping functions near the wall. By switching to the $k-\varepsilon$ formulation in the free stream it limits the $k-\omega$ problem that the model is too sensitive to the inlet free-stream turbulence properties. The SST model also presents a more superior prediction of the shear stress transport behaviour by limiting the over prediction of eddy viscosity. The model has found extensive application in flows with adverse pressure gradients (ANSYS, 2009).

The weakness of the eddy-viscosity models is that they tend to be insensitive to streamline curvature and system rotation and also tend to be highly dissipative. This has been reported in the research works of others (Tokyay and Constantinescu, 2005; Suerich-Gulick et al., 2006; Chen et al., 2012). Here, the poor results obtained in modelling vortex flows with the eddy-viscosity models are postulated to be a direct consequence of excessive generation of turbulence energy P_k. Based on the work of Spalart and Shur (1997) a modification of the production term has been derived to sensitise the two equation models to these effects. The approach has been reported to only require approximately 20% additional computational cost with no degradation of convergence (Shur et al., 2000). The empirical function to account for these effects is defined by:

$$f_{rotation} = (1 + c_{r1})\frac{2r^*}{1+r^*}[1 - c_{r3}tan^{-1}(c_{r2}\tilde{r})] - c_{r1} \qquad (7.18)$$

which serves as a multiplier of the production term by $P_k \rightarrow P_k \cdot f_r$ where:

$$f_r = max\left[0{,}1 + C_{scale}(\widetilde{f_r} - 1)\right] \tag{7.19}$$

and

$$\widetilde{f_r} = max\{min(f_{rotation}, 1.25), 0\} \tag{7.20}$$

where

$$r^* = \frac{S}{\Omega} \tag{7.21}$$

$$\tilde{r} = 2\Omega_{ik}\mathrm{S}_{ik}\left[\frac{D\mathrm{S}_{ij}}{Dt} + \left(\varepsilon_{imn}\mathrm{S}_{jn} + \varepsilon_{jmn}\mathrm{S}_{in}\right)\Omega_m{}^{Rot}\right]\frac{1}{\Omega \mathrm{D}^3} \tag{7.22}$$

The strain rate and vorticity tensor are defined, respectively, using Einstein's summation convention as:

$$\mathrm{S}_{ij} = \frac{1}{2}\left(\frac{\partial U_i}{\partial x_j} - \frac{\partial U_j}{\partial x_i}\right) \tag{7.23}$$

$$\Omega_{ij} = \frac{1}{2}\left(\frac{\partial U_i}{\partial x_j} - \frac{\partial U_j}{\partial x_i}\right) + 2\varepsilon_{mji}\Omega_m{}^{rot} \tag{7.24}$$

where

$$\mathrm{S}^2 = 2\mathrm{S}_{ij}\mathrm{S}_{ij} \tag{7.25}$$

$$\Omega^2 = 2\Omega_{ij}\Omega_{ij} \tag{7.26}$$

$$\mathrm{D}^2 = max(\mathrm{S}^2, 0.09\omega^2) \tag{7.27}$$

The empirical constants C_{scale}, c_{r1}, c_{r2} and c_{r3} are set to equal to 1.0, 1.0, 2.0 and 1.0 respectively. The specific limiter of 1.25 provides a good compromise for different test cases that have been considered using the SST model (Škerlavaj et al., 2014).

The 2nd order closure (second moment closure) (SMC) or Reynolds stress model (RSM) involves solving an equation for transport of the individual Reynolds stress components in the fluid. Modelling the exact production term and inherent modelling of stress anisotropies theoretically make the Reynolds stress models more suited to complex flows

(Wilcox, 1998; Zhang and Yang, 2013). The models also naturally include the effects of streamline curvature, sudden changes in strain rate, secondary motions and buoyancy (Wilcox, 1998). However, the additional complexity of this model results in a reduced numerical robustness as well as being computationally intensive. In this study, the Baseline (BSL) Reynolds stress model (RSM) is employed. The standard RSM in ANSYS CFX is based on the ε-equation (Launder and Sharma, 1974). However, it generally suffers from deficiencies as a result of the underlying ε-equation, particularly in flow separation problems and in low-Reynolds number conditions. For this reason, the BSL Reynolds stress model was developed which overcomes these issues providing a blending between the ε-equation and ω-equation formulations appropriately in a similar fashion to that of Menter's (1994) BSL $k-\omega$ model.

The final turbulence model visited in the current study is that of the Scale-Adaptive Simulation (SAS) (Menter and Egorov, 2010; Egorov et al., 2010) shear stress transport SST which is applied to the URANS equations in a transient simulation. The model resolves the turbulent length scale spectrum in unstable flow conditions. The SAS model therefore behaves like a large eddy simulation (LES) in unsteady flow regions (Cristofano et al., 2014a) while maintaining standard RANS capabilities in the stable regions. In CFX the SAS model is built on the SST which is hence called the SST-SAS model of which the latest model was presented by Egorov and Menter (2008).

7.1.5. Near Wall Turbulence Modelling

The current study deals with a wall-bounded flow where the no-slip boundary condition is applied. For flow near the wall, turbulence behaves much more differently to that across the free stream. Prandtl[30] originally proposed (Prandtl, 1925) that for flows near the solid boundary, the mixing length is proportional to the distance from the surface y_1. This is consistent with the law of the wall which can be observed in Figure 7.2 (Wilcox, 1998). Here, three zones are highlighted: the viscous sublayer, the log layer (fully turbulent wall layer) and the defect layer. The log layer, governed by the following equation:

[30] Ludwig Prandtl, a German engineer, was a pioneer in the development of rigorous systematic mathematical analyses which he used for underlying the science of aerodynamics.

$$U^+ = \frac{1}{k} ln y^+ + B \tag{7.28}$$

generally lies between y^+ =30 and y =0.1δ where δ is the boundary or shear layer thickness (Wilcox, 1998). The viscous sublayer is the region between the wall surface and the log layer where the velocity varies approximately linearly with y^+. In the wall-function approach, the viscous sublayer is bridged using am empirical formula to provide near-wall boundary conditions (e.g. wall shear stress) to the dependent variables at the near wall grid node at Δy_1 which is assumed to lie in the fully-turbulent regime 30 < y^+ < 130.

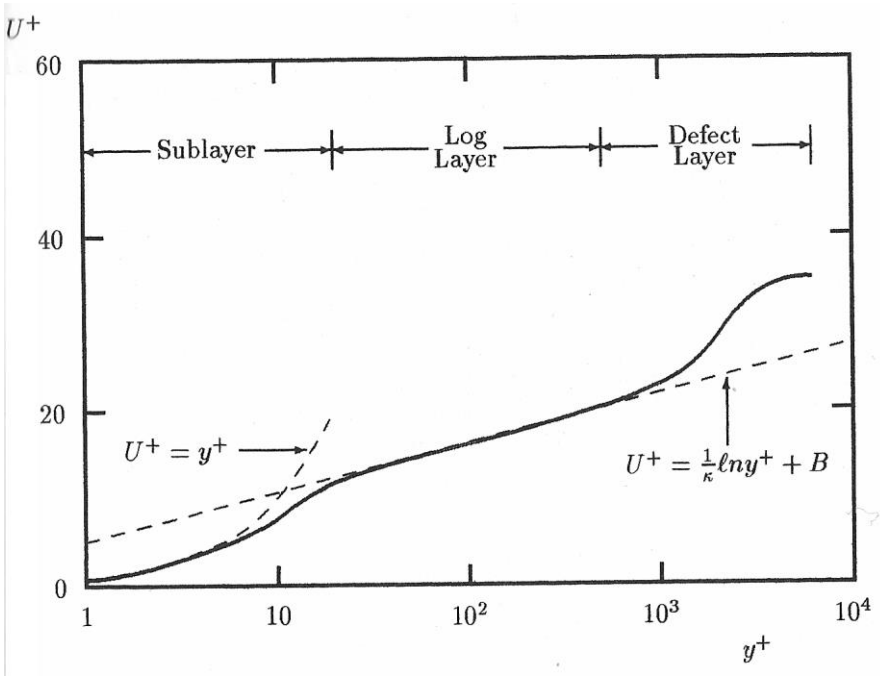

Figure 7.2: Law of the wall describing the near wall laminar sub-layer and the turbulent boundary layer (Wilcox, 1998).

However, one of the main drawbacks of the standard wall-function approach is that that the predictions depend on the location of the point nearest to the wall (y^+) and are sensitive to the near-wall meshing (Grotjans and Menter, 1998). For ε-based models i.e. RNG $k - \varepsilon$ model, a scalable wall function approach is used which imposes a limiter for y^+ =11.06 to ensure that the solver y^+ are not allowed to approach zero. The value of 11.06 is significant because it corresponds to the point of transition between the laminar sublayer and the logarithmic layer.

However, in low-Re flows, significant errors can be obtained using the scalable wall function approach as it fails to model the viscous sub-layer. For this reason, CFX developed a near-wall treatment based model that allows for $k-\omega$ to make a smooth shift from a low-Reynolds number form to a wall function formulation. This automatic near wall treatment provides integration to wall when y^+ is less than 6 and switches to standard wall function when y^+ plus is equal to or greater than 30 while providing a blending function in between. Therefore the computed wall values are largely independent of the value provided by the mesh.

7.1.6. Coupled System of Equations

The linear system of equations obtained by applying the FVM to all elements in the domain are discrete conservation equations written in the form:

$$\sum_{nb_i} a_i^{nb} \varphi_i^{nb} = b_i \tag{7.29}$$

where a denotes the coefficients of the equation, φ is the solution, b is the right hand side, i is the identifying number of the control volume and nb means neighbour (ANSYS, 2009). The whole linear equation system is given by:

$$a_i^{nb} = \begin{bmatrix} a_{uu} & a_{uv} & a_{uw} & a_{up} \\ a_{vu} & a_{vv} & a_{vw} & a_{vp} \\ a_{wu} & a_{wv} & a_{ww} & a_{wp} \\ a_{pu} & a_{pv} & a_{pw} & a_{pp} \end{bmatrix}_i^{nb} \quad \varphi_i^{nb} = \begin{bmatrix} u \\ v \\ w \\ p \end{bmatrix}_i^{nb} \quad b_i = \begin{bmatrix} b_u \\ b_v \\ b_w \\ b_p \end{bmatrix}_i \tag{7.30}$$

7.2. Computational Fluid Dynamics Methodology

7.2.1. Overview

In Chapter four, a literature review of past research work on numerical modelling of strong free-surface vortices was presented. As was discussed, many of these studies involved modelling the flow as a single phase with free-slip fixed lid to simiulate the free-surface. Despite the simplicity of this approach, the problems associated with the single phase modelling of flows with free-surface deformation were conclusive from the review of literature. In this work, free-surface deformations were included in the modelling

process using a two phase multiphase model with interface tracking. Further to the literature discussed in Sections 4.1 and 4.2, an overview of multiphase modelling using the homogeneous Eulerian-Eulerian model is reported. Although the numerical schemes are already well developed in CFX, the decision process in modelling a multiphase flow can still be a difficult one. Therefore, the aim of this section is to provide a comprehensive comparison of the numerical options available to practitioners when modelling strong free-surface vortex flows with ANSYS CFX. The comparison will be implemented by means of physical and numerical insight along with quantitative and qualitative verification of the numerical results using the experimental model data.

The purpose of this comparison will then be to judge the accuracy of the models to provide a best practice guideline whereby engineers and practitioners can make justifiable decisions when modelling multiphase flows vortex flows. An initial discussion is made on the test cases and the boundary condition methodology which is then followed by a presentation of the mesh strategies and the most economic approach to constructing the three-dimensional discretisation grid across the vortex chamber domain. This is subsequently followed by the simulation strategy describing a list of models under consideration (both steady state and transient) in a four phase process. The results are compared with the physical data obtained in Section 6.4 and finally a conclusion was made regarding the practicality of modelling using ANSYS CFX together with a summary of the best practice guidelines for strong free-surface vortex flow simulations.

7.2.2. Test Cases and Boundary Conditions

It was deemed appropriate that a single model of the vortex chamber should be used as a test case to verify the accuracy of the numerical model. By investigation of the model #4.0d1.0d, the observed circulation number $\frac{\pi}{4}$Nr was found to range from $3.76 < \frac{\pi}{4}$ Nr $<$ 25.53 and therefore comprises of a moderate range of vortex flow conditions which were deemed suitable for benchmarking purposes. Furthermore, the subsurface and surface tangential velocity profiles have been investigated for this model arrangement in Section 6.4. Numerical analysis was performed for three physical test cases in the model based on three equally varying approach flows (h/d and Q) which produce a broad range of circulation number conditions outlined in Table 7.1. A comparative study was

subsequently implemented on the numerical simulations using the results of the free-surface profile, sub-surface and surface tangential velocity profiles as well as other qualitative visual observations in the flow field.

Table 7.1 Details of the test cases modelled within the numerical modelling program.

Boundary		**Details**				
A	**Inlet**	**Boundary type**: Mass flow normal to boundary **Other details:** 10 % turbulence intensity				
		Test Cases	*A1*	0.725 l/s	h/d = 1.0 = 67 mm	N_Γ = 21.80
			A2	1.677 l/s	h/d = 2.0 = 134 mm	N_Γ = 6.38
			A3	3.111 l/s	h/d = 3.5 = 235 mm	N_Γ = 3.73
B	**Outlet**	**Boundary type**: Opening with entrainment, zero relative pressure				
C	**Walls**	**Boundary type:** No-slip smooth wall boundary				
D	**Opening**	**Boundary type:** Opening with zero pressure and direction				

The boundary condition configuration that was chosen for this work is that which assigns a mass flow or velocity at the inlet and a static pressure condition at the outlet. This arrangement maintains the highest fidelity in multiphase numerical modelling (ANSYS, 2009). For the current case however, a mass flow inlet required that an artificial condition be assigned in order to best simulate the approach flow depth. Improper specification of the inlet depth may introduce unphysically realistic momentum conditions as a result of the 'drop' of fluid at the chamber inlet as depicted see Figure 7.3 (a). Two alternative configurations were considered for the inlet. The first configuration, Figure 7.3 (b), requires the placement of a 'virtual wall' at the inlet which protrudes a small distance below the approach flow depth h/d. The second configuration Figure 7.3 (c) requires placement of the inlet at the floor of the chamber through the placement of a block, sump or 'false floor'. The use of the false floor method required that it was to be placed at an artificial distance upstream of the physical inlet to ensure that unrealistic conditions are detached from the areas of interest in the model. Due to the increased numerical effort required to compute the extra domain in addition the unnatural effects that could be

introduced in the use of the false floor technique, the inlet was instead modelled using (b) the virtual wall method.

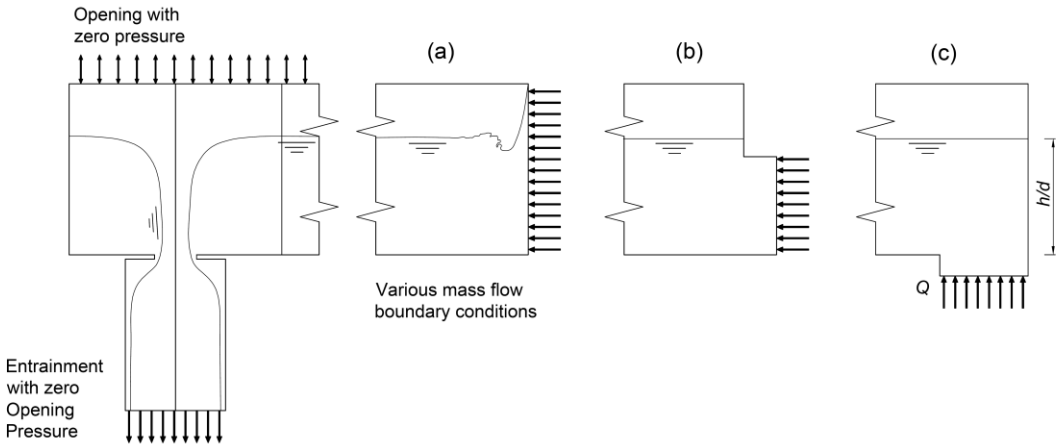

Figure 7.3: Boundary conditions for the numerical model highlighting three various mass flow normal to inlet configurations; (a) normal mass flow resulting in an unphysically realistic inlet condition, (b) false or virtual wall inlet (employed during simulations) and (c) false floor inlet.

Škerlavaj et al., (2014), from initial testing, highlighted that the effect of turbulence intensity on the numerical model tends to be negligible. As a result, the value of 10 % was assigned to the inlet turbulence intensity as it was considered to at least provide a conservative approximation of the conditions at the inlet. A zero pressure outlet boundary was initially imposed which states that fluid flow was only in one direction. Over the course of the solution, the solver placed walls at the outlet to avoid numerical instability, thus indicating that flow recirculation was present at the outlet (ANSYS, 2009). In this case, the outlet was placed at a suitable distance ($= 5d$) downstream of the orifice. This suggested that the passage of air flow in the $z-$ direction was required in order for the solution to be physically valid. Thus, an opening with a zero pressure boundary condition was imposed at the outlet which guaranteed that recirculation of each phase was permitted. The 'entrainment' option was selected which behaves in a similar manner to that of a pressure-specified opening (by maintaining stability and robustness) but does not require a flow direction to be specified. Alternatively, the solver locally calculates the flow direction based on the direction of the velocity field. This offered a more realistic representation of the physical model particularly in the annular jet region.

It was interesting to note that the annular jet in the drop shaft was mildly aerated. Although mixed flow and interphase transfer was not considered in the current study, it was observed that at a small distance downstream of the orifice (and hence the control section) an inception point manifests as a result of the local high Reynolds number and free-surface instabilities. Interphase momentum transfer would no doubt be an influencing factor in this region of the fluid and consequently it was possible that some uncertainty may have arisen in the solution by treating the two phase flow as being fully separated. Thus, this may weaken the validity of the solution, through the use of the homogeneous Eulerian-Eulerian approach in the mildly aerated region. The top of the chamber was simulated as an opening boundary condition with zero relative pressure. This permitted air flow normal to the boundary in both directions (see Figure 7.3). A no slip boundary condition was imposed to the walls of the vessel. The Acrylic physical model possesses a surface roughness of between 0.0015mm and 0.0003 mm. This relative roughness of the walls was considered to be negligible and thus the walls were modelled as a hydraulically smooth surface to permit near wall treatment of the boundary layer described in Section 7.3.5.

7.2.3. Mesh Strategy and Inflation Layer

Two types of mesh were investigated; structured hexahedral meshing and unstructured tetrahedral meshing. In general, an unstructured tetrahedral mesh tends to be much easier to generate and has less nodes than that of its structured counterpart; however, this grid approach generally suffers the cost of decreased numerical accuracy by unrealistic numerical diffusion (false diffusion). Numerical diffusion tends to be less important in structured meshes (Suerich-Gulick, 2013). Both were investigated here in order to report on the comparison for the rotating multiphase flows. ANSYS Workbench Mesh Modeller was used to discretise the domain. The software delivered a range of capabilities to prepare both unstructured and structured mesh arrangements. For unstructured operations, tetrahedrons were constructed in the fluid volume using either a patch conforming (bottom-up approach - creates surface mesh then volume mesh using Dalaunay[31] advancing front) or patch independent (top-down which creates volume mesh

[31] The triangulation is named after Boris Delaunay for his work on this topic from 1934.

and extracts surface mesh from the boundaries).

The Structured mesh generation was implemented namely using three tools.

- Sweep was used to generate prism and/or hexahedral mesh in sweepable bodies.
- Multizone used automated topology decomposition to attempt to automatically create a pure hexahedral or mostly hexahedral mesh in the geometry
- Hex-dominant meshing used an unstructured meshing approach to generate a quad-dominant surface mesh and then converts to hex-dominant mesh.

Both unstructured and structured methods permit local sizing control. In order to facilitate the above-mentioned structured mesh schemes as well as local sizing control, the domain was segmented into seven primary segments consisting of a total of ten sub-segments. Various segmentation processes were originally trialled and an iterative process determined that the most optimum segmentation approach highlighted in Figure 7.4 and 7.5. This configuration tended to be most suitable in terms of mesh generation speed and suitability for processing the various mesh schemes and sizing control. The arrangement was devised as to ensure a local radial sizing control was maintained in the air core region of the model; therefore suitable for resolving the high velocity gradients expected in this region. The primary segments are detailed in Table 7.2. In the structured case, the multi-zone mesh method provided an almost fully structured radial hex-meshing which increases in density close to the vortex core (see Figure 7.6 and 7.7). The local face sizing at the discharge orifice was used to define the core element size. The spiral arm was subsequently constructed of an ordered hexahedral mesh structure through a ‘sweep’ method. In this way, the overall vortex chamber mesh structure was appropriately aligned with the general swirling pattern of the mean flow field in the vortex.

In the unstructured mesh case, the whole fluid volume was meshed using tetrahedrons which were locally sized at the outlet. A single finely unstructured mesh case was analysed where the minimum cell size was approximately 1.5 mm in the outlet region. Details of mesh density for both the unstructured and structured mesh cases are outlined in Table 7.3.

Table 7.2 Segmentation of flow domain for the structured mesh case.

Primary Segment	Number of sub segments	Mesh method	Controls
Outlet shaft and discharge	1	Hex-dominant	Body, face and edge sizing
Central core	1	Multi-zone	body, face and edge sizing
Spiral arm	4	Sweep mesh	mapped face meshing and edge sizing
Contiguous section 1	1	Hex-dominant	body and edge sizing
Contiguous section 2	1	Hex-dominant	body and edge sizing
Inlet region	1	Sweep mesh	mapped face meshing and edge sizing
Upstream and inlet boundary	1	Hex-dominant	body and edge sizing

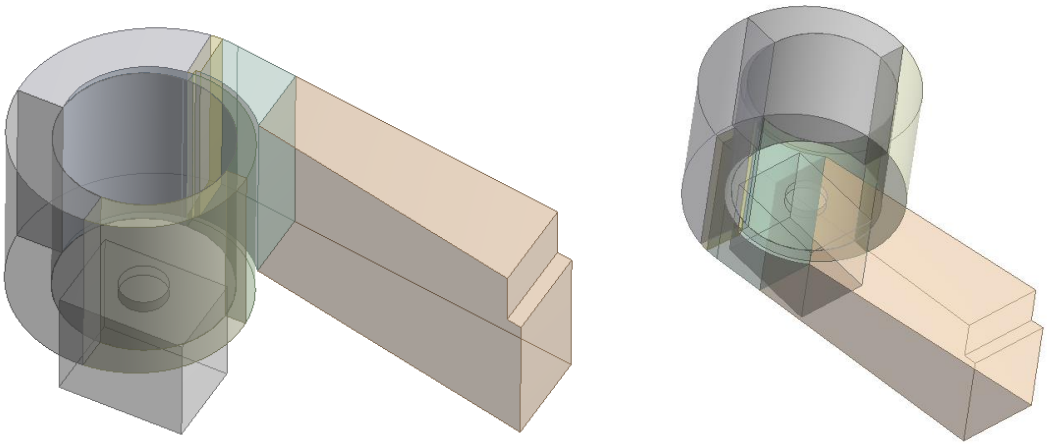

Figure 7.4: Isometric views of the segmented vortex chamber model.

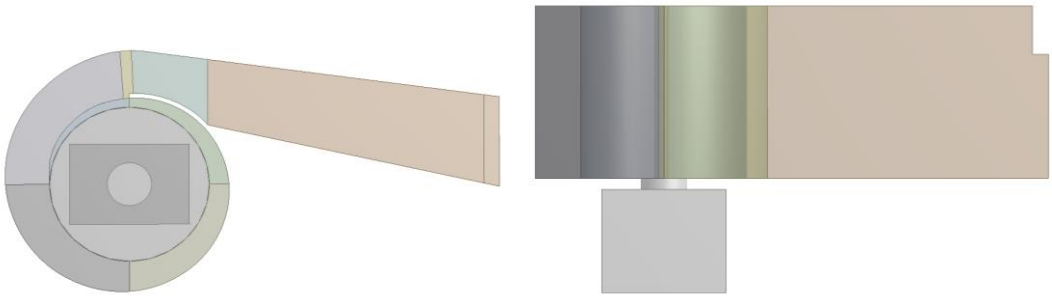

Figure 7.5: (a) Plan and (b) elevation of the segmented vortex chamber model.

Table 7.3 Overview of mesh details for the three tested cases.

Mesh cases	Min. cell size (mm)	No. of elements $\times 10^6$	No. of nodes $\times 10^6$
Unstructured Fine	1.5	2.96	0.52
Structured Coarse	3.0	1.82	1.80
Structured Medium	2.2	2.57	2.53
Structured Fine	1.0	3.18	3.15

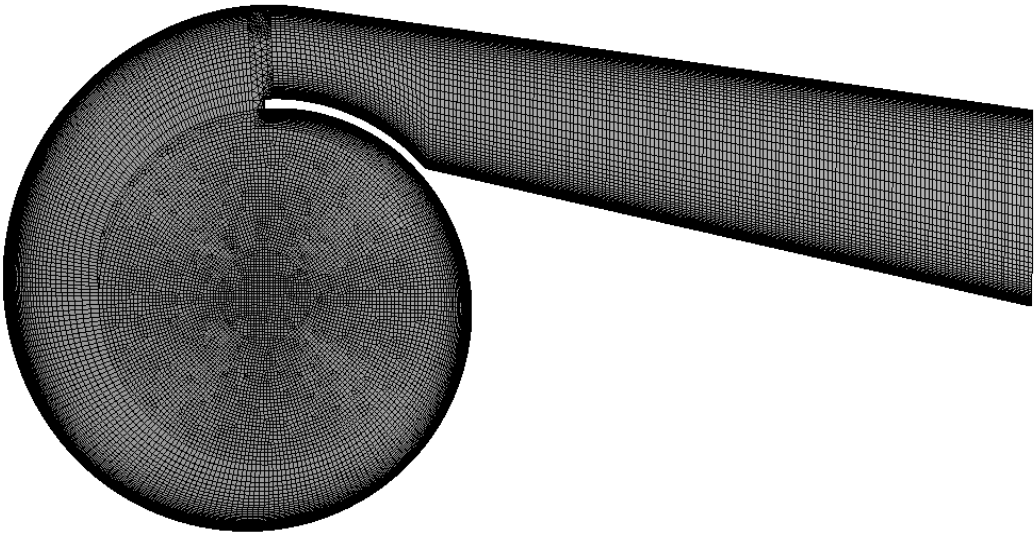

Figure 7.6: Plan view of the medium structured mesh case.

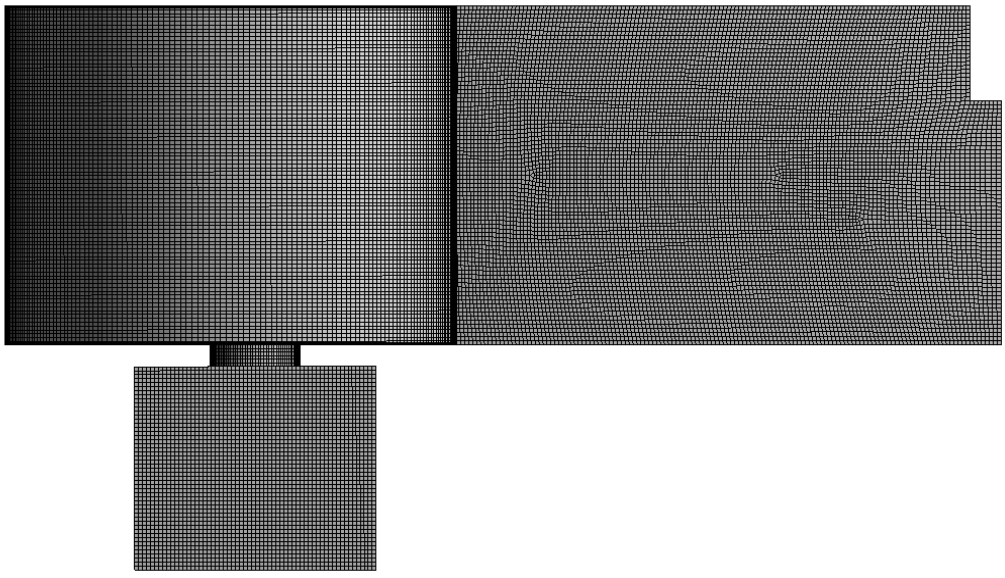

Figure 7.7: Elevation of the medium structured mesh case.

As was discussed in the literature review, a number of investigations (Gang et al., 2011; Chen et al., 2012; Dhakal et al., 2015) have neglected a proper resolution of the boundary layer. Failure to resolve the boundary layer is known to affect the accuracy of the numerical solution (ANSYS, 2009). As was discussed in Section 7.1.5, the effect of the boundary layer on a wall bounded flow in numerical simulation is characterised by the non-dimensional wall distance y^+ which is given by:

$$y^+ = \frac{u_\tau \Delta y_1}{\nu} \tag{7.31}$$

where u_τ is the frictional velocity and y_1 is the distance to the nearest wall. In order to model the boundary layer accurately for the selected turbulence models, $1 < y^+ < 6$ was enforced everywhere in order to satisfy requirements of the typical turbulence models. This was achieved by estimating the first node length from the wall by rearranging Equation (7.31) for Δy_1 by:

$$\Delta y_1 = \frac{y^+ v}{\rho u_\tau} \tag{7.32}$$

where u_τ is the frictional velocity determined by the following equation:

$$u_\tau = \sqrt{\frac{\tau_w}{\rho}} \tag{7.33}$$

and τ_w is the wall shear stress calculated from the free-stream velocity $u_{freestream}$ conditions by:

$$\tau_w = C_f . \frac{1}{2} \rho U^2_{freestream} \tag{7.34}$$

and finally C_f is the skin friction determined from the Schlichting[32] skin-friction correlation given by:

$$C_f = \left[2log_{10}Re_{freestream} - 0.65\right]^{-2.3} \text{ for } Re_{freestream} < 10^9 \tag{7.35}$$

[32] Hermann Schlichting was a German fluid dynamics engineer who's main areas of studies focused on viscous effects and air foil dynamics.

The Reynolds number in the freestream is defined by:

$$Re_{freestream} = \frac{U_{freestream} L_{boundary\ layer}}{\nu} \tag{7.36}$$

Using an estimated free-stream velocity of u = 0.2 - 0.75 m/s the suitable distance from the wall to the first node could then be calculated a priori. The effective length of the $L_{boundary\ layer}$ was calculated from the minimum circumferential length of ($L_{boundary\ layer} = 0.21$ m) in the vortex chamber which was located at the orifice perimeter. This calculation (for $1 < y^+ < 6$) requires that the first cell distance be kept between 0.05 and 0.7 mm. It was necessary to provide a smooth transition from the reduced cell size to the arbitrary free-stream cell size using an inflation layer. The layer should inflate at a gradual rate as to ensure that a suitable number of the reduced cell sizes (twenty inflation layers) remains in the boundary layer. In ANSYS meshing, an automatic inflation was available to develop the inflation layer at specified walls. The predetermined first cell distance Δy_1 was specified and an inflation growth rate of 1.2 was applied. This was easily applied to tetrahedral meshed bodies. However, the automatic inflation capability cannot be applied to hexahedral dominant mesh structures and presents significant difficulty when the boundaries of the structured mesh are refined.

In this case, a 'pseudo inflation' was applied using an edge sizing with a high bias factor (80 - 100) and a sufficient number of sizing divisions. The edge sizing was applied at vertical edges to resolve the bottom boundary and at horizontal edges to resolve the walls to first cell distances Δy_1 within pre-calculated values. Figure 7.8 highlights a closer view of the pseudo inflation technique as applied to the chamber walls.

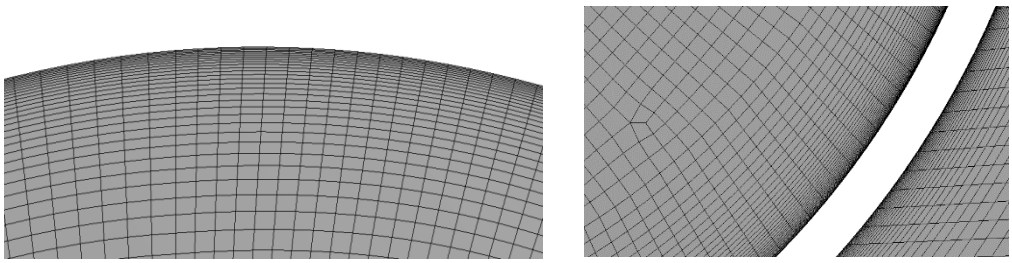

Figure 7.8: Examples of the highly refined mesh at the boundary layers of the vortex chamber walls.

7.2.4. Simulation Strategy and Computation

In order to efficiently investigate the numerical model using the various turbulence closure methods for both steady state and transient approaches, a logistical CFD methodology had to be developed. This was finalised in a novel four phase process which, as far as the author is aware, was not performed in past studies on numerical modelling of vortex flows. The approach differs in that it is ordered sequentially to isolate and discard weak modelling methods and promote more suitable methods. So far, no multiphase numerical modelling study of a vortex flow taking into account the mesh sensitivity, steady and transient turbulence and time step sensitivity has been performed in the current literature. The four phase process is outlined as follows:

Phase 1 – Mesh Sensitivity. Both unstructured and structured schemes outlined in Table 7.3 were investigated using the standard shear stress transport model. In past studies, the standard SST was shown to compute the flow field reasonably well for a low computational expense (Škerlavaj et al., 2014). Therefore the results of Phase 1 will help distinguish a case when the solution is essentially independent of mesh density.

Phase 2 – **Steady State Turbulence Modelling.** In phase two, the laminar and four candidate turbulence models are investigated and compared using a steady state approach. The steady state comparison will distinguish the most suitable turbulence models which can then be further modelled in the transient URANS approach.

Phase 3 – **Transient Turbulence Modelling.** Finally the selected turbulence models are investigated in a transient numerical scheme using three varying time-steps. The aim of phase three is to identify a case where the solution is independent of the time step as well as the accuracy and practicality of the tested turbulence models.

Phase 4 – **Test Cases**. Using the best-practice guidelines established from phases 1 - 3, the test cases for three of the approach flow conditions are analysed and compared to the physical data in detail.

Phases 1 – 3 (outlined in Table 7.4) were analysed first by comparing the physical and numerical data to the test case A3 for (a) the tangential velocity distribution for a sub-surface depth z/d = 1 and (b) the free-surface profile. Both the tangential and free-surface profiles were checked against available data that spanned from the inlet to the orifice.

Test case A3 provides the most turbulent conditions both at the inlet and at the orifice as well as increased transient conditions due to a decrease of the circulation number. Therefore it was considered that it would be only necessary to carry out an initial comparison of Phases 1 - 3 based on this single test case to avoid excessive computational effort. Subsequently, the remaining test cases (A2 and A1) are investigated using the remaining available experimental data.

Table 7.4 Computational matrix for modelling Phases 1 - 3. Real simulation time for transient simulations is 40 seconds. Transient simulations initiated from previous solution results files are simulated for an additional 10 seconds. Each simulation performed on A3 test case.

	Simulation Name	Mesh Type	Turbulence Model	Stationary or Transient	Initial Conditions from:	Time Steps (s)
Phase 1	SST_Unstruct_F	Unstruct_F	SST	St	New	Auto
	SST_Struct_C	Struct_C	SST	St	New	Auto
	SST_Struct_M	Struct_M	SST	St	New	Auto
	SST_Struct_F	Struct_F	SST	St	New	Auto
Phase 2	Laminar_St	Struct_F	Laminar	St	New	Auto
	RNG $k-\varepsilon$ _St	Struct_F	RNG $k-\varepsilon$	St	New	Auto
	SST – CC_ St	Struct_F	SST – CC	St	SST_Struct_F	Auto
	BSL – RSM_ St	Struct_F	BSL – RSM	St	SST – CC_ St	Auto
Phase 3	SST – CC_ T0.1	Struct_F	SST – CC	Tr	New	0.100
	SST – CC_ T0.01	Struct_F	SST – CC	Tr	New	0.010
	SST – CC_ T0.005	Struct_F	SST – CC	Tr	New	0.001
	BSL – RSM_ T0.1	Struct_F	BSL – RSM	Tr	SST – CC_ T0.1	0.100
	BSL – RSM_ T0.01	Struct_F	BSL – RSM	Tr	SST – CC_ T0.01	0.010
	BSL – RSM_ T0.005	Struct_F	BSL – RSM	Tr	SST – CC_ T0.005	0.005
	SAS – CC_ T0.1	Struct_F	SAS – CC	Tr	SST – CC_ T0.1	0.100
	SAS – CC_ T0.01	Struct_F	SAS – CC	Tr	SST – CC_ T0.01	0.010
	SAS – CC_ T0.005	Struct_F	SAS – CC	Tr	SST – CC_ T0.005	0.001

F = Fine, C = Coarse, M = Medium, Unstruct = Unstructured, Struct = Structured, St = Steady State, Tr = Transient

Table 7.5 Computational matrix for Phase 4

	Simulation Name	Mesh Type	Turbulence Model	Initial Conditions from:	Simulation Time (s)
Phase 4	SST-CC_Tr_0.01_A2	Struct_F	SST-CC	New	25
	SST-CC_Tr_0.01_A1	Struct_F	SST-CC	New	20
	BSLRSM_Tr_0.01_A2	Struct_F	BSLRSM	SST-CC_Tr_0.01_134	25
	BSLRSM_Tr_0.01_A1	Struct_F	BSLRSM	SST-CC_Tr_0.01_67	20

In Phase 2, the initial conditions stated by 'New' in Table 7.4 were initiated from zero velocity and pressure, where the volume fraction of water was zero everywhere. The false time step approach (discussed in Section 7.1.1) was then progressed for the steady state model which was treated as an empty vessel. An automatic time scale was enabled in the model which determines a conservative time-scale Δt based on the global length and velocity scales. Mesh adaptation was ignored in the current analysis as its effect on improving the solution was found to be negligible in initial studies. To obtain a converged solution in the steady state analysis, the target value of the normalised residual for each flow variable was set to 10^{-5}. The velocity at a point near the vortex core ($x = 1d, y = 0, = 1d$) as well as the normalized residuals are monitored in each simulation.

In Phase 3, the transient simulations were initiated in a similar fashion to the steady state procedure. A second order Euler backward scheme was employed. The turbulence numerics were modelled using higher order schemes. A conservative physical simulation time of $t = 40$ seconds starting from a 'new' initial condition was chosen for all transient simulations based on laboratory observations of the A3 test case. Here, the time between pump start at $t = 0$ and steady state development of the vortex was determined to be approximately 31 - 36 seconds. In order to reduce file size, the essential flow variables were obtained for every 5 time steps. In phase 4, the A2 and A1 test cases were modelled for a simulation time of 25 and 20 seconds respectively.

The complexity of the numerical models in the CFD program ranged significantly, particularly for the transient simulations as a result of the combined cell populations ($> 3 \times 10^6$), multiphase consideration and increased numerical effort in the advanced turbulence models (e.g. SMC approach). In order to preserve a realistic time frame for the CFD program, 60,000 wall-clock hours of high performance computing (HPC) time was

secured at the Irish Centre for High-End Computing (ICHEC). ICHEC is Ireland's national high performance computer center which provides HPC time to users in academia and industry through the Fionn supercomputer (see Figure 7.9). Fionn is a heterogeneous machine made up the following four components:

1. The Thin component is an SGI ICE X system of 320 nodes or 7680 cores made of 2.4GHz Intel Ivy Bridge cores. Each node has 2×12 core processors, 64GB of RAM and is connected using FDR InfiniBand. This amounts to 20TB of RAM across the partition.
2. The Hybrid partition contains 32 nodes. Each of these nodes has 2x10 core 2.2GHz Intel Ivy Bridge with 64GB of RAM. This partition has accelerators from Intel and NVIDIA. 16 nodes have 32 Intel Xeon Phi 5110P's while the other 16 have 32 NVIDIA K20X's.
3. The Fat section is an SGI UV2000 where 1.7TB of RAM is accessible to 112 cores of Intel Sandy Bridge (14×8 cores processors) and 2 Intel Xeon Phi 5110P's.
4. The final component contains a set of service and administrative nodes to provide user login, batch scheduling, management, tape backup, switches, etc. Storage is provided via a DDN SFA12k-20 with 560TB of capacity to all components of the machine via a Lustre filesystem.

Figure 7.9: Fionn supercomputer at ICHEC (Image from www.ichec.ie/infrastructure/fionn)

CFD simulations are submitted to Fionn using WinSCP (Windows Secure CoPy) which is a secure shell (SSH) file transfer protocol (SFTP) client used to make file transfers between a local and a remote computer. ICHEC provides 100GB of storage in the project working directory. The PuTTY client is used to provide commands to Fionn. The commands are prompted by submitting PBS scripts identifying necessary job details. 24 cores (1 node) are used for steady state simulations and 48 cores (2 nodes) are used for transient simulations. In some cases, 96 cores were used to compute transient RSM simulations and in one case a staggering 120 cores were required. The results of the models are post processed in CFX post using a HP Pavillion 500-326na Desktop PC with a 64bit operating system, 6GB RAM powered by a quad-core AMD A8-6500 APU and AMD Radeon R7 240 graphics card with 1TB storage.

7.3. Results and Discussion

In this section the results of the multiphase numerical model are presented and discussed. Results of Phases 1 – 3 are firstly presented followed by a summary of the individual phases to reflect on the observations and to establish the initial best-practice guidelines accordingly. The results of Phase 4 are then presented to appraise the performance of the selected models for various hydraulic approach flows. In conclusion, the best-practice guidelines will be presented in a textual format based on the findings of the ANSYS CFX numerical code comparative study. Note: Where errors are discussed in the numerical model results, this refers to a percentage error determined on the basis of the experimental value. Throughout the graphs it can be noted that there is a break in the numerical data as a result of the presence of the inlet wall. A dotted line has been placed in each graphs to further highlight the walls position (see Figure 7.10 and 7.11 for example).

7.3.1. Phase 1 - Mesh Sensitivity

The response of the numerical solution to global mesh refinement using the standard shear stress transport (SST) model is presented in Figure 7.10 and 7.11 for the free-surface and tangential velocity distribution respectively. The poor performance of the finely unstructured tetrahedral mesh was immediately noticeable. Although the position and centrality of the simulated vortex structure was relatively accurate, the location of the air

water interface was severely under predicted. An error of 43 % was observed at the inlet and far-field water surface profile. The radial position of the vortex core at the outlet was over predicted by 68 %. It was concluded that a significant amount of numerical diffusion (false diffusion) was taking place across the core region as a result of the tetrahedral mesh not properly aligned with the general flow pattern of the vortex. The higher levels of diffusivity exhibited in the numerical simulation was significantly higher than that of the true medium therefore limiting the generation of the tangential velocity gradient radially in the chamber. As a result of this false diffusivity, the results manifested as a smeared tangential velocity gradient of larger magnitude and lower approach flow depth with an extensive air core diameter. It is therefore suggested that unstructured mesh systems are to be avoided at all costs when modelling vortex flows or any strongly curving flow for that matter. By aligning a structured mesh with the general flow pattern, the solution was improved significantly (error in predicting the inlet water level is reduced to 27 % for the coarse mesh).

Using the structured mesh cases, the solution appeared to become independent of the mesh size both at the water surface and for the tangential velocity profile when the fine mesh was used. The largest velocity gradients were to be expected at the outlet both in the axial, radial and circumferential directions. By taking this section as a control, it can be stated that, for the SST turbulence model, it should be ensured that the mesh size at the orifice should be no greater than 1.5 % of the diameter of the outlet in order to obtain mesh independent numerical results in the dominating core region. However, even at this result, the solution still exhibited 27 % errors in predicting the free-surface and 100 % error in over predicting the tangential velocity distribution, particularly in the far-field.

Although a high-order advection scheme should reduce a majority of the numerical smearing error, artificial numerical diffusion can still account for significant error even in structured grids. In addition, based on the findings of previous studies (Chen et al., 2012; Suerich-Gulick, 2013; Sarkardeh et al., 2014) it was also likely that standard RANS formulations overestimate the turbulent kinetic energy, turbulent dissipation rate and turbulent viscosity in the vortex. As a result, unrealistic levels of eddy diffusivity tend to smear the tangential velocity gradient thus not permitting the vortex from developing in a physically realistic manner. Moreover, two-equation eddy-viscosity models are highly

dissipative meaning that they are not likely to be triggered into unsteady mode unless the flow instabilities are strong (Davidson, 2009). The fine mesh scenario was subsequently analysed in Phase 2 in order to investigate the effects of more advanced turbulence formulations accordingly.

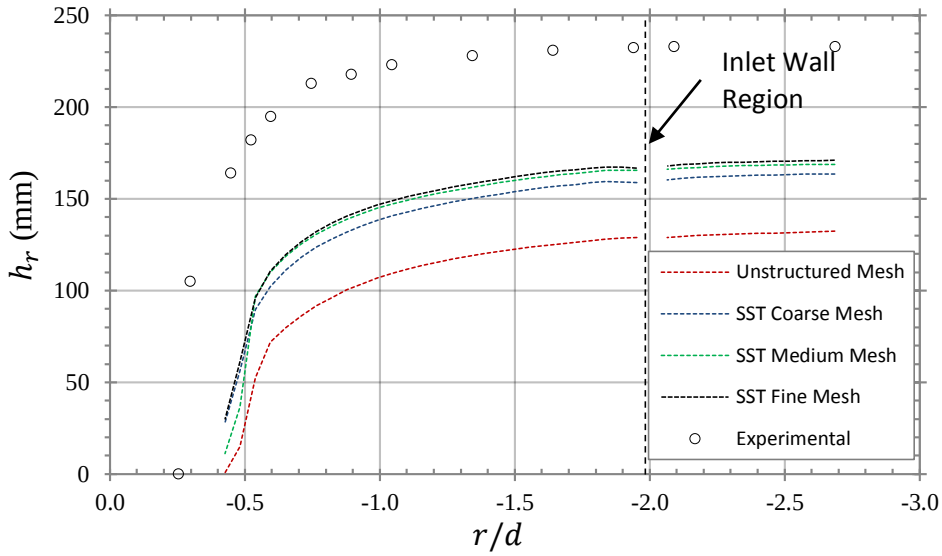

Figure 7.10: Mesh sensitivity analysis comparing the unstructured and structured mesh schemes to the experimental tangential velocity data for the A3 test case. Data is presented for the water surface ranging from the inlet at $r/d = 2.7$ to the orifice at $r/d = 0$.

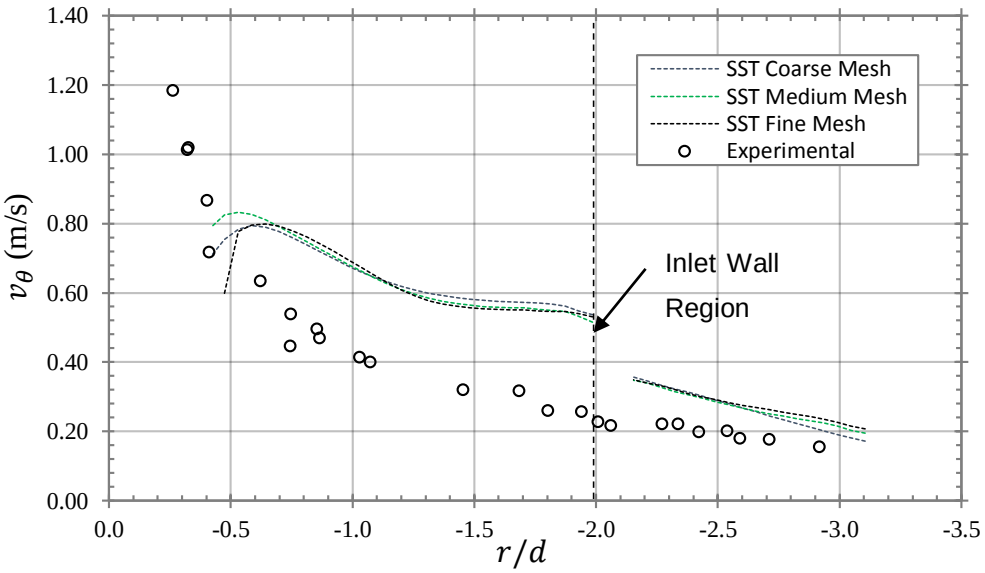

Figure 7.11: Mesh sensitivity analysis comparing the unstructured and structured mesh schemes to the experimental tangential velocity data for the A3 test case at a sub-surface depth of z/d = 0.5. Data is presented for the water surface ranging from the inlet at $r/d = 2.7$ to the orifice at $r/d = 0$.

7.3.2. Phase 2 – Steady State Turbulence Modelling

The results of the Laminar, RNG $k-\varepsilon$, SST, SST-CC and BSL RSM obtained from the finely structured mesh case are presented together with the physical data in Figures 7.12 and 7.13 for the free-surface and tangential velocity distribution at z/d = 0.5. In summary, the results show again that the position and centrality of the vortex agrees well with the experimental data for all turbulence models. Figure 7.14 (a − f) further presents a qualitative comparison of the free-surface using an iso-surface plotted for a water.volume ϕ_w fraction of 0.5. It can be observed from these figures that the symmetry of the vortex structure was also very well maintained. In a number of model presentations there was evidence of free-surface instabilities developing at the water surface. This observation provides an early visual indication that the steady state model was probably unable to resolve the transient features of the flow field. From Figure 7.12 and Figure 7.13 it is shown that each turbulence model exhibits differing results in predicting both the free-surface and tangential velocity. The laminar solution provides a reasonable prediction of the general shape and position of the vortex structure. It was interesting to note that the laminar solution yields similar results to the SST model when predicting the free-surface but increases the accuracy of predicting the tangential velocity by 17 %.

Both Figures 7.12 and Figure 7.13 further highlight that the RNG $k-\varepsilon$ exhibits extremely poor performance compared to the other tested models. The model appeared to show large discrepancies in the water surface at the inlet and on approaching the vortex core. A similar finding was made by Škerlavaj et al., (2014) where the vortex core is observed to be quite wide.The model also significantly overestimates the tangential velocity distribution and furthermore predicts the tangential velocity distribution to be almost constant. This contradicts the results of Chen et al. (2012), at least when simulating strong vortex flows. In their work Chen et al. (2012) compared the RNG $k-\varepsilon$ formulisation to that of the standard $k-\varepsilon$ and therefore the results may be misconceiving and detrimental to the solution when employed in industrial cases (Dhakal et al., 2015).

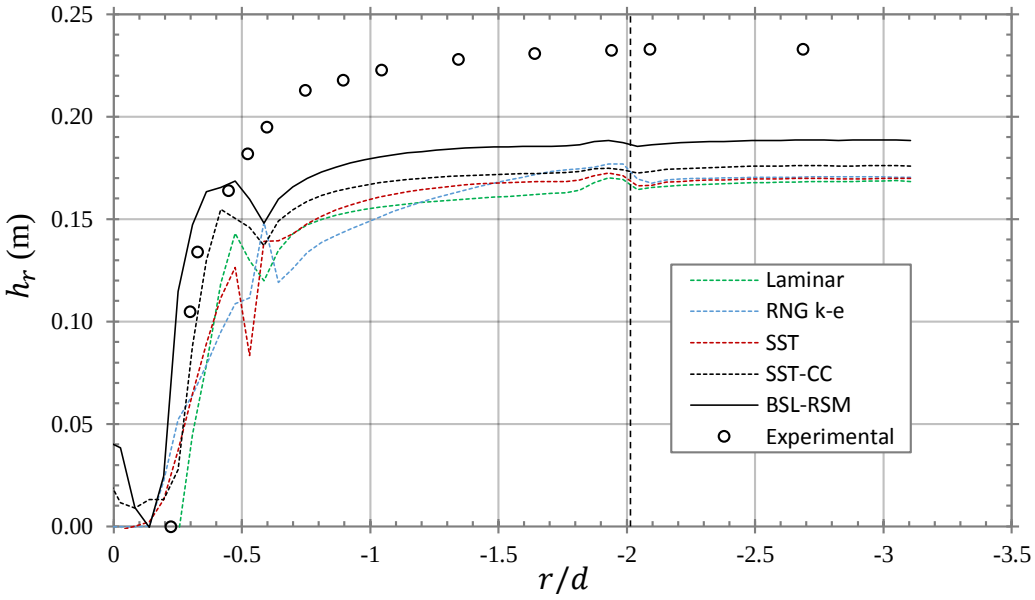

Figure 7.12: Steady state turbulence modelling comparison for the finely structured mesh scheme for the A3 test case. Data is presented for the water surface ranging from the inlet at $r/d = 2.7$ to the orifice at $r/d = 0$.

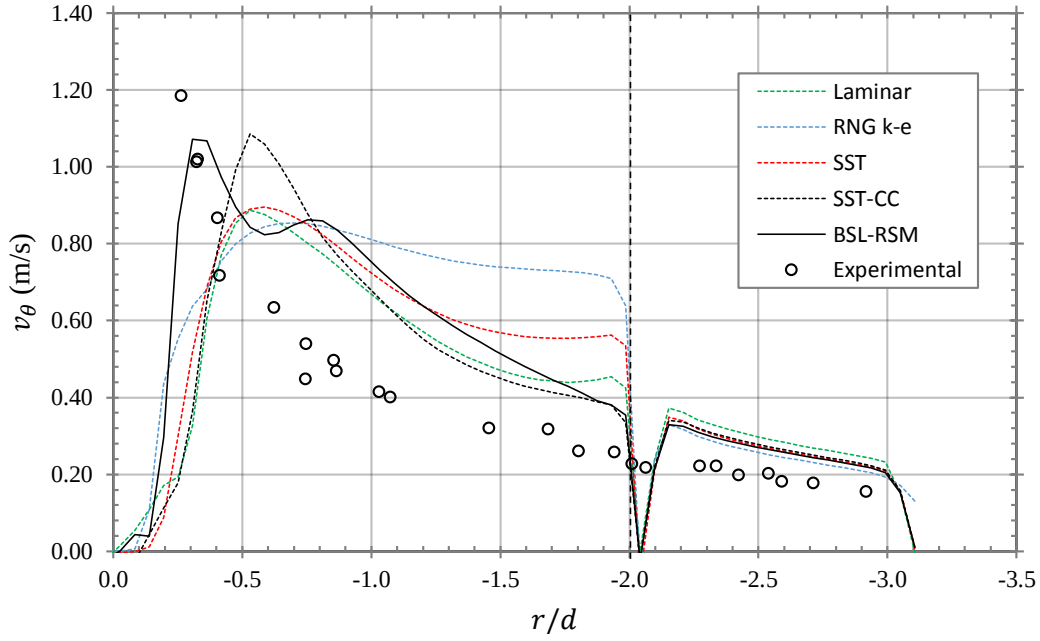

Figure 7.13: Steady state turbulence modelling comparison of tangential velocity data for the finely structured mesh scheme for the A3 test case at a sub-surface depth of z/d = 0.5. Data is presented for the water surface ranging from the inlet at $r/d = 2.7$ to the orifice at $r/d = 0$. Note, the recution of the profile to zero values in the region of $r/d = 2$ complies with the position of the inlet wall, hence, the no slip boundary condition comes into effect.

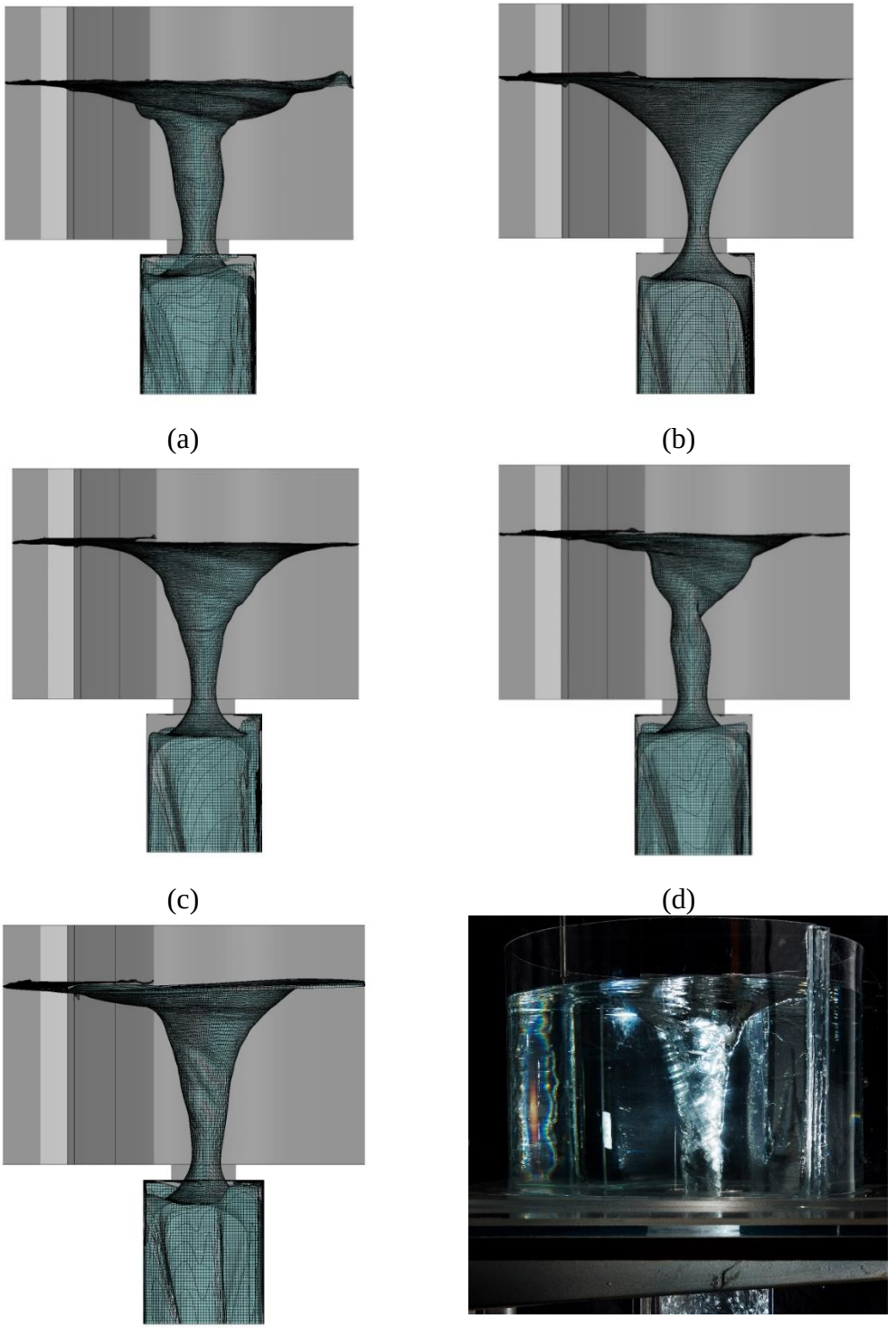

Figure 7.14: Comparison of results for the A3 test case with the laminar and various turbulence models; (a) laminar, (b) RNG $k-\varepsilon$, (c) SST, (d) SST-CC, (e) BSL RSM and (f) physical model. The free-surface is resolved by plotting an isosurface at a water.volume fraction of 0.5.

It is pondered that, regardless of the re-normilisation group (RNG) process, the turbulence model nonetheless over predicted the turbulence through excessive production of eddy viscosity and turbulent kinetic energy k in the vortex core region (see Figure 7.15 and 7.16). Furthermore, its inability to correctly model areas of adverse gradients was limiting the application of the model in various regions.

The standard SST model reduced the over generation of eddy viscosity (see Figure 7.15). As a consequence of the locally large values of eddy viscosity, standard RANS models failed to resolve small eddy structures. By inclusion of the curvature correction CC option (Spalart and Shur, 1997; Shur et al., 2000) in the SST model, it was shown that both the eddy viscosity and the turbulence kinetic energy was substantially reduced (Figure 7.15 and 7.16). As a result, the overall vortex structure and tangential velocity gradient developed in strength as was observed in Figure 7.12 and 7.13. Therefore, for just a 10 % increase in computational time, a significant increase in the computational accuracy could be obtained through the use of the CC option.

The BSL Reynolds Stress model appeared to present the most accurate solution of all the tested turbulence models in Phase 2. By using this second order moment closure (SMC) method, the errors in predicting the free-water surface are reduced to approximately 19 %. The solution however, still suffers from an over prediction of the tangential velocity field in the mid-field, but the prediction of the near-field peak tangential velocity was improved substantially. The RSM naturally included the effects of streamline curvature, sudden changes in the strain rate, secondary flows or buoyancy compared to turbulence models using the eddy-viscosity approximation. However, the superiority was traded for a 20 % increase of computation time which can be regarded as reasonable for a steady state model.

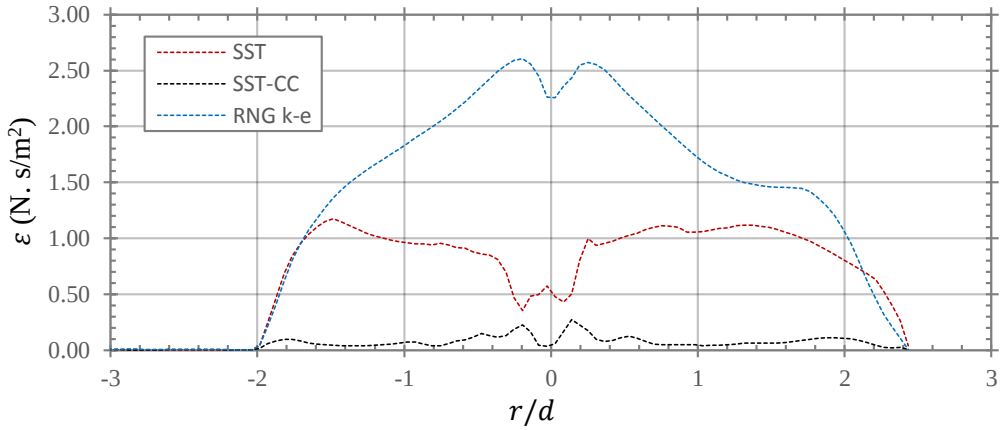

Figure 7.15: Prediction of eddy viscosity across the vortex core for the three tested eddy viscosity models at z/d = 0.5.

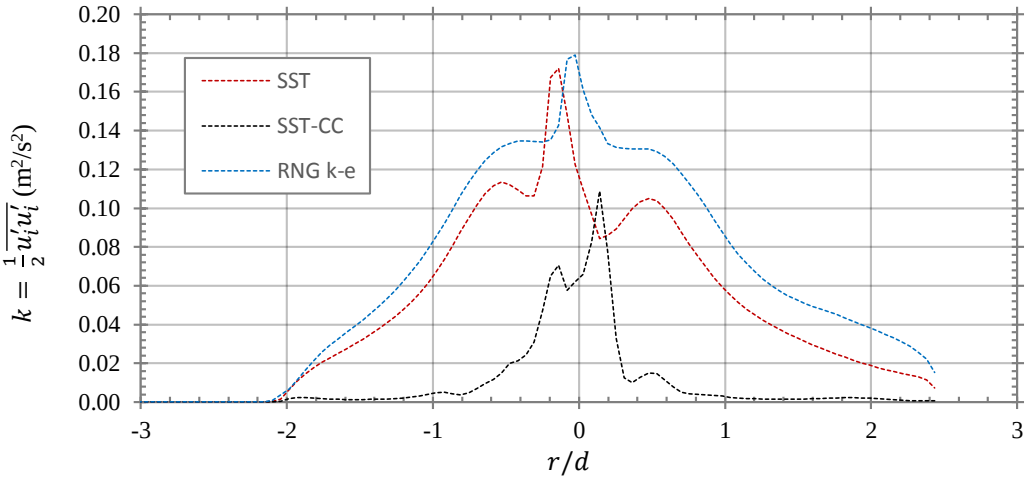

Figure 7.16: Prediction of turbulent kinetic energy across the vortex core for the three tested eddy viscosity models at z/d = 0.5.

Concluding from Phase 2, both the BSL RSM and the SST-CC models are recommended for modelling flows strong streamline curvature. Nonetheless, the models still exhibit significant discrepancies in predicting the tangential velocity field and water surface profile. Returning to a note that was made earlier in this section regarding local unsteadiness, the qualitative presentation of the various free-surface interfaces in Figures 7.14 confirm the appearance of free-surface instabilities/waves and oscillations in the multiphase flow. Such phenomena can be excessively large as to be modelled accurately with a steady state approach. This is further reinforced by observing the steady state residual plots for the SST-CC and BSL RSM in Figure 7.17. It can be seen that none of

the variable values achieved the desired convergence of 1.00E-05 but instead settled around a fluctuating high residual level. This fluctuation was a direct indication of transient behaviour in the flow field. By observing the monitor point for the radial velocity near the vortex core (Figure 7.18) the transient behaviour in this region was apparent in the fluctuations of the radial velocity component. In conclusion, the unsteady features in the flow field are probably excessively large and therefore cannot be properly resolved using a steady state model. It was concluded that further transient modelling of the multiphase flow model was required to improve solution accuracy further.

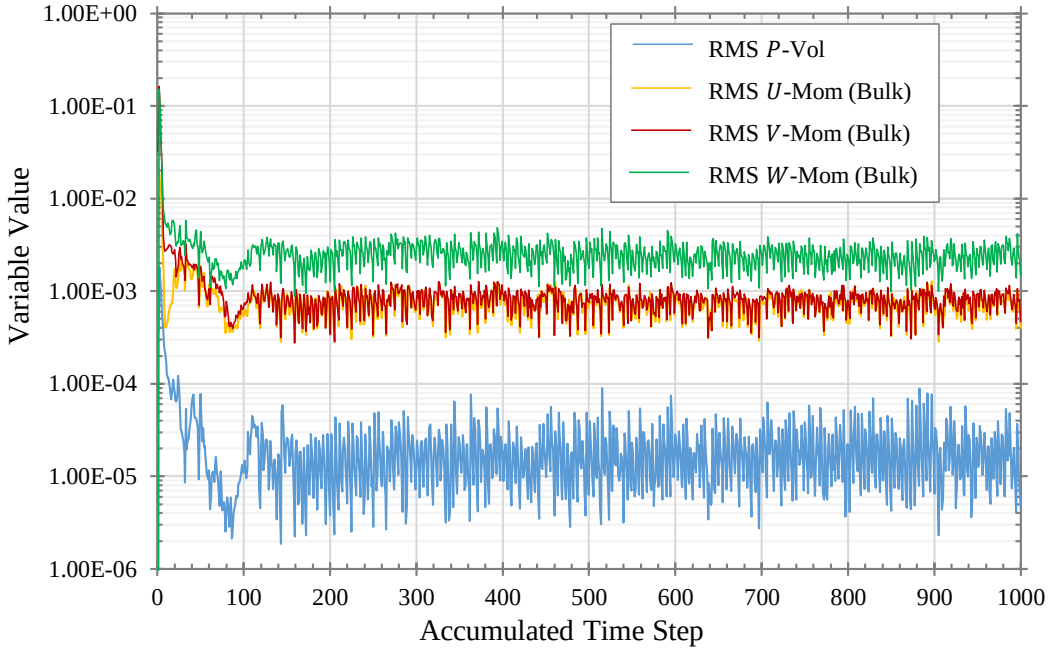

Figure 7.17: Residual plot for the SST-CC case. 1000 time steps computed in 3 hours and 47mins using 24 cores.

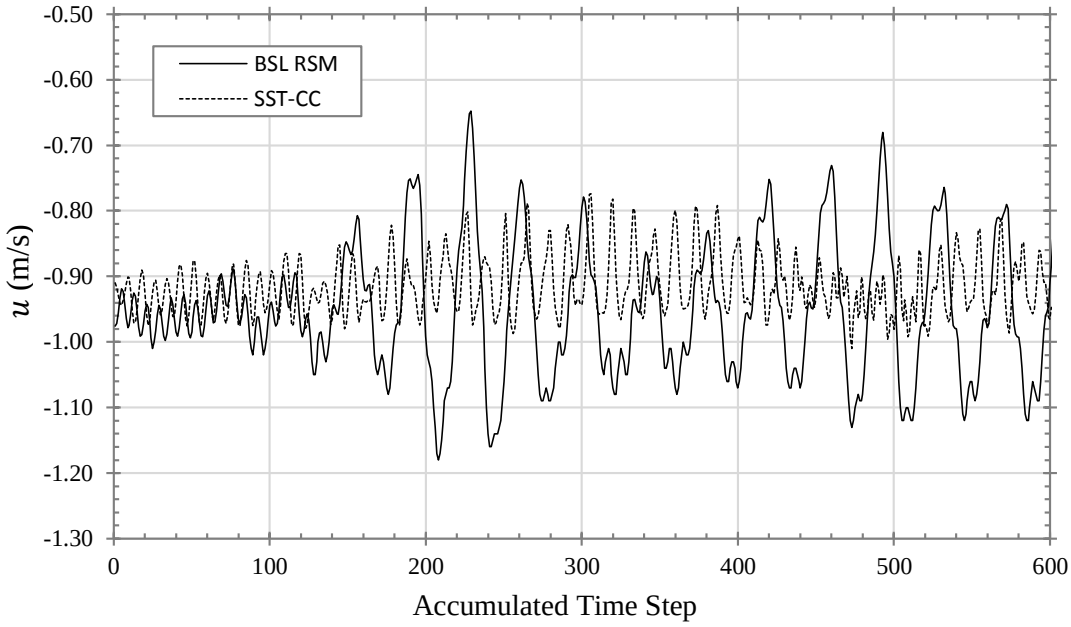

Figure 7.18: Radial velocity fluctuation at the three-dimensional co-ordinate $\frac{x}{d}, \frac{y}{d}, \frac{z}{d} = 1, 0, 1$

7.3.3. Phase 3 - Transient Turbulence Modelling

It was concluded from Phase 2 that reasonable performance can be gained from CFD simulations using the SST with curvature correction in addition to using the second moment closure method. Furthermore, by observing the residual plots, it was evident that macro unsteady features which manifest as velocity and pressure fluctuations were causing the steady state solution to converge poorly. In order to properly resolve these unsteady features, the flow field was modelled using the transient URANS and SMC unsteady turbulence formulisations. In this section the results of the SST-CC, SAS SST-CC and the BSL RSM are employed. The effect of the time step on the solution is also investigated. The results of this phase are presented in Figures 7.19 - 7.22.

As an initial comment, the effect of modelling the unsteady flow field has been shown to increase the simulation accuracy for both the tangential velocity and free-surface predictions. The SST-CC accuracy improves by approximately 38 % and 11 % in predicting the mid-field tangential velocity and inlet water surface respectively. A noticeable improvement of the model was observed in all figures in predicting the near-field free-surface and tangential velocity profile. The tangential velocity profile, unlike those observed for previous steady state formulations (Figures 7.10, 7.11 and 7.13),

resembles that of a potential vortex distribution with a sharp decrease to zero when $r/d < 0.5$ which is typical of a strong full air core vortex. Overestimations of the tangential velocity field, similar to that observed by Škerlavaj et al., (2014) can bee seen in Figures 7.19-7.21. The effect of the time step on the tangential velocity profile in all turbulence models appeared to have little impact on the numerical accuracy, particularly below a time step of $\Delta t = 0.01$ s. This finding was in close agreement with the observations made by Škerlavaj et al., (2014). The water surface profile converged towards the experimental values when the time step was reduced. However, in the SAS-CC model, when the time step was reduced from 0.01 s to 0.005 s, the free-surface prediction diverged.

By an interrelationship of each turbulence model in Figure 7.22 (a) and (b) illustrates that there is virtually no difference between the SST-CC and SAS-CC formulations which was also observed by Škerlavaj et al., (2014) in their analysis of the circumferential velocity distribution. It is concluded that the unsteadiness in the flow field was not large enough as to permit the merits of the SAS-CC model to take effect and instead reproduces similarities of a low fidelity URANS solution. This was also said to be the case in (Škerlavaj et al., 2014). The BSL RSM achieved the highest solution accuracy in both the free-surface and tangential velocity distribution prediction. Errors in predicting the free-surface and the tangential velocity are found to be 12 % and 22 % respectively. The main drawback when employing the BSL RSM in a multiphase approach is the likelihood of failure due to numerical instability. In order to avoid this, the simulations had to be performed using double precision[33]. The double precision consequently increases computation time significantly which was already a significant problem when performing SMC simulations. The end result was a substantial increase in computation time (i.e. 1 day and 21 hours for 0.01s time steps using 96 computer cores). When employing the SST-CC method, a similar simulation could be performed in just 8 hours using 72 cores. The small 2 - 3 % increase in accuracy using the BSL RSM approach is thus not a very economic choice when performing such industrial simulations unless accuracy and minimum uncertainty is absolutely necessary.

[33] Double-precision floating-point format is a computer number format which occupies 8 bytes (64 bits) in computer memory and represents a wide, dynamic range of values by using a floating point. The precision complies with a significand of approximately 16 decimal digits.

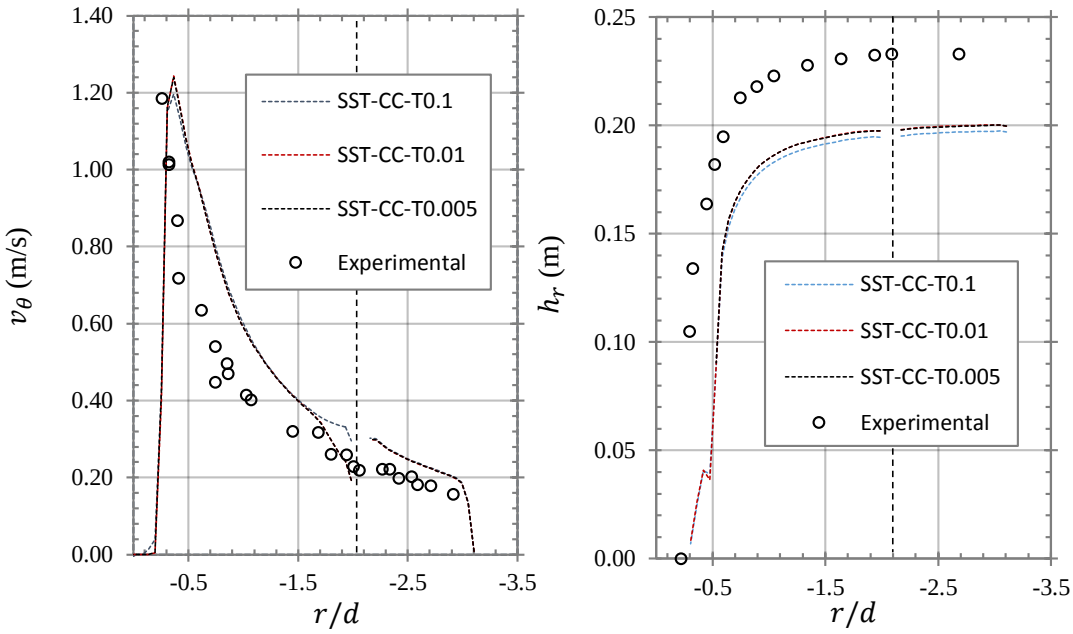

Figure 7.19: SST-CC Transient modelling comparison of (a) the tangential velocity solution data at z/d = 0.5 and (b) free-surface solution data and solution sensitivity to time step for the A3 test case. Data is presented for the section spanning from the inlet at r/d = 2.7 to the orifice at r/d = 0.

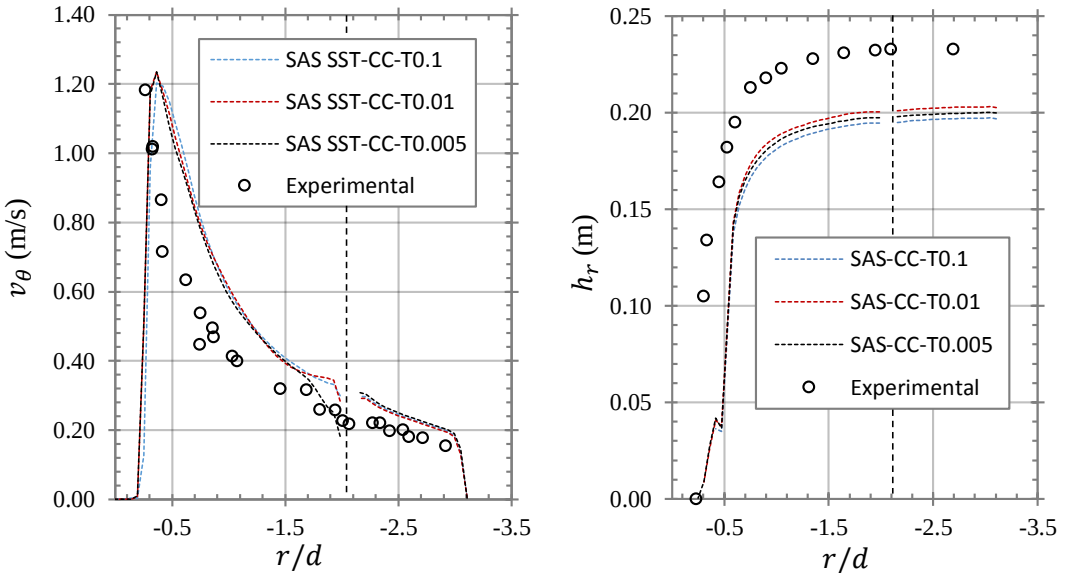

Figure 7.20: SAS SST-CC Transient modelling comparison of (a) the tangential velocity solution data at z/d = 0.5 and (b) free-surface solution data and solution sensitivity to time step for the A3 test case. Data is presented for the section spanning from the inlet at r/d = 2.7 to the orifice at r/d = 0.

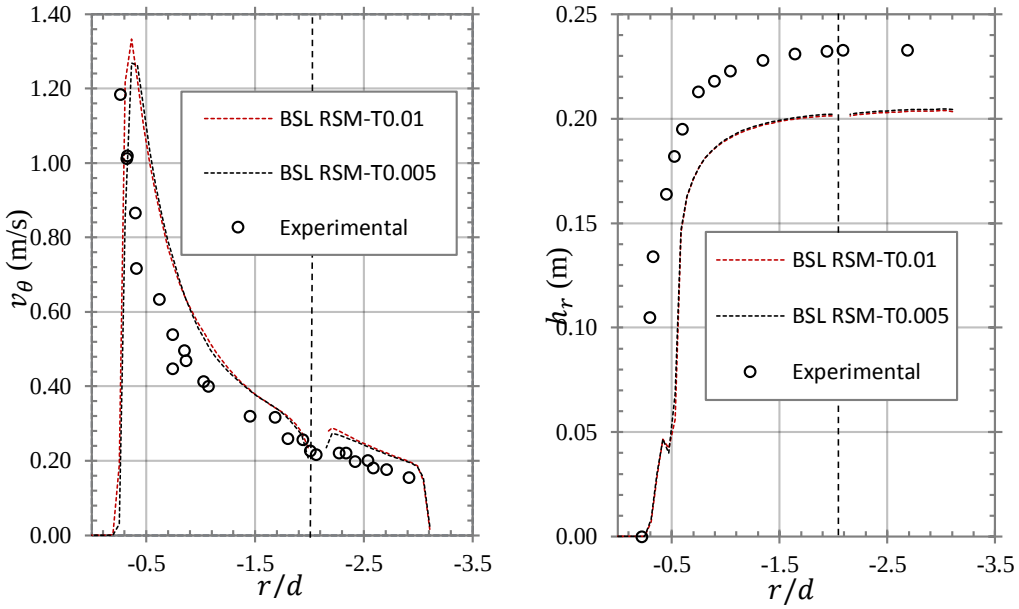

Figure 7.21: BSL RSM transient modelling comparison of (a) the tangential velocity solution data at z/d = 0.5 and (b) free-surface solution data and solution sensitivity to time step for the A3 test case. Data is presented for the section spanning from the inlet at r/d = 2.7 to the orifice at r/d = 0.

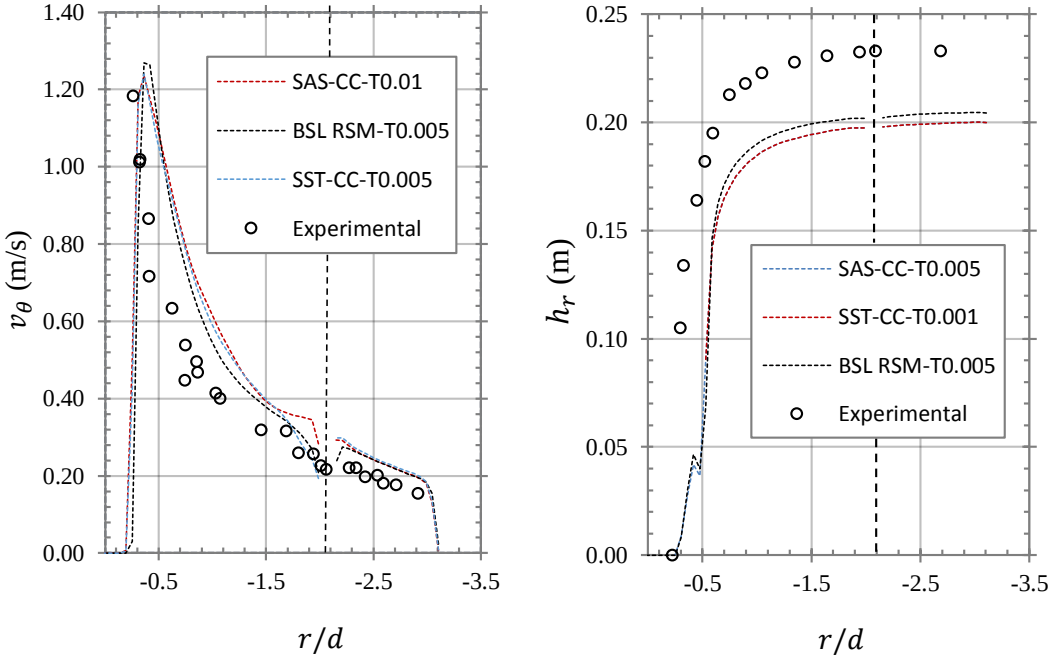

Figure 7.22: Comparison of turbulence models for the unsteady analysis using the maximum solution accuracy obtained from each. (a) the tangential velocity solution data at z/d = 0.5 and (b) free-surface solution data and solution sensitivity to time step for the A3 test case. Data is presented for the section spanning from the inlet at r/d = 2.7 to the orifice at r/d = 0.

7.3.4. Summary of Phases 1-3

It has been shown that consecutive phasing of numerical analysis will result in isolating and eliminating CFD approaches of poor performance to achieve the maximum solution accuracy. A summary of consecutive phasing of approaches in the CFD code to achieve the maximum solution accuracy is highlighted in the flow chart of Figure 7.23.

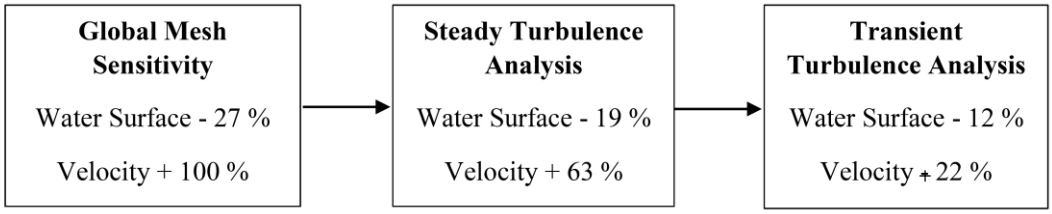

Figure 7.23: Minimum error pertained in modelling the free-surface and tangential velocity field as per phases 1 – 3. Note – Minimum errors for phases 2-3 are obtained using the BSL RSM model.

Although qualitatively the results are in fair agreement with the experimental data in terms of trend characteristics, particularly for phase three, quantitative numerical errors are still present. The measured error, for example in the tangential velocity distribution, is however much less than that observed by Škerlavaj et al., (2014) even for large approach flow depths. Therefore it may be concluded that a multiphase approach provides an increased accuracy over a single phase (fixed free-slip lid) case due to the model taking account of the free-surface deformation. It may be argued that an accuracy in the region of 80 - 90 % is so far very impressive for three-dimensional multiphase modelling of rotating fluids, however the practicality of the approach is nonetheless questionable. At this moment in time, access to high-performance computing can be difficult, even in privileged industrial settings. Therefore, one may argue if the CFD approach is viable when accuracies in the region of 96 % are already achievable for one-dimensional analytical models. However, the access to a creditable amount of complex field variables as a result of a relatively accurate CFD simulation is a major feature that would persuade otherwise the use of a CFD approach. Some of these complex field variables (i.e. unsteadiness, turbulent kinetic energy, and poorly accessible velocity data) are unobtainable even in a well-designed experimental facility. As a result of an increased understanding of HPC's potential within commercial organisations, the market for HPC

is poised to expand at 4.6 % annual compound growth rate in the next three years alone (Research, 2014). The long term ease of access to HPC will eventually render complex multiphase flow problems solvable through CFD studies. Therefore, to conclude on this discussion, the writer suggests that if the numerical accuracy could be increased further, CFD modelling of strong vortex flows will be a viable and rewarding approach. It is necessary herewith to discuss briefly where the problem may lie with the current numerical models (outlined in Phase 3) in order to suggest methods to improve the current solutions.

In the transient models, the root mean square (RMS) residuals for each variable achieved values in the region of $10^{-4.9}$ and below in the SST-CC and SAS-CC models. Furthermore, the global imbalances were found to be small (< 0.00001 %) in each simulation and therefore conservation is essentially achieved. The RMS residuals for the BSL RSM model were well below 10^{-5} as required for each of the variables. However, the maximum residuals were found to be of the order of 10^{-2} - 10^{-3} which was considered to be relatively high. By plotting the volumes of the max residuals across the flow domain, it was possible to locate where the mesh may be expecting convergence issues in order to pinpoint where the mesh should be subsequently refined. The weakest convergence was observed for the RMS W-mom residuals in each model and is therefore analysed. This was performed by plotting Iso-volumes for W-mom bulk residuals of 0.00001 in the domain. The visualisation is presented together with the free-surface in Figure 7.24 for both the SST-CC model and the BSL RSM.

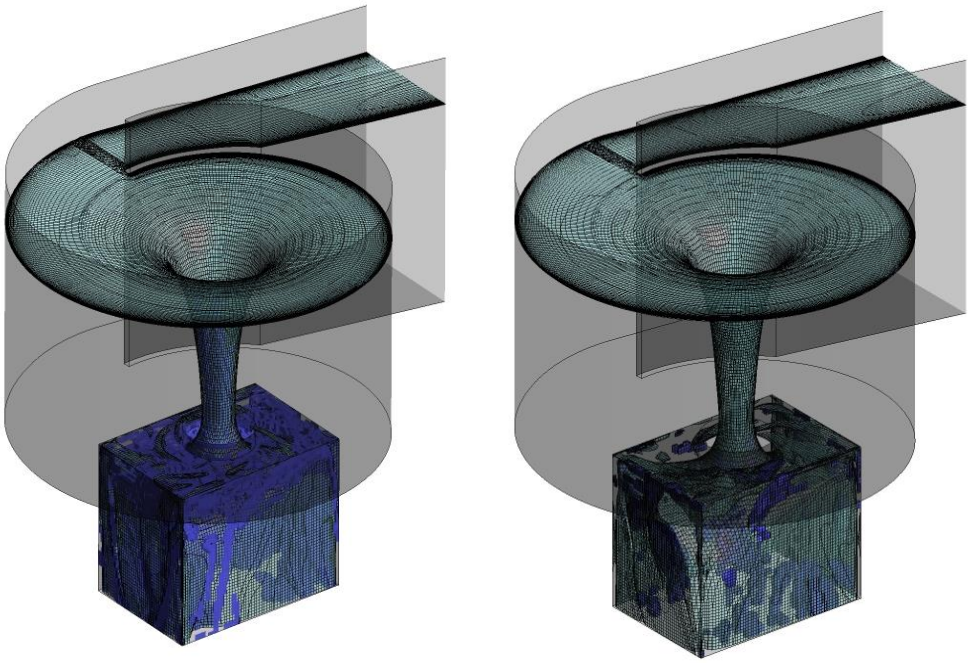

Figure 7.24: Plot of free-surface and W-mom bulk residuals at a variable value of 0.00001 for (a) the SST-CC model and (b) the BSL RSM. The visualisation is constructed using iso-volumes for the residuals and an iso-surface ($\phi_w = 0.5$) for the free-surface.

The results indicated that the solution suffers from poor convergence in the region of the vortex air-core and the annular jet in the drop shaft. The RSM obtained a better convergence in this region when compared to the SST-CC formulation. The physical model showed that the air water surface in this region was oscillating rapidly. Furthermore, the flow in this region was comprised of both the primary circumferential flow as well as the secondary axial and radial flows. The turbulence experienced in this region exhibited extremely chaotic and highly anisotropic properties which most likely indicated the reason for a stronger convergence obtained using the RSM. The solver y^+ is found to be less than one for the walls and vessel floors in the far-field. However, close to the orifice the values increase no greater than 10. In the orifice flow region as well as the drop shaft levels of the y^+ are in the region of $25 - 30$. The global values were slightly higher in the RSM case. Therefore, one suggestion as to why the accuracy of the model was not being achieved was likely to be as a result of a poorly resolved turbulent boundary layer in the orifice and annular drop shaft region where the local Reynolds number was correspondingly high.

The maximum Courant number was found to be less than 80 in the each model. Naturally, for a numerical model it is important to keep the CFL condition reasonably low. By observation of the cells containing Courant C numbers of 10 in each simulation (Figure 7.25) it was shown that these cells reside around the vortex air core and annular jet free-surface interface. It was suspected that further refinement of the air water interface throughout the model should be made in order to better capture a sharp interface. This would be particularly important for modelling the instabilities and fluctuations in the annular jet free-surface downstream of the orifice in a transient simulation.

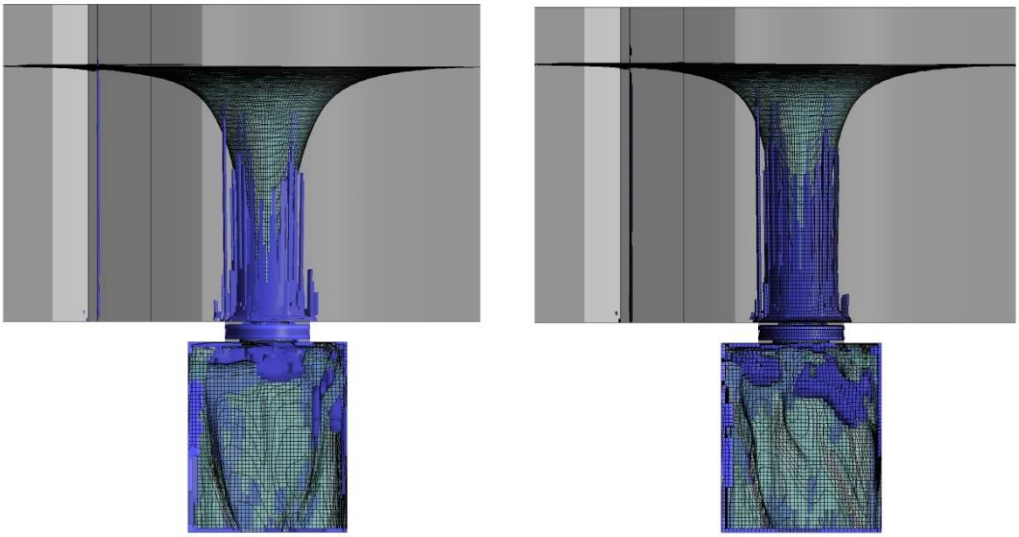

Figure 7.25: Plot of courant number CFL = 10 for (a) the SST-CC model and (b) the BSL RSM. The visualisation is constructed using iso-volumes for Courant number and an iso-surface ($\phi_w = 0.5$) for the free-surface.

Finally, one of the main sources of uncertainty that resided in the model is the assumption of a fully separated multiphase flow using the homogeneous Eulerian-Eulerian method. It was observed that the flow downstream of the orifice was in fact mildly aerated. The validity of the model would then begin to break-down in the annular jet downstream of the inception point which may also suggest why there was poor convergence in this region. Enabling the inhomogeneous Eulerian-Eulerian model would substantially increase computational expense, not to mention a significant reduction in numerical instability. Although at this stage this approach would be considered uneconomic with

regards the return of accuracy for computational investment, it would nonetheless be a very interesting study in future numerical investigations.

Another condition which may have contributed to the observed discrepancies was associated with the boundary conditions in this region. An assumption was originally made in that the drop shaft chamber downstream of the orifice was not vented and formed a closed conduit. In fact, the interface between the drop shaft and the orifice was not fully sealed, thus small amounts of ventilation may exist in the experimental facility. In a subsequent study, this could be simply checked by assigning an opening boundary condition at this region.

Overall, it is concluded that there is significant potential to increase the accuracy of the numerical solution further. Through physical and numerical insight, the writer suggests that by refining the mesh in the areas of the air core and annular jet interface as well as in the boundary layer of the drop shaft walls, it might be possible to immediately increase the accuracy of the model to within a reasonable level in a future study.

7.4. Phase 4 – Test Case Interrelationship

In the final phase of the numerical comparison, a physical-numerical comparison between all of the test cases will be presented. The SST-CC model was used for all simulations due to its practicality, however, the BSL RSM was also evaluated due to its superior accuracy in simulating the previous test case. The numerical data was compared to the free-surface profile, tangential, radial and axial velocity and air core diameter data obtained in the experimental analysis. A final comparison of the vortex steady state evolution is also presented for the A3 test case.

7.4.1. Free-Surface Profile Prediction

Figure 7.26 - 7.28 presents a qualitative comparison between the free-surface prediction in both the transient SST-CC and BSL RSM models compared to that of the experimental free-surface. Similar to the findings in Phase 3, the location, centrality and shape of the free-surface was well predicted in each case. The Reynolds stress model indicated a slightly higher free-surface at the inlet. The A1 test case revealed that there existed a level jet detachment activity and instability of the annular jet in the drop shaft which is typical

of the low approach flow condition. This is not experienced in the RSM. A quantitative comparison between all three test cases is highlighted in Figure 7.29. Again, the slight increase in accuracy of the RSM was observed in each case. The percentage error in predicting the far-field (inlet) free-surface was recorded to be 12 %, 11 % and 16 % for A3, A2 and A1 respectively.

The increased error in the A1 test case was not very surprising. In Section 6.1, the similarity of the physical models were reviewed. It was found that, 4 of 72 approach flow conditions did not achieve the criteria for the Weber number specified by Jain et al. (1981) with one of the failed approach flows existing in the #4.0d1.0d for $h/d = 0.5$. Therefore, although the A1 test case achieved the Jain et al. criteria ($We_d = 186 > 120$), there was still a high risk of the surface tension effecting some areas of flow field, particularly that of the free-surface. In the simulations presented, the effect of surface tension was neglected. However, Škerlavaj et al., (2014) showed that the effect of the surface tension in a vortex chamber could become significant for small discharges. Škerlavaj et al. (2014) showed that by accounting for the surface tension the prediction of the air core length could be improved. This calculation was based on an analytical method proposed by Sakai et al. (2008) coupled with a surface tension correction approach (Ito et al., 2010). Similarly, it was expected that if the surface tension force was included through the continuum surface force model of Brackbill et al. (1992), the model should recover from effects of surface tension during low discharge rates for $We_d < 120$.

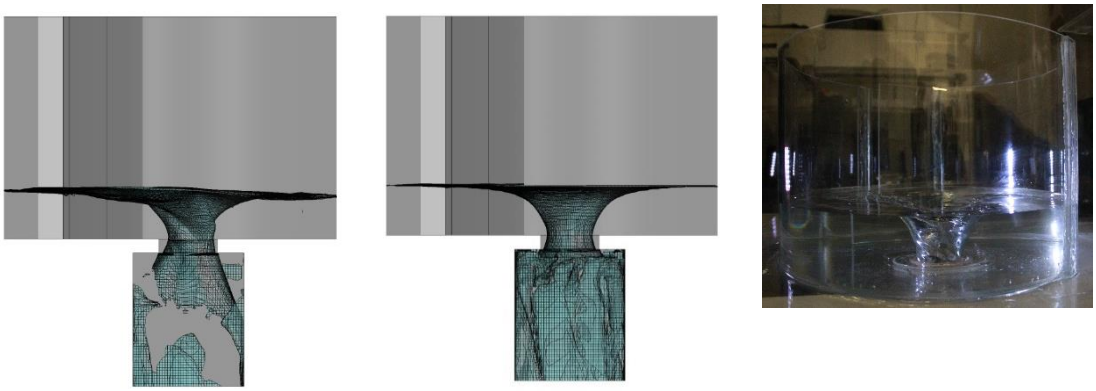

Figure 7.26: Plot of the free-surface in (a) the SST-CC model and (b) the RSM compared to (c) the experimental model for the A1 test case.

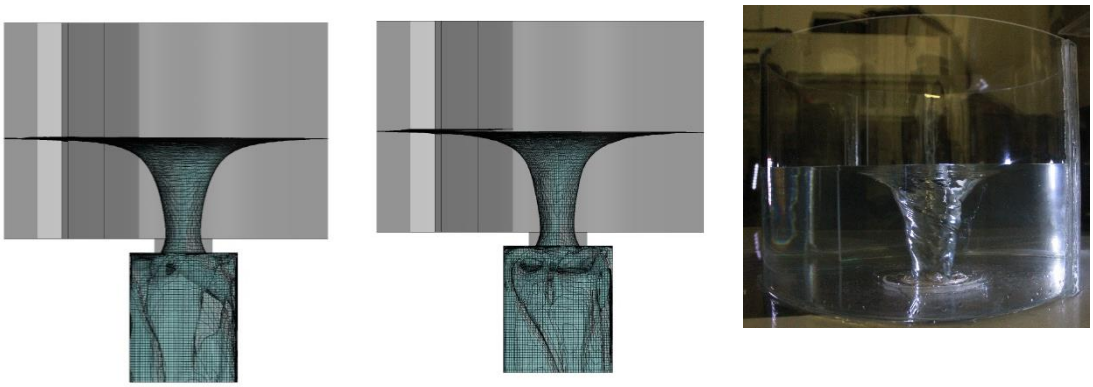

Figure 7.27: Plot of the free-surface in (a) the SST-CC model and (b) the RSM compared to (c) the experimental model for the A2 test case.

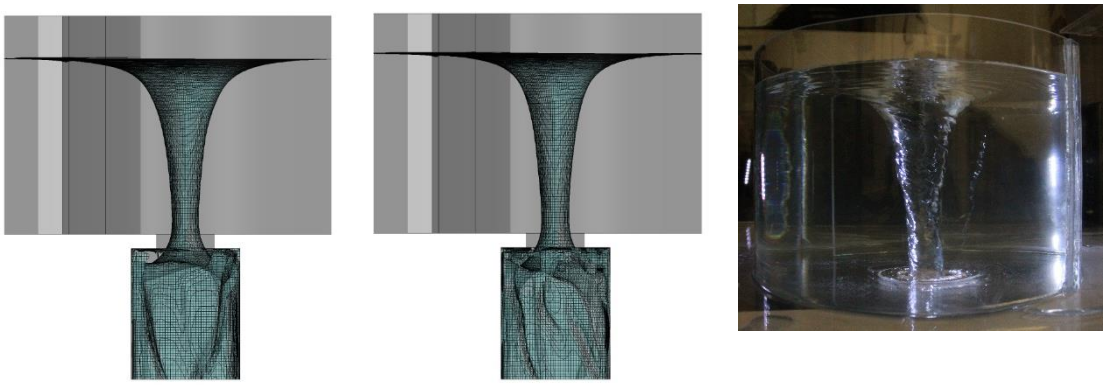

Figure 7.28: Plot of the free-surface in (a) the SST-CC model and (b) the RSM compared to (c) the experimental model for the A3 test case.

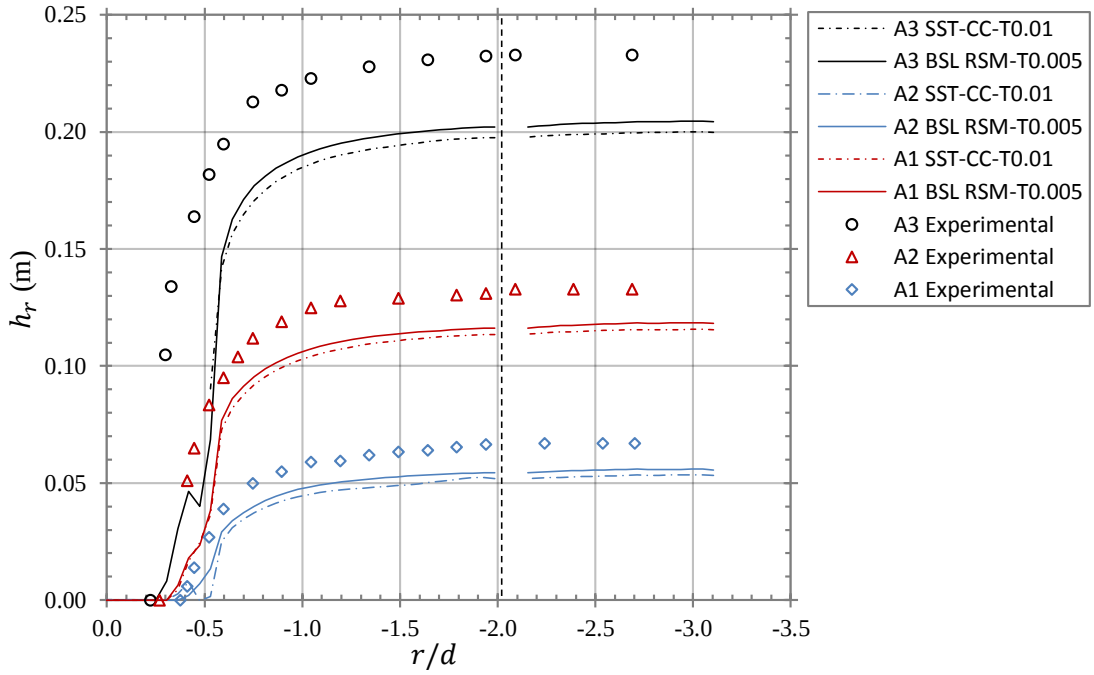

Figure 7.29: Quantitative comparison of the free-surface profile for the three test cases. The error equates to 12 %, 11 % and 16% in A3, A2 and A1 respectively.

7.4.2. Tangential Velocity Profile Prediction

The tangential velocity profile for the transient SST-CC and the RSM's are presented in Figure 7.30 together with the experimental profiles for each test case. Again, each model revealed a similar trend which was typical of an air core vortex tangential velocity profile. In each case the tangential velocity profile was overestimated. The RSM presents overestimation percentage errors of 15 %, 12 % and 45 % for the A3, A2 and A1 test cases. Again, the larger discrepancy was assumed to be as a result of the low Weber number for this approach flow and consequently the onset of surface tension effects. The near-field errors were found to be in the range of 25 %, 33 % and 35 % for A3, A2 and A1 respectively.

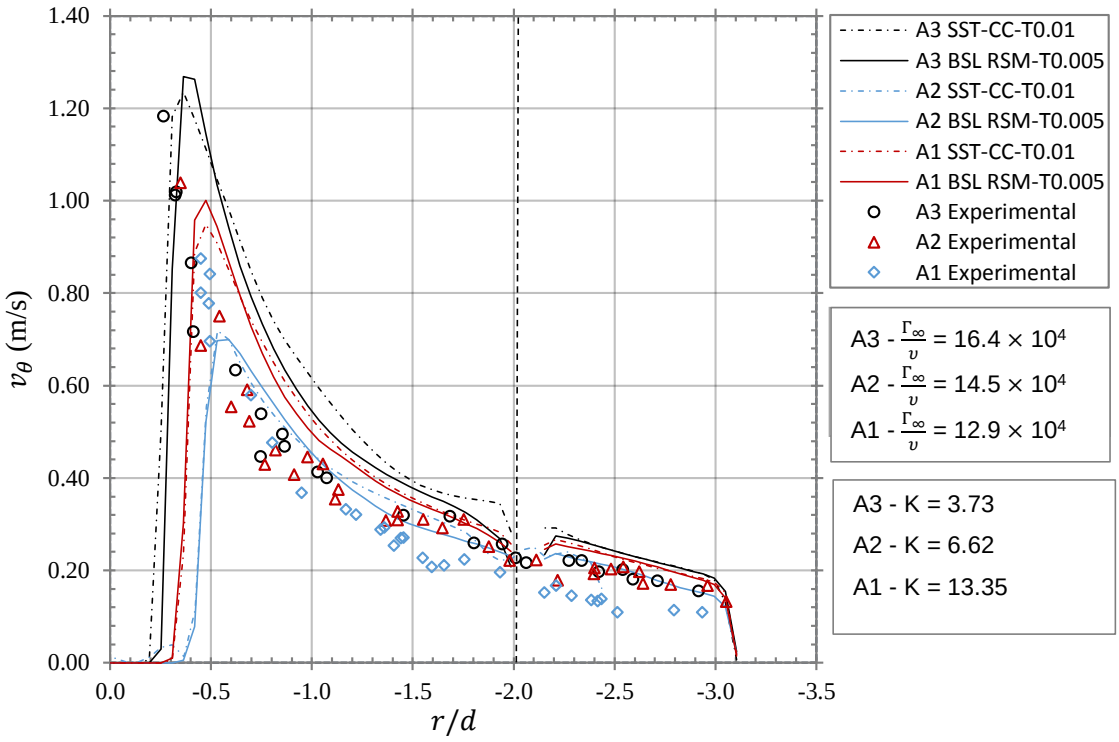

Figure 7.30: Tangential velocity comparison for the transient SST-CC, RSM and experimental data in each test case.

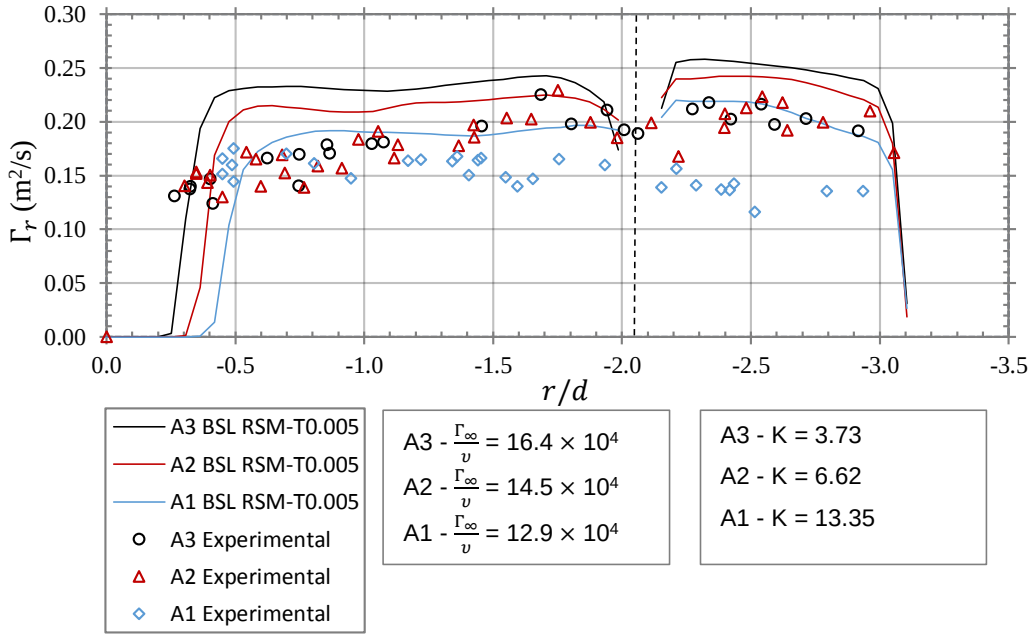

Figure 7.31: Tangential velocity comparison for the transient SST-CC, RSM and experimental data in each test case.

The radial position of the maximum velocity was slightly overestimated as a result of an increased air core diameter but the peak velocity magnitude itself was well predicted in each case. By considering the distribution of circulation across the vortex chamber, similar discrepancies are observable (Figure 7.31). The prediction of each circulation distribution Γ_r present to decrease slightly on approaching the air core which was in agreement with the experimental measurements. Furthermore, the inlet vertical velocity distribution is presented in Figure 7.32 which again highlights the discrepancies. It was concluded that, based on these quantitative observations, residual numerical error in the models which may manifest as sources of false diffusion or unphysical eddy viscosities result in an inconsistent numerical-physical relationship. These errors then behaved as a resistant to the flow and therefore a vortex of an arbitrary approach flow depth required greater energy or inlet bulk discharge conditions in order to sustain the vortex flow of a certain magnitude. As a result in the greater requirement of flow at the inlet, an unrealistically large circulation field is developed across the vortex.

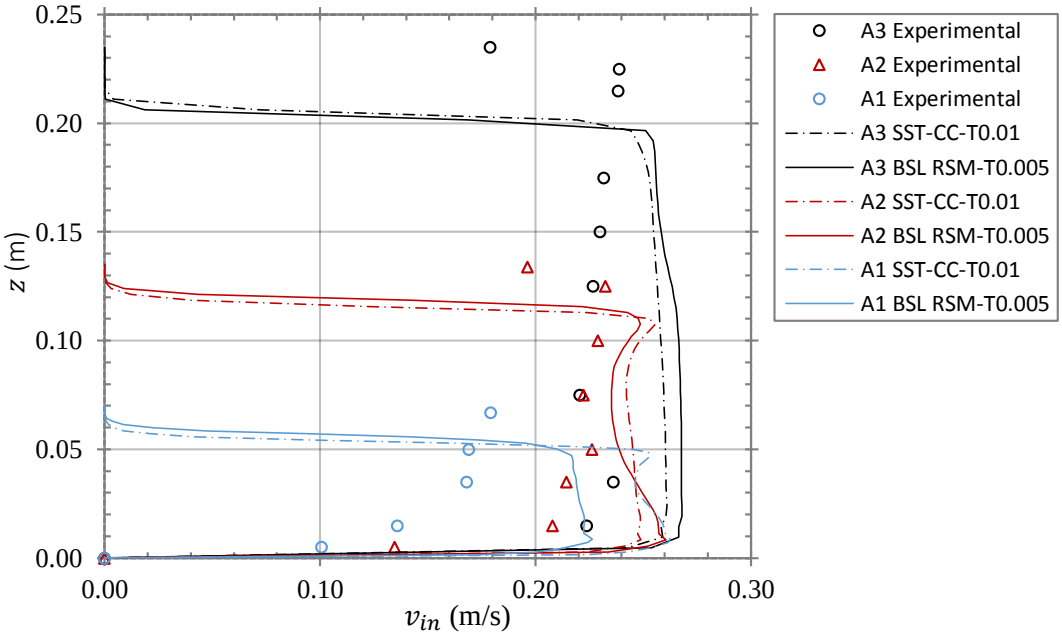

Figure 7.32: Vertical distribution of the field circulation Γ_∞ for three approach flows including the SST-CC and RSM models.

7.4.3. Radial Velocity Profile Prediction

Although it was somewhat difficult to detect a trend in the radial velocity profile in the experiments due to their magnitude and infrequency, a brief physical-numerical comparison was made between the distinguishable experimental radial profiles and the averaged transient model results. The physical and numerical data is presented in Figure 7.33 and indicates that the radial velocity in the chamber was slightly under-estimated. At each datum of interest no negative velocities were apparent in the RSM (similarly in the SST-CC model). It was shown in Section 7.3.2 that the radial velocity component is however a fluctuating (time dependent) variable in the flow field. Based on the scatter of the physical data, it was also possible to argue in favour of this fact. Therefore, the averaging process of the radial velocity field in the transient model would be responsible for lowering the peak velocities and increasing (if in existence) the negative velocities to the RMS average presented. Therefore it can be concluded, based on the available data that there is a reasonable agreement in the radial flow field.

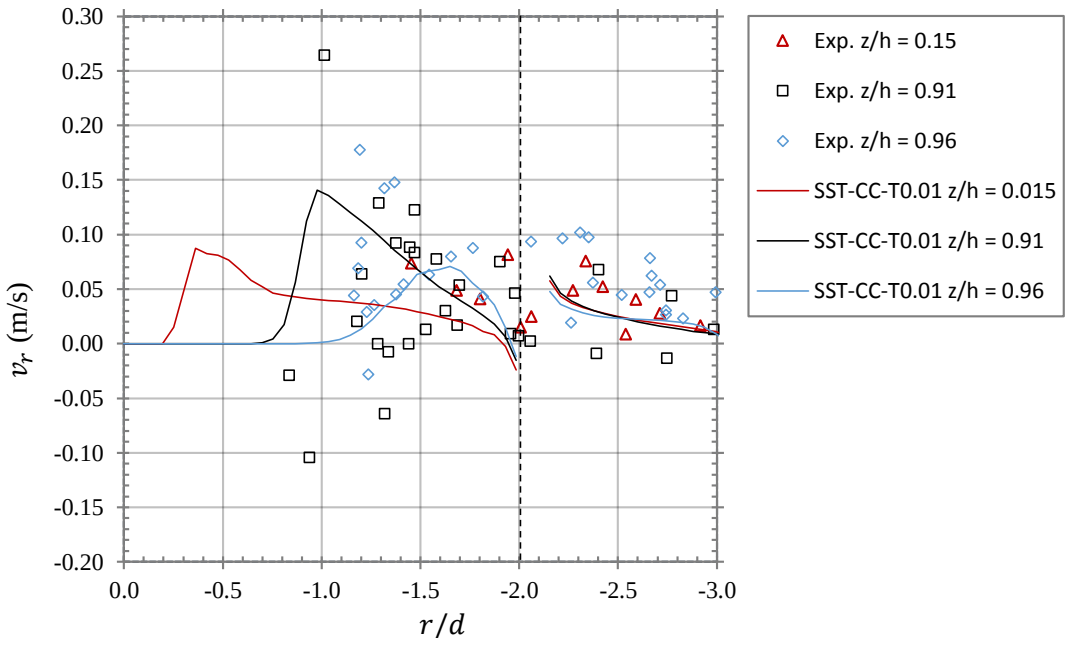

Figure 7.33: Radial velocity comparison for the transient SST-CC and experimental data in each test case.

7.4.4. Axial Velocity Prediction

The axial velocity gradient is compared with the numerical data in Figures 7.34 (a) and (b). Although the quantity of data obtained for the axial velocity distribution using the PSV technique was diminutive, the available trends for each test case provided an effective means to validate the numerical model capabilities when simulating the axial gradients. The RSM model is presented only in regions that could be monitored using the PSV technique i.e for $r/d < 1$ and $0.3 < z/d <$ 3.0. A respectable agreement was observed for both the A2 and A3 test cases with the A2 RSM data slightly under predicting the axial velocity gradients. It was also interesting to point out that the numerical data for the axial gradient parameter does not manifest in a single curve as was suggested in Anwar's analysis (Anwar, 1969) but instead the data was grouped into a well-defined envelop categorising individual profiles of the flow. Thus, in the near-field, close to the core, the axial velocity gradients exist as $\frac{\partial v_z}{\partial r}$ and $\frac{\partial v_z}{\partial z}$ .Therefore, this secondary flow field was shown to be highly non-linear in nature. Škerlavaj et al., (2014) also reported similar agreements between the SST-CC and the 'downward' velocity profile.

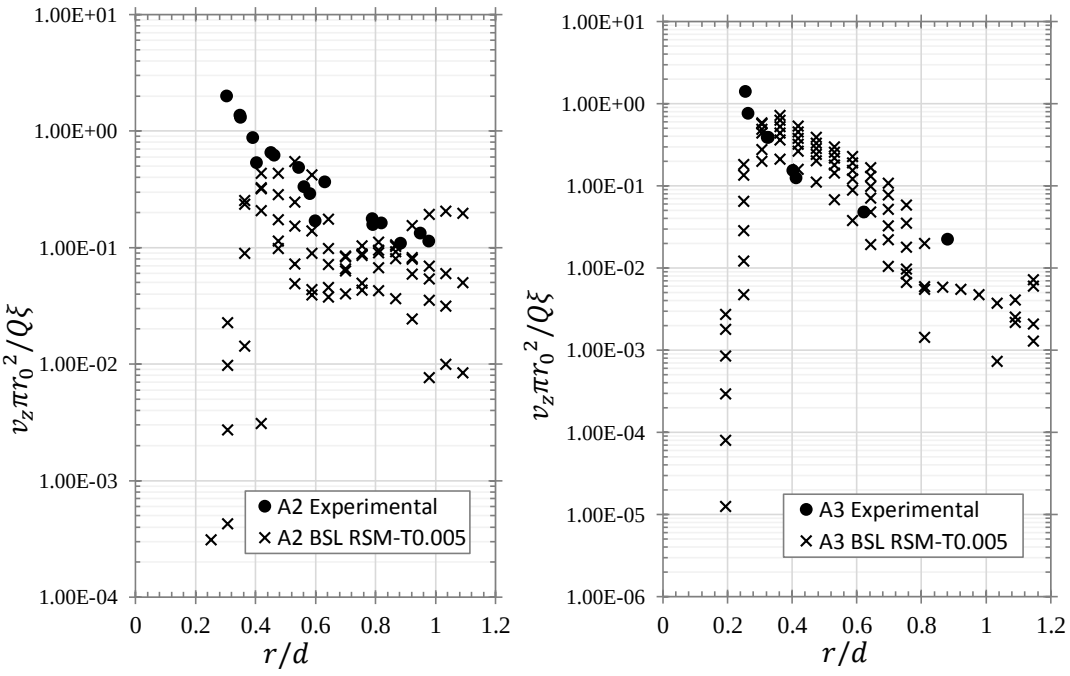

Figure 7.34: Vertical and radial axial velocity gradient comparison for experimental data compared to the BSL RSM. The numerical data is obtained for the spatial extent of $r/d < 1$ and $0.3 < z/d < 3.0$.

7.4.5. Air Core Diameter Prediction

Using the water.volume fraction ϕ_w of the numerical model results it was possible to identify a sharp free-surface interface at the critical section and resolve a_c/d. Furthermore, using the circulation data generated from the numerical solutions, the Kolf number $K = \frac{\pi}{4}N_\Gamma$ can also be computed. The relationship between these numerical plots are compared to the characteristic experimental data obtained for the air core diameters dependence on the field circulation in Section 6.2.4.

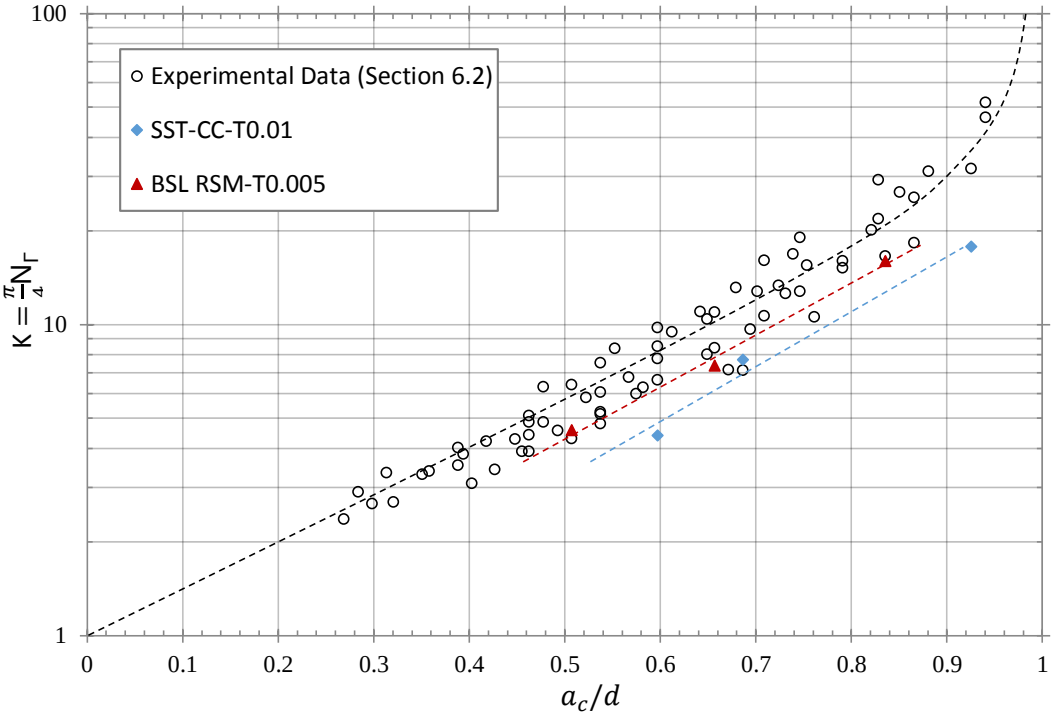

Figure 7.35: Comparison between SST-CC model, RSM and experimental data for the relationship between the Kolf number K and the critical air core diameter a_c/d.

The linear trend on the semi-log plot was in good agreement with the experimental data, however the magnitude of the numerical quantities were underestimated. This was expected based on an original description made in Section 7.4.2. Because of an inherent numerical diffusion and dissipation, the strength and consequently the circulation number or Kolf number of the vortex was reduced accordingly for an arbitrary air core diameter a_c/d.

7.4.6. Transient Evolution of the Free-Surface

Finally, as part of the comparative study, a general qualitative comparison is presented for the evolution of the free water surface in order to further substantiate the models capabilities which may have some importance in various rapid transitory industrial flow systems. The transient model is presented for the A3 test case and compared to a standard video recording obtained from the physical model. The times of frames is presented alongside each visual comparison in Figure 7.36. After 0.6 seconds of initiating the flow, the water reaches the inlet. Both the models show the development of an unsteady standing wave which traveled upstream as a positive surge wave. The wave was produced as a result of the channel constriction resulting in increased velocity head. Some sloshing was also observed inside the vortex chamber for both models at this time frame. Between 1.1 and 3.0 seconds the flow makes one rotation around the chamber to meet the incoming flow. The vortex resembled that of a forced vortex system as a result of the 'not yet balanced' energy levels at the inlet and outlet and therefore the flow remains in unsteady state. At 4 and 5 seconds the vortex height grows rapidly. The first discharge in the drop shaft was observed. The discharge through the orifice was recorded to occur in the experimental model at approximately 1 second before that of the numerical model. A slight asymmetry of the air core around the orifice was observed in both the physical and numerical simulation. The centrality of this system at this time was still poor, which is a typical result of the imbalanced inlet and outlet energy states. From $7 - 10$ s the vortex depth grows further and becomes more stable. The formation began to resemble that of a free vortex profile. Between 15 seconds and 25 seconds the rate of transient evolution decreases as a steady state was approached. The steady flow state was reached in the physical model at 23.5 seconds while it took 26 seconds in the numerical model. The slight lag between the transient evolutions will not be evaluated in technical detail here but the writer hypothesises that this may owe to the over generation of eddy viscosity in the RANS formulation which was increasing the effective viscosity of the fluid and thus hindering the conditions that accelerate a steady state development of the flow. A deeper investigation into this topic with the presented numerical model would no-doubt be an interesting investigation to perform in a future study.

$t = 0.6$ s

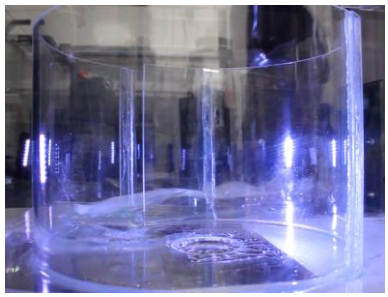

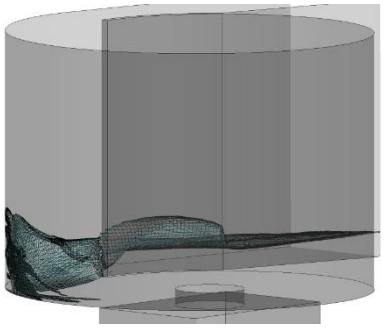

$t = 1.1$ **s**

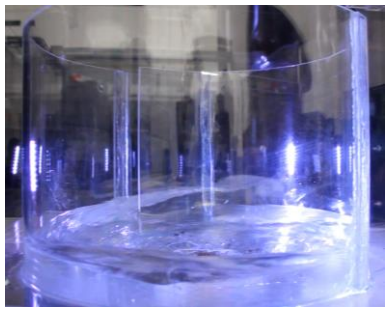

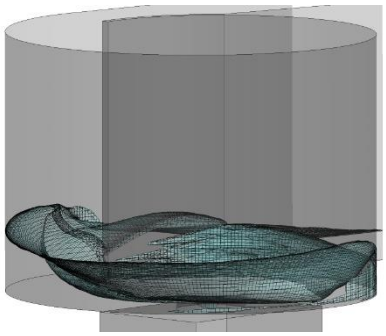

$t = 3.0$ **s**

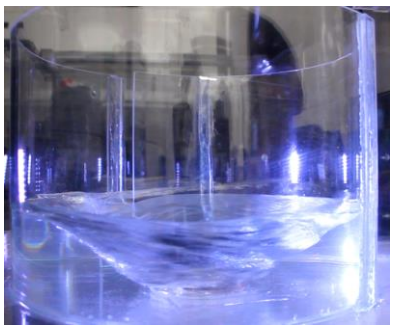

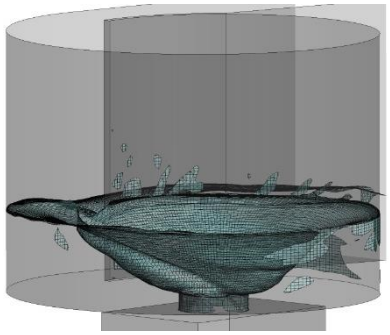

$t = 4.0$ s

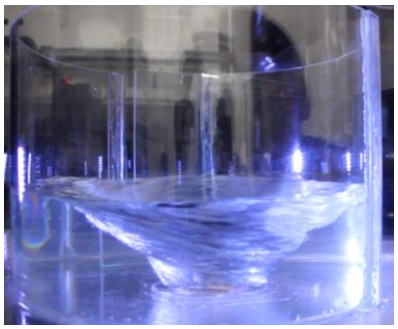

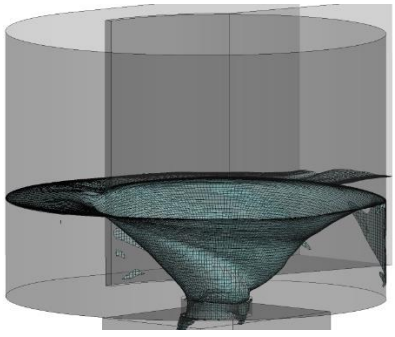

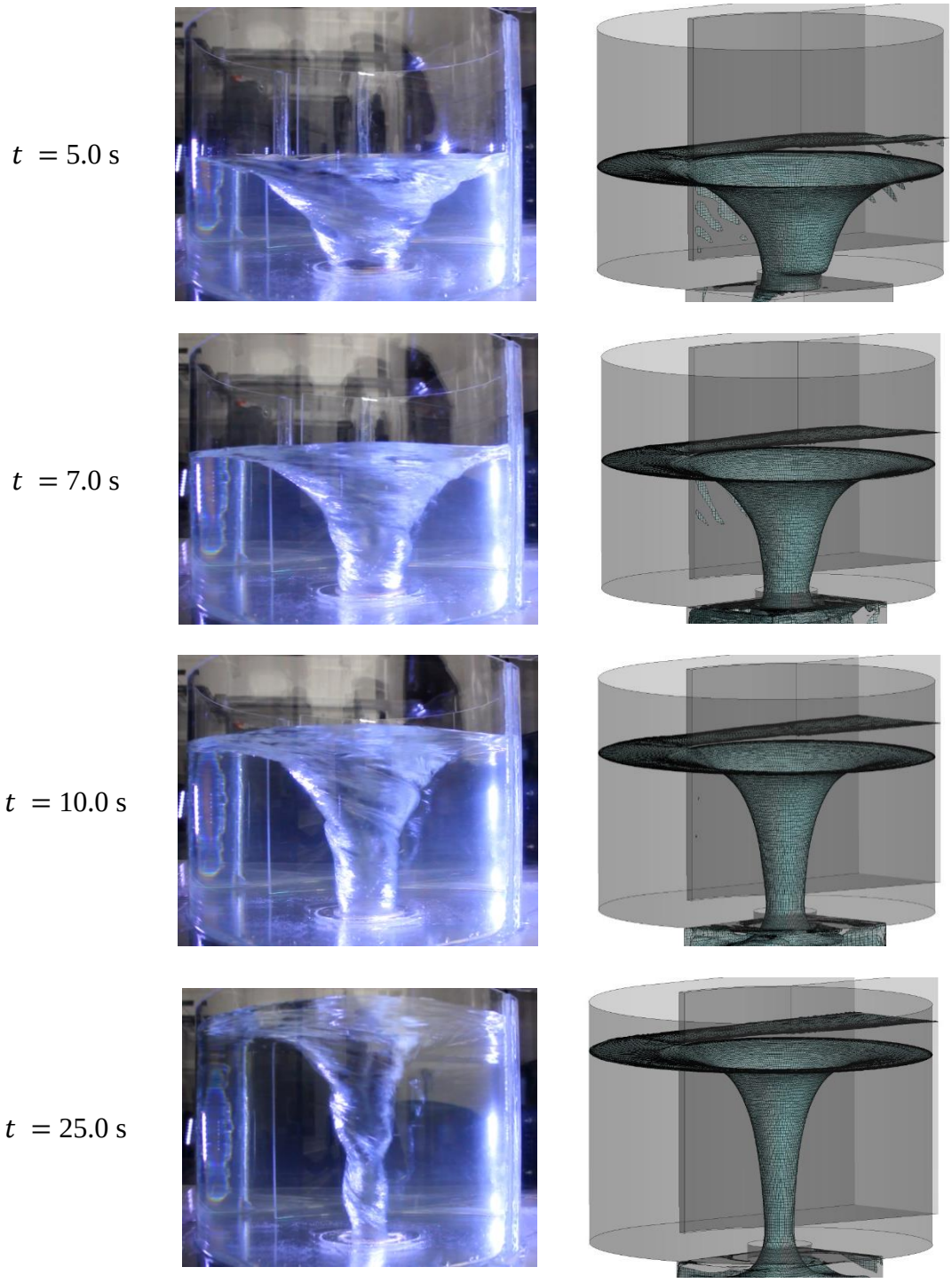

Figure 7.36: Qualitative comparison for the transient evolution of the free-surface from 0.6 s to 25 s. A steady state visually observed to be reached in the physical model at 23.5 seconds while it is obtained at 26 seconds in the numerical model.

7.5. Additional Numerical Analysis

In this section, some additional topics of CFD analysis will be discussed, particularly surrounding the capabilities of the numerical model and complex field variables that can be computed.

7.5.1. Similarity

It was found in Section 7.4 that some discrepancy in the numerical results at low discharge rates may be a direct consequence of neglecting the effects of surface tension in the model. It was concluded that surface tension modelling procedures should be enforced when the Weber number in the model is low. This finding posed another question of significant importance for the application of the model- is the numerical model scalable and should similar errors be experienced in a prototype scenario? The answer to this question will be discussed briefly. The transient Reynolds stress and SST-CC numerical models experienced errors in the region of $10 - 20$ % and therefore the application of the model in an industrial perspective is viable. The writer suggest that, because the comparison was performed on a physical model that achieved the limits of Reynolds number and Weber number, Froude similitude between the model and prototype can be adopted. Moreover, the scalability of the physical data was further validated in testing the empirical depth-discharge equation on a prototype in Section 6.3 which further reinforces this conclusion. It should therefore be expected that the same numerical model configuration and formulation at an increased scale should achieve comparable numerical accuracies. It is stressed however, that the structure and density of the fine mesh arrangement presented in Section 7.2.3 should be reproduced if not enhanced taking into account the suggestions to refine the air core and annular jet free-surface interface to a finer degree. Although these topics will not be addressed in this project, it is also important for engineers performing multiphase simulations on increased scaled systems to consider effects which are absent in the physical model. Such conditions may be meteorological, Coriolis (for large scales) or multiphasic (i.e. sludge flows and three/four phase flows) in nature. The last condition may be a problem in systems containing large

vortex Reynolds numbers resulting in interphase transfer of air and subsequent interphase mixing in the vortex chamber.

7.5.2. Q-Criterion

Although the methods of vortex identification were generally omitted from this analysis, it was considered that some attention should be brought to one such detection technique commonly employed in CFD studies (Škerlavaj et al., 2011). The Q-criterion proposed by Hunt et al. (JCR et al., 1988) identifies vortices of an incompressible flow as a "*connected fluid region with a positive second invariant of* ∇u". The second invariant is defined by:

$$Q = \frac{1}{2}\left(u_{i,i}^2 - u_{i,j}u_{j,i}\right) = -\frac{1}{2}u_{i,j}u_{j,i} = \frac{1}{2}(\|\Omega\|^2 - \|S\|^2) \qquad (7.37)$$

The Q-criterion states that when $Q > 0$, i.e. there is a local dominance of the vorticity magnitude thus defines vortices as areas where the vorticity magnitude is greater than the magnitude of rate-of-strain. In addition, the pressure in the vortex region is required to be lower than the ambient pressure. The Q-criterion is determined from the numerical results of the RSM and is presented for the three test cases in Figure 7.37:

Figure 7.37: Visual presentation of the vortical structures in the flow field of a vortex chamber for the three test cases using the Q-criterion (JCR et al., 1988) (iso-surface Q = 0.05 s^{-2}).

It was revealed that the Q-criterion indeed provides a good visual estimate of the local vortex regions around the vortex core in each case. It was also noted that vorticity appears to be absent throughout the majority of the flow field which at least indicates that the far-

field was quasi-irrotational. This was contrary to that of a weak vortex structure where vorticity would be largely present, particularly close to the air core and localised around the vortex tip. In the current CFX analysis, the magnitude and detection of the vortex system was identified by the free-surface deformation and circulation predictions. However, in a single phase simulation the use of the Q-criterion would no doubt be of an advantage in order to provide an early visual representation of the vertical structures in the flow field (Škerlavaj et al., 2014). Other methods based on similar principles for vortex identification are available in CFX e.g. λ_2 criterion (Jeong and Hussain, 1995), Δ criterion Chong et al. (1990) and the Swirling strength (λ_{ci}) criterion (Zhou et al., 1999) but will not be addressed further in this study.

7.5.3. Primary and Secondary Flow Fields

Despite the fact that the Reynolds stress model suffered from discrepancies, the solution for the flow field could nevertheless be considered to be physically valid in order to critically analyse regions of the flow that are not experimentally accessible. The flow field tangential velocity profiles are presented in Figure 7.38 for various sub-surface depths z/h. The profile is positive in the negative axis and negative in the positive axis as to be consistent with previous graphical formats. It can be seen that the tangential velocity field in the direct vicinity of the vessel floor suffered a significant decrease in magnitude as a result of the boundary layer which was discussed in previous sections. A significant gradient was however observable within the orifice where the vessel floor falls away. For the subsurface depths $0.15 > z/h > 0.75$ the magnitude of the velocity profile was similar, thus indicating its independence of the subsurface depth z which was concluded in the experimental investigation.

However, some variations in the profile are apparent for $a_c/2 < r/d < 1/2$. In this region, the magnitude of the axial velocity field was significant. The combined axial velocity profiles for each subsurface depth is displayed in Figure 7.39. Immediately it clear that the axial velocity profile at z/h = 0 was practically zero everywhere except for the sharp increase for $r/d < 1/2$. The profile resembled that of a square profile for values of r at $a_c/2 < r/d <$ ½ and is therefore is good agreement with the assumptions made

by (Binnie and Hookings, 1948, Ackers and Crump, 1960). To recap on this briefly, the authors (Binnie and Hookings, 1948, Ackers and Crump, 1960), in their derivation of the analytical depth-discharge model, assumed that a constant axial velocity profile exists at the critical section. According to the continuity equation of Equation (2.45) and taking the numerical value obtained for the air core diameter a_c = 0.017, the constant velocity magnitude should equate to approximately $v_z = -1.18$ m/s. By observation of Figure 7.39, the magnitude of the axial velocity varies between -1.13 and -1.17 m/s and thus agrees extremely well with the analytical prediction. The distribution of the axial velocity profile for the remaining sub-surface depths don't appear to exhibit any repeating trends and it was concluded that the axial velocity is neither independent of the depth z or the radial position r. Another feature that is worth discussing is the apparent increase in the positive profile close to the walls inside the vortex chamber. During the laser-induced fluorescence analysis it was shown that the Rhodamine jet is indeed advected upwards in this region. Observing this again in the numerical data ultimately verifies the presence of this newly observed secondary flow pattern.

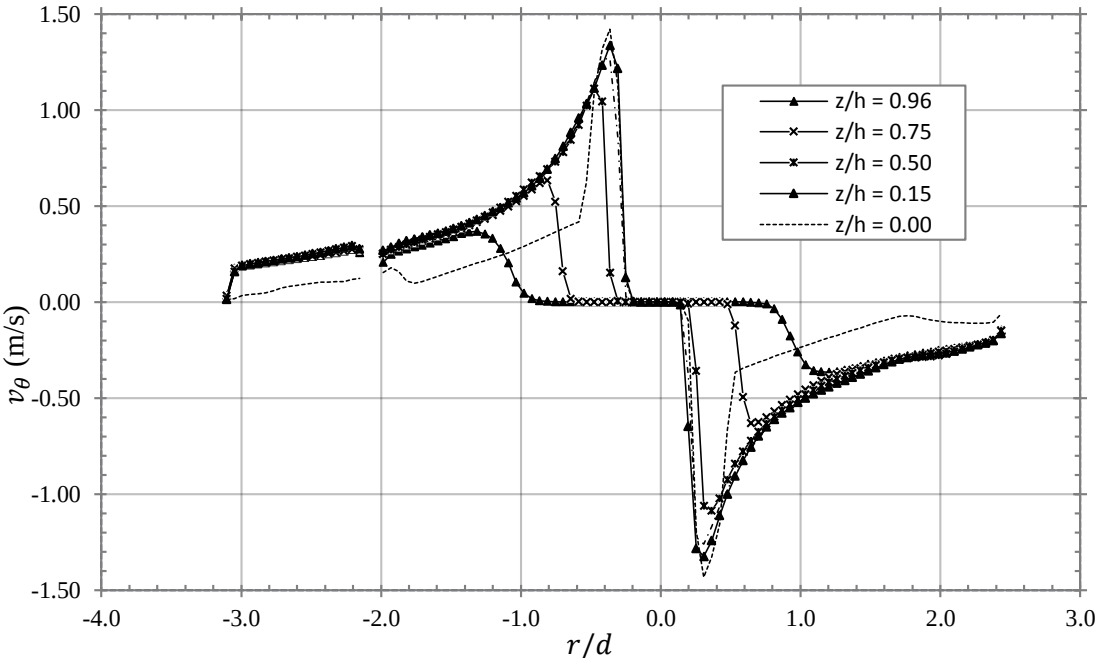

Figure 7.38: Combined tangential velocity profiles for all subsurface depths for $h/d = 3.5$, $\tilde{\Gamma} = 0.220$ m^2/s, Rr = 10305, $N_\Gamma = 3.7261$ and $N_Q = 0.852$.

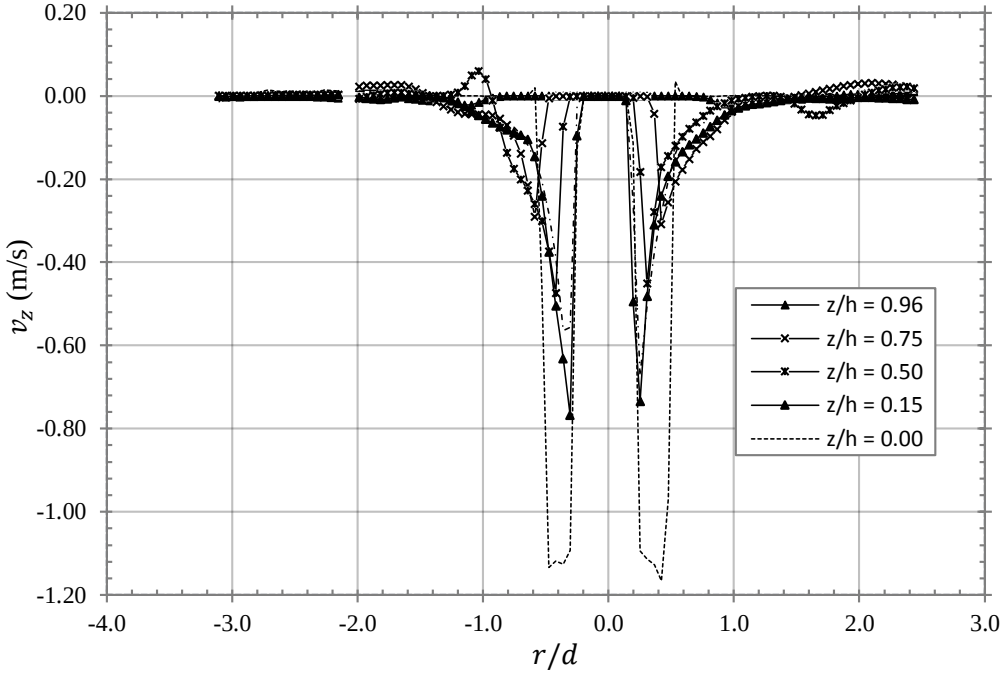

Figure 7.39: Combined axial velocity profiles for all subsurface depths for $h/d = 3.5$, $\tilde{\Gamma} = 0.220$ m^2/s, Rr $= 10305$, $N_\Gamma = 3.7261$ and $N_Q = 0.852$.

Finally, a subject that requires further examination is that of the dependence of the tangential velocity gradient on the $z-$ axis. In most previous analytical studies this was assumed to be negligible in favour of the quasi-cylindrical approximation (Hall, 1966). The Reynolds stress numerical model, owing to its sufficient reliability in predicting other general flow patterns, was used to referee the argument between both points of view. The tangential velocity gradient along the depth z was then plotted in the model for various radial positions r/d which were defined discreetly close to the vortex core. The results were presented in Figure 7.40. Here it confirmed that, in the far-field (away from the orifice) the tangential velocity was indeed independent of the depth which was already been confirmed experimentally in this study and in other studies (Anwar, 1965; Daggett and Keulegan, 1974). Within the orifice however ($a_c/2 < r/d < 1/2$), the tangential velocity ws found to vary gradually along the subsurface depth in this region. The existence, therefore, of the advection quantity $\partial v_\theta/\partial z$ together with significant axial velocities v_z in this region are conflicting the assumptions made in the quasi-cylindrical

approximation in the near-field. It may therefore be that the hypothesis originally proposed by Einstein and Li (1951) and Anwar (1965) on the existence and effect of an apparent eddy viscosity is invalid; at least in the case of strong vortices with axial down flow. Thus, a more realistic approach to modelling the near-field tangential velocity profile in a strong full air core vortex can be obtained in the use of the proposed alternative analytical model presented in Section 6.6.

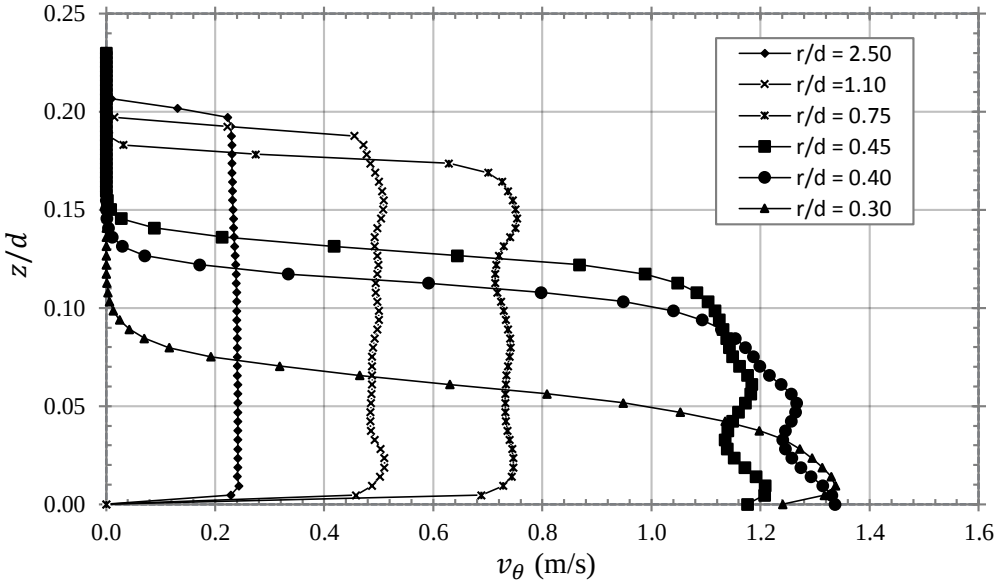

Figure 7.40: Combined depth z/d versus tangential velocity $v_\theta$profiles for a range of radial positions r/d for $h/d = 3.5$, $\tilde{\Gamma} = 0.220$ m^2/s, Rr = 10305, $N_\Gamma = 3.7261$ and $N_Q = 0.852$.

7.5.4. Velocity Contours and Streamlines

The streamlines for various subsurface horizontal planes were computed and presented in Figure 7.41. The presentations show the smooth regularly curved and concentric streamline patterns that manifest throughout the depth of the vortex chamber. Again, close to the vessel floor and free-surface, the radial velocity profiles were significant and result in spiral streamline patterns as a result of the combine tangential and radial in plane components.

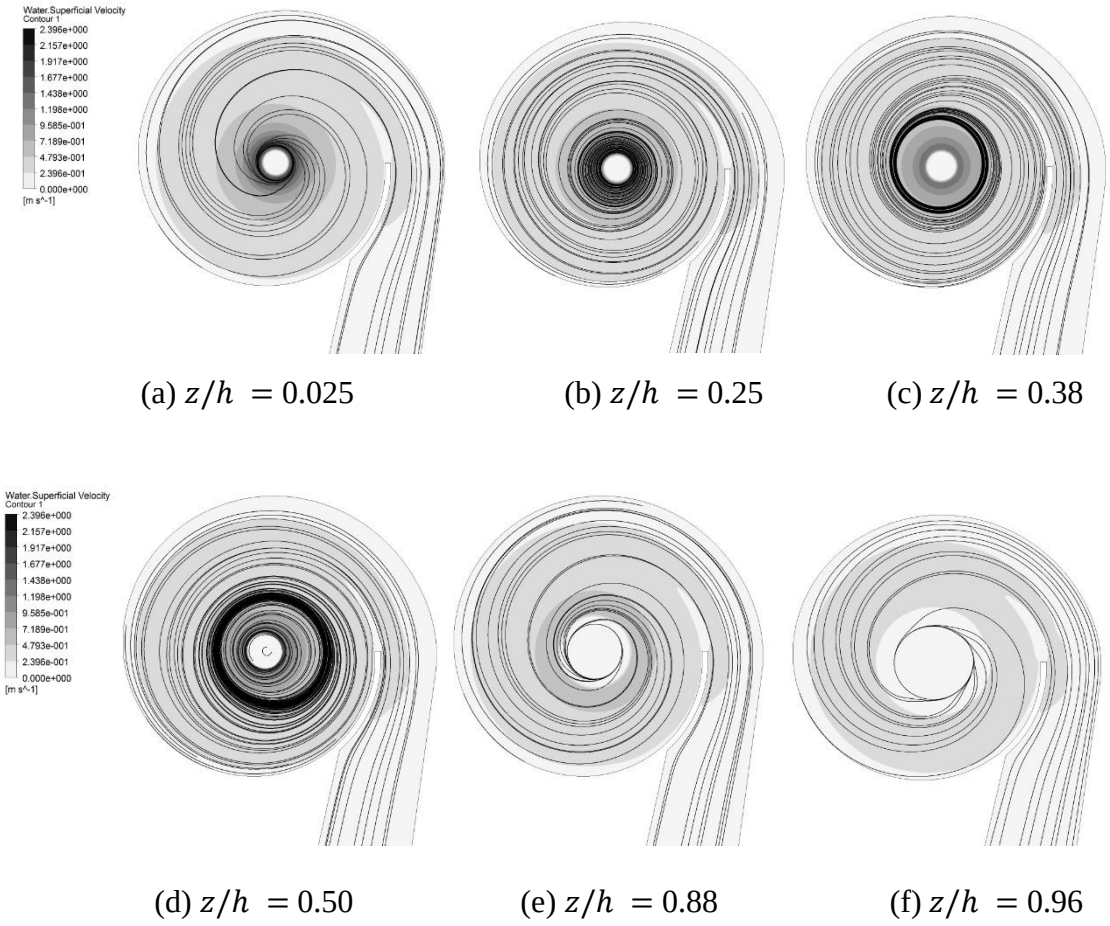

Figure 7.41: Water superficial velocity contours plotted on horizontal planes throughout the depth z/h of the vortex chamber.

7.6. Conclusion

In Chapter 7, a comparative study between the ANSYS CFX numerical code for multiphase fluid model with the available experimental data was implemented to provide a best practice guideline. Observations in the physical model showed that the phases were stratified with very little interphase transfer and mixing. As a result, the multiphase model was treated as fully separated and solved using the homogeneous Eulerian-Eulerian approach. Both unstructured tetrahedral and structured hexahedral mesh structures were investigated along with consecutive refinement of the structured mesh configuration. This comparison indicated that the use of a structured mesh in modelling strong vortex flows is of utmost importance. The unstructured case highlighted significant errors which were a result of numerical diffusion error (false diffusion). The mesh sensitivity study highlighted a case for mesh size independence and stated that this should be achieved when the grid size at the outlet is at least 1.5 % that of the orifice diameter.

Using this fine mesh configuration, an extensive study on the available turbulence models in the code was carried out for both steady and transient modelling approaches. In addition to the SST, SST-CC, RNG $k-\varepsilon$, SST-SAS, SST-SAS-CC and the BSL RSM, a laminar case was investigated. The steady state analysis indicated that the standard SST, RNG $k-\varepsilon$ and the laminar approach performed poorly in comparison to the SST-CC and the RSM. The CC enhancement of the SST model provided a significant improvement to the solution of the free-surface and tangential velocity predictions for just a 10 % increase in computational expense. The results also showed that there was a significant reduction in the generated turbulence and turbulent eddy viscosity which was the source of the improvement in the solution. The RSM inherently accounted for the conditions of system rotation and secondary flows and thus provided a more superior solution.

The results of transient modelling of the flow system as opposed to steady state modelling resulted in a noteworthy increase in the solution accuracy. The SAS –CC model compared almost equally to the results of the SST-CC. It is concluded that the unsteadiness in the flow field was not large enough as to permit the merits of the SAS-CC model to take

effect and instead reproduced similarities of a low fidelity URANS solution. The refinement of the time step had very little effect on the solutions of each turbulence model for the fine mesh configuration. However, the Courant number was found to be quite large in some areas of the model particularly close to the air core. Therefore it was concluded that further refinement of the air water surface in this region should be carried out to enrich the numerical simulation. The RSM presented the most accurate solution (12 % and 22 % in predicting the free-surface and tangential velocity field respectively) and in each case however, only a small increase in accuracy (2 – 3 %) was gained in return for substantial computational effort.

Extensive modelling of each test case using the transient SST-CC and BSL Reynolds stress models indicated that the model is capable of reasonably predicting the flow field. A notable decrease in accuracy was observed for the lowest discharge which was deemed to be as a result of the low Weber number of the physical model and hence, the effect of neglecting the surface tension force. In this analysis, the water surface profiles, tangential, radial and axial velocity gradients in addition to the air core diameter and evolution for the free-surface to a steady flow state were evaluated. Typically, the average radial velocity appeared to be underestimated but the axial velocity compared reasonably well to the experimental data. The air core diameter was slightly over estimated in each case and the discussion highlighted that this was probably a consequence of excessive numerical diffusion/dissipation in the flow field. The transient evolution of the physical and numerical models appeared to agree well qualitatively. Further examination of the tangential and axial velocity profiles in the vortex chambers highlighted features of significance; particularly that associated with the axial gradients $\partial/\partial z$. This supported the underlying assumptions of the proposed model of Section 6.6 as well as the observed secondary flow fields of Section 6.5.

In conclusion, multiphase numerical modelling of flow fields with strong rotation was compared to physical test case. It was suggested that the current model should be adaptable for a range of other natural or industrial processes involving strong free-surface vortices or curving free-surface flow. There was still a measure of inaccuracy in the final

most accurate transient model solution as well as a high cost of computation. It was concluded that following some advancements on the model in addition to improved accessibility to supercomputing in the future, CFD modelling of such multiphase flow phenomena may prospectively be a viable approach for practitioners and engineers in industry.

Chapter 8.

An Alternative Description for the Mechanics of Free-Surface Vortex Flows

SUMMARY

As a final contribution in this study, the author proposes an alternative description for the behaviour of the flow mechanics and stability in free-surface vortices. The concepts were derived from observations made in the experimental and numerical analysis in addition to experiential insight. Particular emphasis is made on the mechanics of the strong free-surface vortex in a newly defined 'Virtual Taylor-Couette' flow description based on the findings of the secondary flow field. In addition, a textual presentation regarding the stability of free-surface vortices as well as a hypothetical transition between the 'weak' and 'strong' vortex types is documented. The descriptions are somewhat qualitative in their current form and further quantitative investigations are required to confirm the overall hypothesis.

8.1. The Virtual Taylor-Couette Theory for Full Air Core Vortices

In Section 6.4 the primary azimuthal flow field was investigated experimentally for a range of sub-surface depths. Following this, the results of the radial and axial velocity profiles suggest that they were concentrated at the vessel boundaries and in the vicinity of the air core respectively. Furthermore, it was speculated that the radial velocity field was highly unsteady. To reinforce the findings on these secondary flow fields the PLIF study indicated that the radial velocity was indeed confined at the vessel floor and free-

surface while the axial velocity, not only being confined around the vortex core, also exists as a positive upward flow close to the tank periphery. Both Anwar (1965) and Daggett and Keulegen (1974) say that "*it is this flow that provides energy to maintain an open vortex*". Although the writer is in agreement with this statement, a proposal for a more refined definition of the mechanics and free-surface vortex flow stability will now be presented.

As can be seen in Figure 6.36, the additional secondary axial flow field at the tank periphery that was observed experimentally in Section 6.5.2 was responsible for delivering the flow from the inlet channel to the free-surface which was then transported radially into the vortex core and subsequently discharged axially. The combined effect of the steady tangential velocity (primary) field and this superimposed secondary flow process was observed to be similar to that of a toroidal (derived from Toroid[34]) vortex as outlined in Figure 8.1.

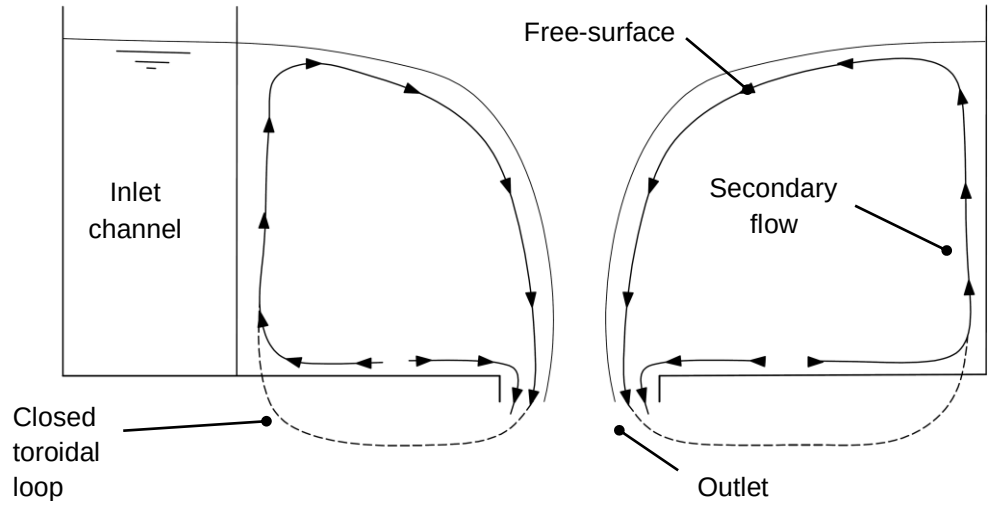

Figure 8.1: Sketch of the secondary toroidal flow structure in a cross-section of a strong free-surface vortex chamber.

In a free-surface vortex chamber, the quasi-toroidal flow structure is maintained by the constant supply of new energy to the system whereas in the full viscous toroidal flow, the

[34] A toroid is a 'doughnut' shaped geometry where its annular shape is generated by revolving a plane geometrical figure about an axis external to that figure which is parallel to the plane of the figure and does not intersect the figure.

system would otherwise form a closed loop and decay over time. This formation of a toroidal vortex is closely related to that of the well know Taylor-Couette flow.

A Taylor-Couette[35] flow is one that arises from viscous fluid motion in the gap between two concentric cylinders. It is said (Stuart, 1986) that experimental work on Taylor-Couette flows began with the work of Taylor (1923) however records date back to the experiments originally proposed by Couette (Couette, 1890). Fluid motion is derived from a difference in angular velocity in the two cylinders. For low angular velocities (based on low Re or Taylor number Ta) the flow is steady and purely azimuthal and is known as circular Couette flow (CCF). On increasing the angular velocity beyond the critical threshold Ta_{cr}, Taylor (1923) showed that the Couette flow becomes unstable and a secondary steady state flow field develops which consists of axisymmetric toroidal vortices stacked on top of each other. These secondary vortices are called Taylor vortices and the flow is then termed Taylor-Couette Flow (TCF). After further increasing the angular velocity and passing the second critical threshold, wavy vortices begin to develop (Taylor, 1923). The third instability experienced upon approaching the third critical threshold is that resulting in the generation of turbulent Taylor vortices and the secondary flow field becomes highly unstable.

To enhance the visual understanding of these possible flow processes in the vortex chamber, surface streamline data from the transient RSM (obtained in Chapter 7) were plotted on an $x - z$ plane passing through the core of the vortex. The plots are presented in Figures 8.2 – 8.4 for the three numerical test cases. Note: The streamline data appears to be asymmetric because of the reducing spiral periphery (i.e. the radial position of the left wall is less than that of the right wall). As shown, similar 'Taylor-like' vortices are observable which generally exist in pairs and are counter rotating. The transient behaviour of these vortices show that these 'Taylor-like' vortices grow unsteady as the approach flow depth is increased and are similar to the wavy vortices reported by Taylor (1923).

[35] Maurice Marie Alfred Couette, a Professor of Physics at the French university of Angers in the late 19th century.

Figure 8.2: Surface streamlines on the $x - z$ plane cutting through the vortex core for the A1 test case revealing Taylor vortices among the secondary flow field.

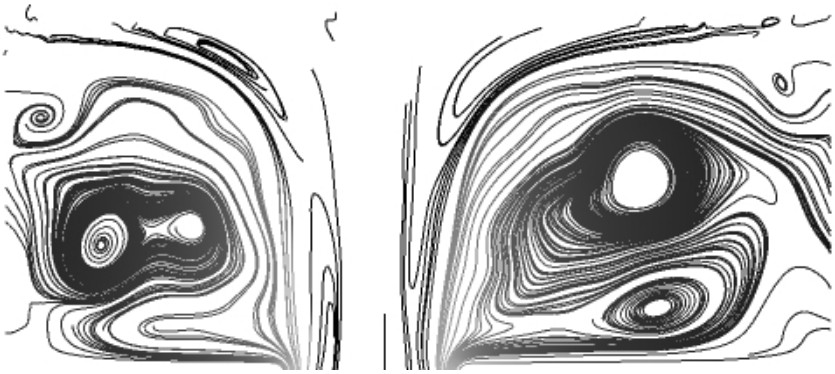

Figure 8.3: Surface streamlines on the $x - z$ plane cutting through the vortex core for the A2 test case revealing Taylor vortices among the secondary flow field.

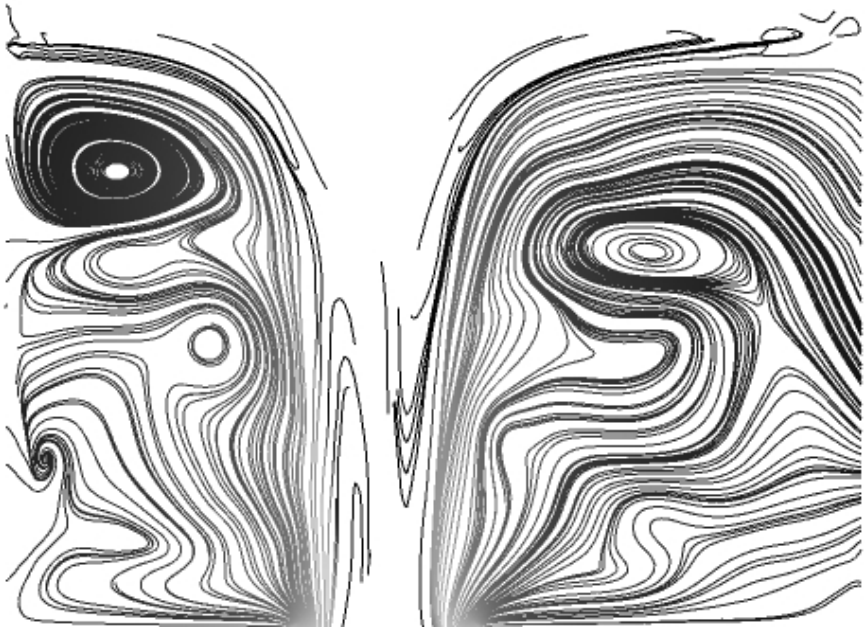

Figure 8.4: Surface streamlines on the $x - z$ plane cutting through the vortex core for the A3 test case revealing unstable Taylor vortices among the secondary flow field.

As a result of the observed similarities between the secondary flow processes in the strong free-surface vortex and that of the well-defined Taylor-Couette flow, the writer suggests a new description for the three-dimensional flow field. Here, an analogous representation for the mechanics of a strong free-surface vortex flow using a Virtual Taylor-Couette (VTC) flow system is made. An illustration of the VTC flow system is outlined in Figure 8.5. In the VTC flow, the critical air core is effectively replaced with that of a virtual internal cylinder (like in the Taylor-Couette system) which rotates at an angular velocity of:

$$\omega_c = \frac{\Gamma_{r_c}}{2\pi {a_c}^2} \tag{8.1}$$

equating to that of the real air core interface angular velocity where $\Gamma_{r_c}$is the quantity of circulation at the critical air core interface a_c. The virtual cylinder has the same effect as that of the internal rotating cylinder except that in this case the energy is continuously being replenished in the system by continuity of inlet and axial discharge. However, in the closed Taylor-Couette flow, rotation is ensured by mechanical energy or other means. If the vortex is wall bounded, such as that in a vortex chamber, then the angular velocity of the wall is zero. When it is unbounded, the flow can be virtually wall bounded with an imaginary cylinder rotating at an angular velocity of that at an arbitrary radius within the irrotational flow field determined by:

$$\omega = \frac{\Gamma_\infty}{2\pi r^2} \tag{8.2}$$

Representing the flow mechanics in such a fashion aids in describing the states of stability of a free-surface vortex in analogy to that of the TCF which will be described in the next section.

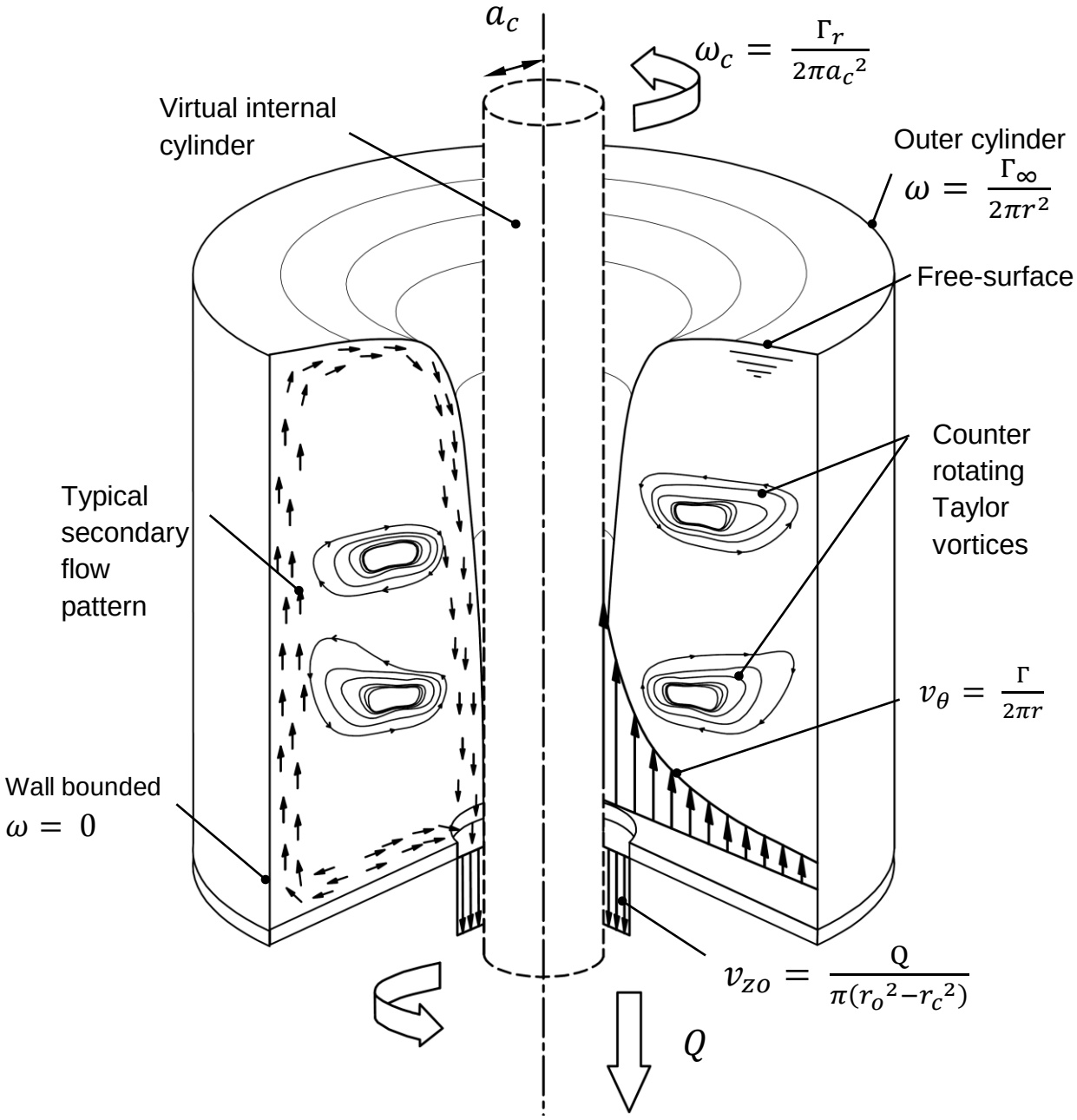

Figure 8.5: The virtual Taylor-Couette (VTC) flow system as a representation for mechanical analysis in free-surface vortices with a full air core. The left hand side is depicted as being wall bounded whereas the right hand side is depicted with an outer cylinder rotating at $\boldsymbol{\omega = \Gamma/(2\pi r^2)}$.

8.2. Stability of the Free-Surface Vortex

Previously an alternative representation for the three-dimensional flow field in a strong free-surface vortex was presented in what is termed a reverse or virtual Taylor-Couette (VTC) flow system. Like the classic Taylor-Couette flow, the VTC is subjected to various states of stability dictated by two non-dimensional numbers. The modified Taylor number given by:

$$\mathrm{Ta} = \frac{\omega^2 {a_c}^4}{\nu^2} = \frac{\Gamma_{a_c}}{2\pi\nu} \tag{8.3}$$

and the circulation number from before given by:

$$\frac{\pi}{4}\mathrm{N}\Gamma = \frac{\pi}{4}\frac{\Gamma_\infty d}{Q} \tag{8.4}$$

By observing Equations 8.3 and 8.4, it is apparent that, although the field circulation Γ_∞ has a purely stabilising effect on the strong vortex flow field, the near-field circulation at the vortex core Γ_{a_c} has the effect of destabilising the flow through the generation of unsteady Taylor vortices. The overall process and a proposed universal understanding for the transition from 'strong' to 'weak' vortex flow is now discussed with reference to Table 8.1.

For low approach flow depths h/d and large circulation Γ_∞ the vortex is in a highly stable state as $\frac{\pi}{4}\mathrm{N}\Gamma$ is large and the Taylor number $\mathrm{Ta} < \mathrm{Ta}_{c1}$. This is represented by a large internal virtual cylinder rotating at a relatively low rate. The secondary 'Taylor-like' vortices are in a relatively steady state as instabilities and perturbations in the flow are damped out by viscous forces. Upon increasing the approach flow depth h/d and discharge Q, the energy supplied to the system is subsequently increased. To conserve angular momentum with this increased energy, the virtual cylinder reduces in diameter as does the critical air core a_c. When $\mathrm{Ta}_{c1} \rightarrow \mathrm{Ta}_{c2}$, the high rotation rate at the air core interface induces a 'wavy vortex' flow (Taylor, 1923) as the secondary flow field becomes unstable. The primary flow field and the vortex structure nonetheless remains in a stable condition. Further increases in the supply energy induces what are called turbulent Taylor vortices as the virtual cylindrical radius $a_c \rightarrow 0$ and the approach flow depth approaches

the critical submergence h_{cr}/d. The Taylor vortices increase the eddy viscosity of the flow system and a turbulent vortex core of radius r_c begins to grow. The previous Taylor number Ta then becomes the turbulent Taylor number Ta_t of the form:

$$\mathrm{Ta_t} = \frac{\omega^2 {a_c}^4}{{\nu_e}^2} = \frac{\Gamma_{a_c}}{2\pi(\nu+\varepsilon)} \tag{8.5}$$

where ν is replaced with the effective viscosity $\nu_e = \nu + \varepsilon$ complying with previous investigations (Einstein and Li, 1951; Anwar, 1969). The extraordinary effect of this number is that it should begin to reduce with further increase in supply energy. This occurrence is hypothesised to be a consequence of the decrease in the near-field tangential velocities in a Rankine (1872) velocity formulation as well as the increase of the effective viscosity divisor in Equation (8.5). Both the primary and secondary flow fields are now in an unstable state and the free-surface vortex may occasionally wander. As the energy is further increased, the vortex is said to be in a dissipative 'weak' state where the turbulent vortex core grows and ultimately extinguishes rotation in the primary flow field, thus $\mathrm{Ta}_t \rightarrow 0$. In conclusion, in the strong vortex, the axial discharge is responsible for destabilising the flow; whereas when the vortex is in a 'weak' state, the destabilising effects are gradually switched to a turbulence dependent instability as a consequence of the growth of the turbulent core radius r_{ct}.

Table 8.1 Proposed stability analysis of the free-surface vortex.

Flow State	**Description**	**Taylor Number**	**Other Characters**
Stable virtual Taylor-Couette flow.	Stable primary field with a stable secondary flow comprising of Taylor-like vortices.	$\mathrm{Ta} < \mathrm{Ta_{c1}}$	$\mathrm{N_\Gamma}$ is large and h/d is low
Partially stable primary field with wavy Taylor vortices.	Semi-stable primary field with an unstable wavy secondary flow field	$\mathrm{Ta} > \mathrm{Ta_{c1}}$	Both $\mathrm{N_\Gamma}$ and h/d are low
Partially unstable primary field with turbulent Taylor vortices.	Formation of turbulent Taylor vortices.	$\mathrm{Ta} > \mathrm{Ta_{c2}}$	$\mathrm{N_\Gamma}$ is low and h/d is high
Transitional state characterised by an unstable weak vortex flow.	Instability is a consequence of a share between the axial effects and the onset of turbulence.	$\mathrm{Ta} \rightarrow \mathrm{Ta_t}$	$\mathrm{N_\Gamma}$ is low and $h/d \rightarrow h_{cr}/d$
Dissipative weak vortex flow.	Growth of the viscous core radius.	$\mathrm{Ta_t} \rightarrow 0$	$h/d > h_{cr}/d$ and $\mathrm{N_\Gamma} \rightarrow 0$

Further development and quantitative verification of this universal free-surface vortex stability hypothesis would no doubt be of substantial importance to this area of study. Such an investigation would require a comprehensive experimental analysis of the free-surface vortex paying particular attention to quantifying the critical values in Table 8.1 with additional focus made for the transitional state for critical submergence h_{cr}/d.

8.3. Conclusion

By observation of the experimental and numerical data, the writer has proposed an alternative description for the inherent flow mechanics and stability in free-surface vortices. The concept is largely founded upon the newly defined 'Virtual Taylor-Couette' (VTC) representation of the three-dimensional flow field. The VTC is analogous to that of the Taylor-Couette flow upholding all the same flow properties (existence of secondary 'Taylor-like' vortices) in the presence of a 'virtual' cylinder which occupies the physical air core of the real vortex. Both systems differ however through the inlet energy which is replenished through flow continuity in the real model and through virtual cylinder rotation in the VTC. As a result of this description, the stages of stability can be envisioned by progressive critical states of the Taylor number which are steady, wavy, turbulent and finally dissipative. In the latter state it is hypothesised that the growth of the core radius resulting from near-field turbulent eddy viscosity generation will progressively destroy the vortex motion when the Taylor number ultimately tends to a zero value. Albeit this description is somewhat qualitative as a result of the concepts early stage, it is believed that the overall description will play a significant role in the development of a universal understanding of the nature of 'weak' and 'strong' free-surface vortex flows upon further mathematical and experimental validation.

Chapter 9.

Conclusions

9.1. Summary

The subject of strong free-surface vortex flows in research is one which has not been given extensive review under certain topics relating to the primary and secondary flow fields. Contrary to its 'weak' counterpart, strong vortex flows have a stabilising effect on the flow field through a domination of the primary azimuthal flow field and therefore its applications in industry are quite extensive. It is postulated, following an increased interest in the application of free-surface vortex flows, that there was a necessity to revise this area in order to formulate methods of analysis which will subsequently aid in the development of a generic design procedure for engineering practitioners. In this dissertation, an extensive analysis of the strong free-surface vortex in a subcritical approach flow arrangement was carried out using analytical, experimental and numerical methods.

Twelve models of the vortex chamber were analysed to investigate the effects of the dependent hydraulic variables. The chamber geometries were tested in a customised hydraulic test rig designed specifically for the purpose of analysing free-surface vortex flows of various orders of magnitude. The flow was circulated through the system from a lower storage reservoir and was monitored using a magnetic flow meter. A depth gauge is used to traverse the flow field to map the approach flow depths and the free-surface profiles. The test rig was constructed primarily of planar acrylic in order to permit optical access for flow visualisation and velocimetry techniques. Particle tracking velocimetry (PTV), particle streak velocimetry (PSV) and laser induced fluorescence (LIF) techniques were employed. Illumination in the PTV and LIF techniques was provided by a Nd:YAG laser and light sheet optics. As a result of the experimental data, relationships between

the dependent parameters were constructed which highlighted the dependence of the primary flow field on the approach flow geometry. Consequently, based on these relationships, an alternative depth-discharge equation was proposed which was empirical in nature and provided a solution of the flow rate in a vortex based on the approach flow geometry alone. The new model also reproduced the curvature of the depth-discharge equation for approach flows with a high inlet Froude number Fr_i.

In addition to analysing the dependent hydraulic parameters, the mean tangential, radial and axial profiles were investigated for a radial section of the flow field assuming that the overall system was strongly axisymmetric. The data confirmed that the tangential velocity profile was independent of its subsurface depth in the far-field and away from the tank boundaries. Close to the vessel floor and water surface, the tangential velocity decreased due to effects of the secondary flow fields. The secondary flows manifest as radial and axial components. The radial velocity increased in magnitude close to the vessel floor and at the free-surface. The axial velocity was found to exist as a negative flow component near the vortex air core. Observations of a positive axial velocity field were observed near the vessel perimeter.

Regarding the tangential velocity field, it was subsequently shown that the experimental profile agrees with the ideal irrotational vortex model in the far-field with a discrepancy observed in the near-field. In the past it was assumed that this discrepancy owes to the increase of the apparent or eddy viscosity in core region. However, evidence from this work obtained in the numerical and experimental data strongly suggests that the decrease in the tangential velocity field was as a result of the strong axial velocity component and variations in the $z-$axis in this region; at least in the case of a strong vortex with a full air core. In the light of this observation, a modified tangential velocity equation was presented which corrected the ideal velocity profile to within pragmatic levels. Regarding scaling, it was found that the all of the models achieved Anwar's criterion for the Reynolds number and therefore scale effects due to viscosity were disregarded. However, out of the 72 model approach flow investigations, 4 models did not achieve the Weber number criteria and effects due to the surface tension force were expected for these approach flow conditions. Finally, in the experimental study, fluid visualisation was

performed on the secondary flows of the strong vortex using LIF. Here it was identified that the secondary flow consisted of inward positive radial bands at the vessel floor and water surface as well as an upward positive axial band at the outer walls and a downward axial velocity band superimposed around the vortex air core.

In addition to the experimental work, an extensive comparative analysis was performed on the ANSYS CFX numerical code using a multiphase homogeneous Eulerian-Eulerian approach. A case for mesh independence was highlighted which was to be strictly structured and densely refined around the vortex core. A number of turbulence model formulations were investigated for both steady state and transient analysis. The comparison showed that the shear stress transport with curvature correction SST-CC in addition to the Reynolds stress model RSM were the most suitable for modelling free-surface rotating flows where the former was the most economic and the latter was the most accurate. Transient modelling was necessary to resolve the unsteady flow field, however, the solution was found to be insensitive to time step refinement below 0.01 s. The comparison of both numerical models to all the test cases indicated that the model was capable of predicting the tangential, radial and axial velocity profiles as well as the free-surface, air core diameter and transient evolution reasonably well. Further capabilities of the model were emphasised in post processing the results for the near-field tangential and axial velocity fields as well as the secondary flow fields described previously.

Finally, in the final chapter, a proposal for an alternative description of free-surface vortex flows s made based on the insight into the experimental and numerical data. It was noted that the secondary flows observed in the LIF analysis resembled a quasi-toroidal flow. This evidence points towards a secondary flow field which was similar to that of a toroidal vortex or a Taylor-Couette flow that was maintained by the influx of new energy from the inlet. From further observation of the Reynolds stress numerical model, the secondary flow field appeared to be further comprised of ‘Taylor-like’ vortices. A newly defined ‘virtual Taylor-Couette’ representation for the strong free-surface vortex was made based on these findings. The new representation was analogous to Taylor’s (1923) description and it was hypothesised that various states of the Taylor number governed the stability of

the free-surface vortex. A hypothetical stability description was proposed which serves to provide a universal understanding for both 'weak' and 'strong' vortices and the transition between each state. Albeit the flow descriptions were qualitative in their current form, further quantitative work is required to confirm the new hypothesis.

9.2. Flow in a Strong Turbulent Free-Surface Vortex: Principle Findings

The overall deliverables and scientific/engineering contributions from the project are as follows:

- Formulated the design of an innovative test facility for studying vortex flows using non-intrusive velocimetry methods of particle tracking velocimetry and laser induced fluorescence.
- Determined a direct relationship between the air core diameter and the circulation number.

$$C_d = 0.7 - 0.68 a_c/d$$

- Revised the relationship between the Vortex number and the coefficient of discharge originally proposed by Stevens and Kolf (1959). This revised relationship consists of a two part piecewise linear curve that takes into account high circulation numbers and states that the coefficient of discharge is always a non-zero number. The relationships are described as follows:

$$C_d = \begin{cases} 0.8 - 0.25\mathrm{N_v}, & 1 < \mathrm{N_v} < 2.75 \\ 0.16 - 0.018\mathrm{N_v}, & \mathrm{N_v} > 2.75 \end{cases}$$

and when:

$$\mathrm{N}\Gamma = \infty, \; C_d \neq 0$$

- Identified the transitionally subcritical state of the flow for ($0.7 < Fr_i < 1$).
- Composed an alternative depth-discharge relationship for analysing the flow in a strong free-surface vortex. The Equation has the following form:

$$Q = \frac{k_\alpha}{\left(\frac{5\alpha d}{h}\right)^{n_\alpha}} \sqrt{g} d^{\frac{5}{2}}$$

where the auxiliary parameters are given by:

$$k_\alpha = -0.12\alpha^3 + 0.79\alpha^2 - 0.62\alpha + 0.36 \qquad \text{for } 0 < \alpha < 6 \qquad (9.1)$$

$$n_\alpha = 0.05\alpha^2 - 0.39\alpha - 0.55 \qquad \text{for } 0 < \alpha < 6 \qquad (9.2)$$

- Obtained subsurface tangential velocity data using far-field and near-field velocimetry methods.
- Confirmed that the tangential velocity is independent of the subsurface depth in a strong vortex in the far-field.
- Showed that the radial velocity is confined at the free-surface and at the vessel floor using velocimetry and PLIF techniques.
- Strong negative axial velocity gradients were observed around the vortex air core. The PLIF results also suggests that there exists a positive axial gradient at the peripheral walls of the chamber which supplies flow to the free-surface radial flow.
- Derived an alternative model to analyse the tangential velocity profile in a strong free-surface vortex given by:

$$v_\theta(r) = \frac{\Gamma_\infty}{2\pi r}\left(1 - \left(\frac{4}{\pi N_\Gamma}\right)^{\frac{mr}{d}}\right)$$

or as a function of the approach flow geometry governed by α:

$$v_\theta(r) = \frac{\Gamma_\infty}{2\pi r}\left(1 - \left(\frac{h}{5\alpha d}\right)^{\frac{mr}{d}}\right)$$

where $m = 2$ is found to provide the best approximation of the flow field using the available data.

- A multiphase numerical model was fully investigated and a comparative analysis with the available experimental data shows to reproduce physical data to within a 20 % accuracy.
- A textual best practice guideline as a result of this study is described as follows: Two phase fluid modelling using a numerical model can provide reasonable accuracy provided that a finely structured mesh is used with refinement to within 1.5 % of the orifice or air core diameter in addition to using a proper transient turbulence model formulation such as the shear stress transfer model with curvature correction or the Reynolds stress model with time steps below at least 0.01s.
- Observed the generation of steady and unsteady Taylor vortices in the secondary flow field using the numerical data.
- Proposed the virtual Taylor-Couette (VTC) flow system as a representation of the flow mechanics in addition to the likely stages of 'weak' and 'strong' free-surface vortex stability based on a modified Taylor number Ta.

9.3. Recommendations and Outlook

As a result of this study, the writer is currently compiling the following papers:

- Mechanics of Strong Free-surface vortex flows: An alternative tangential velocity model.
- Turbulence modelling of strong free-surface vortex flows using a transient multiphase simulation.
- Discharge coefficient in a strong free-surface vortex.
- Introduction to the 'Virtual Taylor Couette' (VTC) flow description of strong free-surface vortices.

However, throughout this study a number of other very interesting topics surfaced which unfortunately could not be addressed in further technical detail. The list of topics are outlined below and the author suggests that each would form the core of an excellent

future hydraulics research study. The recommended areas for further research are as follows:

- Refinement of the near-field velocimetry technique to resolve the vortex core velocity profiles in greater detail. The result would lead to resolving the dependence of the tangential velocity field on the z −axis in this region as well as other trends.
- Investigate, in detail, the growth of the turbulent vortex core by measuring the maximum tangential velocities as a means to indirectly observe the turbulent eddy viscosity.
- Perform a quantitative study on the concept of the 'virtual Taylor-Couette' flow system.
- Perform a study of the stability of the vortex core in a free-surface vortex flow by monitoring the viscous and turbulent vortex cores and near- and far-field tangential velocities in order to observe the development of the modified Taylor number with particular focus on the hypothesised critical states outlined in Table 8.1 of Section 8.2.
- Experimental velocity analysis of the annular jet in the drop shaft in addition the generation of shear and strain rate in the energy dissipation process.
- Investigate and refine the scale effects of strong free-surface vortex flows with regards surface tension and viscosity.
- Evaluate the m-number in the modified tangential velocity profile to observe its dependence on the approach flow geometry.
- Further investigate the effect free-surface and courant number refinement around the air core and annular jet in the CFX multiphase numerical model.
- Investigation of the effect of interphase transfer using the in-homogeneous multiphase flow model. It would also be important to analyse the effects of surface tension force in the model based on proposed methods.

- Numerical analysis of the ‘Taylor-like’ vortices in the secondary flow field of a free-surface vortex.

The overall study has thus provided a good framework from which future studies can be based or developed including strong recommendations for prospective investigations which should significant implication in this field, both theoretical and practical in nature.

References

Aboelkassem, Y. (2003) *On the decay of strong concentrated columnar vortices.* Concordia University.

Aboelkassem, Y. and Vatistas, G. H. (2007) 'On the refracted patterns produced by liquid vortices', *Acta Mechanica Sinica,* 23(1), pp. 11-15.

Aboelkassem, Y., Vatistas, G. H. and Esmail, N. (2005) 'Viscous dissipation of Rankine vortex profile in zero meridional flow', *Acta Mechanica Sinica,* 21(6), pp. 550-556.

Ackers, P. and Crump, E. S. (1960) 'The vortex drop'. *ICE Proceedings*: Thomas Telford, 433-442.

Adami, A. (1967) 'Analisi del moto in uno scaricatore a vortice'. *L'Energia Elettrica.*

Adrian, R. J. (1991) 'Particle-imaging techniques for experimental fluid mechanics', *Annual review of fluid mechanics,* 23(1), pp. 261-304.

Adrian, R. J. and Westerweel, J. (2011) *Particle image velocimetry.* Cambridge University Press.

Al'tshul, A. and Margolin, M. S. (1968) 'Effect of vortices on the discharge coefficient for flow of a liquid through an orifice', *Hydrotechnical Construction,* 2(6), pp. 507-510.

Amphlett, M. (1978) *Air-entraining Vortices at a Vertically Inverted Intake.* Hydraulics Research Station, Wallingford, England.

Andersen, A., Bohr, T., Stenum, B., Rasmussen, J. J. and Lautrup, B. (2006) 'The bathtub vortex in a rotating container', *Journal of Fluid Mechanics,* 556, pp. 121-146.

Anderson, S. H. (1961) 'Model Studies of Storm-Sewer Drop Shafts'. St. Anthony Falls Hydraulic Laboratory

Ansar, M., Nakato, T. and Constantinescu, G. (2002) 'Numerical simulations of inviscid three-dimensional flows at single-and dual-pump intakes', *Journal of Hydraulic Research,* 40(4), pp. 461-470.

ANSYS 2013. Lecture 3: Volume of Fluid (VOF) - Advanced Multiphase Training.

ANSYS, C. (2009) 'ANSYS CFX-solver theory guide', *ANSYS CFX Release,* 11, pp. 69-118.

Anwar, H. (1965) 'Flow in a free vortex', *Water Power,* 4, pp. 153-161.

Anwar, H. (1968a) 'Prevention of vortices at intakes', *Water Power,* Vol. 20, No. 10, pp. 393-401.

Anwar, H. (1968b) 'Vortices in a viscous fluid', *Journal of Hydraulic Research,* 6(1), pp. 1-14.

Anwar, H. (1969) 'Turbulent flow in a vortex', *Journal of Hydraulic Research,* 7(1), pp. 1-29.

Anwar, H. O. (1966) 'Formation of a weak vortex', *Journal of Hydraulic Research,* 4(1), pp. 1-16.

Anwar, H. O. and Amimilett, M. (1980) 'Vortices at vertically inverted intake', *Journal of Hydraulic Research,* 18(2), pp. 123-134.

Anwar, H. O., Weller, J. A. and Amphlett, M. B. (1978) 'Similarity of free-vortex at horizontal intake', *Journal of Hydraulic Research,* 16(2), pp. 95-105.

Barth, T. J. and Jespersen, D. C. (1989) 'The design and application of upwind schemes on unstructured meshes'. 27th Aerospace Sciences Meeting

Benjamin, T. B. (1962) 'Theory of the vortex breakdown phenomenon', *Journal of Fluid Mechanics,* 14(04), pp. 593-629.

Benjamin, T. B. (1965) 'Significance of the vortex breakdown phenomenon', *Journal of Fluids Engineering,* 87(2), pp. 518-522.

Berge, J. (1966) 'A study of vortex formation and other abnormal flow in a tank with and without a free surface', *La Houille Blanche*.

Bhagwat, M. J. and Leishman, J. G. (2002) 'Generalized viscous vortex model for application to free-vortex wake and aeroacoustic calculations'. *Annual Forum Proceedings-American Helicopter Society*: American Helicopter Society.

Binnie, A. (1938) 'The use of a vertical pipe as an overflow for a large tank', *Proceedings of the Royal Society of London. Series A, Mathematical and Physical Sciences*, pp. 219-237.

Binnie, A. (1964) 'Some experiments on the bath-tub vortex', *Journal of Mechanical Engineering Science,* 6(3), pp. 256-257.

Binnie, A. and Davidson, J. (1949) 'The flow under gravity of a swirling liquid through an orifice-plate', *Proceedings of the Royal Society of London. Series A, Mathematical and Physical Sciences*, pp. 443-457.

Binnie, A. and Hookings, G. (1948) 'Laboratory experiments on whirlpools', *Proceedings of the Royal Society of London. Series A. Mathematical and Physical Sciences,* 194(1038), pp. 398-415.

Binnie, W. (1937) 'Bellmouthed Weirs and Tunnel Outlets for the Disposal of Flood Waters', *Transactions of the Institution of Water Engineers,* 42, pp. 103-146.

Borghei, S. and Kabiri Samani, A. (2003) 'Critical submergence of vertical intakes using anti-vortex plates'. *Proc. of,* 59-66.

Boussinesq, J. (1877) 'Théorie de l'écoulement tourbillant', *Mem. Présentés par Divers Savants Acad. Sci. Inst. Fr,* 23(46-50), pp. 6.5.

Brackbill, J., Kothe, D. B. and Zemach, C. (1992) 'A continuum method for modeling surface tension', *Journal of computational physics*, 100(2), pp. 335-354.

Brocard, D. N., Beauchamp, C. H., & Hecker, G. E. (1983). 'Analytic predictions of circulation and vortices at intakes'. Final report. Worcester Polytechnic Inst., Holden, MA (USA). Alden Research Lab..Brombach, H. (1982) 'Flow control for the outlets from stormwater retention basins', *Wasserwirtschaft*, 72(2), pp. 44-52.

Buckingham, E. (1915) 'The principle of similitude', *Nature*, 96, pp. 396-397.

Burgers, J. (1995) 'Hydrodynamics.—Application of a model system to illustrate some points of the statistical theory of free turbulence', *Selected Papers of JM Burgers*: Springer, pp. 390-400.

Burgers, J. M. (1948) 'A mathematical model illustrating the theory of turbulence', *Advances in applied mechanics*, 1, pp. 171-199.

Carriveau, R., Kopp, G. A. and Baddour, R. E. (2009) 'Free-surface stretching-sustained intake vortices', *Journal of Hydraulic Research*, 47(4), pp. 486-491.

Casulli, V. (2015). Lecture notes on advanced numerical methods for free-surface hydrodynamics. Stanford, June 1993 - Trento, January 2015.

Casulli, V. and Cheng, R. T. (1992) 'Semi-implicit finite difference methods for three-dimensional shallow water flow', *International Journal for numerical methods in fluids*, 15(6), pp. 629-648.

Chen, Y., Wu, C., Wang, B. and Du, M. (2012) 'Three-dimensional numerical simulation of vertical vortex at hydraulic intake', *Procedia Engineering*, 28, pp. 55-60.

Chen, Y.-l., Chao, W., Mao, Y. and Ju, X.-m. (2007) 'Hydraulic characteristics of vertical vortex at hydraulic intakes', *Journal of Hydrodynamics, Ser. B*, 19(2), pp. 143-149.

Chong, M., Perry, A. E. and Cantwell, B. (1990) 'A general classification of three-dimensional flow fields', *Physics of Fluids A: Fluid Dynamics (1989-1993)*, 2(5), pp. 765-777.

Ciaravino, G. and Ciaravino, L. (2007) 'Verification of an alternative mathematical model for design of vortex dropshafts'. *Proceedings of the congress- International association for hydraulic research (IAHR)*, 677.

Ciaravino, G., Galasso, V., Mancini, P. and Pulci Doria, G. (1987). A mathematical model for vortex shaft: Theory and experimental control.

Constantinescu, G. and Patel, V. (2000) 'Role of turbulence model in prediction of pump-bay vortices', *Journal of Hydraulic Engineering*, 126(5), pp. 387-391.

Constantinescu, S. G. and Patel, V. C. (1997) *Numerical simulation of flow in pump bays using near-wall turbulence models.* University of Iowa.

Conway, A. E. (1971) *Guide to fluidics.* London: Macdonald.

Couette, M. F. A. (1890) *Etudes sur le frottement des liquides.* Gauthier-Villars.

Cristofano, L., Nobili, M. and Caruso, G. (2014) 'Experimental study on unstable free surface vortices and gas entrainment onset conditions', *Experimental Thermal and Fluid Science,* 52, pp. 221-229.

Cristofano, L., Nobili, M. and Caruso, G. (2014) 'Numerical evaluation of gas core length in free surface vortices'. *Journal of Physics: Conference Series*: IOP Publishing.

Cristofano, L., Nobili, M., Romano, G. and Caruso, G. (2014) 'Velocity profiles in bathtub vortices: validation of analytical models'. *32nd UIT Heat Transfer Conference*.

Daggett, L. L. and Keulegan, G. H. (1974) *Similitude Conditions in Free-Surface Vortex Formations*: DTIC Document.

Denny, D. (1956) 'An experimental study of air-entraining vortices in pump sumps', *Proceedings of the Institution of Mechanical Engineers,* 170(1), pp. 106-125.

Desmukh, T. S. and Gahlot, V. (2010) 'Simulation of Flow Through a Pump Sump and its Validation', *Civil Engineering Department, MANIT, Bhopal, IJRRAS,* 4(1).

Dhakal, S., Timilsina, A. B., Dhakal, R., Fuyal, D., Bajracharya, T. R., Pandit, H. P., Amatya, N. and Nakarmi, A. M. (2015) 'Comparison of cylindrical and conical basins with optimum position of runner: Gravitational water vortex power plant', *Renewable and Sustainable Energy Reviews,* 48, pp. 662-669.

Dhillon, G. (1979) 'Vortex Formation at Pipe Intakes and its Prediction: a Status Report', *Irrigation and Power Research Institute, Punjab, Report No. HY.*

Dracos, T. (1996) *Three-dimensional velocity and vorticity measuring and image analysis techniques: lecture notes from the short course held in Zuerich, Switzerland, 3-6 September 1996.* Springer Science & Business Media.

Drioli, C. (1947) 'Su un particolare tipo di imbocco per pozzi di scarico (scaricatore idraulico a vortice)', *L'Energia Elettrica,* 24(10), pp. 447-452.

Drioli, C. (1969) 'Esperienze su installazioni con pozzo di scarico a vortice', *L'Energia Elettrica,* 66(6), pp. 399-409.

Durgin, W. and Hecker, G. 'The modeling of vortices at intake structures'. (1978) *Proceedings of the ASCE/ASME/IAHR Joint Symposium on the Design and Operation of Fluid Machinery, Fort Collins, Colo,* 12-14.

Dyakowski, T. and Williams, R. (1993) 'Modelling turbulent flow within a small-diameter hydrocyclone', *Chemical Engineering Science,* 48(6), pp. 1143-1152.

Echavez, G. and McCann, E. (2002) 'An experimental study on the free surface vertical vortex', *Experiments in Fluids,* 33(3), pp. 414-421.

Egorov, Y. and Menter, F. (2008) 'Development and application of SST-SAS turbulence model in the DESIDER project', *Advances in Hybrid RANS-LES Modelling*: Springer, pp. 261-270.

Egorov, Y., Menter, F., Lechner, R. and Cokljat, D. (2010) 'The scale-adaptive simulation method for unsteady turbulent flow predictions. Part 2: Application to complex flows', *Flow, Turbulence and Combustion,* 85(1), pp. 139-165.

Einstein, H. A. and Li, H. (1951) 'Steady vortex flow in a real fluid', *Proc. Heat Transfer and Fluid Mechanics Institute, Stanford University*, pp. 33-43.

ETH (1977) *ETH, Jahresbericht, 1977 der Versuchsanstalt fur Wasserbau*, Hydrologie und Glaziologie an der ETH, Zurich, Switzerland.

Ezure, T., Kimura, N., Miyakoshi, H. and Kamide, H. (2011) 'Experimental investigation on bubble characteristics entrained by surface vortex', *Nuclear Engineering and Design,* 241(11), pp. 4575-4584.

Feynman, R. P. (1955) 'Chapter II Application of quantum mechanics to liquid helium', *Progress in low temperature physics,* 1, pp. 17-53.

Gang, L., Jian-min, Z., Jian-Gang, C., Fei, Y. and Lu, L. (2011) '3-D Numerical simulation research of flow in a vortex drop shaft which have two volute chambers with aeration'. *Proceedings of the 34th World Congress of the International Association for Hydro-Environment Research and Engineering: 33rd Hydrology and Water Resources Symposium and 10th Conference on Hydraulics in Water Engineering*: Engineers Australia, 1779.

Gordon, J. (1970) 'Vortices at intakes', *Water Power,* 22(4), pp. 137-138.

Green, S. I. (1995) *Fluid vortices: fluid mechanics and its applications.* Springer Science & Business Media.

Grotjans, H. and Menter, F. (1998) 'Wall functions for general application {CFD} codes'.

Gulliver, J. S. (1988) 'Discussion of "Free-Surface Air Core Vortex" by A. Jacob Odgaard (July, 1986, Vol. 112, No. 7)', *Journal of Hydraulic Engineering,* 114(4), pp. 447-449.

Hager, W. H. (1985) 'Head-discharge relation for vortex shaft', *Journal of hydraulic engineering,* 111(6), pp. 1015-1020.

Hager, W. H. (1990) 'Vortex drop inlet for supercritical approaching flow', *Journal of Hydraulic Engineering,* 116(8), pp. 1048-1054.

Hager, W. H. (2010) *Wastewater hydraulics: Theory and practice.* Springer Science & Business Media.

Haindl, K. (1959) 'Contribution to Air Entrainment by a Vortex (Paper 16-D)'. *Proceedings of the XIX IAHR Congress: New Delhi, India*, 2-7.

Hall, M. (1966) 'The structure of concentrated vortex cores', *Progress in Aerospace Sciences,* 7, pp. 53-110.

Hecker, G. E. (1981) 'Model-Prototype Comparision of Free Surface Vortices', *Journal of the Hydraulics Division,* 107(10), pp. 1243-1259.

Heller, V. (2011). Scale effects in physical hydraulic engineering models. Journal of Hydraulic Research, 49(3), 293-306.

Helmholtz, H. (1858) 'About integrals of hydrodynamic equations related with vortical motions', *J. für die reine Angewandte Mathematik,* 55, pp. 25.

Hirt, C. (1992) 'Volume-fraction techniques: Powerful tools for flow modeling', *Flow Sci. Rep. FSI-92-00,* 2.

Hirt, C. W. and Nichols, B. D. (1981) 'Volume of fluid (VOF) method for the dynamics of free boundaries', *Journal of computational physics,* 39(1), pp. 201-225.

Hite Jr, J. E. and Mih, W. C. (1994) 'Velocity of air-core vortices at hydraulic intakes', *Journal of hydraulic Engineering,* 120(3), pp. 284-297.

Hughes, R. L. (1975). Similitude in free-surface vortex formation - Discussion ASCE-AMER Soc. Civil Engineers, New York, NY.

Ito, K., Sakai, T., Eguchi, Y., Monji, H., Ohshima, H., Uchibori, A. and Xu, Y. (2010) 'Improvement of Gas Entrainment Prediction Method—Introduction of Surface Tension Effect—', *Journal of nuclear science and technology,* 47(9), pp. 771-778.

Jain, A. K., Garde, R. J. and Ranga Raju, K. G. (1978) 'Vortex formation at vertical pipe intakes', *Journal of the Hydraulics Division,* 104(10), pp. 1429-1445.

Jain, S. C. (1984) 'Tangential vortex-inlet', *Journal of Hydraulic Engineering,* 110(12), pp. 1693-1699.

Jain, S. C. (1988) 'Air transport in vortex-flow drop shafts', *Journal of Hydraulic Engineering,* 114(12), pp. 1485-1497.

Jain, S. C. and Ettema, R. (1987) 'Vortex-flow intakes', in Knauss, J. (ed.) *Swirling flow problems at intakes, IAHR Hydraulic Structures Design Manual*. Balkema, Rotterdam,The Netherlands, pp. 125–137.

Jain, S. C. and Kennedy, J. F. (1983) *Vortex-flow drop structures for the Milwaukee Metropolitan Sewerage District inline storage system.* Iowa Institute of Hydraulic Research, the University of Iowa.

JCR, H., Wray, A. and Moin, P. (1988) 'Eddies, stream, and convergence zones in turbulent flows', *Center for turbulence research report CTR-S88,* pp. 193-208.

Jeanpierre, D. and Lachal, A. (1966) 'Dissipation d'énergie dans un puits à vortex', *La Houille Blanche,* (7), pp. 823-832.

Jeong, J. and Hussain, F. (1995) 'On the identification of a vortex', *Journal of fluid mechanics,* 285, pp. 69-94.

Jevdjevich, V. and Levin, L. (1953) 'Entrainment of air in flowing water and technical problems connected with it'. *Proceedings Minnesota International Hydraulic Convention*: ASCE, 439-454.

Johansson, L., Ovesen, M., & Hallberg, C. (2002), Self-organizing Flow Technology. Institute of Ecological Technology, Scientific and Technical Reports – 1, Malmo, Sweden.

Kabiri-Samani, A. and Borghei, S. (2013) 'Effects of anti-vortex plates on air entrainment by free vortex', *Scientia Iranica,* 20(2), pp. 251-258.

Kalinske, A. (1940) 'Hydraulics of vertical drain and overflow pipes', *Iowa Institute of Hydraulics Research*.

Kassner, R. and Knoernschild, E. (1950) *Friction laws and energy transfers in circular flow.* Air Materiel Command.

Kaufmann, W. (1962). Uber die ausbreitung kreiszlindrischer Wirbel in Zahen Flussigkeiten. Ing. Arch.

Kellenberger, M. H. (1988) 'Wirbelfallschächte in der Kanalisationstechnik', *Mitteilungen der Versuchsanstalt fur Wasserbau, Hydrologie und Glaziologie an der Eidgenossischen Technischen Hochschule Zurich,* (98), pp. 1-367.

Keller, J., Egli, W. and Exley, J. (1987) 'Force-and loss-free transitions between vortex flow states', *Studies of Vortex Dominated Flows*: Springer, pp. 63-75.

Keller, J. J. (1995) 'The critical cross-section of a vortex', *Zeitschrift für angewandte Mathematik und Physik ZAMP,* 46(1), pp. 122-148.

Kelvin, W. T. B. (1869) *On vortex motion.* Royal Society of Edinburgh.

Kimura, N., Ezure, T., Tobita, A. and Kamide, H. (2008) 'Experimental study on gas entrainment at free surface in reactor vessel of a compact sodium-cooled fast reactor', *Journal of nuclear science and technology,* 45(10), pp. 1053-1062.

Kleinschroth, A. and Wirth, H. (1981) *Dimensionierung von Wirbelfallschächten unter Berücksichtigung verschiedener Zuflussbedingungen.* Lehrstuhl für Hydraulik u. Gewässerkunde, Techn. Univ. München.

Klimenko, A. (1998) 'Evolution of vorticity in the bathtub vortex', *Proceedings of the13th Australasian Fluid Mechnaics Conference,* Monash University, Melbourne Australia, pp. 18.

Knapp, F. H. (1960) *Ausfluss, Überfall und Durchfluss im Wasserbau: eine angewandte Hydraulik auf physikalischer Grundlage.* G. Braun.

Knauss, J. (1972) *Vortices and Swirling Flow at Low Head Intakes in Pumped Storage Schemes.* Technical University in Munich, Research Institute for Hydraulic Engineering.

Knauss, J. E. (1987) *Swirling flow problems at intakes.* A A Balkema.

Kolf, R. and Zielinski, P. (1959) 'The vortex chamber as an automatic flow-control device', *Journal of the Hydraulics Division,* 85(12), pp. 1-8.

Kolmogorov, A. N. (1991) 'Equations of turbulent motion in an incompressible fluid'. *Dokl. Akad. Nauk SSSR,* 299-303.

Lamb, H. (1932) *Hydrodynamics.* Cambridge university press.

Launder, B. and Sharma, B. (1974) 'Application of the energy-dissipation model of turbulence to the calculation of flow near a spinning disc', *Letters in heat and mass transfer,* 1(2), pp. 131-137.

Laushey, L. M. (1953). Studies show Pittsburgh how to drop sewage 90ft vertically to tunnel interceptors. Engineering News Records.

Laushey, L. M. and Mavis, F. T. (1952) *Flow in vertical shafts,* Algheny County Sanitary Authority: Department of Civil Engneeing and Construction. Carnegie Institute of Technology. Pittsburgh. Pennsylvania.

Levi, E. (1983) 'A fluidic vortex device for water treatment processes', *Journal of Hydraulic Research,* 21(1), pp. 17-31.

Li, H.-f., Chen, H.-x., Zheng, M. and Yi, Z. (2008) 'Experimental and numerical investigation of free surface vortex', *Journal of Hydrodynamics, Ser. B,* 20(4), pp. 485-491.

Li, S., Lai, Y., Weber, L., Silva, J. M. and Patel, V. (2004) 'Validation of a three-dimensional numerical model for water-pump intakes', *Journal of Hydraulic Research,* 42(3), pp. 282-292.

Lima, M., Palma, J. and Areal, P. (2002) 'Scalar Measurements by Laser Induced Fluorescence'. *Proceedings do 11th International. Symposium on Applications of Laser Techniques to Fluid Mechanics,* 8-11.

Lugt, H. J. (1983) 'Vortex flow in nature and technology', *New York, Wiley-Interscience, 1983, 305 p. Translation.,* 1.

Lundgren, T. (1985) 'The vortical flow above the drain-hole in a rotating vessel', *Journal of Fluid Mechanics,* 155, pp. 381-412.

Majumdar, S. (1988) 'Role of underrelaxation in momentum interpolation for calculation of flow with nonstaggered grids', *Numerical Heat Transfer,* 13(1), pp. 125-132.

Marris, A. (1967) 'Theory of the bathtub vortex', *Journal of Applied Mechanics,* 34(1), pp. 11-15.

Martinerie, R., Müller, M., De Cesare, G. and Boillat, J.-L. (2008) 'Vortices at intake works of pump-storage schemes'. *6th ISUD-International Symposium on Ultrasonic Doppler Methods for Fluid Mechanics and Fluid Engineering*: Czech Technical University in Prague-Institute of Hydrodynamics AS CR, vvi.

McCorquodale, J. (1961) 'Discussion of "scale effects in swirling flows"', *J. Hydr. Div., ASCE,,* 95(1).

Menter, F. and Egorov, Y. (2010) 'The scale-adaptive simulation method for unsteady turbulent flow predictions. Part 1: theory and model description', *Flow, Turbulence and Combustion,* 85(1), pp. 113-138.

Menter, F. R. (1993) 'Zonal two equation k-turbulence models for aerodynamic flows', *AIAA paper,* 2906, pp. 1993.

Menter, F. R. (1994) 'Two-equation eddy-viscosity turbulence models for engineering applications', *AIAA journal*, 32(8), pp. 1598-1605.

Mih, W. (1990) 'Analysis Of Fine Particle Concentrations In A Combined Vortex: GH Vatistas, Vol 27, No. 3, 1989, pp. 417-427'.

Mihalas, D. and Weibel-Mihalas, B. (1999) *Foundations of radiation hydrodynamics.* Courier Corporation.

Morton, B. R. (1966) 'Geophysical vortices', *Progress in Aerospace Sciences*, 7, pp. 145-194.

Motzet, K. M. and Valentin, F. (2002) 'Efficiency of a vortex chamber with horizontal bottom under supercritical flow'. *IX International Conference on Urban Drainage*.

Monji, H., Shinozaki, T., Kamide, H., & Sakai, T. (2010). Effect of experimental conditions on gas core length and downward velocity of free surface vortex in cylindrical vessel. Journal of Engineering for Gas Turbines and Power, 132(1), 012901.

Mudkavi, V. Y. (1993) 'The phenomenon of vortex breakdown'.

Mulligan, S. and Casserly, J. (2010) 'The Hydraulic Design and Optimisation of a Free Water Vortex for the Purpose of Power Extraction', *Final Year Civil Engineering Project, Institute of Technology Sligo*.

Mulligan, S. and Hull, P. (2010) 'Design and optimization of a water vortex hydropower plant', *Eng. Thesis, Institute of Technology Sligo, Sligo, Irland*.

Möller, G. (2013) *Vortex-induced air entrainment rate at intakes.* Diss., Eidgenössische Technische Hochschule ETH Zürich, Nr. 21277, 2013.

Möller, G., Detert, M. and Boes, R. (2012) 'Air entrainment due to vortices—state-of-the-art'. *Proc. 2ndIAHR European Congress Munich, Germany*.

Nakayama, A. and Jiao, D. (2001) 'Velocity-gradient tensor and local topology of three-dimensional flows in intake bay'. Proceedings of the Congress – International Association for Hydraulics Research, 442-447.

Odgaard, A. J. (1986) 'Free-surface air core vortex', *Journal of Hydraulic Engineering*, 112(7), pp. 610-620.

Ogawa, A. (1992) *Vortex flow.* CRC Press.

Okamura, T., Kamemoto, K. and Matsui, J. (2007) 'CFD prediction and model experiment on suction vortices in pump sump'. *Proceedings of the 9th Asian International Conference on Fluid Machinery. Jeju, Korea.*

Padmanabhan, M. and Hecker, G. E. (1984) 'Scale effects in pump sump models', *Journal of Hydraulic Engineering*, 110(11), pp. 1540-1556.

Pandazis, P. and Blömeling, F. (2014) 'Investigation of the critical submergence at pump intakes based on multiphase CFD calculations', *Advances in Fluid Mechanics X*, 10, pp. 143.

Pica, M. (1968). Discussion: Scale Effects in Swirling Flow. Universita Di Napoli Istituti Idraulici.

Pica, M. (1970) 'Scaricatori a vortice', *L'Energia Elettrica,* 47(4), pp. 1-18.

Posey, C. and Hsu, H. (1950) 'How the vortex affects orifice discharge', *Engin. News-Record*.

Prandtl, L. (1925) 'Report on investigation of developed turbulence', *NACA Report TM-1231*.

Quick, M. C. (1961) *A study of the free spiral vortex.* University of Bristol.

Quick, M. C. (1970) 'Efficiency of air-entraining vortex formation at water intake', *Journal of the Hydraulics Division,* 96(7), pp. 1403-1416.

Quick, M. C. (1990) 'Analysis of spiral vortex and vertical slot vortex drop shafts', *Journal of Hydraulic Engineering,* 116(3), pp. 309-325.

Raffel, M., Willert, C. E. and Kompenhans, J. (2013) *Particle image velocimetry: a practical guide.* Springer.

Rajendran, V., Constantinescu, S. and Patel, V. (1999) 'Experimental validation of numerical model of flow in pump-intake bays', *Journal of hydraulic Engineering,* 125(11), pp. 1119-1125.

Rankine, W. J. M. (1872) *A manual of applied mechanics.* Charles Griffin and Company.

Research, I. (2014). Worldwide High Performance Computing 2013 Total Market Model and 2014–18 Forecast.

Reynolds, O. (1886) 'XXVIII. On the flow of gases', *The London, Edinburgh, and Dublin Philosophical Magazine and Journal of Science,* 21(130), pp. 185-199.

Reynolds, O. (1894) 'On the dynamical theory of incompressible viscous fluids and the determination of the criterion', *Proceedings of the Royal Society of London,* 56(336-339), pp. 40-45.

Rhie, C. and Chow, W. (1983) 'Numerical study of the turbulent flow past an airfoil with trailing edge separation', *AIAA journal,* 21(11), pp. 1525-1532.

Rider, W. J. and Kothe, D. B. (1998) 'Reconstructing volume tracking', *Journal of computational physics,* 141(2), pp. 112-152.

Rosenhead, L. (1930) 'The spread of vorticity in the wake behind a cylinder', *Proceedings of the Royal Society of London. Series A, Containing Papers of a Mathematical and Physical Character*, pp. 590-612.

Rott, N. (1958) 'On the viscous core of a line vortex', *Zeitschrift für angewandte Mathematik und Physik ZAMP,* 9(5-6), pp. 543-553.

Rouse, H. (1943) *On the role of eddies in fluid motion*: DTIC Document.

Rutschmann, P., Volkart, P. and Vischer, D. (1987) 'Design recommendations. Intake structures', *Swirling flow problems at intakes. IAHR hydraulic structures design manual. Rotterdam*.

Sakai, T., Eguchi, Y., Monji, H., Ito, K. and Ohshima, H. (2008) 'Proposal of design criteria for gas entrainment from vortex dimples based on a computational fluid dynamics method', *Heat Transfer Engineering*, 29(8), pp. 731-739.

Sarkardeh, H., Reza Zarrati, A., Jabbari, E. and Marosi, M. (2014) 'Numerical Simulation and Analysis of Flow In A Reservoir In The Presence of Vortex', *Engineering Applications of Computational Fluid Mechanics*, 8(4), pp. 598-608.

Sarkardeh, H., Zarrati, A. R. and Roshan, R. (2010) 'Effect of intake head wall and trash rack on vortices', *Journal of Hydraulic Research*, 48(1), pp. 108-112.

Schmitt, F. G. (2007) 'About Boussinesq's turbulent viscosity hypothesis: historical remarks and a direct evaluation of its validity', *Comptes Rendus Mécanique*, 335(9), pp. 617-627.

Scorer, R. (1967) 'Local instability in curved flow', *IMA Journal of Applied Mathematics*, 3(3), pp. 250-265.

Scully, M. (1975) *Computation of helicopter rotor wake geometry and its influence on rotor harmonic airloads*. Massachusetts Institute of Technology.

Shabara, H., Yaakob, O., Ahmed, Y. M., Elbatran, A. and Faddir, M. S. (2015) 'CFD Validation for Efficient Gravitational Vortex Pool System', *Jurnal Teknologi*, 74(5).

Shabara, H. M., et al. (2015). 'CFD Simulation of Water Gravitation Vortex Pool Flow for Mini Hydropower Plants.' Jurnal Teknologi.

Shapiro, A. (1969). Film Notes for Vorticity. Encyclopedia Britannica Educational Corporation, Chicago, Illinois.

Shapiro, A. H. (1962) 'Bath-tub vortex', *Nature*, 196, pp. 1080-1081.

Shaari, K. Z. K., and Awang, M. (Eds.). (2015). Engineering Applications of Computational Fluid Dynamics. Springer International Publishing.

Shetty, R., Vogel, S. N., Ostriker, E. C. and Teuben, P. J. (2007) 'Kinematics of spiral-arm streaming in M51', *The Astrophysical Journal*, 665(2), pp. 1138.

Shi, X., Yang, F., Dai, R., Chen, T. and Wu, Y. (2012) 'Simulation of free-surface vortex produced by a rotating cylindrical wall below a static barrel'. *IOP Conference Series: Earth and Environmental Science*: IOP Publishing, 052034.

Shur, M. L., Strelets, M. K., Travin, A. K. and Spalart, P. R. (2000) 'Turbulence modeling in rotating and curved channels: Assessing the Spalart-Shur correction', *AIAA journal*, 38(5), pp. 784-792.

Sibulkin, M. (1983) 'A Note on the Bathtub Vortex and the Earth's Rotation', *American Scientist,* 71, pp. 352-353.

Škerlavaj, A., Škerget, L., Ravnik, J. and Lipej, A. (2011) 'Choice of a turbulence model for pump intakes', *Proceedings of the Institution of Mechanical Engineers, Part A: Journal of Power and Energy*, pp. 0957650911403870.

Škerlavaj, A., Škerget, L., Ravnik, J. and Lipej, A. (2014) 'Predicting Free-Surface Vortices with Single-Phase Simulations', *Engineering Applications of Computational Fluid Mechanics,* 8(2), pp. 193-210.

Sommeria, J., Meyers, S. D. and Swinney, H. L. (1988) 'Laboratory simulation of Jupiter's great red spot', *Nature,* 331(6158), pp. 689-693.

Spalart, P. and Shur, M. (1997) 'On the sensitization of turbulence models to rotation and curvature', *Aerospace Science and Technology,* 1(5), pp. 297-302.

Stephens, D. and Mohanarangam, K. (2010) 'Turbulence model analysis of flow inside a hydrocyclone', *Progress in Computational Fluid Dynamics, an International Journal,* 10(5-6), pp. 366-373.

Stevens, J. C. and Kolf, R. C. (1959) 'Vortex flow through horizontal orifices', *Transactions of the American Society of Civil Engineers,* 124(1), pp. 871-883.

Stuart, J. (1986) 'Taylor-vortex flow: a dynamical system', *SIAM review,* 28(3), pp. 315-342.

Suerich-Gulick, F., Gaskin, S., Villeneuve, M., Holder, G. and Parkinson, E. (2006) 'Experimental and numerical analysis of free surface vortices at a hydropower intake'. *Proceedings of the 7th International Conference on Hydroscience and Engineering*, 1-11.

Suerich-Gulick, F., Gaskin, S. J., Villeneuve, M. and Parkinson, É. (2013) 'Characteristics of Free Surface Vortices at Low-Head Hydropower Intakes', *Journal of Hydraulic Engineering,* 140(3), pp. 291-299.

Suerich-Gulick, F., Gaskin, S. J., Villeneuve, M. and Parkinson, É. (2014) 'Free surface intake vortices: theoretical model and measurements', *Journal of Hydraulic Research,* 52(4), pp. 502-512.

Suerich-Gulick, I. F. (2013) *Axial stretching, viscosity, surface tension and turbulence in free surface vortices at low-head hydropower intakes.* PhD Thesis. McGill University.

Taghvaei, S., Roshan, R., Safavi, K. and Sarkardeh, H. (2012) 'Anti-vortex structures at hydropower dams', *International Journal of Physical Sciences,* 7(28), pp. 5069-5077.

Tang, X., Wang, F., Li, Y., Cong, G., Shi, X., Wu, Y. and Qi, L. (2011) 'Numerical investigations of vortex flows and vortex suppression schemes in a large pumping-station sump', *Proceedings of the Institution of Mechanical Engineers, Part C: Journal of Mechanical Engineering Science,* 225(6), pp. 1459-1480.

Taylor, G. I. (1923) 'Stability of a viscous liquid contained between two rotating cylinders', *Philosophical Transactions of the Royal Society of London. Series A, Containing Papers of a Mathematical or Physical Character*, pp. 289-343.

Taştan, K. and Yildirim, N. (2010) 'Effects of dimensionless parameters on air-entraining vortices', *Journal of Hydraulic Research*, 48(1), pp. 57-64.

Tokyay, T. and Constantinescu, S. (2005) 'Coherent structures in pump intake flows: A Large Eddy Simulation study'. *31st International Association Hydraulic Research Congress, Seoul, Korea*: Citeseer.

Trefethen, L. M., Bilger, R., Fink, P., Luxton, R. and Tanner, R. (1965) 'The bath-tub vortex in the southern hemisphere'. Nature 207, 1084 – 1085.

Trivellato, F. (2010) 'Anti-vortex devices: Laser measurements of the flow and functioning', *Optics and Lasers in Engineering*, 48(5), pp. 589-599.

Trivellato, F., Bertolazzi, E. and Firmani, B. (1999) 'Finite volume modelling of free surface draining vortices', *Journal of computational and applied mathematics*, 103(1), pp. 175-185.

Trivellato, F. and Ferrari, (2002) W. 'A finite difference model for intake vortices'. *Proc. 3rd Int. Congress on Hydraulic Engineering, Holguin, Cuba*.

Trivellato, F. and Springhetti, F. (2001) *Comparison of Anti-vortex Devices:(experimental Database)*. Università di Trento. Dipartimento di ingegneria civile ed ambientale (IS).

Tsubota, M. (2009) 'Quantum turbulence: from superfluid helium to atomic Bose–Einstein condensates', *Contemporary Physics*, 50(3), pp. 463-475.

Urbani, C. and Steinmann, A. (2010) 'Research and Development Project for the hydrological, electrical and materials technological optimization of water vortex power plants', Report Version 09.11.2010, Water Vortex Power Plants Switzerland.

Vatistas, G., Lin, S. and Kwok, C. (1986) 'Theoretical and experimental studies on vortex chamber flows', *AIAA journal*, 24(4), pp. 635-642.

Vatistas, G. H., Kozel, V. and Mih, W. (1991) 'A simpler model for concentrated vortices', *Experiments in Fluids*, 11(1), pp. 73-76.

Viparelli, M. (1950) 'Su un particolare tipo di imbocco e sull'efflusso con vortice', *L'Energia Elettrica,* 27(10), pp. 610-624.

Viparelli, M. (1954) 'Trasporto di aria da parte di correnti idriche in condotti chiusi', *L'Energia elettrica,* (11), pp. 813-826.

Wang, Y.-k., Jiang, C.-b. and Liang, D.-f. (2010) 'Investigation of air-core vortex at hydraulic intakes', *Journal of Hydrodynamics, Ser. B*, 22(5), pp. 696-701.

Weller, J. A. (1974) 'Similitude in free-surface vortex formations; Discussion of Daggett & Keulegan', *Journal of the Hydraulics Division ASCE*, 101, HY11.

Wendt, J. (2008) *Computational fluid dynamics: an introduction.* Springer Science & Business Media.

White, A. C., Anderson, B. P. and Bagnato, V. S. (2014) 'Vortices and turbulence in trapped atomic condensates', *Proceedings of the National Academy of Sciences,* 111(Supplement 1), pp. 4719-4726.

Wilcox, D. C. (1988) 'Reassessment of the scale-determining equation for advanced turbulence models', *AIAA journal,* 26(11), pp. 1299-1310.

Wilcox, D. C. (1998) *Turbulence modeling for CFD.* DCW industries La Canada, CA.

Woodford, D. (1964) 'Prediction of the length of the air core in vortices of weak circulation', *La Houille Blanche,* (8), pp. 889-898.

Wójtowicz, P. and Szlachta, M. (2013) 'Aeration performance of hydrodynamic flow regulators', *Water Science & Technology*, 67(12), pp. 2692-2698.

Yakhot, V., Orszag, S., Thangam, S., Gatski, T. and Speziale, C. (1992) 'Development of turbulence models for shear flows by a double expansion technique', *Physics of Fluids A: Fluid Dynamics (1989-1993),* 4(7), pp. 1510-1520.

Yang, J., Liu, T., Bottacin-Busolin, A. and Lin, C. (2014) 'Effects of intake-entrance profiles on free-surface vortices', *Journal of Hydraulic Research,* 52(4), pp. 523-531.

Yildirim, N. and Jain, S. C. (1981) 'Surface tension effect on profile of a free vortex', *Journal of the Hydraulics Division,* 107(1), pp. 132-136.

Yu, D. and Lee, J. H. (2007) 'Design of tangential vortex intakes for stormwater diversion'. *Proc. 32nd Congress of the International Association of Hydraulic Engineering and Research (IAHR), Venice*.

Yu, D. and Lee, J. H. (2009) 'Hydraulics of tangential vortex intake for urban drainage', *Journal of hydraulic engineering*, 135(3), pp. 164-174.

Zhou, J., Adrian, R. J., Balachandar, S. and Kendall, T. (1999) 'Mechanisms for generating coherent packets of hairpin vortices in channel flow', *Journal of Fluid Mechanics,* 387, pp. 353-396.

Zielinski, P. B. and VillemoZhang, Q., & Yang, Y. (2013). A new simpler rotation/curvature correction method for Spalart–Allmaras turbulence model. Chinese Journal of Aeronautics, 26(2), 326-333.nte, J. R. (1968) 'The Effect of Viscosity on Vortex-Orifice Flow', *Journal of the Hydraulics Division ASCE,* 94, No. HY3, pp. 745-752. .

Zotloeterer, F. (2009) Hydroelectric power station. Google Patents.

Appendix A

Physical Model Design

This section briefly outlines the construction practice employed in building the physical models that are used in the experimental study in Section 5.3. The step by step guide is as follows:

Plywood Jig Fabrication

1. Using the geometry for the periphery of the vortex chamber walls (determined from the equation of the logarithmic spiral in Section 5.3), a template is accurately marked on a sheet of 20 mm plywood. The template has an inward reduced size of 8 mm throughout the tank periphery in order to account for moulding the 6 mm acrylic wall on a 2 mm plywood surface. The template is terminated at the inlet.
2. The templates are carefully cut along the template lines using a band saw.
3. The exact length of each templates outside periphery is measured. The length is transferred to a sheet of bending or flexi-ply with a width of 250 mm (vortex chamber depth) and is cut accordingly.
4. The bending plywood cut in Step 3 is secured onto the plywood edges of each template using tack nails. This is started from the inside (smallest radius) as shown in Figure A1 while progressing outwards along the tank periphery to complete the jig.

Figure A.1: Securing the flexible plywood to the template as per Step 5.

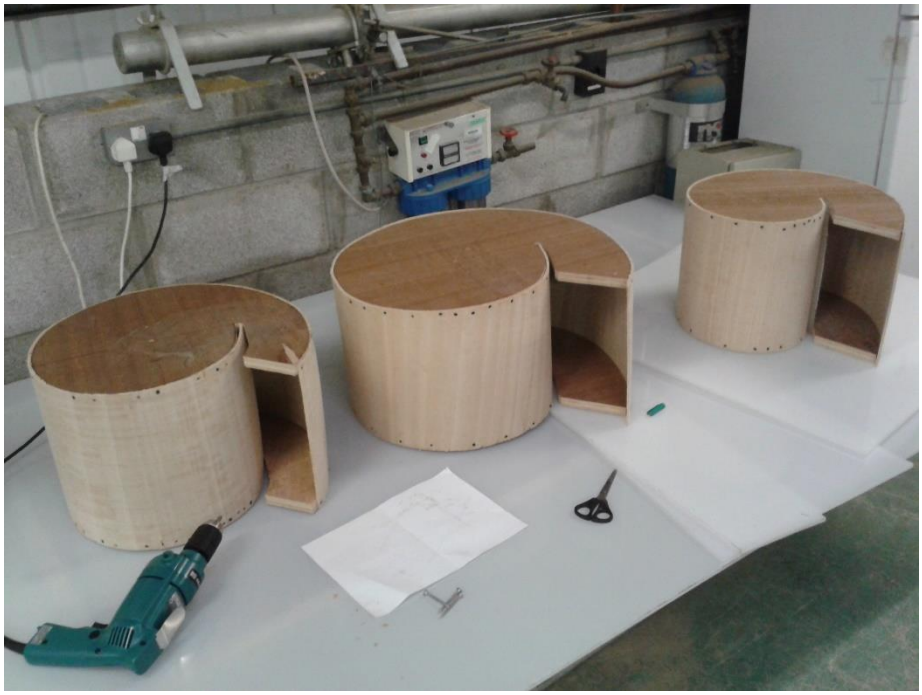

Figure A.2: Three of the finished acrylic forming jigs.

Acrylic forming

1. Using the length measurement obtained in Step 3 of the previous section along with the known width of 250 mm, corresponding to the chamber height, a 6 mm thick rectangular section of acrylic is accurately cut.
2. The heating device (in this case, a geotechnical drying furnace) is preheated to 165°, the temperature recommended to oven form acrylic.
3. The acrylic is left resting horizontally in the oven on a steel grill for approximately 12-15 minutes. It is checked regularly to monitor its mouldability. When the acrylics flexibility is high enough (marked by its ability to be easily folded) it is deemed to be in the correct state for moulding.
4. The acrylic sheet is quickly removed from the oven and is formed into the jig. Starting from the innermost radius, the acrylic is formed around the spiral surface of the jig by rolling. Any kinks or irregularities can easily be 'ironed' out using a plate and heat gun while the acrylic is still hot.

Base and inlet walls

1. Apart from the acrylic wall fabrication previously discussed, the base is considered the second most important Step of the fabrication process. This is because it must be designed and cut correctly as to fit in the correct location in the test rig.
2. The acrylic base is pre-marked using a template established from the test tank in which it will be fitted. The marked base is cut accordingly.
3. The 67 mm orifice is bored subsequently. Because the orifice plays a significant role in the model performance, this process is performed using a power drill and a moderate speed along with constant monitoring of the orifice diameter using a vernier callipers.
4. Using the dismantled jig from before, one of the templates is used to mark the position of the wall on the base which accurately centred around the orifice. This marking then highlights the exact position of the inlet walls which are measured back to the flow inlet at the tank corner.

5. The precise length of the inlet walls are measured accordingly. The walls (250 mm high) are then cut out on 6 mm acrylic.
6. Two grooves are accommodated at the base to fix the inlet water tight sealing plates. The grooves are 7 mm thick in order to accommodate the 6 mm acrylic and the 1.5 mm neoprene material after it is compressed.
7. The plates are measured according to the base geometry and are cut out on 6 mm acrylic. This section finishes the fabrication of each model component which in total consist of 2 × inlet walls, 2 × water tight plates, 1 × base and 1 × spiral wall.

Assembly

1. Beginning with the Chamber periphery, the spiral wall is aligned with the base markings of the previous step. The wall is 'tacked' in position initially using an impact solvent adhesive. Some irregularities in the tank position as a result of cooling may need to be forced into position and held in place at this stage.
2. When the periphery is secured in place, the inlet walls are secured in a similar fashion using the template marking on the base.
3. Finally the water tight sealing plates are positioned and fixed using the impact solvent adhesive.
4. In order to ensure the whole chamber is water tight, a clear silicone sealant is subsequently injected into all the gaps throughout the model. The sealant is applied from the outside as to ensure that there are no inconsistencies on the model inner surface which may affect measurements.
5. The exact area of the sealing plates are measured and transferred to 1.5 mm neoprene which is cut using a stanley blade. A similar cutting is made for a square 200 × 200 mm at the base of the tank which to also perform as a water tight seal at the inlet. The neoprene is glued to the water tight plates using a compression grip.
6. The overall model(s) are left to dry.
7. Finally, the position of the 15 bolt holes, for installing in the test rig are marked on the water tight sealing surfaces. The holes, 6 mm in diameter are subsequently bored using a power drill.

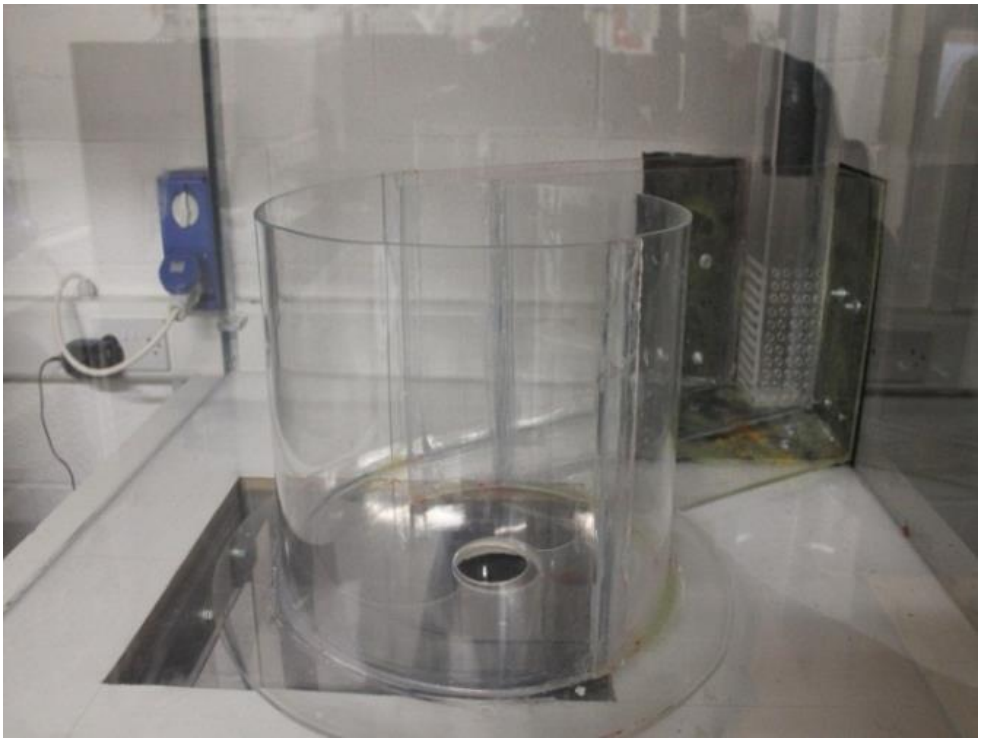

Figure A.3: Model #4.0d1.0d installed in the tank

Figure A.4: 12 fabricated vortex chamber geometries.

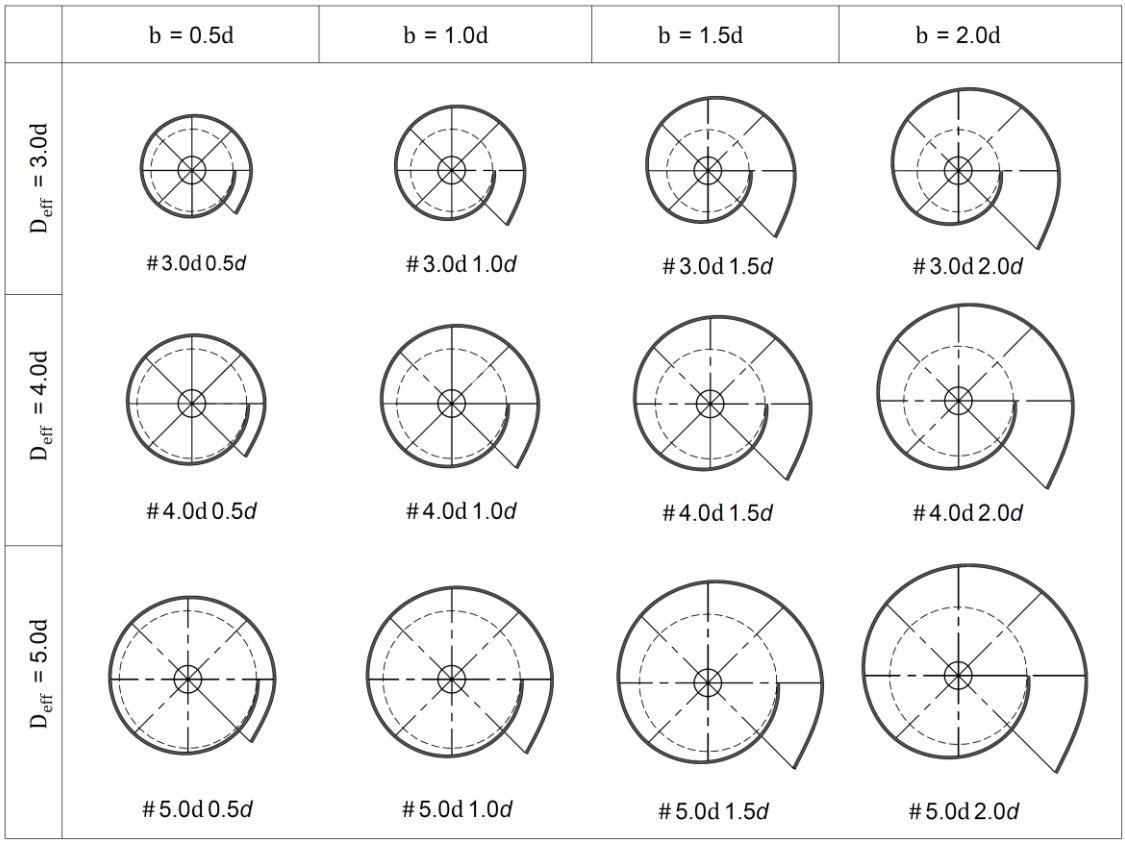

Figure A.5: 12 vortex chamber geometries.

Appendix B

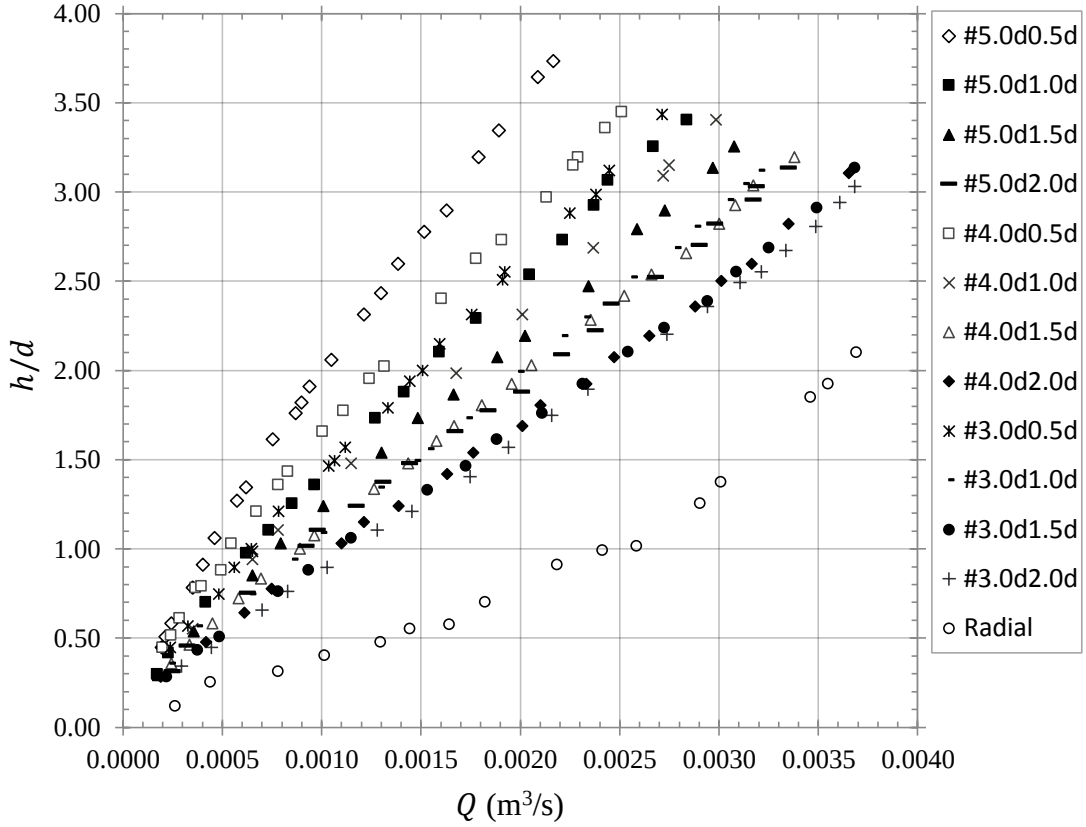

Figure B.1: Approach flow depth $\boldsymbol{h/d}$ v discharge $\boldsymbol{Q}$ for all vortex chambers and the radial flow model. The curves only indicate the trend of the experimental data.

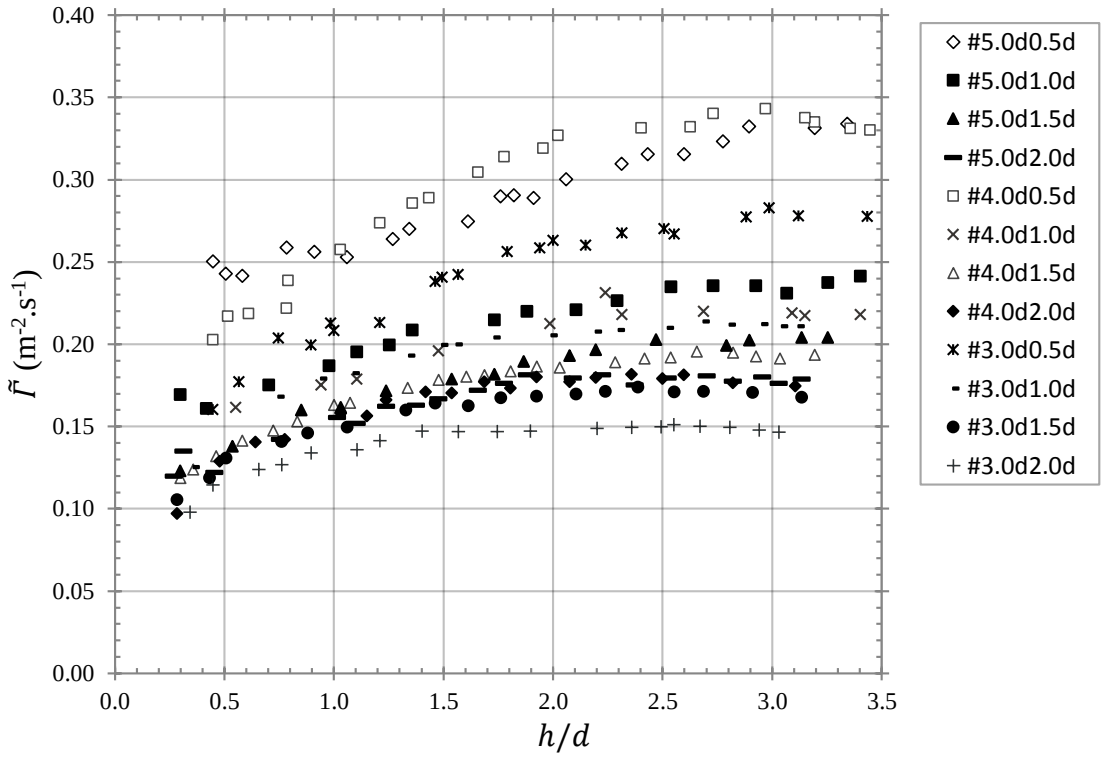

Figure B.2: Bulk circulation $\tilde{\Gamma}$ v approach flow depth h/d for all vortex chambers. The curves only indicate the trend of the experimental data.

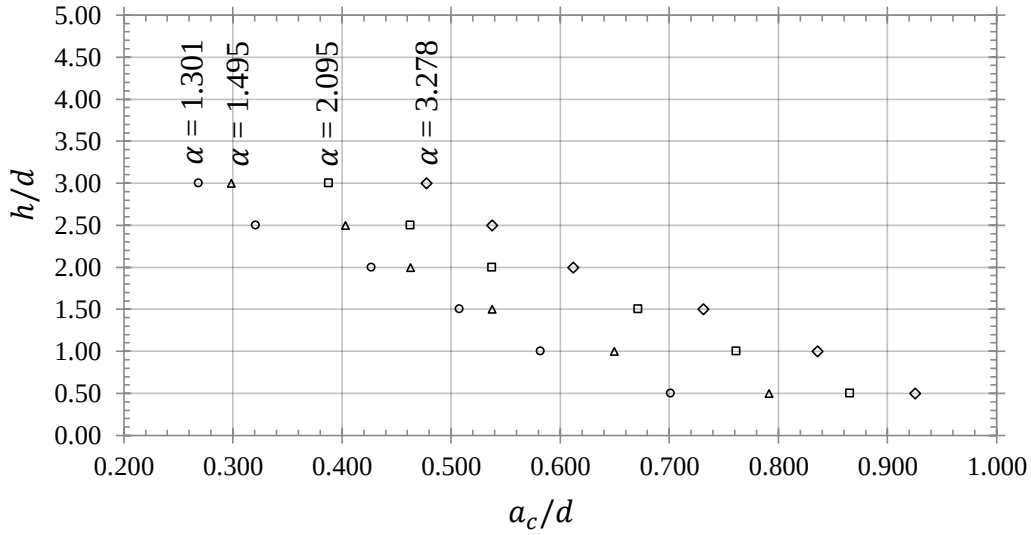

Figure B.3: Approach flow depth $\boldsymbol{h/d}$ v critical air core diameter $\boldsymbol{a_c}$ for the #3.0$\boldsymbol{d}$ model series. The curves only indicate the trend of the experimental data.

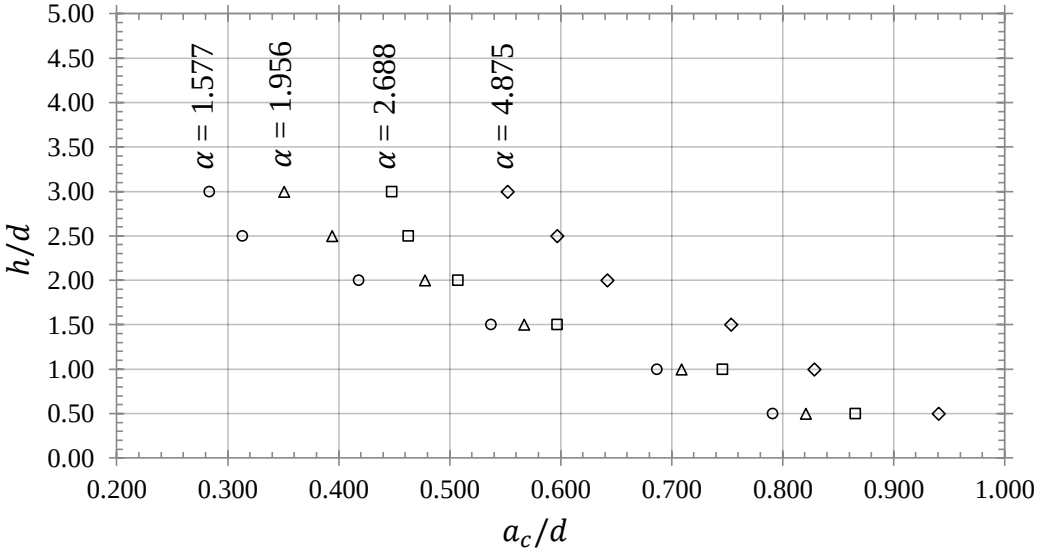

Figure B.4: Approach flow depth $\boldsymbol{h/d}$ v critical air core diameter $\boldsymbol{a_c}$ for the #4.0$\boldsymbol{d}$ model series. The curves only indicate the trend of the experimental data.

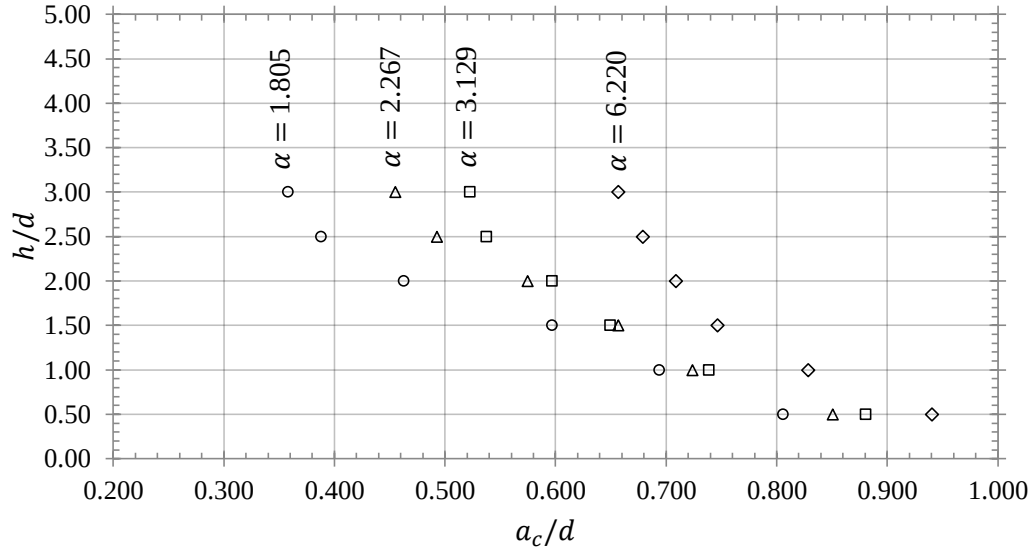

Figure B.5: Approach flow depth $\boldsymbol{h/d}$ v critical air core diameter $\boldsymbol{a_c}$ for the #5.0$\boldsymbol{d}$ model series. The curves only indicate the trend of the experimental data.

Circulation and Discharge Number Trends

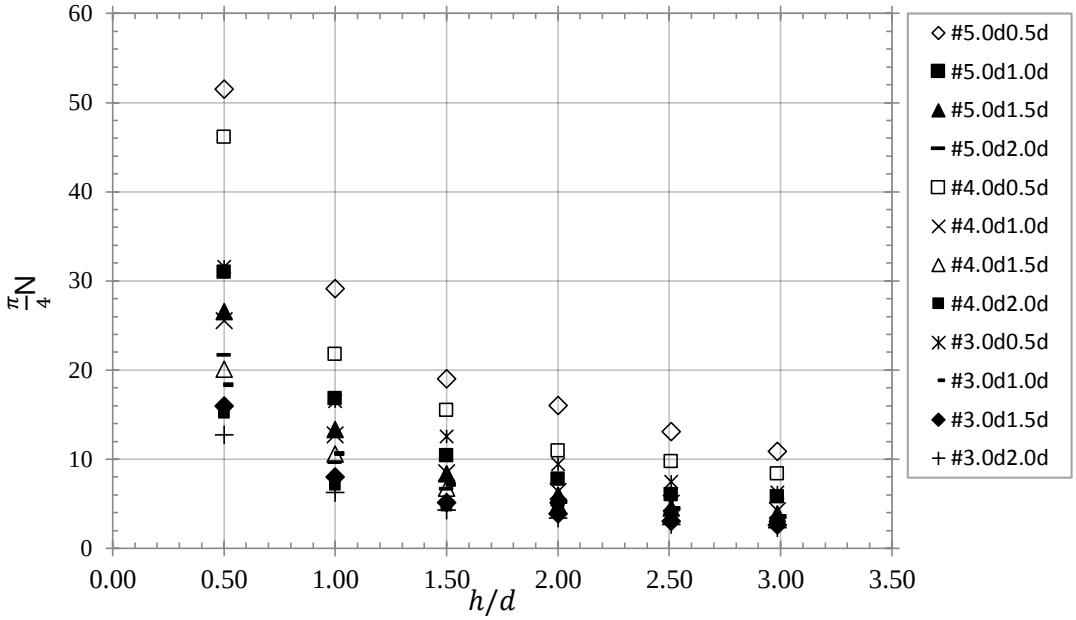

Figure B.6: Circulation number $\frac{\pi}{4}N_\Gamma$ versus approach flow depth $\boldsymbol{h/d}$ for all models. The curves only indicate the trend of the experimental data.

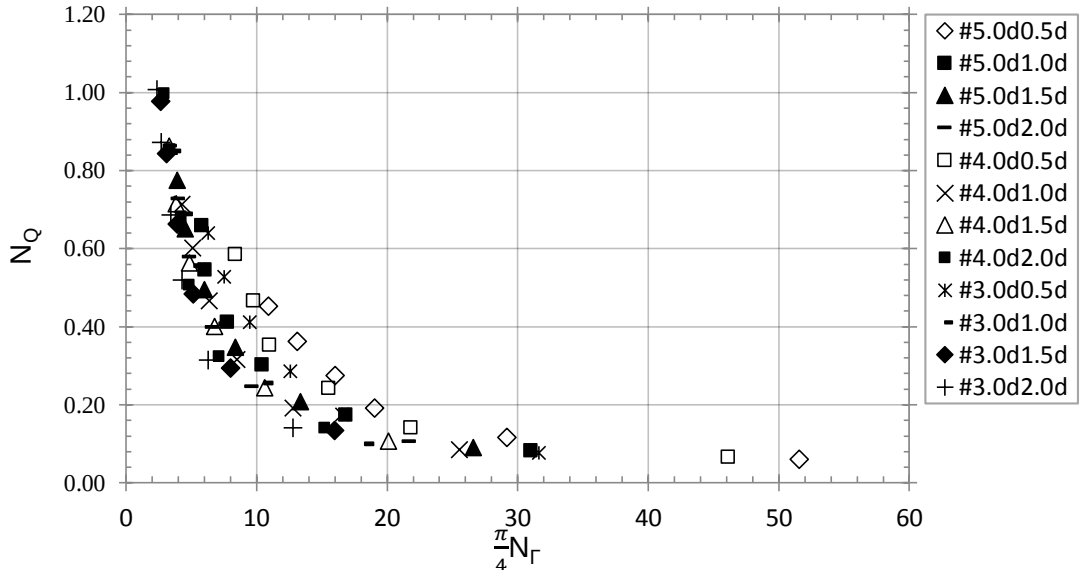

Figure B.7: Discharge number N_Q versus the circulation number $\frac{\pi}{4}N_\Gamma$ for all models. The curves only indicate the trend of the experimental data.

Appendix C

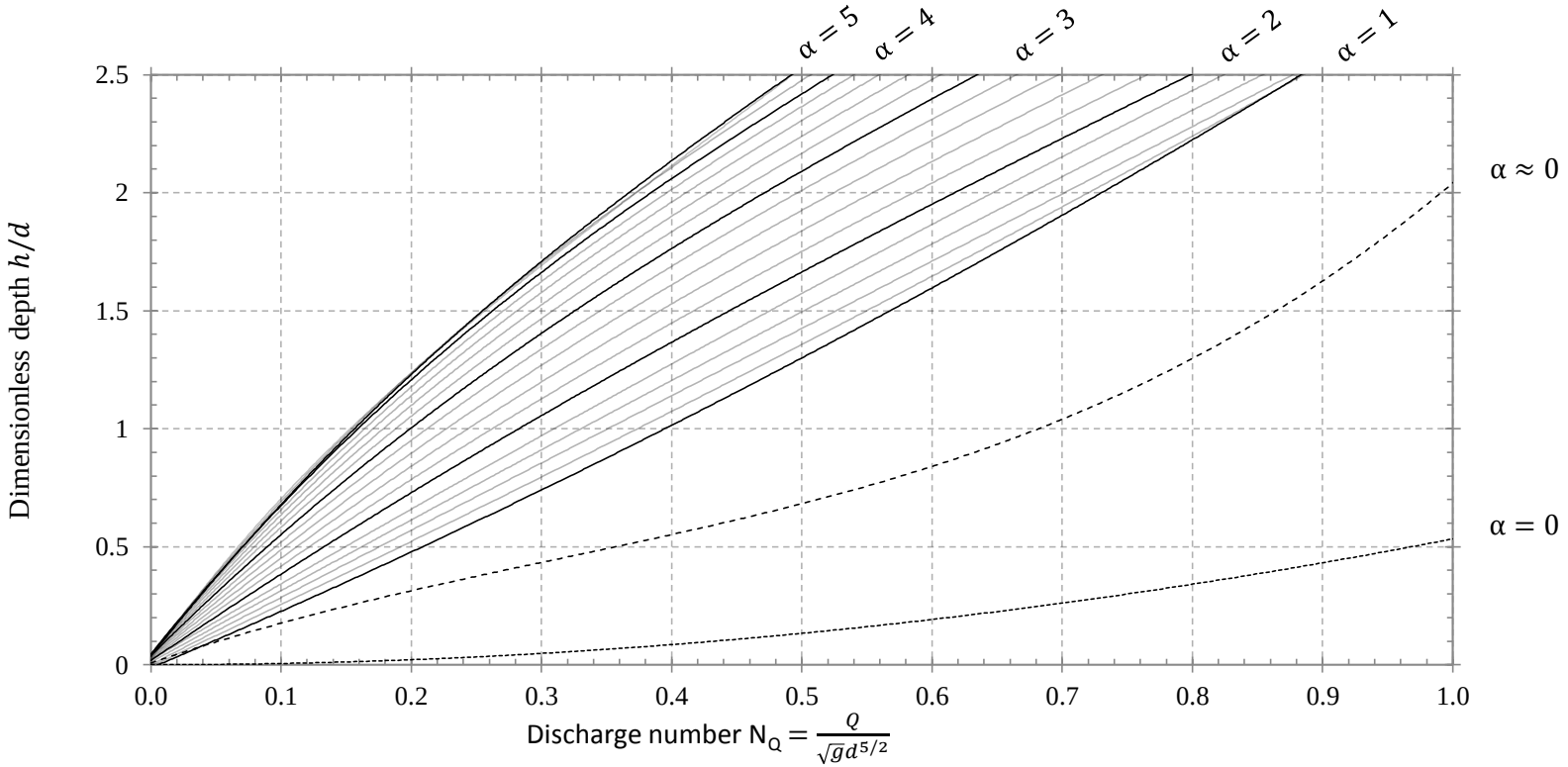

Figure C.1: Depth-discharge chart for strong free surface vortices with a subcritical approach flow.

Appendix D

Peer Reviewed Research Papers

Paper 1

Hydrodynamic Investigation of Free-Surface Turbulent Vortex Flows with Strong Circulation in a Vortex Chamber

5th International Junior Researcher and Engineer Workshop Spa, Belgium, 28-30 August 2014 on Hydraulic Structures (IJREWHS2014)

S. Mulligan, J. Casserly and R. Sherlock

Published at the University of Liege -
http://popups.ulg.ac.be/IJREWHS2014/index.php?id=168)

Paper 2

Experimental Modelling of Flow in an Open Channel Vortex Chamber

E-proceedings of the 36th IAHR World Congress 28 June – 3 July, 2015, The Hague, the Netherlands.

S. Mulligan, J. Casserly and R. Sherlock

Paper 3

Experimental and Numerical Modelling of Free-Surface Turbulent Flows in Full Air-Core Water Vortices

In Advances in Hydroinformatics (pp. 549-569). Springer Singapore.

S. Mulligan, J. Casserly and R. Sherlock

Paper 4

Effects of Geometry on Strong Free-Surface Vortices with a Subcritical Approach Flow

Submitted to the Journal of Hydraulic Engineering (ASCE) (May 2015)

S. Mulligan, J. Casserly and R. Sherlock